NASA-CR-178,109

NASA-CR-178109
19860018903

NASA Contractor Report 178109

FEASIBILITY STUDY OF OPTICAL BOUNDARY LAYER TRANSITION DETECTION METHOD

M. Azzazy, D. Modarress, and J. D. Trolinger

SPECTRON DEVELOPMENT LABORATORIES, INC.
Costa Mesa, California

Contract NAS1-17293
June 1986

NASA
National Aeronautics and
Space Administration

Langley Research Center
Hampton, Virginia 23665

TABLE OF CONTENTS

N86-28375 #

TABLE OF CONTENTS CONTINUED

TABLE OF CONTENTS CONTINUED

LIST OF FIGURES

LIST OF FIGURES CONTINUED

LIST OF FIGURES CONTINUED

APPENDICES

LIST OF FIGURES CONTINUED

NO. PAGE

LIST OF FIGURES CONTINUED

LIST OF FIGURES CONTINUED

LIST OF FIGURES CONTINUED

LIST OF TABLES

1.0 INTRODUCTION

1.1 Theoretical Basis

Numerical validation of the flow field around aerodynamic prototypes tested in wind tunnels often requires independent knowledge of the region where transition from laminar flow to turbulent flow takes place. Boundary layer transition is a function of several parameters, such as model surface roughness, the level of freestream turbulence, the flow Reynolds number and Mach number ... etc. Therefore, the region of transition not only depends on the fluid flow parameters, but the model and wind tunnel conditions affect the transition region as well. Determination of the location of boundary layer transition is also important to other applications such as Laminar Flow Control (LFC) which has been used extensively to reduce the skin friction drag, and to improve the range, endurance, payload and fuel consumption of long range aircraft. Hefner, et al, and Hough reviewed the different methods of delaying the region of transition in the boundary layer, however, the anatomy of transition and its relation to turbulent flow still requires more research.

The transition region is generally recognized by the onset of turbulent spots which play a key role in the evolution of laminar to turbulent boundary layer flows. Turbulent spots and their relation to transition received special attention since the classical experiments of Schubauer and Klebanoff. A turbulent spot in a laminar boundary layer at constant pressure is essentially a single large horseshoe (Perry, et al, called it Λ-shaped) vortex structure which moves downstream with its ends slipping along the surface (Cantwell et al). Wygnanski, et al, and Coles, et al, showed that the apex of the Λ-shaped vortex which rests on the line of symmetry, moves at 0.77 U_∞, while the tails of that vortex lag behind at 0.64 U_∞, where U_∞ is the freestream velocity. At high speed flows, viz., transonic or supersonic, the transition region is characterized by density and temperature fluctuations as well as velocity fluctuations. Therefore, measuring the density fluctuations has become the focus of several methods leading to a boundary layer transition detector at transonic and supersonic speeds. Since the heat transfer coefficient in the transition region experiences a tremendous increase over its laminar or turbulent flow value due to high temperature fluctuations in the flow, surface gages based on measuring the amount of heat transfer became a popular tool in detecting the transition region. However, surface gages are difficult to implement and use on aerodynamic prototypes. Optical techniques to measure small density fluctuations and, hence, detect boundary layer transition provide an alternative to measuring the heat transfer. Holographic and interferometic techniques can measure optical pathlength variations (density fluctuations) on the order of a small fraction of a wavelength, however, such techniques need more modifications to be applied to boundary layer transition detection.

1.2 Survey of Boundary Layer Transition Detectors

Techniques for detection of boundary layer transition presently used for tests in transonic and supersonic wind tunnels are generally intrusive and model dependent. Oil sublimation methods (Cassels et al), and smoke wire techniques (Betill et al) were used as a tool to visually locate the region of transition. Flow visualization techniques, although providing valuable information about the interface separation between the laminar and turbulent regions, do not yield any quantitative results about the transition area, and moreover, it is not certain how the presence of the pigments on the model or the wire in the flow influences the transition zone.

Although thin film gages are routinely used to detect the region of transition, they suffer serious drawbacks. A large number of thin film gages has to be installed on the model surface in order to exactly locate the region of transition. The relatively large area of the thin film gages measures the macroscopic temperature fluctuations at the transition region, and does not give any information about the microscopic fluctuations which might lead to erroneous results. Moreover, the frequency content of the signal due to boundary layer transition is lost as a result of the large area of the thin film. A detailed description of thin film techniques (sometimes referred to as hot film) can be found in Fancher 1980 and 1982, and Stallings, et al). In summary, thin film gages are model specific and require additional instrumentation for every model.

Nonintrusive techniques provide a capability to detect boundary layer transition without disturbing the flow and are generally independent of the test model. Havener developed a boundary layer transition detector based on holographic interferometry. The method, however, is applicable only to 2-dimensional or axisymmetric flows, and the integrated density fluctuations along the beam path, i.e. pathlength difference, should be higher than the laser wavelength to produce detectable fringes. Laderman, et al, developed an optical interferometer to detect density fluctuations in the boundary layer. The technique, although more sensitive than holographic interferometry, suffers the same drawbacks as holographic interferometry. Recently, O'Hare developed a technique to detect boundary layer transition over an axisymmetric cone in a supersonic high Reynolds number flow. O'Hare's results show that the interferometer signal has a sharp peak in the frequency domain which corresponds to the region of transition. The technique, although applicable to 2-dimensional or axisymmetric flows, cannot readily be extended to detect the transition over 3-dimensional aerodynamic models. Detection of boundary layer transition over three-dimensional flow models of arbitrary shapes requires a technique that has the capability of measuring small density fluctuations in a direction perpendicular to the flow model. This configuration imposes the stringent condition of high sensitivity beyond the capability of holography or common interferometry techniques.

1.3 High Sensitivity Differential Interferometry

The method developed in this study is based on differential interferometry, which is capable of detecting optical pathlength difference in the order of $\lambda/1000$ in a direction normal to the aerodynamic model, where λ is the laser wavelength. The method, which is a variation of the Smeets and George interferometer, utilizes two beams of orthognal polarization. The two beams are incident normal to the model surface. The reflected beams are made to interfere at the plane of a detector via a Wollaston prism whose optical axis bisects the angle between the two planes of polarization. A phase-lock loop which comprises a Pockels cell, a difference amplifier, and a high voltage power supply is used to compensate the phase difference due to model vibration. The detector signals are then converted into the corresponding intermittent density fluctuations.

1.4 Organization of the Report

In Chapter II, the optical and electronics systems developed for the boundary layer transition detector are described in detail. The mathematical description of the system including signal interpretation and data reduction are considered in Chapter III. The effects of speckles and the misalignment uncertainty are also documented in Chapter III. Chapter IV is an analysis of the characteristics of retroreflecting materials relevant to the boundary layer transition detector. The first part of Chapter V describes a series of tests and experiments to validate the system, while the second part of Chapter V deals with the tests at the Unitary Wind Tunnel at NASA Langley Research Center. The experimental results supporting the development and verification of the instrument as well as the results obtained at the Unitary tunnel are presented in Chapter VI. Recommendations for future tests and research activities are described in Chapter VII.

2.0 INSTRUMENT DESCRIPTION

The design and development of a high sensitivity differential interferometer was the major focus of this study. The instrument was reported in earlier papers by Modarress, et al, and Azzazy, et al. Although the instrument concept was developed as a boundary layer transition detector, it was applied to measure the surface roughness and surface height profiles of camshafts (Azzazy). A full discussion of the applications of the high sensitivity differential interferometer is beyond the scope of this report. In this chapter, detailed descriptions of the optical, compensator, and electronic systems of the differential interferometer are presented.

The instrument developed here embodies several novel features. It has the ability to detect weak phase variations in the order of $\lambda/1000$ in a direction normal to the model. A schematic block diagram of the instrument concept is shown in Figure 1. The system encompasses three major elements: optical system, compensator system and electronics system. A detailed description of each system will follow herein.

2.1 Optical System

The instrument optical system is illustrated in Figure 2. A Wollaston prism, Wollaston (1), is used to split a linearily polarized laser beam into two-plane polarized beams (S and P polarizations). The polarization directions and the orientation of the optical axes of the various components in the system are crucial to the performance of the interferometer. In the present configuration the original polarization

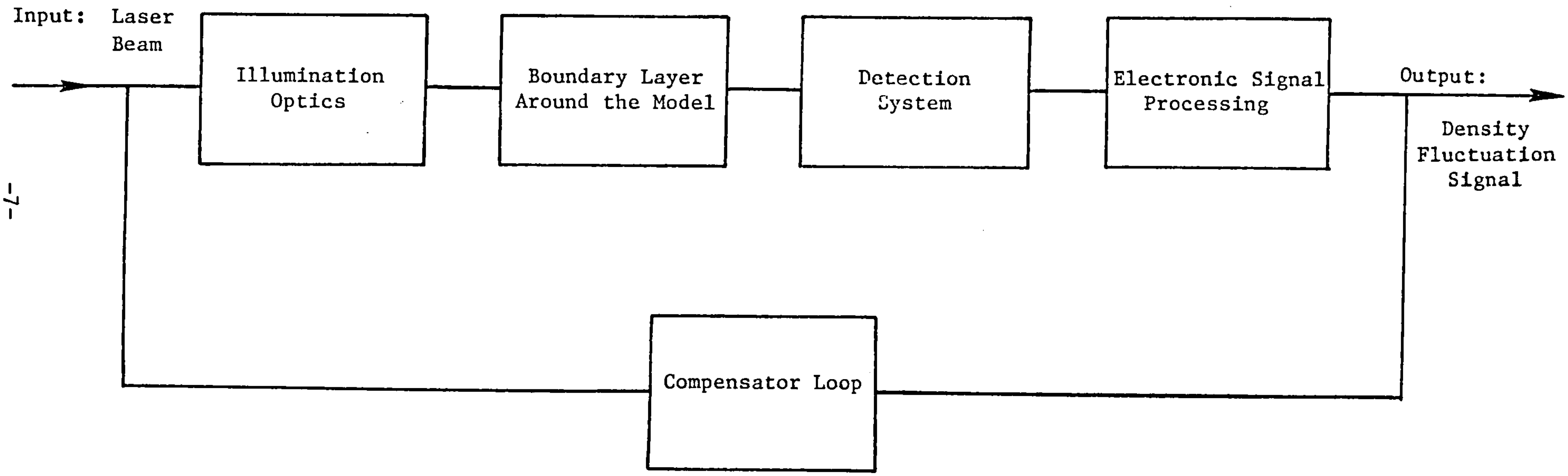

Figure (1) Block Diagram Describing the Instrument

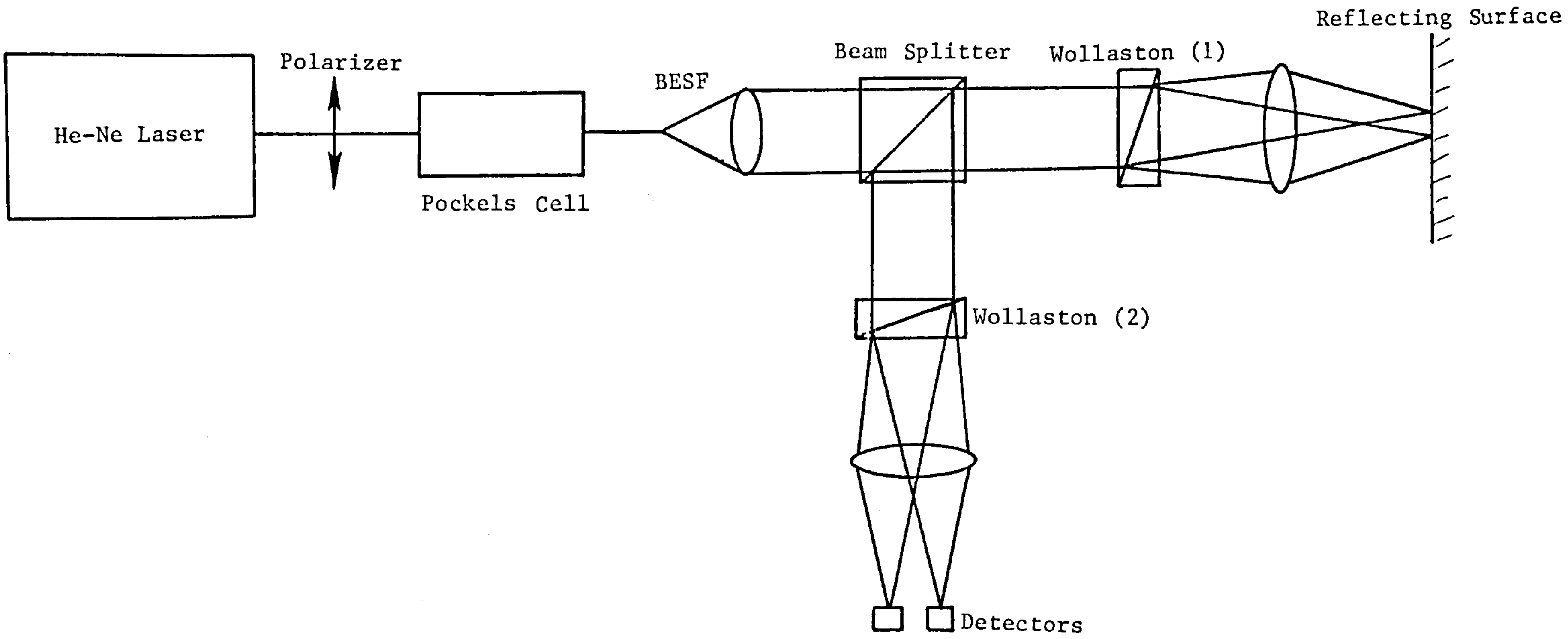

Figure (2) Schematic Diagram of the Optical System direction of the laser beam was at 45° with respect to the scattering plane, which is defined as the plane that contains the direction of laser beam propagation and the detector. The optical axis of Wollaston (1) and the Pockels cell were perpendicular to the scattering plane. The two beams were then focused on the aerodynamic model. The scattered light of the two beams was collected and recombined by Wollaston (1). No interference is possible at this stage since the two beams are of opposite polarizations. The rest of the detection system includes another Wollaston prism, Wollaston (2), whose optical axis is oriented at 45° with respect to Wollaston (1). This orientation results in interference of the two beams at the detector plane. Figure (3) illustrates the coordinate system used and the orientation of the Wollaston prisms.

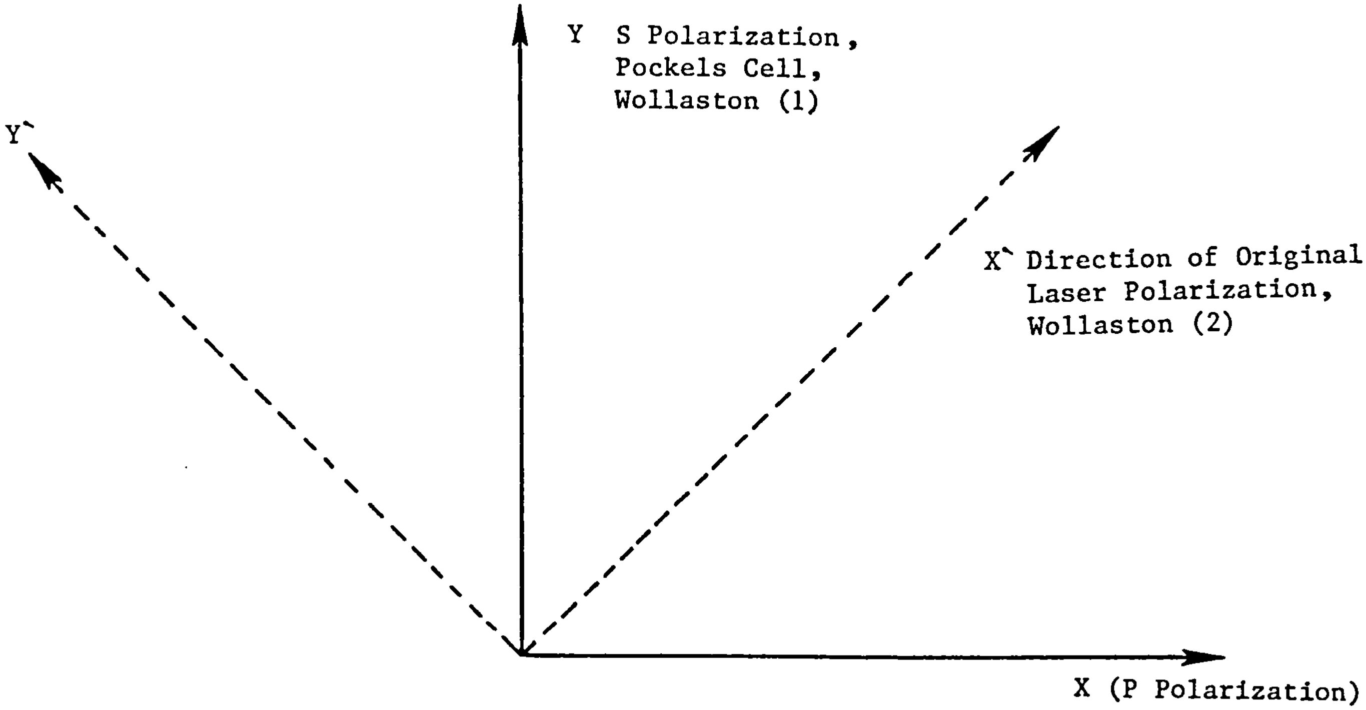

Figure (3) Coordinate System

2.2 Compensator System

The interference pattern of the two beams emanating from Wollaston (2) are detected by a quadrant detector. The two signals, A and B, are 180° out of phase, that is,

$$\begin{aligned} S_A &= S_o + S_1 \cos(\delta + \delta_v + \gamma) \\ S_B &= S_o + S_1 \cos[\pi + (\delta + \delta_v + \gamma)] = S_o - S_1 \cos(\delta + \delta_v + \gamma) \end{aligned} \tag{1}$$

where δ is the phase difference due to density fluctuations (low amplitude and large frequency), δ_v, the phase due to model vibration (large amplitude and low frequency) and γ the phase introduced by the Pockels cell. The amplitudes S_o and S_1 are proportional to the laser power, and fringe visibility. The signals S_A and S_B were combined in a differential amplifier to produce a signal proportional to the cosine of the phase difference, that is

$$S_C = 2S_1 \cos(\delta + \delta_v + \gamma) \tag{2}$$

The quadrature condition is achieved when $\delta + \delta_v + \gamma = \frac{\pi}{2} + m\pi$, $(m = 0, 1, 2, \ldots)$. The feedback loop used to realize the quadrature condition is generally classified as a phase-tracking homodyne detection system (PTDC) (Giallorenzi et al). The output from the differential amplifier normalized by the sum of the signals A and B, is defined as an error signal. The phase γ can be made to exactly cancel the signal δ_v, thus driving the error signal to zero. For small excursions from the quadrature condition the system of Figure (4) is a simple linear feedback system, which attenuates low frequency signals, i. e., vibration induced signals.

2.3 Electronics System

The electronics system designed to meet the requirements of the compensator system is shown in Figure (5). Special features of the electronics system embodies the following:

1. Minimum voltage to the divider numerator is #250 mV.
2. Maximum voltage to the divider denominator is #10 V.
3. Frequency bandpass of the system is 200 kHz.
4. Correction signal to the Pockels cell is low frequency ~ 7 kHz.
5. Output signal frequency is > 7 kHz.

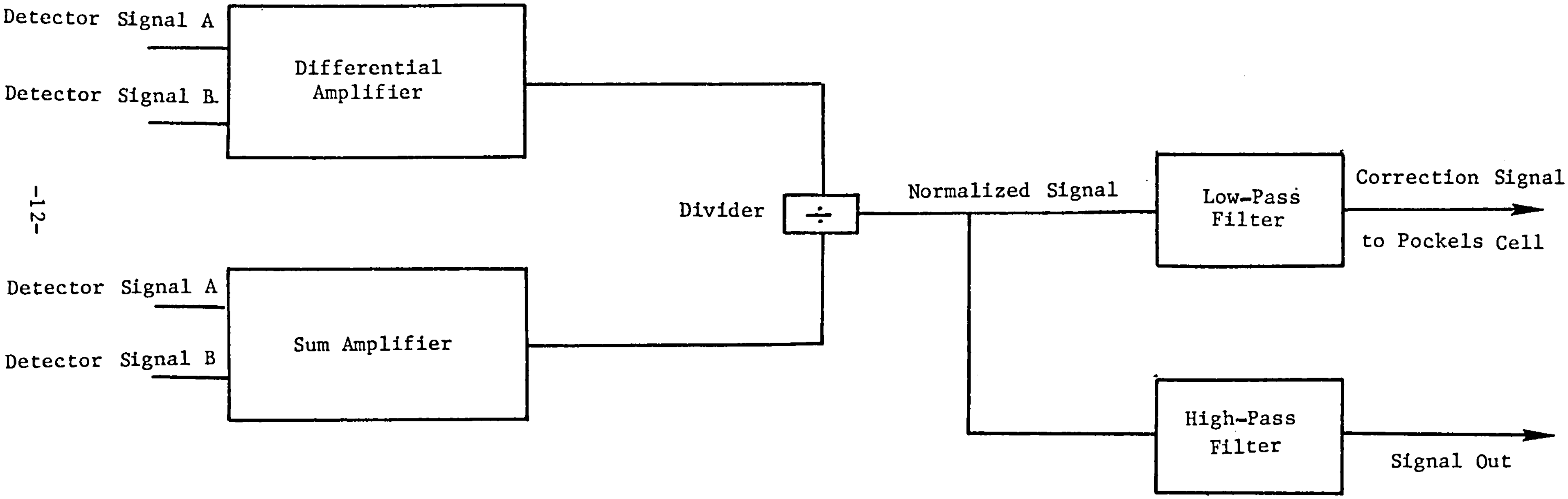

Figure (4) Block Diagram of Compensator System

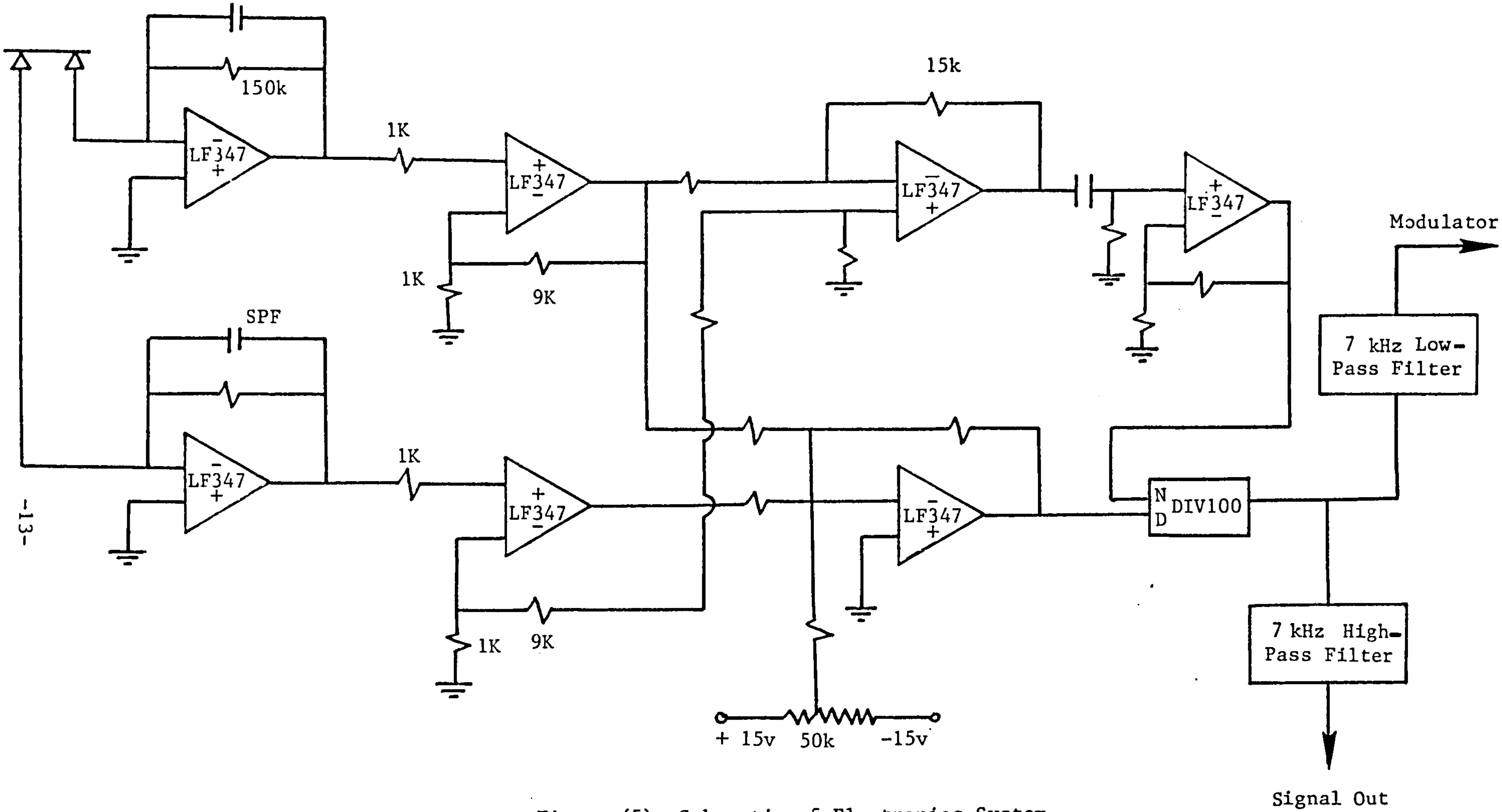

Figure (5) Schematic of Electronics System

3.0 SYSTEM ANALYSIS

The present chapter is divided into 3 parts. The mathematical foundation of the interferometer system is first outlined, then used to interpret the signal. The mathematical analysis of the system is not only imperative to the full understanding of the functions of each optical element, but also to the understanding of the overall system performance. Uncertainty analysis of the system misalignment constitutes the second part, and the third part of the chapter is a discussion of the speckles and their effect on the signal.

3.1 Mathematical Analysis

The electric field amplitude of each polarization can be treated independently since the two polarizations are orthogonal and, therefore, cannot feel the presence of each other. Using Jones' calculus (Swindell) the electric field entering through Wollston (1) can be presented as

$$E_m = e^{i(\omega t + kz)} \left\{ \begin{bmatrix} a_s e^{ik\gamma} \\ 0 \end{bmatrix} + \begin{bmatrix} 0 \\ a_p \end{bmatrix} \right\} \quad (3)$$

where ω is the laser frequency, k the wave number, γ the phase introduced by the Pockels cell, a_s and a_p the electric field amplitude in the S and P polarization directions, respectively. After passing through Wollaston (1), the electric field amplitude, E_m, remains the same provided that the optical axes of Wollaston (1) and the Pockels cell are parallel. A complete analysis of misalignment uncertainties is given in the next section. The scattered light, E_{sc}, from the surface can be represented by a deterministic complex function, ρ, describing the reflectance of the surface (amplitude) and profile (phase), such that

$$E_{sc} = \rho : E_m \tag{4}$$

where the complex function, ρ, is defined as

$$\rho = \begin{bmatrix} e^{ik\delta_x} & 0 \\ 0 & e^{ik\delta_y} \end{bmatrix} \tag{5}$$

where δ_x and δ_y are the disturbances in the optical pathlength due to the passage of the laser beams through the fluid flow.

Since Wollaston (2) is oriented at 45° to Wollaston (1), interference of the scattered beams can be achieved in the plane of the photodetectors. Therefore, electric field amplitude at the detector plane, E_{sig}, can be represented as a function of the scattered electric field such that

$$E_{sig} = \frac{1}{\sqrt{2}} \begin{bmatrix} 1 & 1 \\ 1 & -1 \end{bmatrix} \begin{bmatrix} E_{sc1} \\ E_{sc2} \end{bmatrix} \tag{6}$$

Since the detector signal is proportional to the square of the electric field amplitude, the detector signals after algebraic manipulation become

$$S = S_o \begin{bmatrix} 1 \\ 1 \end{bmatrix} + S_o V \cos[k(\delta_x - \delta_y + \gamma)] \begin{bmatrix} 1 \\ -1 \end{bmatrix} \tag{7}$$

where $S_o = a_s^2 + a_p^2$ is the laser power, and $V = 2\ a_s a_p/S_o$ is the fringe visibility. The phase difference $\delta_\chi - \delta_y$ can be divided into 2 parts:

1. Vibration induced phase difference, δ_v, at low frequency.
2. Phase difference due to density fluctuations in the flow field, δ.

Therefore, the signals A and B of the two detectors can be further reduced such that

$$\begin{aligned} S_A &= S_o + S_o V \sin\left[\frac{\pi}{2} - k\ (\delta + \delta_v + \gamma)\right] \\ S_B &= S_o - S_o V \sin\left[\frac{\pi}{2} - k\ (\delta + \delta_v + \gamma)\right] \end{aligned} \tag{8}$$

The quadrature condition is achieved when

$$k\ (\delta_v + \gamma) = \frac{\pi}{2} + m\pi, \qquad m = 0,\ 1,\ 2\ \ldots \tag{9}$$

An error signal S (S is defined as $S = \frac{S_-}{S_+}$ where $S_- = S_A - S_B$ and $S_+ = S_A + S_B$) is used as a feedback control to the Pockels cell.

The Pockels cell controller introduces a phase shift, γ, at all times such that Equation (9) is realized. The normalized interferometer signal S can be used to interpret the optical pathlength variation (density fluctuations) through the relation:

$$S = V \sin 2\pi \frac{\delta}{\lambda} \tag{10}$$

Figure (6) is a schematic presentation of the two signals A and B and the error signal S.

3.2 Uncertainty Due to Misalignment

Serious deficiencies in the operation of the high sensitivity differential interferometer arise due to misaligning Wollaston (1) with respect to the Pockels cell. For a small angle, α between the optical axes of the Pockels cell and Wollaston (1), the quadrature condition, Equation (9) becomes

$$\cos k(\delta + \gamma) = \alpha^2 \cos k(\delta - \gamma) \tag{11}$$

Equation (11) has complex multiple roots which lead to a diminished and discretized signal. When the angle α tends to zero, Equation (11) reduces to the familiar quadrature condition, Equation (9), which is highly desirable for the performance of the diffuse-point differential interferometer system.

Misaligning Wollaston (2) will only result in a decreased signal, however, it does not affect the performance of the interferometer as does Wollaston (1).

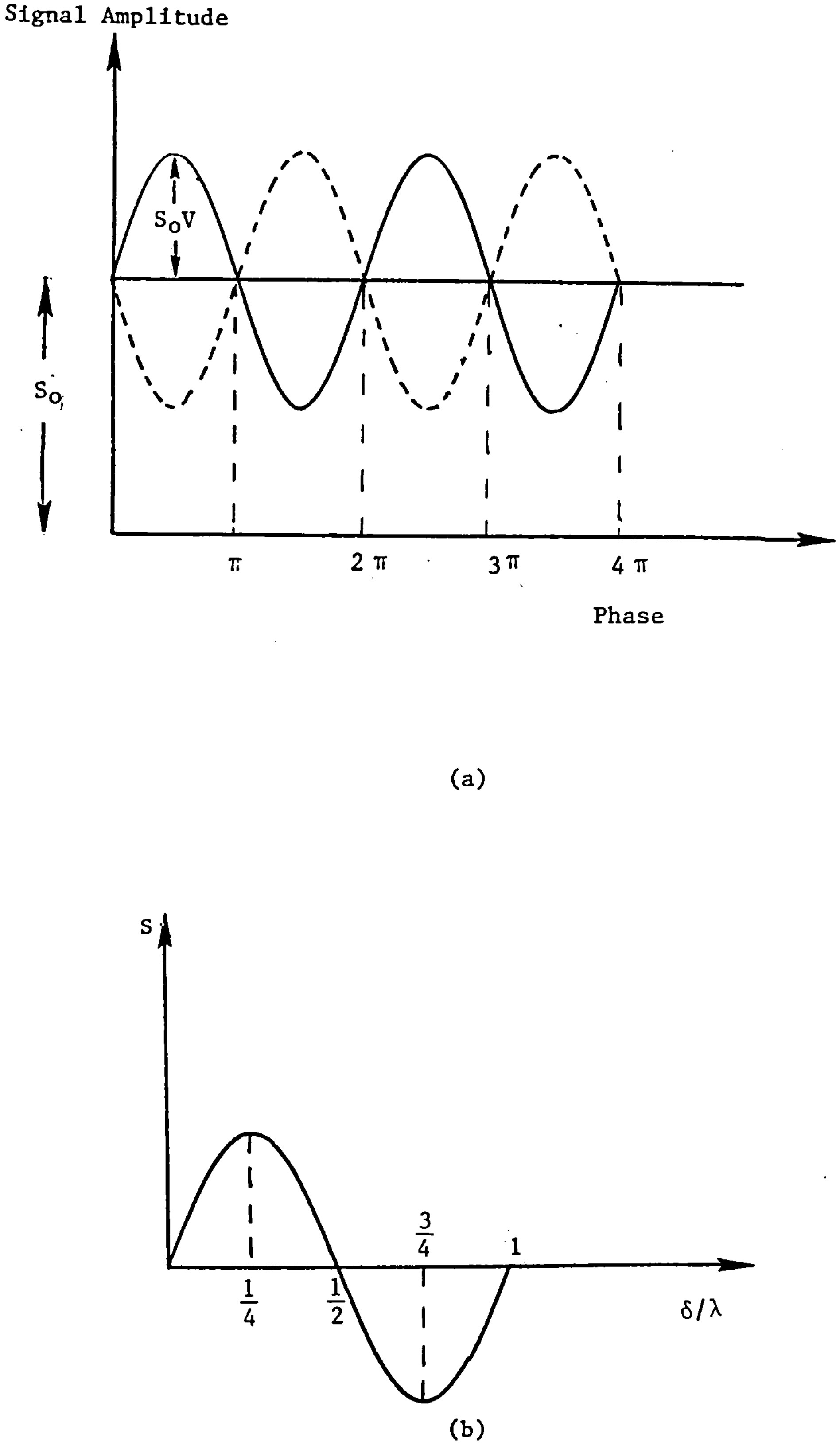

(a)

(b)

Figure (6) Relationship Between the Signal and Phase

3.3 Speckle Analysis

When an object is illuminated by a laser beam, the reflected wavefront appears to be granular in shape (speckles). The detailed structure of this granularity bears no obvious relationship to the microscopic properties of the illuminated surface. Speckles appear to be chaotic and unordered and can be best described by the methods of probability theory and statistics. Goodman, studied the statistical properties of laser speckle patterns. The probability distribution function of the scattered light intensity obeys the circular Gaussian statistics, while the phase probability density function can vary from uniform statistics (totally diffuse surface), to a delta function (specular surface). Azzazy demonstrated that a speckled wavefront can be made to interfere with a plane wavefront and the resultant interference pattern carries phase information of the surface height of the diffuse object. The analysis was extrapolated to show that the interference pattern resulting from two speckled wavefronts can be used to measure the phase difference between the two waves.

In general, surface roughness of aerodynamic models does not produce speckles that influence the interferometer performance since the signal due to the surface roughness is static and the signal of interest is dynamic. However, speckles can produce dynamic signals due to model vibration which affect the interferometer performance. Since model vibration causes the focused laser beams to be scattered off different speckles, the signal due to speckles has approximately the same frequency information as the model vibration. Discrimination against such a signal is done through the compensator system. It is also of importance to note that the effects of speckles result in decreasing the visibility fringe contrast and hence, smaller signal-to-noise ratio.

The characteristic size of the speckles is measured by the autocorrelation function of the reflected intensities. Goodman, derived an expression for the autocorrelation function of the scattered intensity where the surface is illuminated by a uniform intensity beam of diameter D such that

$$R_I(r) = \langle I\rangle^2 \left[1 + \left| 2 \frac{J_1\left(\frac{\pi D r}{\lambda f}\right)}{\frac{\pi D r}{\lambda f}} \right|^2 \right] \tag{12}$$

where J_1 is Bessel function of the first order, and f is the distance between the lens and the object. The speckle pattern expressed by Equation (12), can be considered to be made up of a set of gratings of varying spatial frequencies. The maximum spatial frequency, f_{max}, is that of the grating formed by the interference of the light scattered from the edges of the illuminated area. Therefore, the maximum spatial frequency is

$$\frac{1}{f_{max}} \simeq \frac{\lambda f}{a} \tag{13}$$

where a is the diameter of the viewing lens aperture and f is the focal length. It is interesting to note that the speckle size is not a function of the surface roughness, but rather a function of the optics.

In conclusion, the speckle effects do not prevent interference between the two scattered beams. The interference pattern carries phase information about the pathlength difference between the two beams. Speckles lead to smaller signal-to-noise ratio through the reduction of visibility. The maximum speckle size is in the same order as the broadcast beam diameter.

4.0 OPTICAL DIAGNOSTICS ACCESS IN WIND TUNNELS

4.1 Introduction

4.1.1 General Background

In general, an optical instrument works by passing a conditioned electromagnetic wave into a test facility to a location which scatters radiation from the wavefront or impresses information onto the wavefront. A receiving system then collects a sufficient amount of the modified wavefront from which to extract the desired information. This may require passing the radiation back to the outside of the test facility. This must be accomplished in a way that noise added to the signal is either negligible or accountable.

The optical access problem is often drastically different for different types of instruments. The major focus of this program has been on the application of the differential interferometer to the location of boundary layer transition. Therefore, a separate task was defined to treat this problem for the differential interferometer. Moreover, NASA personnel extended the objective of the task to cover the general case of all optical diagnostic instruments.

4.1.2 The Problem

The basic problem is caused by the fact that in most wind tunnels optical access is severely restricted. Table 1 summarizes the problem for five different classes of optical instruments. The types of

TABLE 1. OPTICAL ACCESS RESTRICTIONS IN WIND TUNNELS

TYPE OF DIAGNOSTIC	REQUIREMENT	RESTRICTION
LDV/LTA - Forward Scatter	High resolution access to point of interest. Large collecting access for output. Nearly straight through optical access.	Input and output window size, quality, location. Access blocked by model.
Schlieren Shadowgraph Interferometry Deflectometry	High optical quality access in and out. Straight through access. Size of either input or output equal to field of view.	Window size, quality, location. Access blocked by model.
Photography	Access to point photographed. Illumination access.	Window size, quality, location. Access blocked by model.
Holography (Transmission)	Straight through access. Size of either input or output equal to field of view.	Window size, location. Access blocked by model.
Reflection Interferometry Holography	Input/output access model reflectivity	Window location.

restictions include window size, location, quality, and blockage by the model or other components.

Specifically, when an instrument is used to probe boundary layers, the model is immediately adjacent to the sample volume. In the case of the differential interferometer, the optimum case exists when the light wave can pass straight through the sample volume to the detector. This case exists at no more than two points along each perimeter. Therefore, the problem is to find other ways to optimize collection of the information bearing wave. In fact, getting the light to the sample volume without imposing uninterpretable information upon it is not always a trivial problem. Not only must the window be carefully considered, but also the affect of the wind tunnel boundary layer and the region between the instrument and the sample volume must be understood.

4.2 Methods for Getting Light In and Out

Table 2 summarizes the approaches that can be exercised to solve the problem. When input or output windows are too small, or are in the wrong place, one approach is to install part of the optics inside the wind tunnel. This may require that mirrors be used to conduct the light to or from the sample volume. The problem of the aerodynamics and aero-optics of the components inside the flow must then be considered. The wall itself may sometimes be used as an optical element. The aero-optics of the wall itself must not be overlooked. For example, a turbulent boundary layer can impress unacceptable modulation on the beam.

A number of methods have been devised to deal with the case for which the model blocks access to either the transmitted or received

TABLE 2. OPTICAL ACCESS SOLUTIONS

RESTRICTION	CONDITION	APPROACHES
Input window location	Cannot access point of interest from window.	Mirrors inside tunnel. Transmitter inside tunnel.
Input window size	Insufficient input beam size.	Optics inside tunnel.
Output window location	Radiation of interest misses window.	Mirrors inside tunnel. Use light scattered from tunnel wall.
Output window size	Insufficient output beam size.	Optics inside tunnel.
Access blocked by model	Radiation of interest strikes model.	Prepare model surface. - Use light scattered from model - Make model reflective - Make model transparent Put receiver in model. Put transmitter in model.

light. Fiber optics are playing an ever-increasing role in this regard; to convey light into or out of a model. Figure 7 illustrates the concept. Fiber optics also can be used to miniaturize the sensing part of the diagnostics device so that it becomes possible to locate it inside the wind tunnel or even in the model itself. Other approaches illustrated in the figure include making the model transparent or inserting windows in the model.

4.2.1 Using Existing Model Surface Optical Properties

4.2.1.1 Mirrored Surfaces

A particular approach addressed in this program is that of using the model surface optical properties or preparing the model surface to have optical properties that aid in the desired optical access. The simplest of these is to use the light reflected or scattered from the model. If the model is a mirrored surface then it reflects the forward radiation in a direction depending on the angle between the normal to the surface and the angle of incidence. If the mirror is of high quality, then this is essentially equivalent to having a transparent surface with a window on the opposite side.

For a surface to act as a mirror, it must be polished to a surface smoothness of the same order as the wavelength of light being used. Any curvature of the surface will be impressed on the light wave as a phase modulation. This approach is useful when the surface can be highly polished or when a mirror can be replicated on the surface and when the surface is tilted in the proper direction to allow the light to be retrieved.

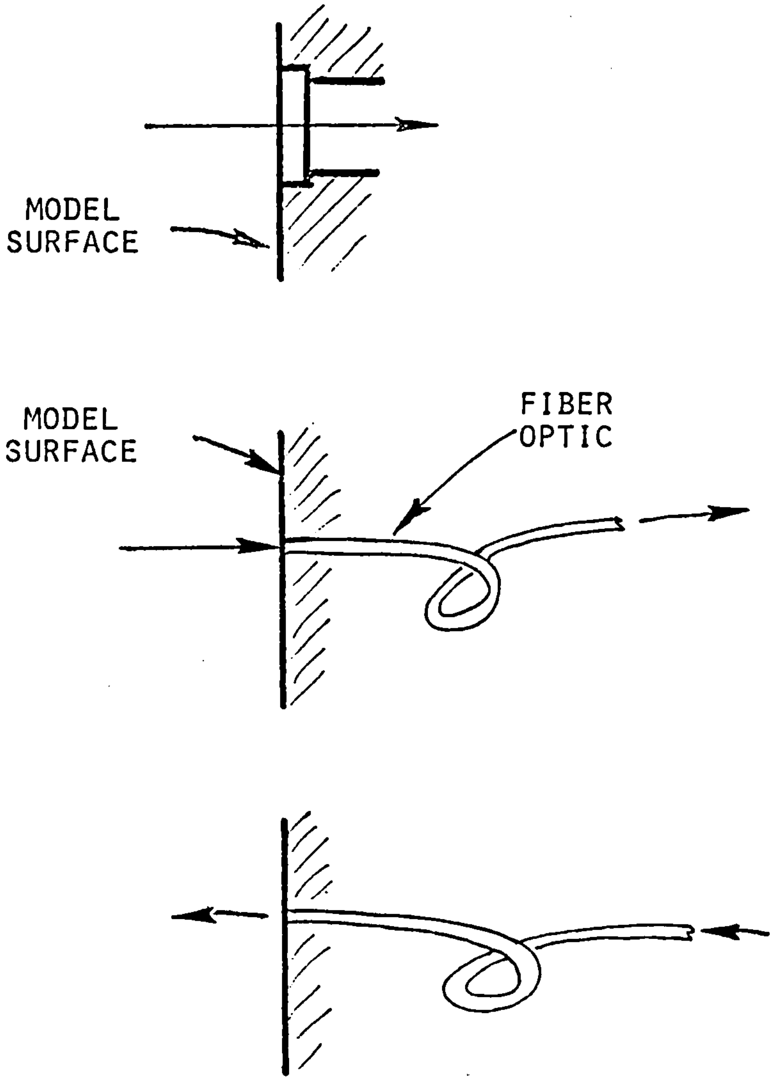

TRANSPARENT MODEL

RECEIVER IN MODEL

TRANSMITTER IN MODEL

Figure (7) Transmitting Light Into or From a Model

Since it is not always possible to meet the above criteria, we have examined alternative ways to prepare the model surface or to use it in an unprepared state to achieve the required optical function. Table 3 summarizes methods which have been considered. For all the cases to be discussed here the light source is considered to be a laser.

4.2.1.2 Diffuse Surfaces

The reflection of coherent light from a diffuse surface presents a difficult problem with many instruments, especially those that focus light onto the surface. The problem is manifested in the speckle present in the reflected beam. The light has a random spatial distribution in both amplitude and phase, a condition which is not easily handled by many instruments. This is especially true when the model is vibrating by an amount which is in the same order as the illuminated area. In such a case large spatial fluctuations occur in the amplitude and phase of the reflected light.

4.2.2 Changing Surface Optical Properties

For some applications, it is advantageous to alter the surface optical properties by coating the surface with a film, a paint, or by inserting optical components into the surface. Figure 8 summarizes some of the possibilities and their properties. We have examined commercially available materials in detail to determine their optical properties.

TABLE 3. MODEL SURFACE PREPARATION OPTIONS

CONDITION WANTED	TYPE OF PREPARATION	LIMITATION
Wide angle scattering	Etched to provide diffuse surface.	Speckle pattern induced on scattered radiation.
Specular reflection	Polished to λ smoothness. Replicated mirror.	Curved surface aberration. Flat surface required.
Retroreflection	Spherical (cats eye) coating add surface roughness.	<100 micron diameter spheres.
	Corner, cube coating.	Diffraction noise added to beam.
Preferential reflection direction	Mirror inside model. Diffraction grating on surface. Holographic optical element.	Curved surface aberration. Limitation on angular access.
Forward scattering	Mirror inside model. Transparent model. Receiver in model. Transmitter in model.	Curved surface aberration.

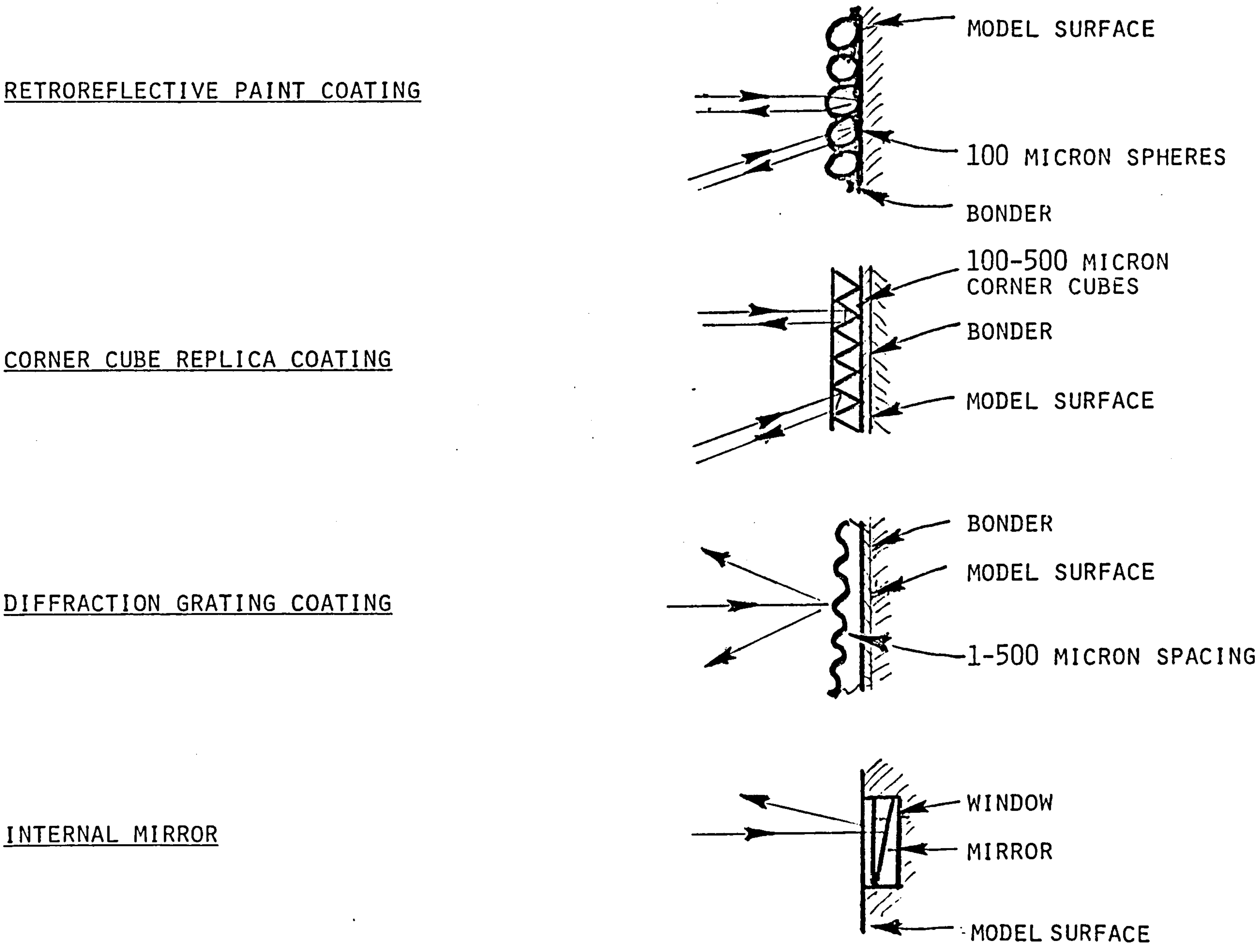
RETROREFLECTIVE PAINT COATING

CORNER CUBE REPLICA COATING

DIFFRACTION GRATING COATING

INTERNAL MIRROR

Figure (8) Enhancing Surface Reflectivity

4.2.2.1 Retroreflective Materials

Commercially available retroreflective coatings comprise a variety of materials. Figures 9 and 10 are microphotographs of the surfaces of some of these. Retroreflective paints contain a mixture of pigment and glass spheres of nominally 50 to 100 micrometers in diameter. When properly applied the spheres are nested in pigment with a significant portion of clear glass exposed. However, it can be seen from this photograph that a significant distance exists between the glass spheres and that on a microscale much of the surface is not retroreflecting. Applying this material requires care to achieve acceptable results. Such procedures include heat drying the paint to insure that the pigment does not cover the retroreflecting sphere.

Other retroreflecting coatings are applied to adhesive backing (shown in Figures 9b and c). These are significantly better than the paints since the number of glass spheres per unit area is much higher. The so-called scientific grade material is the most efficient since, as can be seen in these figures, the spheres are somewhat more uniform and slightly larger. Also, they are accurately mounted in a pigment backing chosen to make the reflection from the back of the sphere optimum.

A major concern often expressed about these types of coatings is that they may change the surface roughness, adding roughness heights due to the spheres, typically of 25 to 50 micrometers. This argument in fact, applies only to the paint. The other two materials described above have a smooth, plastic, protective coating which would reduce their effect. An alternative which relieves this problem is an embossed plastic material containing corner cube reflectors of nominal 200 micrometers in diameter. The outer surface of the material is flat and

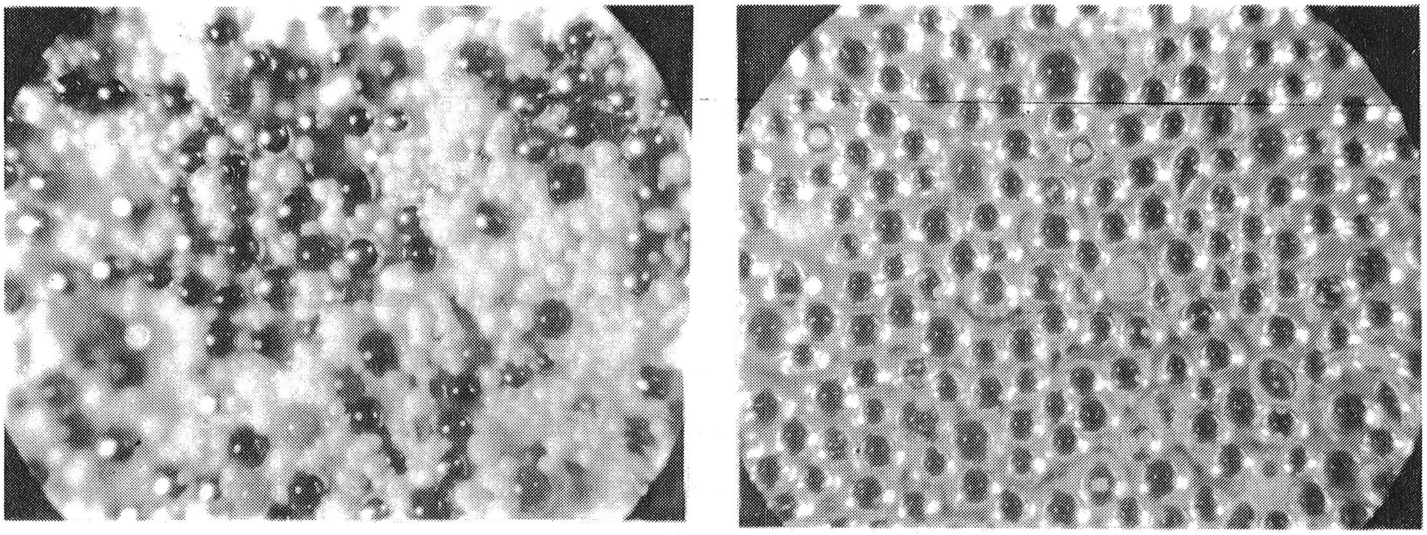

(a) 3-M "Codit Paint

(b) 3-M Scotchlight Engineering Grade

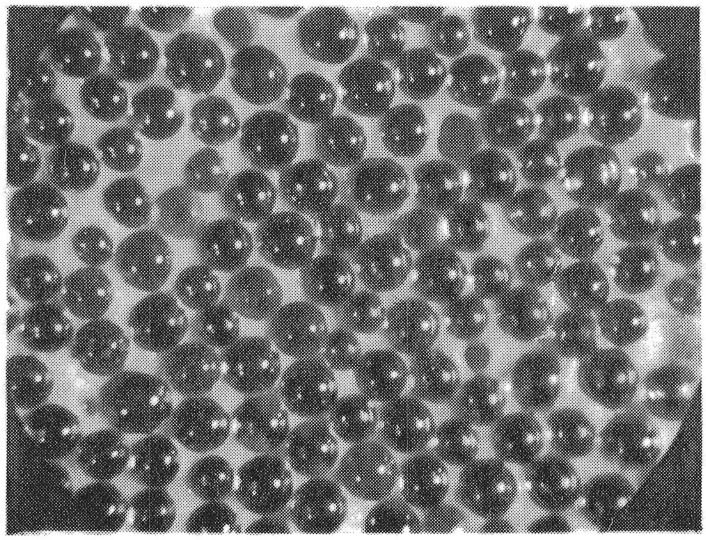

(c) 3-M Scotchlight Scientific Grade

Figure (9) Retroreflective Coatings-Glass Spheres

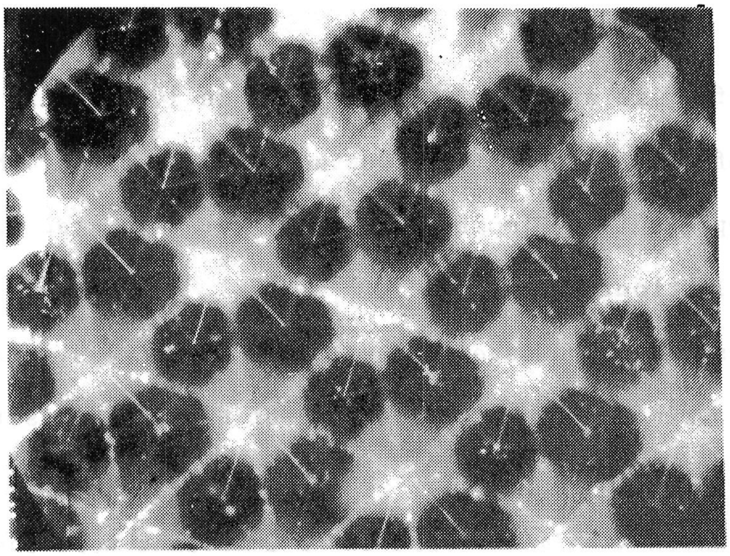

(a) Front Surface

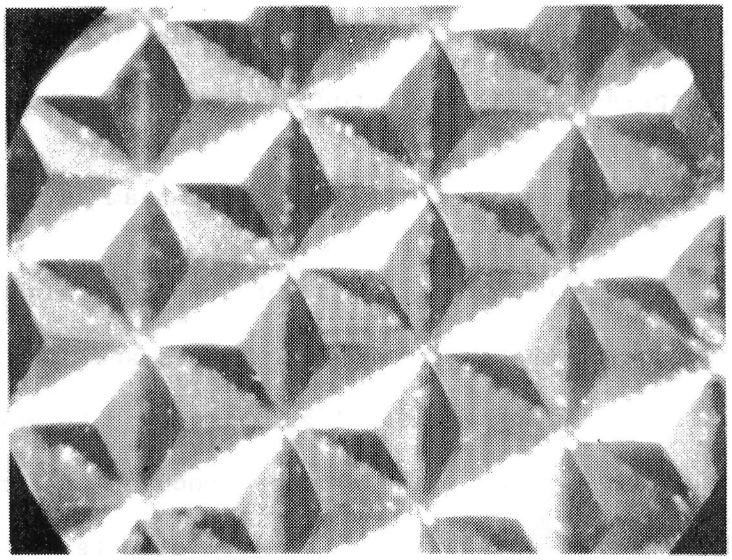

(b) Rear Surface

Figure (10) Retroreflective Materials-Corner Embossings would not disturb flow in a boundary layer. Figure 10 contains photomicrographs of the front and rear surface of a sample of this material. This represents the most efficient material tested in this study for retroreflection.

Because these are candidates for use in wind tunnels, and since we were not able to find published properties of the materials in a number of critical areas, a study was completed to measure such properties. Properties which were considered to be important were the following:

1. Reflection efficiency
2. Angular spread of the reflected beam
3. Reflection efficiency as a function of angle of incidence
4. Angular spread of the reflected beam as a function of angle of incidence
5. Intensity distribution in the reflected beam as a function of angle of incidence

These properties were measured for all of the materials illustrated and were compared to the properties of mirrors and diffuse white surfaces. Figure 11 shows the experimental geometry used to make the first series of measurements. The materials were mounted on a rotary mount to control the angle of incidence. The retroreflected beam was directed by a beam splitter to a detector that was traversed through the center of the reflected beam by a linear translator. It should be emphasized that all measurements reported here were done at 633 nanometers and the results are likely to differ at other wavelengths. However, the results should not vary drastically for Argon-ion lasers

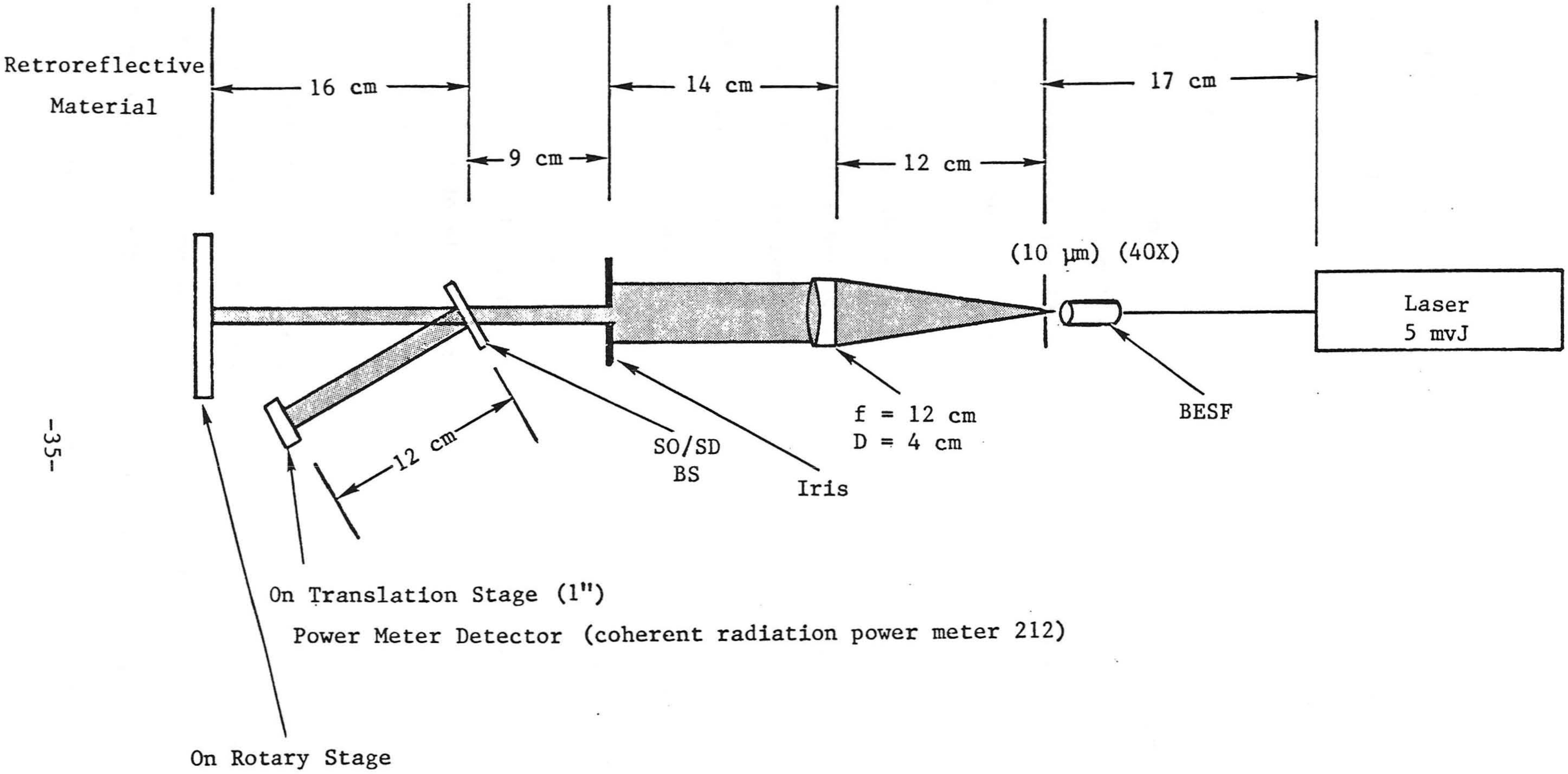

Figure (11) Experimental Geometry

Figure 12 shows the resulting intensity profiles as compared to a mirror and to each other for a normally incident beam. The mirror is, of course, the most efficient in this case. This is followed by the corner cube material at an efficiency of about ten percent. The reduced efficiency is due largely to diffraction effects. The beam-spread can be observed by comparing the individual curves with the one for the mirror. Beam-spread is surprisingly small for all materials. Because the process changes the beam profile this is difficult to quantify, but if half power points are chosen then the retroreflecting materials are almost as good as the mirror.

Using the same apparatus the intensity at the center of the retroreflected beam was measured as a function of angle of incidence onto the materials (Figure 13). The corner cube material falls off the fastest. Two of the materials fall off surprisingly little at angles of incidence as high as 40 degrees. This graph indicates the applicability of the materials to highly curved models.

The profiles of the retroreflected beams were then measured as a function of the angles of incidence. Figures 14 and 15 show the results at 20 degrees and at 45 degrees. At 20 degrees angle of incidence the corner cube material still excels. However, at 45 degrees the 3M scientific grade material is best.

Finally, photographs of the diffraction pattern were made for the different materials at 0 and 45 degrees angles of incidence. The results are illustrated in Figure 16. The appearance of the raw beam is depicted in (a) since the reflector is a mirror. The two spots result since there is a beam splitter in the setup with two reflecting

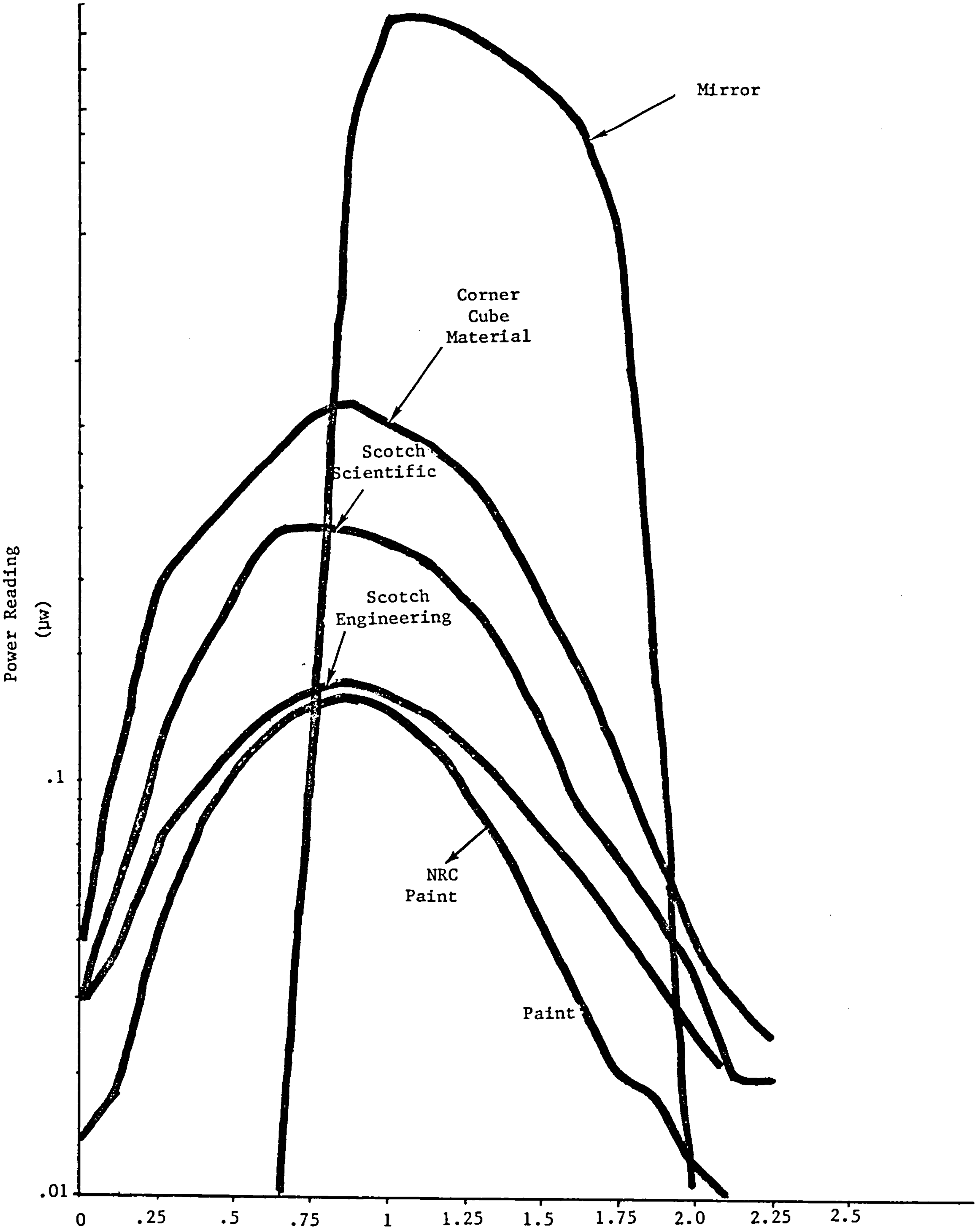

Figure (12) Retroreflection - Intensity Profiles for a Number of Materials

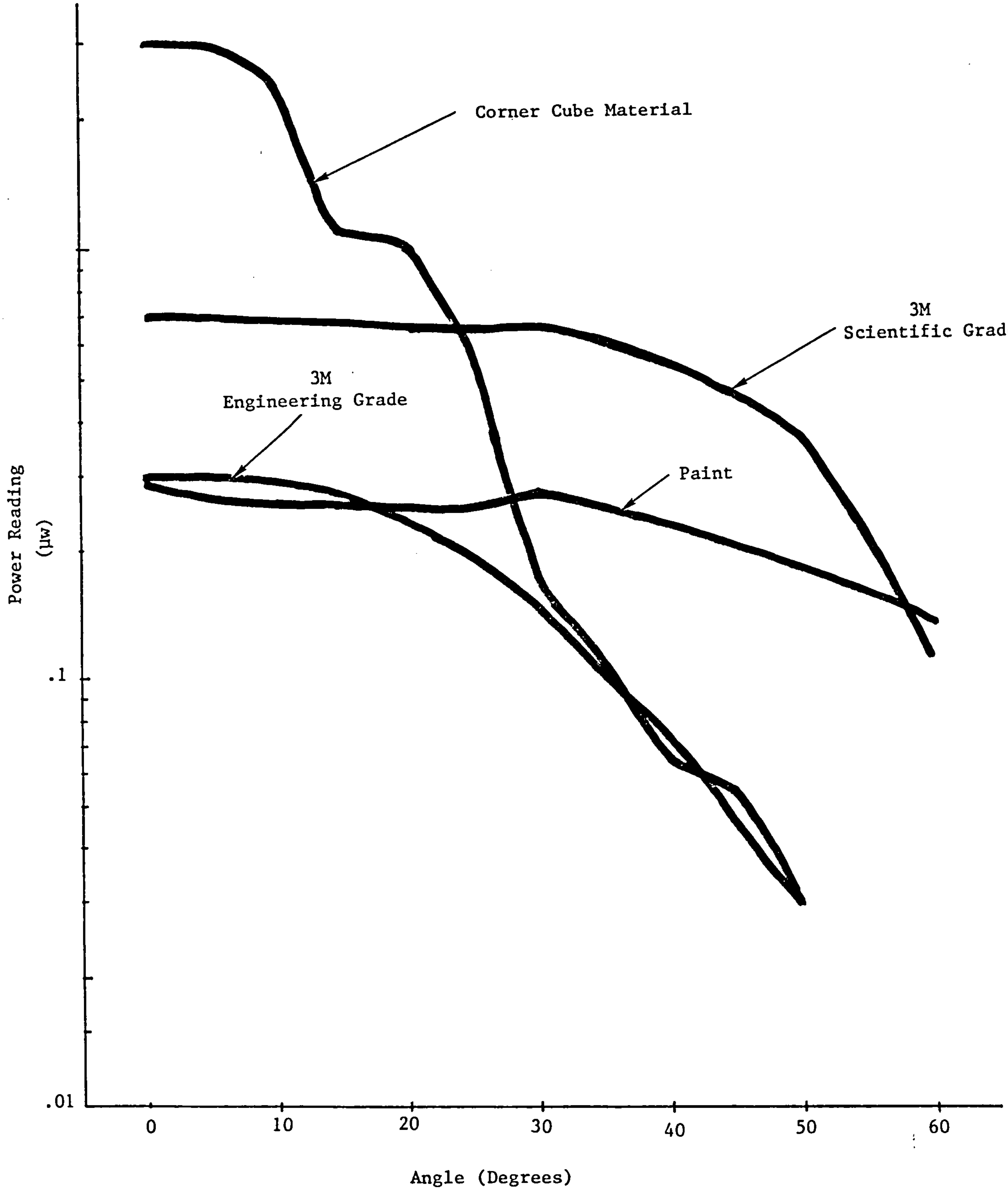

Figure (13) Reflectivity Vs. Angle of Incidence of Various Retroreflective Materials

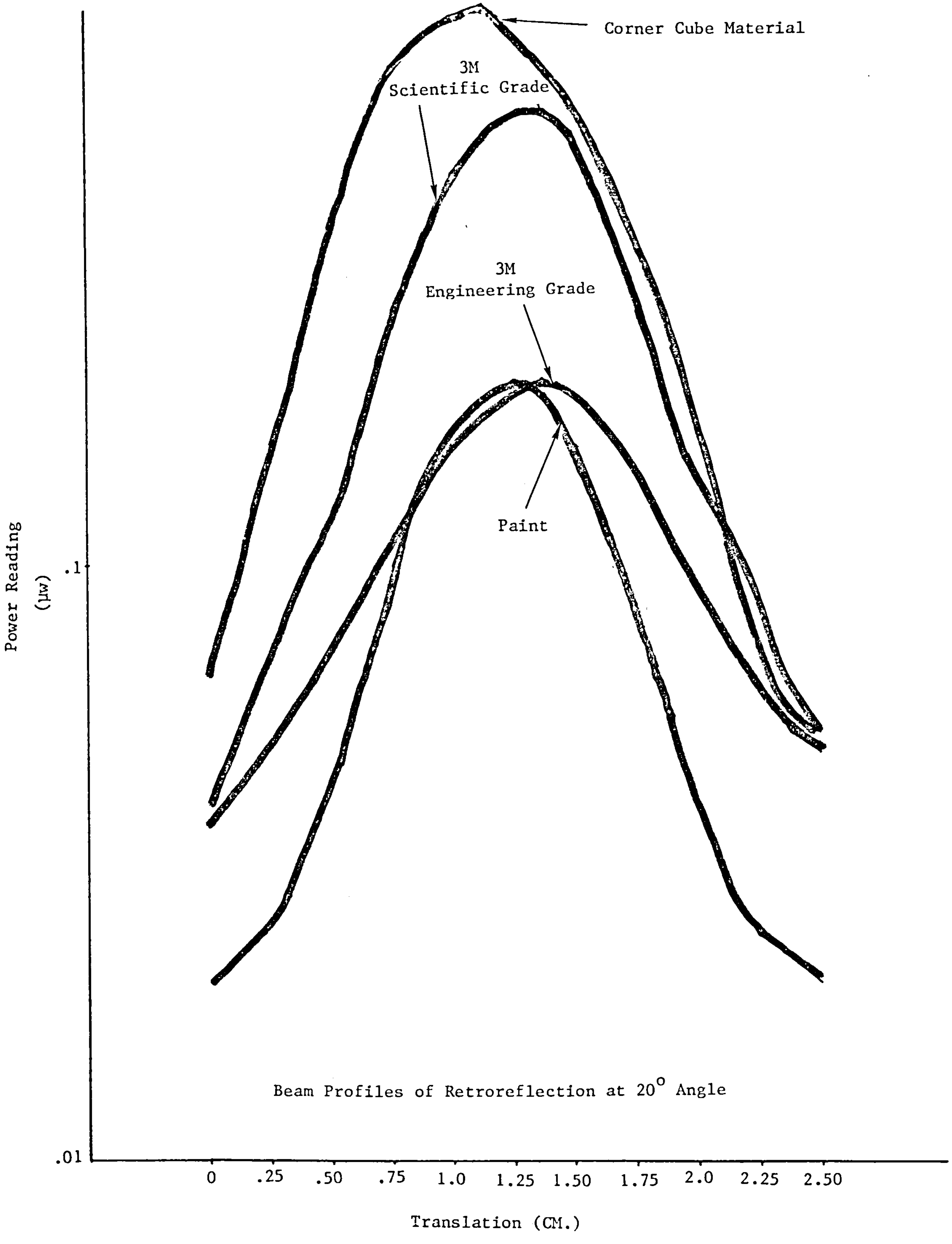

Figure (14) Beam Profile of the Retroreflected Beam for a 20° Angle of Incidence

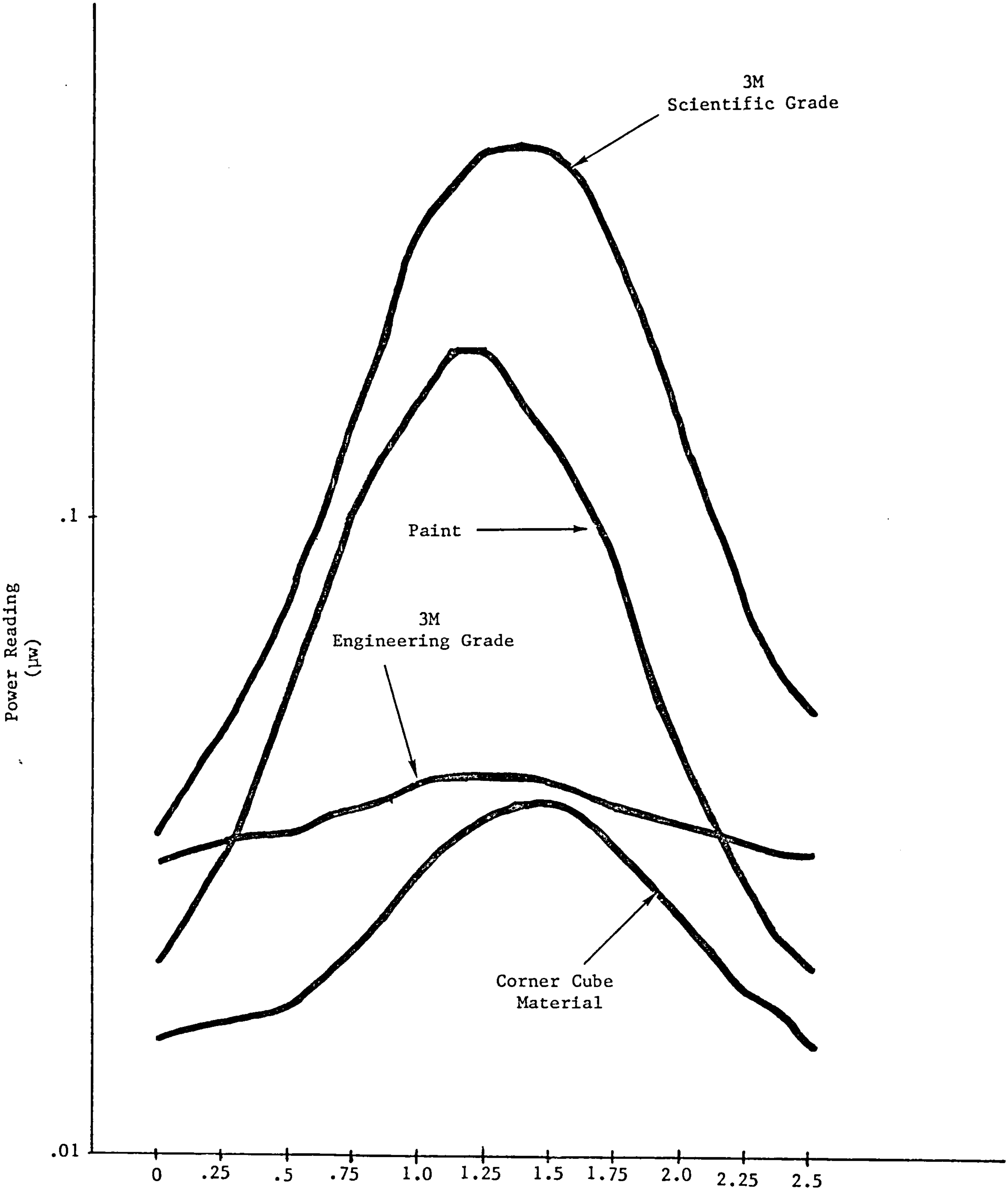

Figure (15) Beam of Retroreflection at 45° Angle

(a) ALUMINUM MIRROR

(b) 3M SCIENTIFIC GRADE

(c) CORNER CUBE MATERIAL

(d) 3M ENGINEERING GRADE

(e) PAINT

(f) FIRST SURFACE REFLECTION - CORNER CUBE MATERIAL

(g) FIRST SURFACE REFLECTION - 3M SCIENTIFIC GRADE

(h) ANGLE OF INCIDENCE 45° 3M SCIENTIFIC GRADE

Figure (16) Diffraction Patterns of the Various Reflectors at Normal Incidence Angles.

surfaces. The diffraction pattern shown in (b) attest to the fact that the glass spheres in the scientific grade material are relatively monodisperse in size. Theory concludes that the Fraunhofer diffraction pattern of a large number of circular apertures which are randomly oriented and of equal diameter has the same form as that of one of the apertures. Figure 16 suggests that the sphere used to make the 3M engineering grade material are rather widely dispersed in size. The conclusion to be drawn from (e) is that the paint uses more monodisperse spheres.

Except for the paint, the materials have, in addition to a retro-reflecting property, a specular reflecting property from a first surface. Since, in each case, this is a plastic material, its optical quality is not as good as the mirror. Since the corner cube material is made of typically thicker plastic, its reflection is better than that seen with the thinner 3M materials. This reflection must be considered when the angle of incidence is nearly 90 degrees, but it can be eliminated by tilting the material slightly away from the normal.

The diffraction pattern at 20 degree angles of incidence is virtually unchanged. At 45 degree angle of incidence, the diffraction pattern can be observed to change slightly as shown in Figure 15h.

4.2.2.2 Other Forms of Surface Preparation

Rarely does a normally machined surface exhibit the properties of either a mirror or a diffuse surface. To make a mirror of such a surface requires that the surface be ground and polished. By using the same techniques used for grinding mirrors on glass, an essentially perfect mirror can be produced on any metal. This includes the use of buffing wheels and grits of various degrees of coarseness. After such a surface is produced, it can be protected with easily removable coatings until ready for use. Without such coatings, most metal will oxidize unless coated with a gold or proper dielectric coating. The most common dielectric coating for mirrors is silicon monoxide. The surface can be made optically diffuse by etching after polishing.

An untreated machined surface commonly acts optically like a grating (see Figure 8), producing diffraction orders separated by angles that increase as the tool marks become closer together. This can cause most of the scattered light to miss the receiver, if not taken into account. The condition can be used to advantage if the receiver is placed in one of the strongest diffraction orders, or if the machine marks are deliberately tailored for the application. In fact, gratings could be ruled on the model, or on another material which is attached to the model. In principle, diffraction orders can be directed to as many places as desired and to any desired location by the correct ruling. The most general case is that in which the surface is converted into a reflection hologram, the subject of the next section.

4.3 Holographic Optical Elements (HOE)

4.3.1 General

A HOE is a reflecting or transmitting film which, through the process of diffraction, converts an illuminating wavefront of one form into a second wavefront which emulates whatever form of wavefront was used to form the hologram. The surface of the hologram can have any shape whatever so long as it remains fixed after the hologram is formed. Therefore, if the surface of the model is converted to a hologram, then any known illuminating wave can be converted into any other desired wavefront and directed to any desired direction regardless of the shape of the model.

Figure 17 illustrates the production and use of a HOE on an arbitrary surface. One method for forming a hologram on a metal surface of arbitrary shape is to first coat the surface with a photosensitive material, such as a photographic emulsion or photoresist, in which to make the recording. In producing the hologram, the reference wave is chosen to be like the wave that will later be used to illuminate the surface during the application and depends upon the characteristics of the instrument for which the surface is being constructed. The object wave used to produce the hologram is a wavefront like the one which is desired to leave the surface after it is illuminated.

If a photographic emulsion were used, the entire model would be treated like a photographic plate. After exposure, normal development and fixing procedures would be used. The developed hologram would then be bleached to form a high efficiency reflection hologram. If the emulsion were placed on a mirror-like surface bleaching would not be necessary. This would form a good optical surface but it would be rather fragile.

Alternatively, the photosensitive material can be photoresist. After exposure, the surface would be etched, forming a surface relief hologram. This also is an extremely fragile surface; however, the surface can be metal coated, making it a more rugged surface. The latter

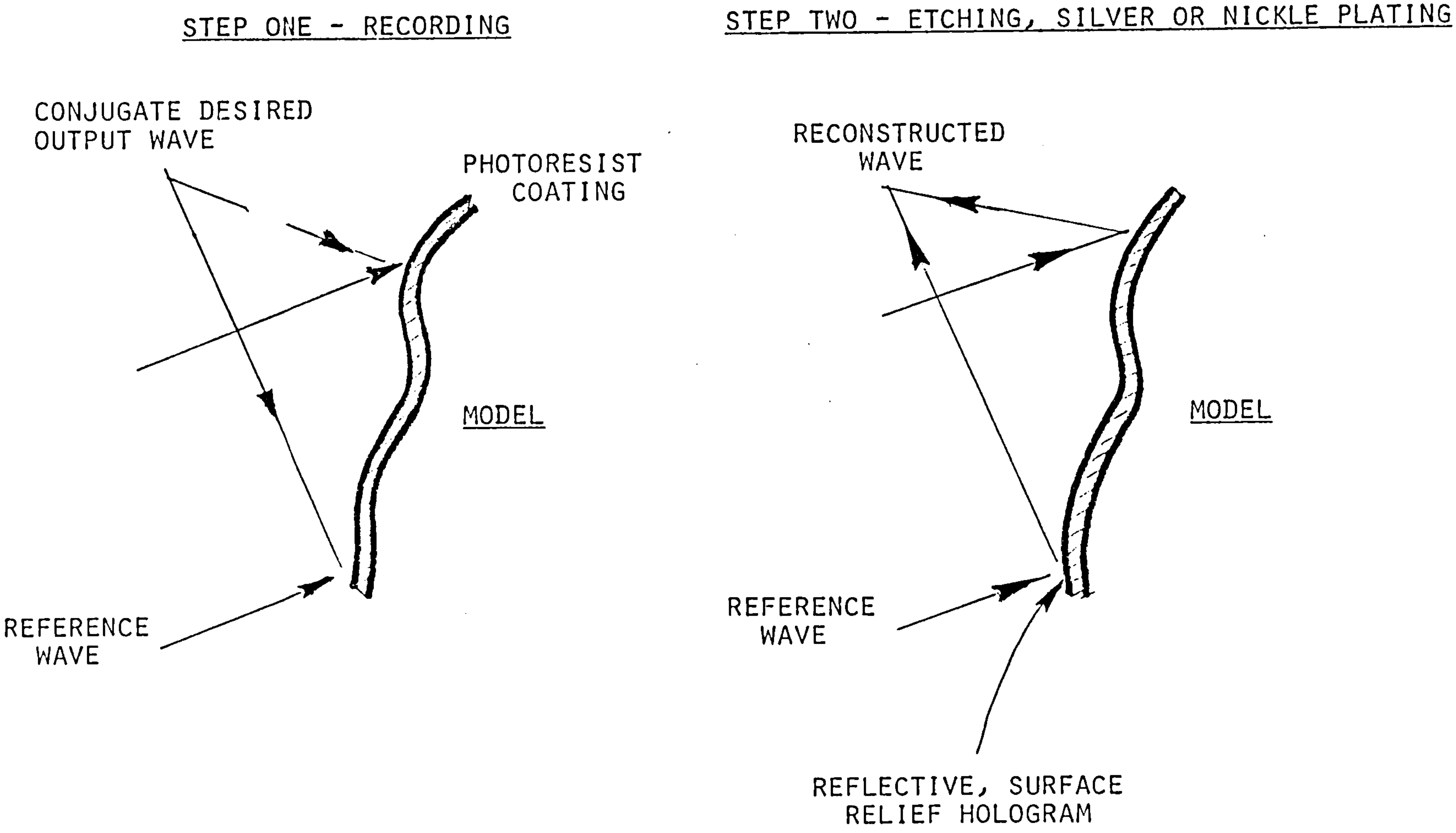

Figure (17) Producing and Using a HOE on an Arbitrary Surface type of HOE was produced during this program. These metal surface relief holograms can be used to replicate identical holograms by pressing into plastics (to be discussed later).

4.3.2 Conceptual Application

Before discussing further the production of HOE's, a discussion of potential applications will be given. Figure 18 illustrates a set of applications in a wind tunnel. The holographic element is formed on a curved model. In example A, a collimated input wave emerges as a collimated output wave directed at some convenient angle. In example B, a collimated input wave emerges as a wave which comes to a focus at some desirable point near the model. This might, for example, be a small window located at the point. In example C, an input wave emerges as a pair of waves. There is, in principle, no limit to the number of waves that can be made to emerge from the surface.

Now consider how such waves might be put to use in flow dignostics. Figure 19 illustrates a potential application in Laser Doppler Velocimetry. A model surface is coated with a HOE which reflects a collimated input wave as two collimated waves with an angle between them. In the overlap region, the familiar interference fringes encountered in Laser Doppler Velocimetry will be found. Therefore, one has created an LDV sample volume immediately at the surface of the model. Detecting optics, which are set between the two reconstructed beams, will be operating in the forward scatter mode - the most easily applied mode.

Figure 20 carries the concept a step further by coating the surface with a more complex HOE. In this case, a collimated input wave is converted into a number of output waves which focus and cross at points

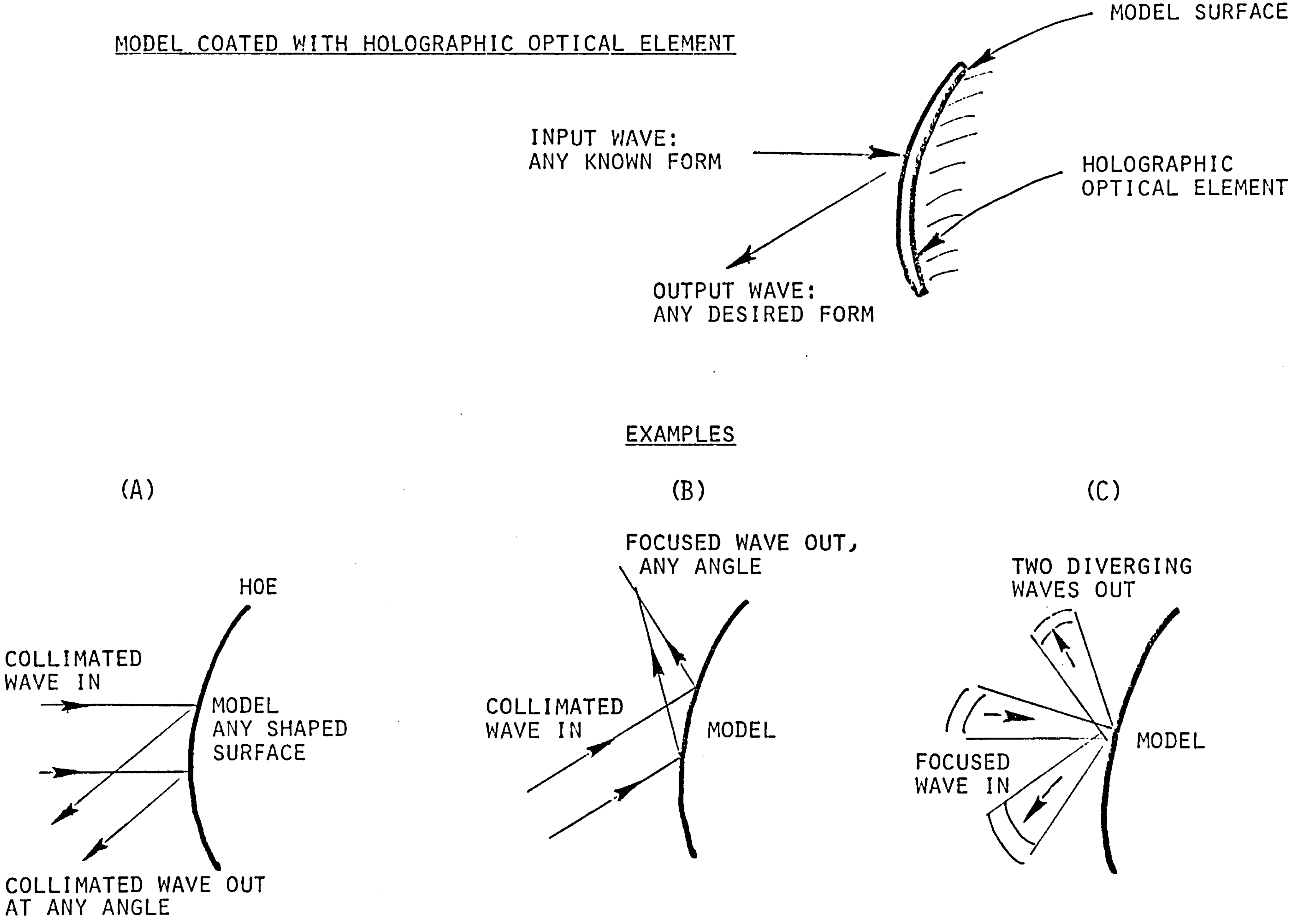

Figure (18) Example HOE Application - In Wind Tunnels

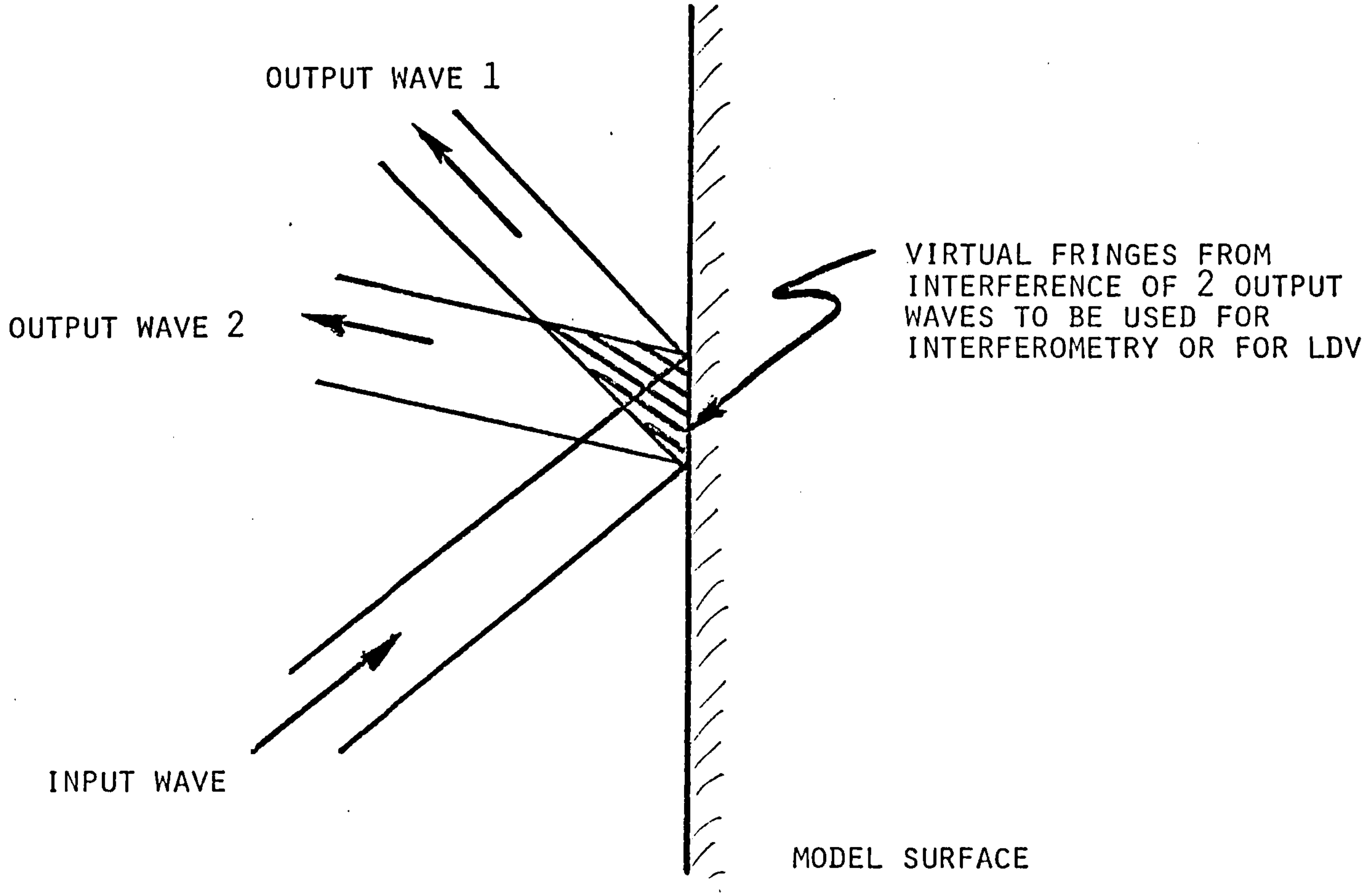

Figure (19) Laser Doppler Velocimetry Made Possible by HOE

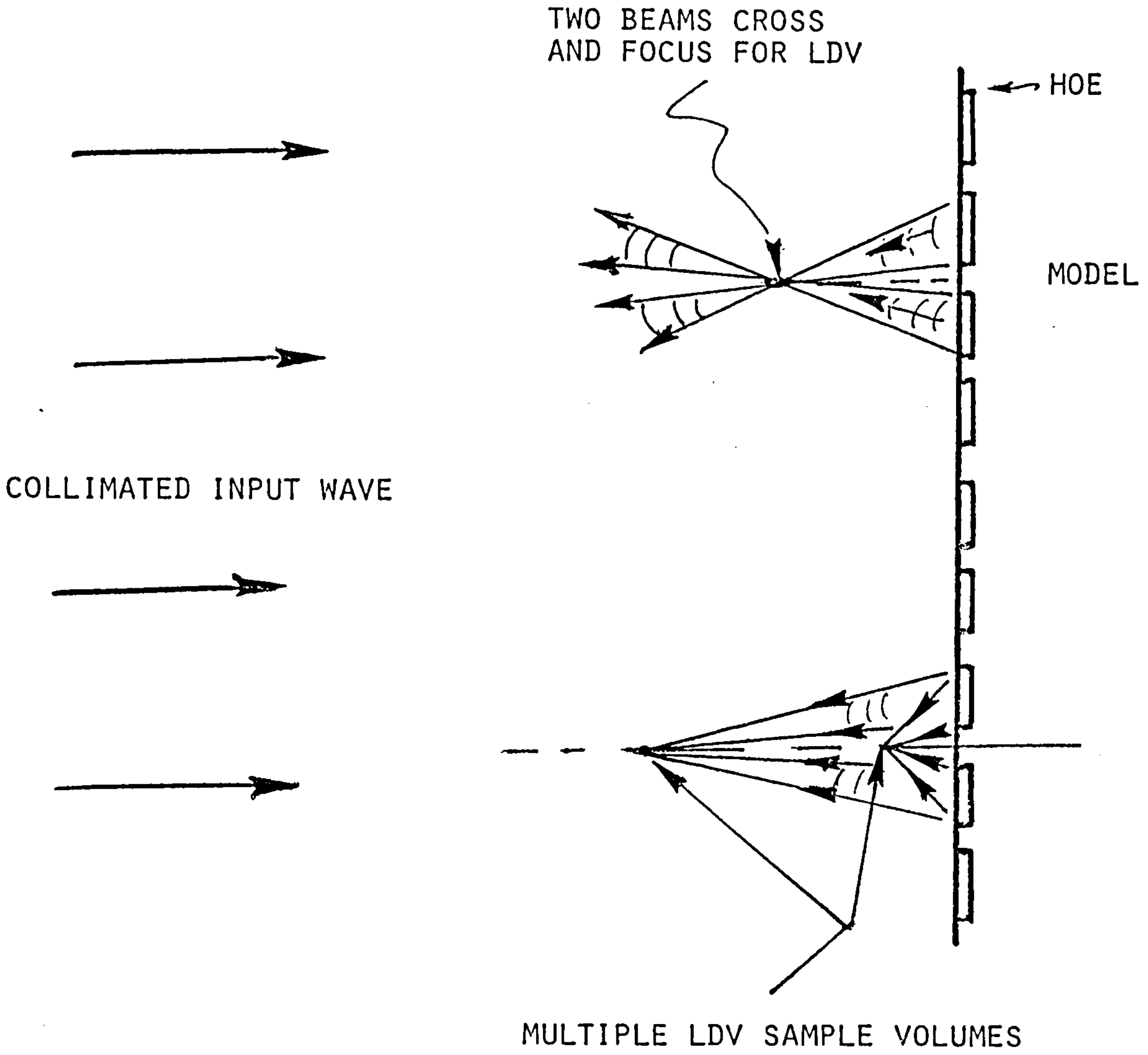

Figure (20) Multiple Point LDV Systems Generated by HOE's near the surface. Each point where two waves cross becomes an LDV sample volume. In this way, many points could be sampled for velocity at the same instance. A striking feature of such an application is that with only a single input wave the equivalent of many LDV systems is achieved.

Figure 21 illustrates a HOE application which makes flow visualization possible in regions where the model blockage otherwise prevents using conventional techniques from applicability. In this case, a collimated wave, which passes across the region of interest, strikes the model surface on which a HOE has been formed to keep the wave collimated, and to direct it to a place where it can be recorded in the form of a shadowgraph or interferogram. Without the HOE, the reflected wave would have been a badly distorted, diverging and astigmatic wavefront that would have been uninterpretable.

The same principle can be used wherever an aberrating element such as a curved window exists in the optical train, otherwise preventing schlieren, shadowgraph or LDV from being used. An aberration correcting HOE can be introduced to provide the required wavefront. A prime example of this is the diagnostics of flows in cylindrical pipes.

4.3.3 Construction of a HOE for High Efficiency Indirect Shadowgraph or Holographic Interferometry.

A potential application of HOE for high-efficiency indirect shadowgraph or holographic interferometry was carried to the point of producing and laboratory testing the the HOE. The objective was to produce a HOE which would receive light from a projector at some angle, a,

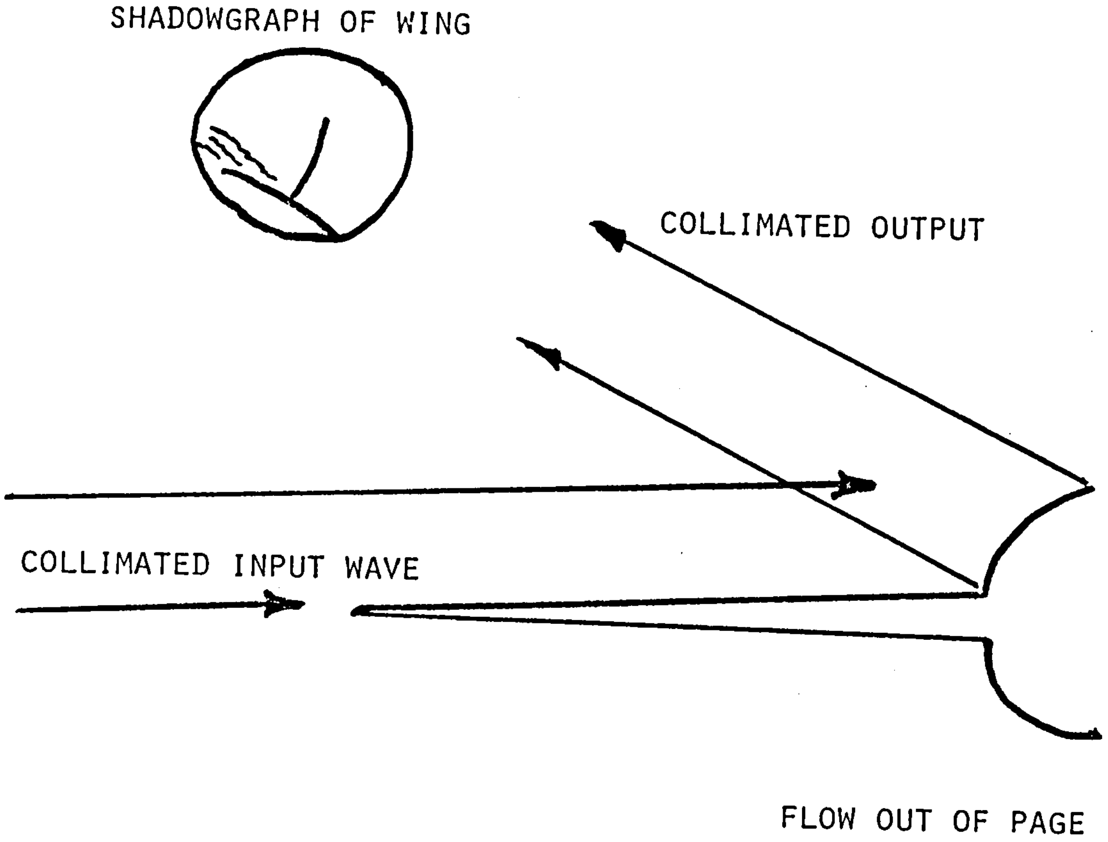

Figure (21) Flow Visualization in Model Blocked Regions by HOE and concentrate the reflected light in an aperture around an axis at an angle, θ, not the specular angle. Figure 22 illustrates the requirement.

In a separate program, contract number NG1339-84-C-0026, for the U.S. Naval Training Equipment Center, the production of sample replicas or embossed screen material for accomplishing a similar task was an objective.

Large hologram arrays were produced by replication. The individual hologram geometry is illustrated in Figure 23. A computerized traverse was assembled and software was developed to automate hologram array production (see Figure 24). Replication begins by coating the photoresist with a conductive silver layer about one or two molecules thick. A 0.024" layer of nickel (see Figure 25) is electro-deposited and is peeled off the photoresist, destroying the photoresist layer in the process. This surface is a negative of the hologram. Next, positive "matrices" are produced by plating this negative and peeling of the resulting plate. Up to about twenty plates can be made before deterioration is observed.

The nickel master is used in a hot press to produce the aluminized mylar replicas. Large quantities of aluminized mylar can be produced at a moderate cost. This material comes with a peel-off backing such that it can be fixed onto another surface.

Alternative methods to produce replicas include injection molding and plastic casting. Casting heated acrylic onto a master can produce a nearly perfect replica. The acrylic must then be aluminized to attain maximum efficiency.

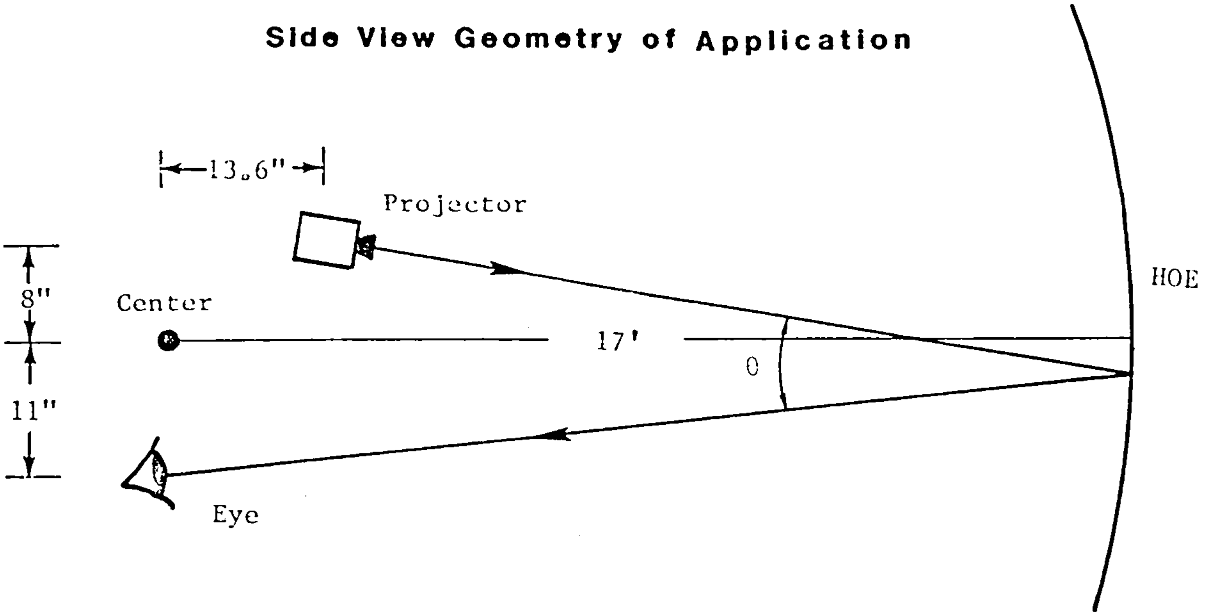

Side View Geometry of Application

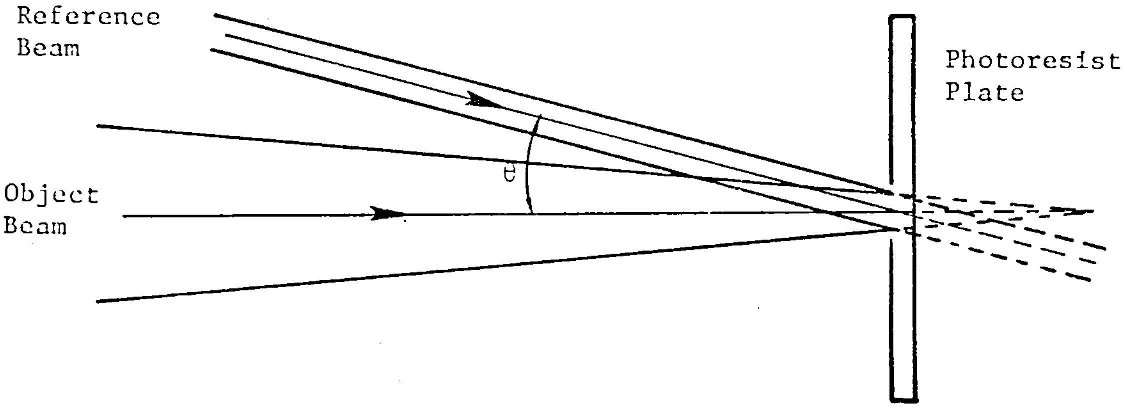

Hologram Construction

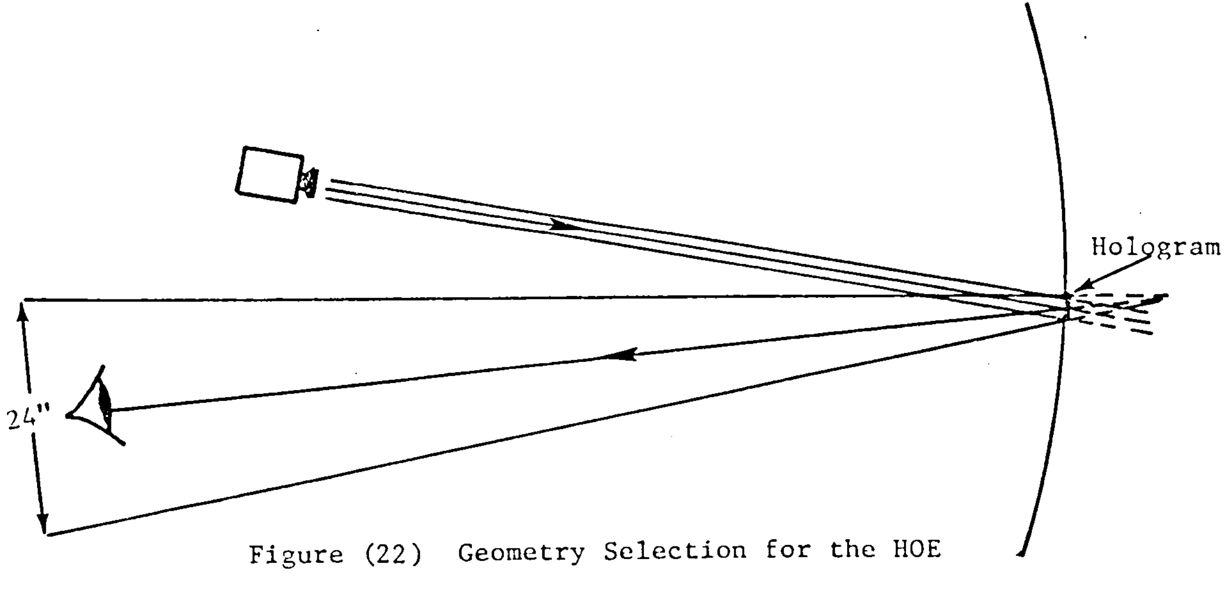

Hologram Reconstruction

Figure (22) Geometry Selection for the HOE

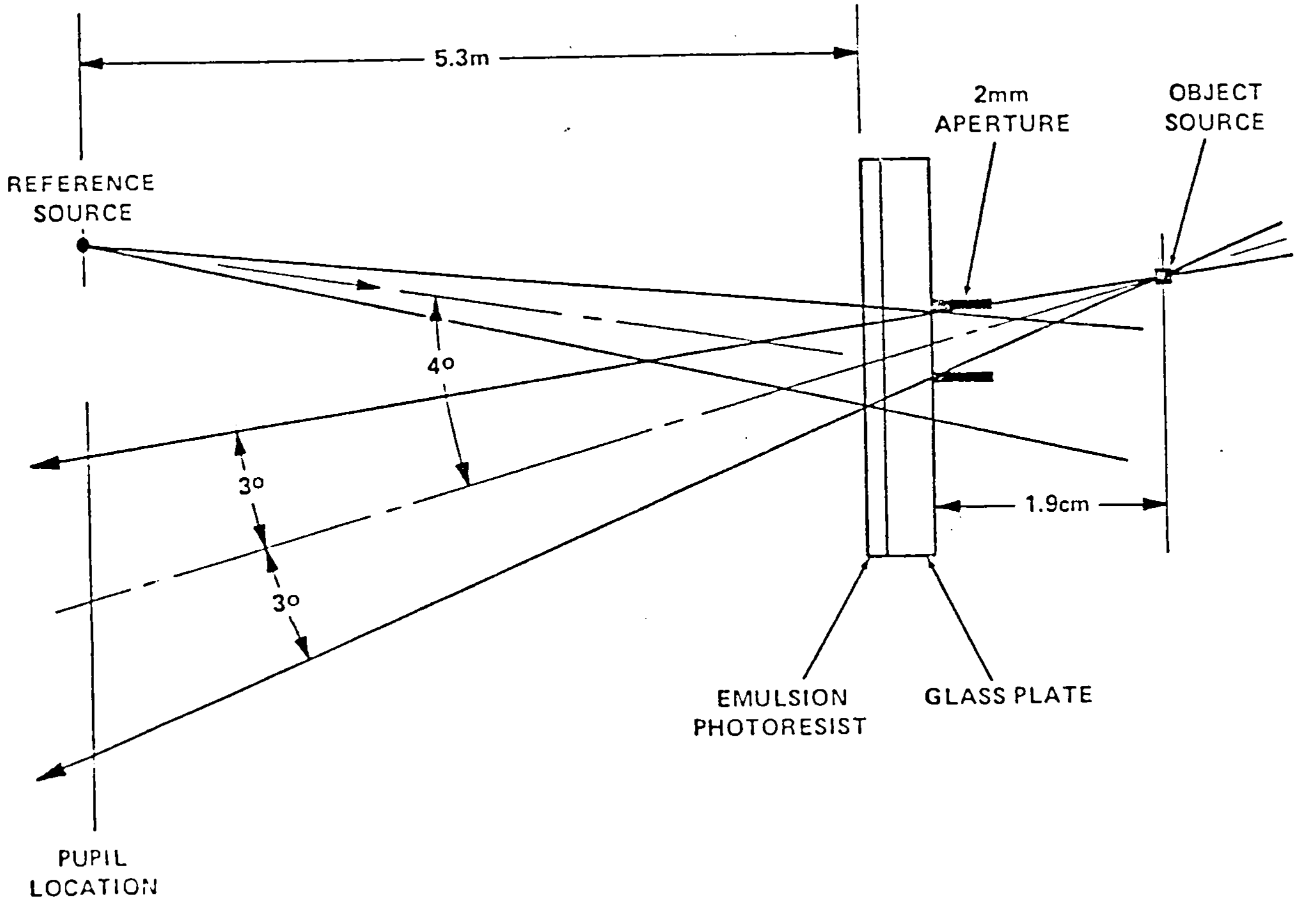

Figure (23) Exposure Geometry for Experimental Nonspecular Holographic Pupil-Forming Screen.

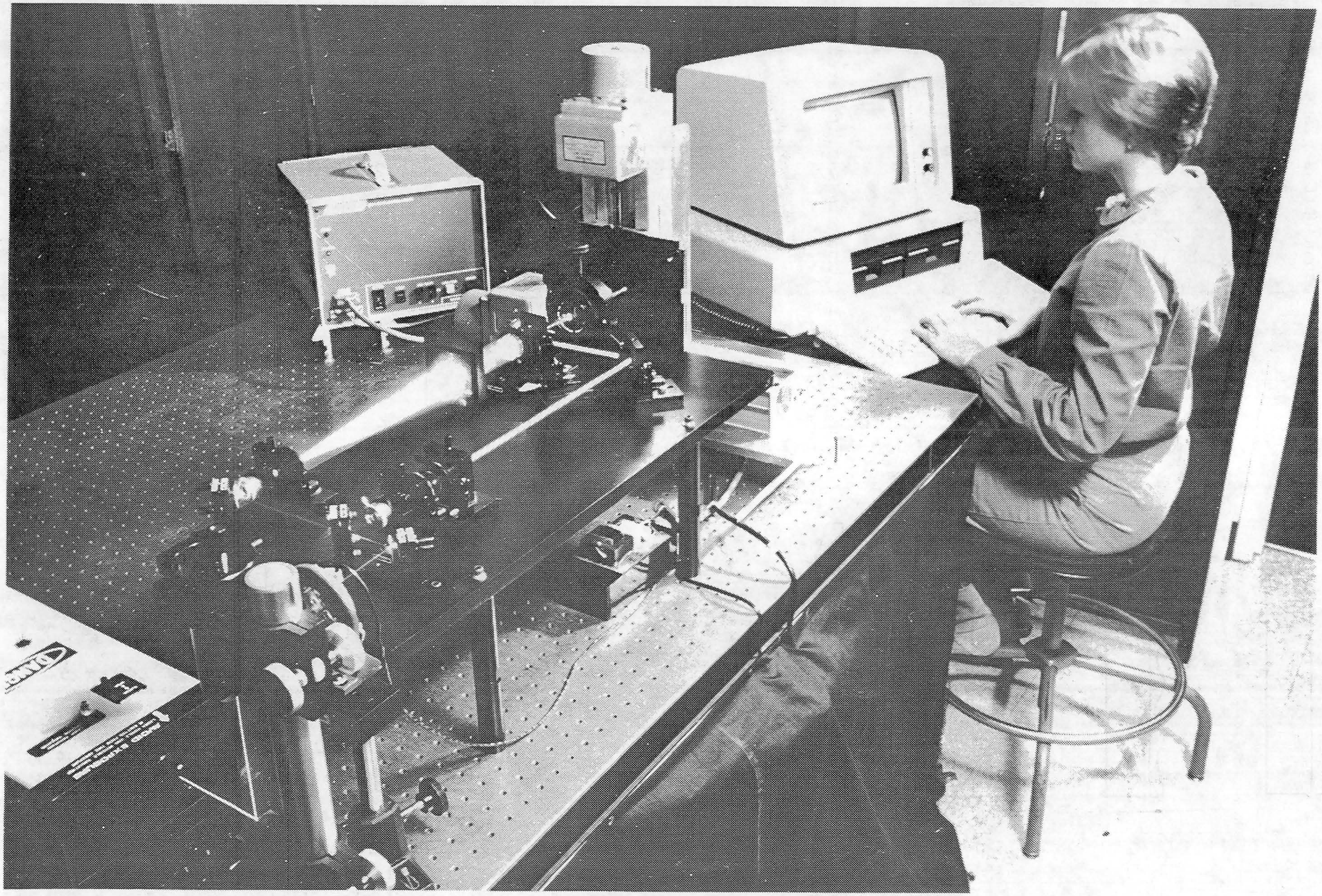

Figure (24) Computer Controlled Hologram Generation Station

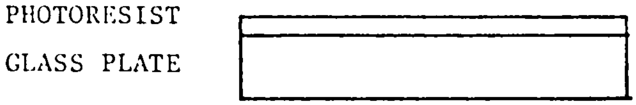

Photoresist is spun onto a glass plate.

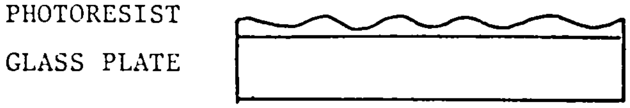

Exposure to light followed by development causes permanent surface deformation in the photoresist. The irregularities will diffract light to recreate the original image.

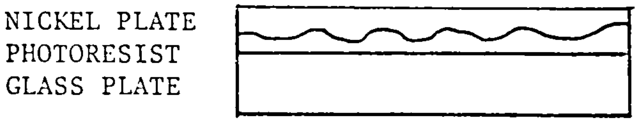

Nickel is plated on the deformed photoresist to create a master plate.

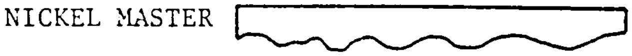

The photoresist and glass plate are removed.

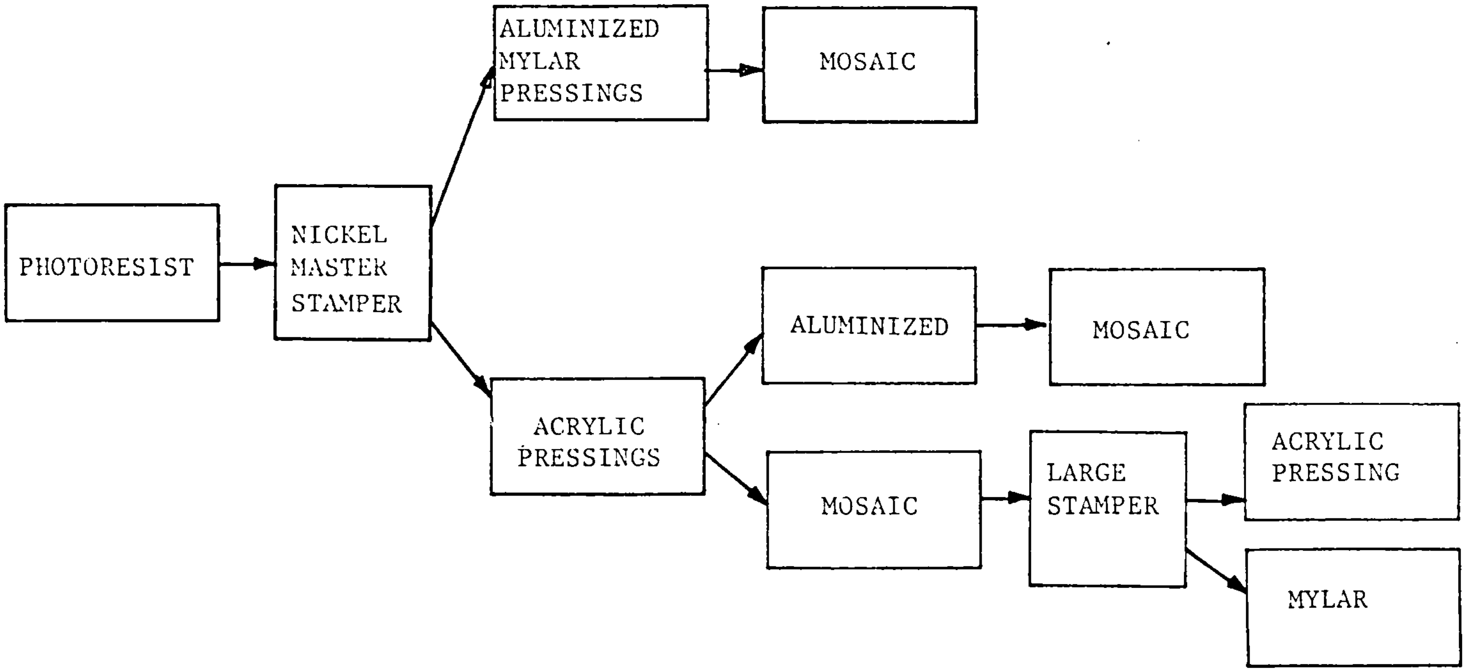

Figure (25)

Creating a High-Gain Projection Screen From Glass Plate Holograms

The final product was a 6-inch by 50-foot roll of hologram arrays embossed on aluminized mylar. This was produced by American Banknote Corporation, the same company that produces holographic VISA and Mastercards and produced the holographic cover of National Geographic Magazine.

In total, seven different master arrays had been produced ranging in size from 3" x 4" to 5" x 7". Each array contained from 4,000 to 7,000 holograms and the time required to produce each array ranged from six to eleven hours.

Tests were performed on the best samples. These are included in detail herein. Figure 26 illustrates one such test of the master hologram.

Figure 27 is a resulting appearance of a combined white and holoscreen near the desired viewing aperture. The high screen gain is evident. Screen gains as high as 20 were measured.

4.4 Preparation of Surfaces For Differential Interferometry

The ideal surface for differential interferometry is the case of no surface at all, that is, wherein the light passes directly through the region of interest and on to the receiver. The equivalent of this is when the surface is a perfect mirror and the light reflects from it, returning to the detector with phase information being influenced by the flow field only. This provides a signal of highest possible signal-to-noise ratio. When it is possible to prepare the model surface to a mirror surface and when the optical axis can be oriented normal to the surface this should be done. When this is not possible, alternative

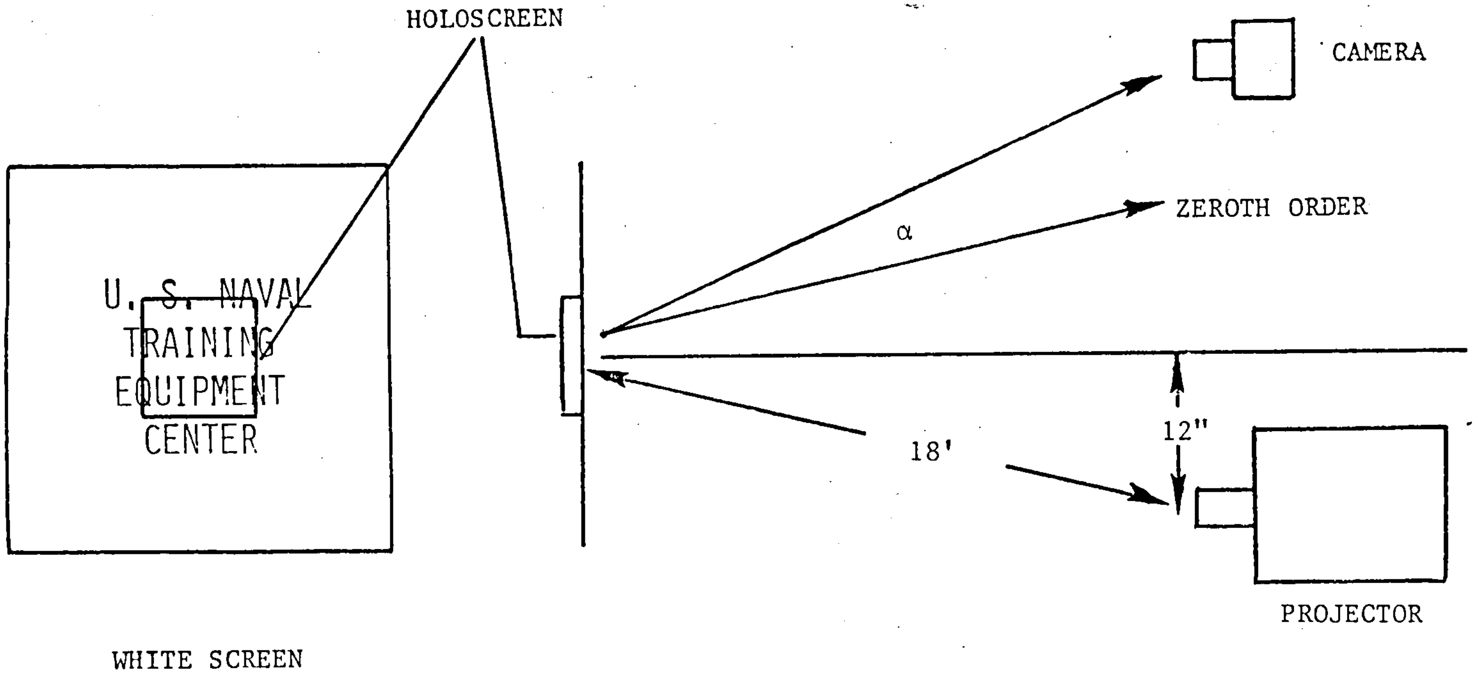

Figure (26) Holoscreen Measurement Experimental Configuration

ALL EXPOSURES ARE THE SAME.

NOTE - ZERO POSITION IS IN THE CENTER OF THE VIEWING APERTURE 18 FEET FROM THE SCREEN.

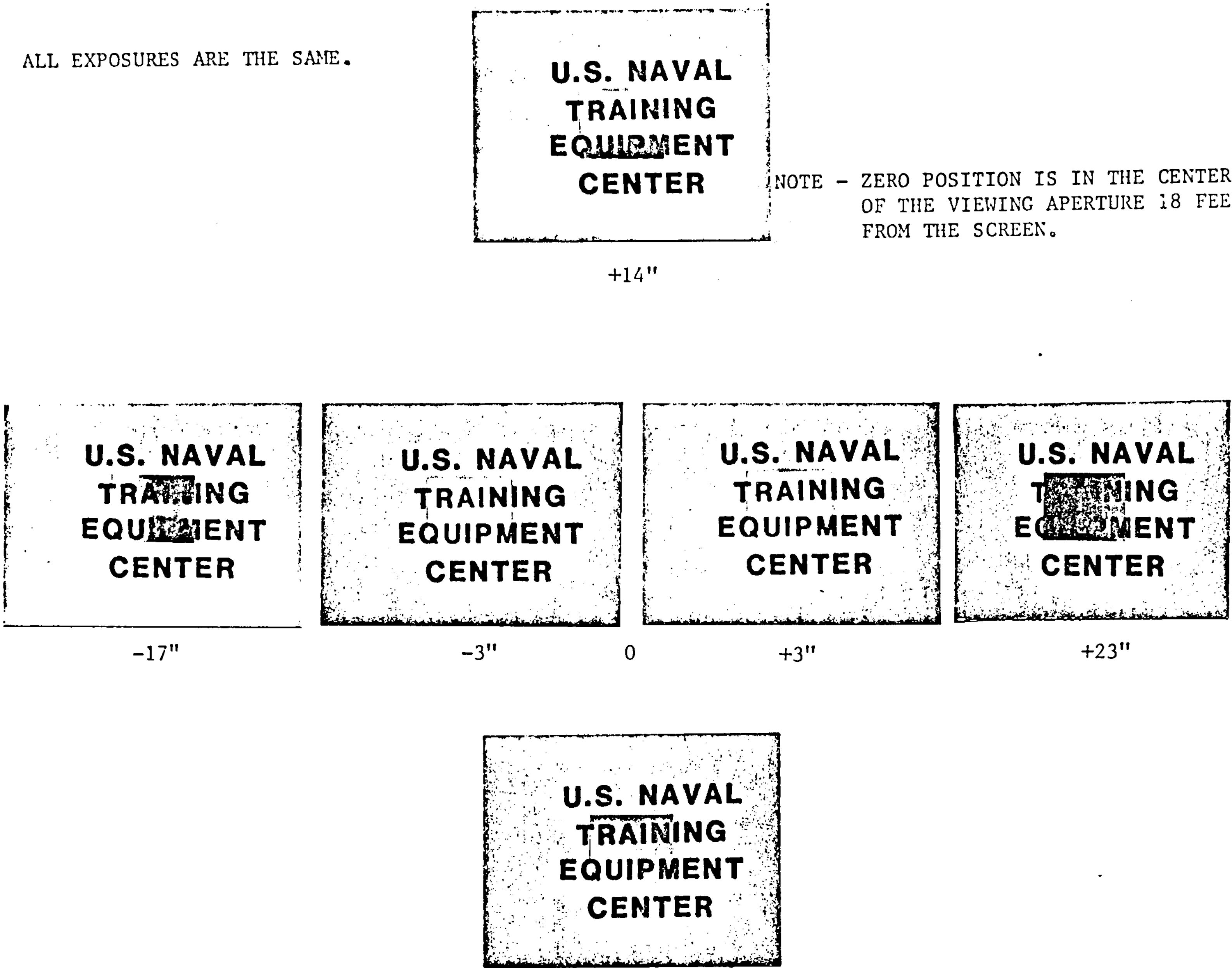

+14"

-17" -3" 0 +3" +23"

-14"

Figure (27) Photograph of the Uncoated Holoscreen at the Center and Near the Edge of the Aperture approaches described above which provide signal-to-noise ratios almost as good have been tested.

For cases with angles of incidence less than about 20 degrees, the corner cube material produced by Avery International proved superior. At angles up to about 45 degrees the scientific grade retroreflecting material produced by 3M Company excelled.

The production and testing of HOE's for this application were beyond the scope of this project; however, in theory, these could approach the mirrored surface for signal quality regardless of the surface shape.

4.5 Recommendations

The use of mirrored surfaces and retroreflective materials appear to be adequate for surface preparation for the differential interferometry. However, in this study, the introduction of the principle of HOE application in the general area of flow diagnostics has led to extremely exciting possibilities and could represent a major breakthrough in the study of flows in otherwise inaccessible locations.

Therefore, it would seem to be of great importance to continue the investigation of this concept and its application to important problems in experimental aerodynamics.

5.0 EXPERIMENTAL TESTS

This chapter describes two sets of experiments performed to validate the interferometer system. The first set of tests were performed in low-speed wind tunnels. Controlled temperature fluctuations were used to simulate the density intermittency encountered in supersonic flows. The tests included two wind tunnel experiments: 1) shear layer and 2) turbulent spot. The shear layer experiment was an open system, i.e., the optical access to the point of interest did not require a window. The turbulent spot experiment involved propagating the laser beam through a window, where the effects of window boundary layer have been assessed.

The second set of tests were performed in a supersonic wind tunnel (NASA Langley Unitary Wind Tunnel). The experiments embodied: 1) turbulent tripping wire experiment, 2) turbulent wedge, and 3) natural transition. A description of the apparatus and experimental procedures will follow herein.

5.1 Low Speed Wind Tunnel Tests

The differential optical path, Δp, can be expressed in terms of the temperature difference, ΔT, such that

$$\frac{d}{dx}\left(\frac{\Delta p}{\lambda}\right) = \frac{K}{\lambda} \cdot \left(\frac{\rho}{T}\right) \cdot \Delta T(x) \tag{14}$$

where x is the distance along the beams' line of sight, K is the Gladstone-Dale constant ($K_{air} = 2313 \times 10^{-7}\ m^3/kg$), ρ and T are the freestream density and temperature respectively.

5.1.1 Shear Layer Experiment

A shear layer assembly with an output cross section of 1 cm x 10 cm, as shown in Figure 28 was used to calibrate the system. Variable temperature differential in the shear layer behind the splitter plate was produced by applying a variable voltage across the heating element. Temperature fluctuation at the measurement point was then caused by the fluctuation of the flow behind the splitter plate.

The laser beams were positioned normal to the flow and parallel to the splitter plate. The two beams were focused at 2.5 cm behind the splitter plate. The two beams were separated by 2 mm in such a way that one beam was 1 mm above the splitter plate and the second beam was 1 mmm underneath the splitter plate. Two experiments have been performed, one used a mirror to reflect back the laser beams, and the other used a diffuse surface (simulating aerodynamic prototypes) to scatter back the laser beams. Figure 29 is a schematic illustration of the optical setup of the reflecting mirror or diffuse surface.

The temperature fluctuations were measured using a Tungsten wire with no overheat (cold wire). The cold wire was installed 2 mm downstream of the optical measurement station. The temperature fluctuation profile along the optical path was measured to reduce the measured temperature difference into pathlength difference via Equation (14).

5.1.2 Turbulent Spot Experiment

The turbulent spot experiment was performed in a test section 20 x 20 cm suction type low speed subsonic wind tunnel. A flat plate was placed in the test section perpendicular to the direction of the laser beams at 13 cm from the window as shown in Figure 30. The incompressible boundary layer flow over the flat plate, with freestream velocity of 4.3 m/sec was disturbed by a periodic flow of heated air through an orifice in the surface of the plate 0.32 cm in diameter and located 9 cm behind the leading edge as shown in Figure 30. The heated air originated from a compressor, through a heating chamber. It was then passed through a solenoid valve, which was driven by a signal generator. The two output ports of the valve were connected to the ambient and to the orifice inlet in the flat plate. Proper frequency and amplitude setting of the driver signal resulted in a periodic flow of heated air through the port. The line pressure was set such that the penetration depth of the heated air into the boundary layer did not exceed the boundary layer thickness, about 0.45 cm.

The interferometer beams were focused on the machined surface of the flat plate 1 cm from the orifice. The beams were separated by 0.2 cm and positioned such that the heated air would pass through only one of the two beams. A cold wire was placed behind the laser beams as a check on the performance of the interferometer, and also to measure the temperature fluctuations along the beam path. The cold wire has also been used to measure the profile of the temperature fluctuations to quantify the phase difference via the integration of Equation (14).

A 0.5 cm diameter vertical heating rod was placed at the entrance to the test section in the wind tunnel inside the optical access boundary layer 0.63 cm from the window. Temperature disturbance to the outer B.L. was controlled by connecting the rod to a rheostat. Temperature fluctuations up to about 15 °C could be obtained through such an

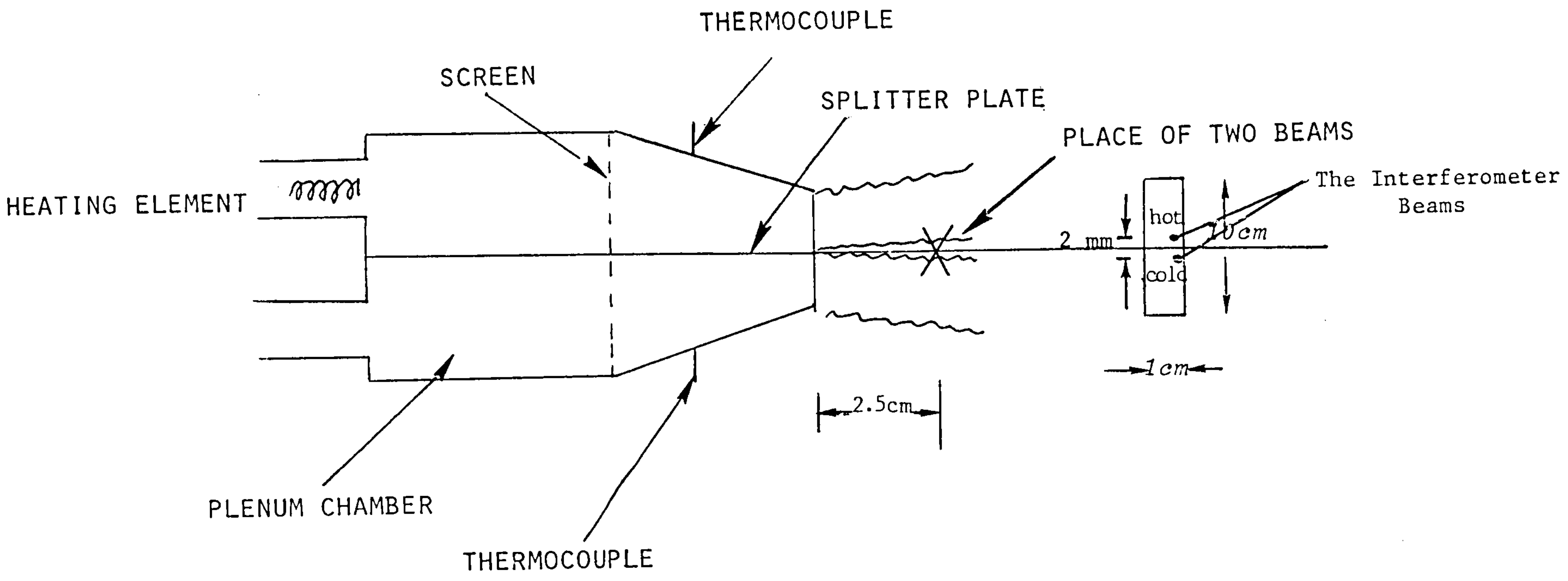

Figure (28) Schematic of the Shear Layer Assembly

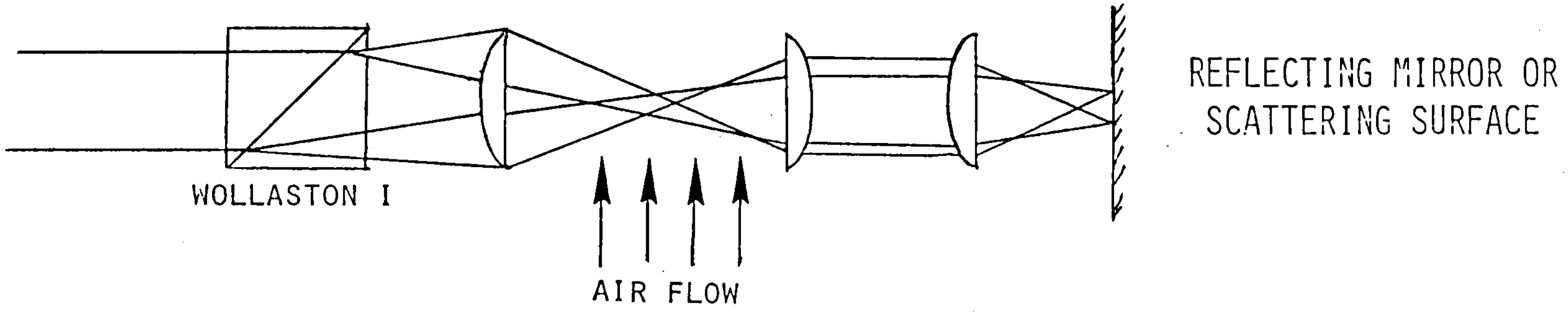

Figure (29) Schematic Illustration of the Optical Setup of the Reflecting Mirror/Scattering Surface

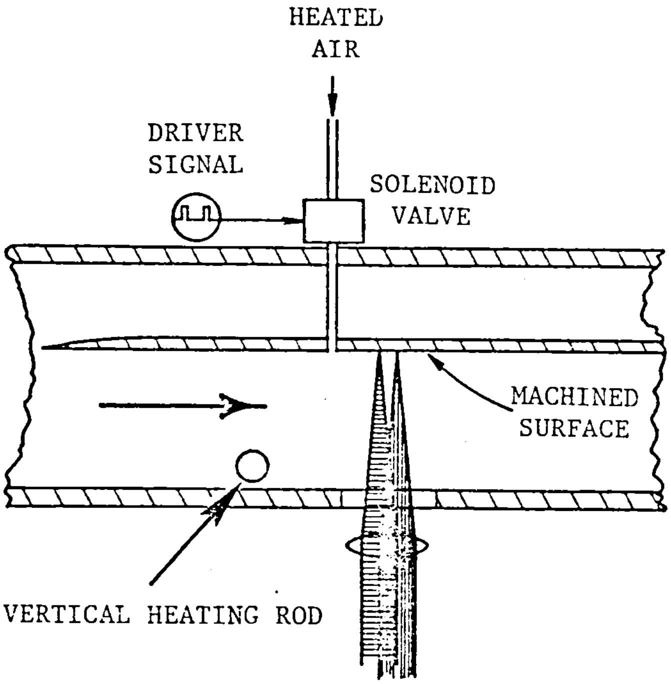

Figure (30) Schematic of the turbulent spot experiment.

arrangement. The laser beams out of the first Wollaston prism located at 12.5 cm from the optical window propagated through the outer B.L. to get to the flat plate. A parametric study of the effects of the disturbance created by the rod on the detectability limit of the signal of interest were performed.

5.2 Supersonic Wind Tunnel Tests

5.2.1 Tunnel Conditions

The tests were conducted at Test Section II at the Langley Unitary Plan Wind Tunnel which is a variable pressure continuous flow facility. The tunnel conditions were:

- Mach number = 2.36
- Stagnation temperature = 339 °K
- Stagnation pressure range = 38 to 189 KN/m^2
- Reynolds number range (m^{-1}) = $3.3(10)^6$ to $1.6(10)^7$
  (ft^{-1}) = $(10)^6$ to $5(10)^6$

Table (4) is a summary of the tunnel conditions. The Gladstone-Dale coefficient used corresponds to that of air, $K = 0.0002317\ m^3/Kg$, and the wavelength is the He-Ne red line, $\lambda = 6328$ °A.

TABLE 4. SUMMARY OF TUNNEL CONDITIONS

Re/ft	P_o KN/m^2	ρ_o Kg/m^3	ρ Kg/m^3	$K\rho/\lambda$ $\cdot m^{-1}$
$(10)^6$	38	0.39	0.06	22
$2(10)^6$	76	0.78	0.12	43.97
$3(10)^6$	114	1.17	0.18	65.95
$4(10)^6$	152	1.56	0.24	87.94

The model was a flat plate with a zero angle of attack. Table 5 is a list of the boundary layer thickness, δ, and the difference in path length, $\Delta p/\lambda$. The density fluctuations $\Delta\rho/\langle\rho\rangle$ has been assumed to be 1% over half the boundary layer thickness.

TABLE 5. BOUNDARY LAYER THICKNESS AND OPTICAL PATH DIFFERENCE AS A FUNCTION OF REYNOLDS NUMBER

R_e/ft	δ(mm)	$\Delta p/\lambda$[at x = 4"]
$(10)^6$	1.23	1/3690
$2(10)^6$	0.871	1/2611
$3(10)^6$	0.7112	1/2132
$4(10)^6$	0.616	1/1846

5.2.2 Instrument Conditions

The instrument parameters were as follows:

A) Optical

- Wollaston (1) divergence angle = 1°
- Beam expander magnification = 3
- Focal length of the focusing lens = 30"
- Beam separation of the focal plane = 5 mm
- Beam diameter at the focal plane = 32 μm
- Beam coincidence at the window boundary layer = 83%

B) Electronics

- Signals were recorded on a direct drive recorder
- Frequency bandpass = 200 kHz
- Low-pass filter = 7 kHz

5.2.3 Unitary Wind Tunnel Tests

Two tests simulating transition were attempted: the turbulent wire experiment and the turbulent wedge experiment. The turbulent wire experiment involved a size 30, sand-wire located at 3.75" from the leading edge. In this experiment the two beams were horizontal with 5 mm beam separation at the focal plane. Three different Reynolds numbers were used ($R_e/ft = 2 \times 10^6$, 3×10^6 and 4×10^6). Scans were conducted at 0.0", 0.25", 1.25" and 3.25" from the wire.

The turbulent wedge experiment involved installing a roughness element at 2.4" from the leading edge. The beams were 5 mm apart at the focal plane, however, the beams were vertical. Vertical scans every 0.125" between y = +1" and y = -1" were conducted at 1.6" and 2.6" downstream from the roughness, where y = 0 is the roughness location. The measurements were done for the same Reynolds number as the previous experiment.

A natural transition test was attempted with the beams in the horizontal configuration. Measurements were conducted at 0.25", 0.375", 1", 2", 3", 4", 5", 6", 8", 9" and 12" from the leading edge. The flow Reynolds numbers were the same as previously stated.

Concurrent with the interferometer measurements, thin film gages which were installed at 4", 5" and 6" from the leading edge were used to measure the transition location.

6.0 RESULTS

The experimental results of the tests described in the previous chapter are presented herein. The laboratory results of the low speed wind tunnel tests are first presented, followed by the unitary supersonic wind tunnel results.

6.1 Shear Layer Experiment

Figure 31 shows the strength of the signal as a function of temperature fluctuations in the shear layer experiment for both the mirror and the scattering surface. The temperature fluctuations have been reduced to pathlength differences using Equation 14 as shown by the second abscissa in Figure 31. The signal strength reflected back off the reflecting mirror is about 5 times that scattered off the diffuse surface. The figure also shows that the signal is linearily proportional to small temperature fluctuations, while for large temperature fluctuations, the signal strength becomes nonlinear. For large temperature differences, the shear layer becomes 3-dimensional which results in temperature fluctuations in the transverse direction giving rise to the nonlinearity effects.

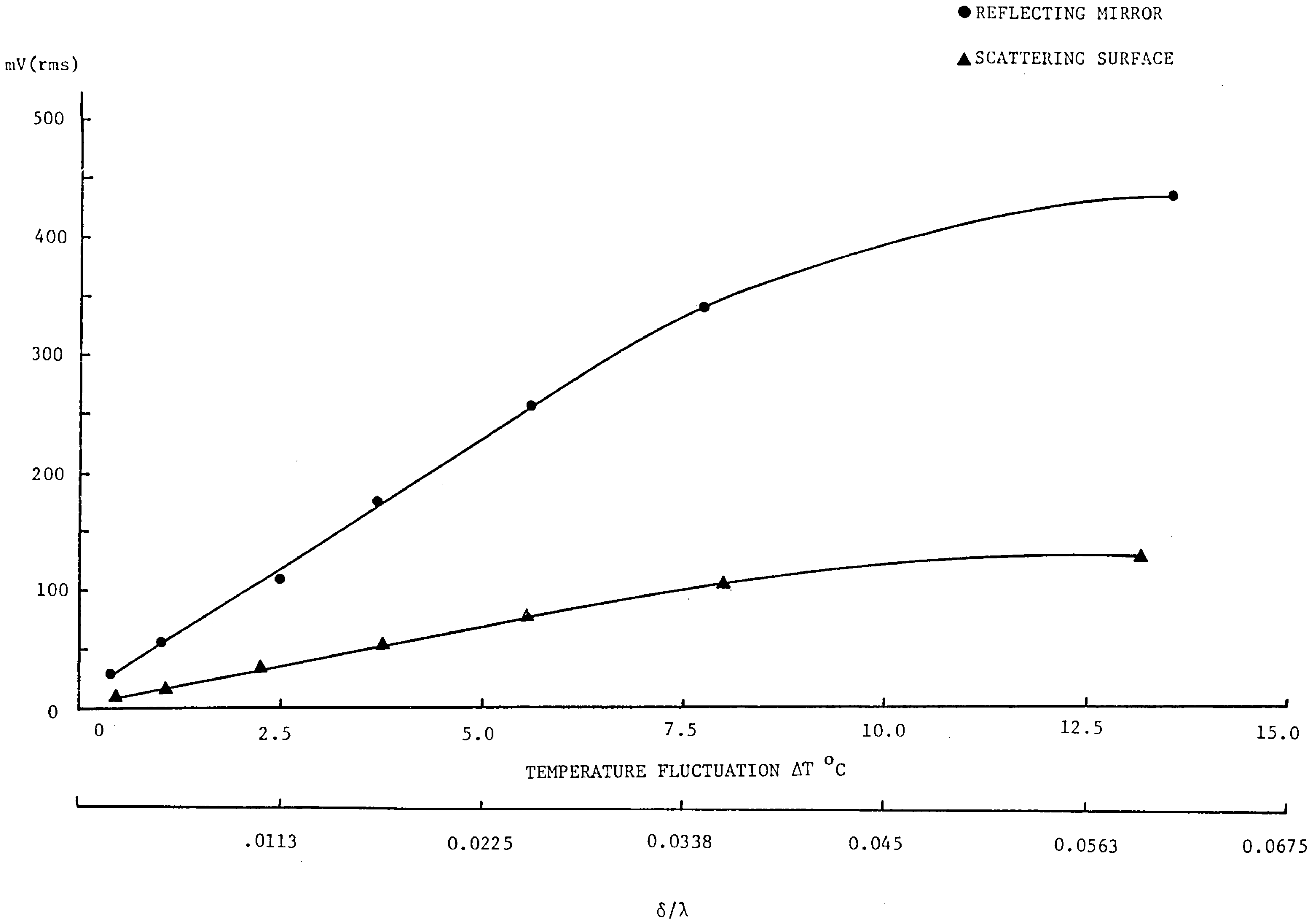

Figure (31) Laser Interferometer Signal RMS as a Function of Temperature Fluctuations for Both the Reflecting Mirror and the Scattering Surface.

6.2 Turbulent Spot Experiment

Three experimental configurations have been used to evaluate the performance of the high sensitivity differential interferometer: (1) diffuse surface, (2) retroreflecting surface, and (3) retroreflecting surface in the presence of boundary layer disturbance at the access optical window. Retroreflecting coatings of the model surface reflect back the incident laser beams along the incident beam, enhance the signal strength and the S/N ratio, reduce the speckle effects and eliminate diffraction due to tooling marks on the model. Several retroreflecting coatings were tried; the best performance was obtained from corner cubes coating, generically known as "scientific retroreflector", which was used throughout the present study.

The response characteristics of the interferometer system have been examined by comparing the output signal of the interferometer with that of the cold wire. The temperature fluctuations profile for both the diffuse surface and retroreflecting coating, measured by the cold wire along the optical path of the interferometer in the turbulent spot experiment, is shown in Figure 32. The air velocity in all turbulent spot experiments was 4.3 m/sec.

Figure 33 shows the frequency spectrum of the vibration level under a no heating condition as measured by the interferometer. The dominant natural frequencies of the low-speed wind tunnel were 64, 78, and 245 Hz.

Figures 34a and 34b represent the interferometer signal scattered off the diffuse surface of the flate plate and the cold wire, respectively, in the frequency domain. The frequency of the pulsating heated air through the orifice, in this case, was 305 Hz. The other

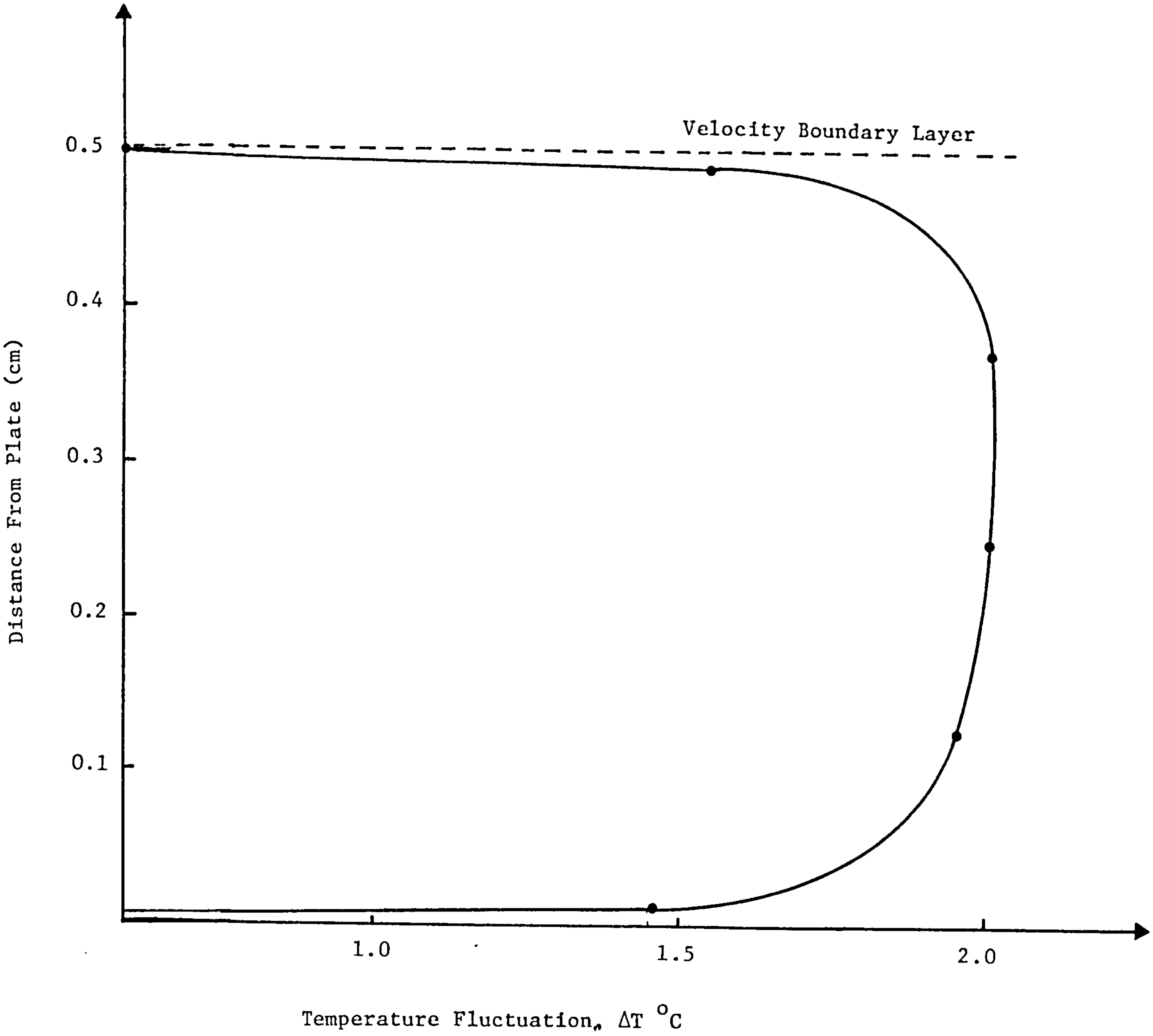

Figure (32) Temperature Profile of the Pulsed Jet Measured by the Cold Wire

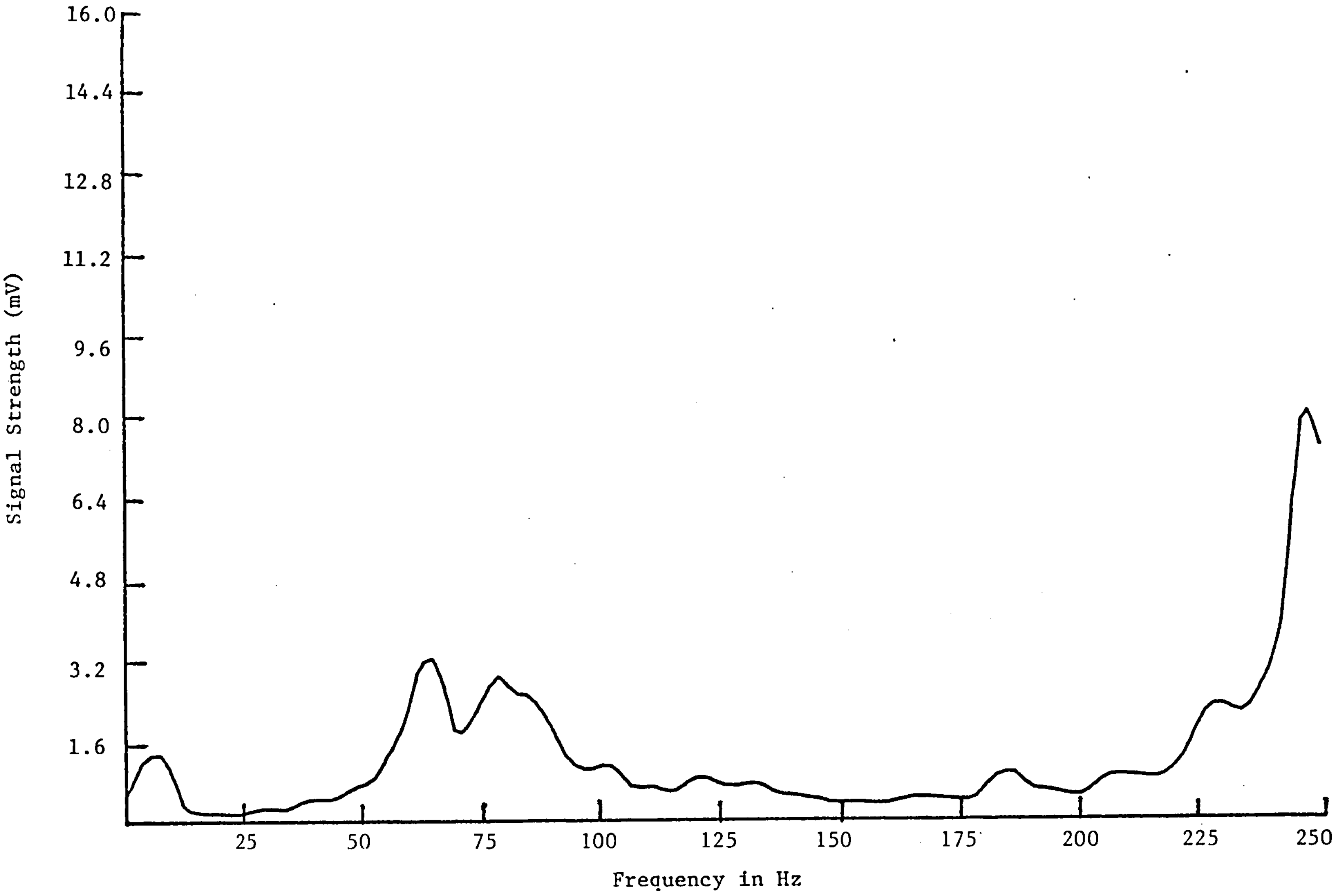

Figure (33) Vibration Level as Detected by the Laser Interferometer.

peaks in the frequency spectrum of the interferometer system are attributed to the vibration. No attempt was made to filter the vibration noise because the vibration fundamental frequencies were of the same order as the jet pulsations. However, numerical filters have been used to mathematically reduce the effects of vibrations. Figure 34c shows the interferometer signal strength after using the numerical filter to reduce the peaks due to vibration frequencies.

Figures 35a, 35b and 35c show the signal strength of the interferometer system using retroreflecting coating on the flat plate surface, the cold wire signal, and the interferometer signal after reducing the vibration effects, respectively. The orifice flow conditions were: frequency 115 Hz and $\Delta T = 1.4°C$. The cold wire shows a second harmonics signal at 230 Hz. The laser interferometer system also shows the same behavior as shown in Figures 35a and 35c.

Figure 36 illustrates the signal/noise ratio as a function of the temperature fluctuations. Both the first and second harmonics for a fundamental orifice frequency of 115 Hz are shown in the figure. The figure shows that the minimum detected first harmonics signal which corresponds to a phase difference of 1.41×10^{-3}, the laser wavelength, has a signal-to-noise ratio of about 150. The results shown in this figure confirm the ability of the interferometer system to follow small amplitude perturbations in the fluid flow with high signal-to-noise ratios.

Figures 37a and 37b show the effects of the window boundary layer disturbance on the detectability limit of the high sensitivity differential interferometer. Figure 37a shows the signal superimposed on the

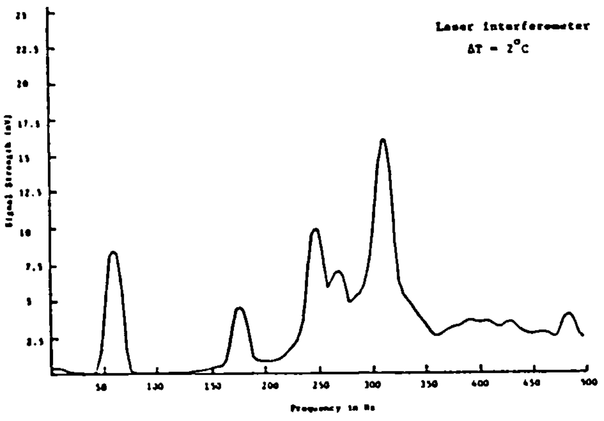

Figure 34a Spectrum of the laser interferometer signal for pulsating frequency of 305 Hz

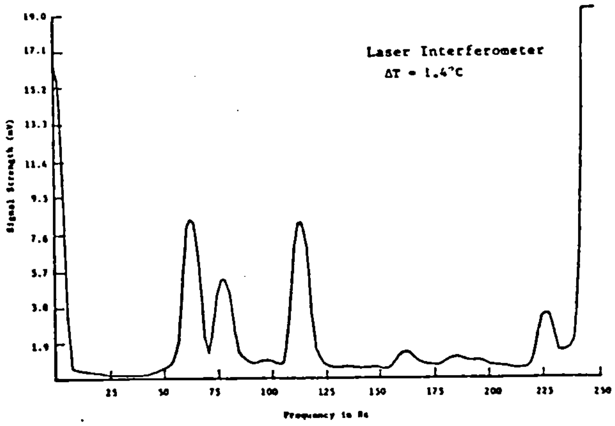

Figure 35a Spectrum of laser interferometer signal for pulsating frequency of 120 Hz using scientific retro-reflector

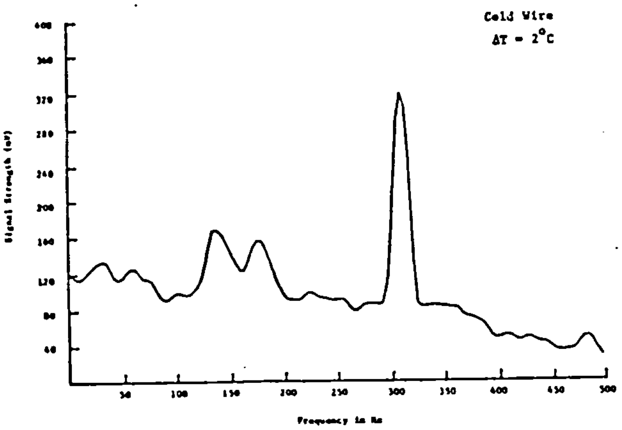

Figure 34b Spectrum of cold wire data for pulsating frequency of 305 Hz

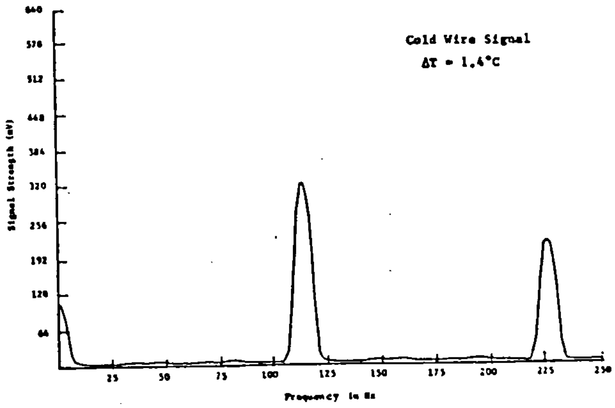

Figure 35b Spectrum of cold wire signal for pulsating frequency of 120 Hz

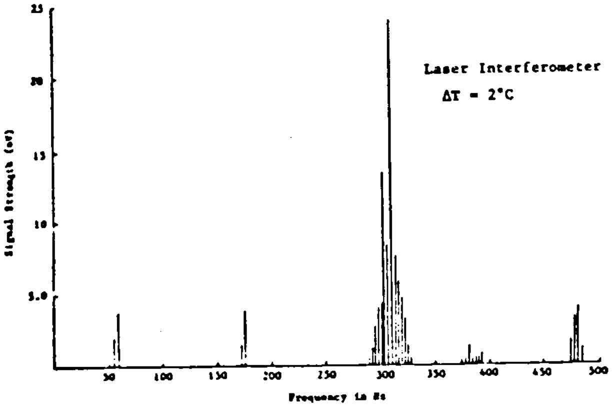

Figure 34c The digitized interferometer signal after filtering out the effect of vibration

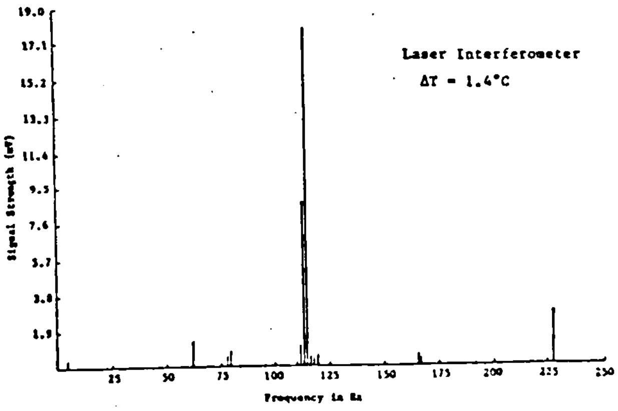

Figure 35c The digitized interferometer signal after filtering out the effect of vibration

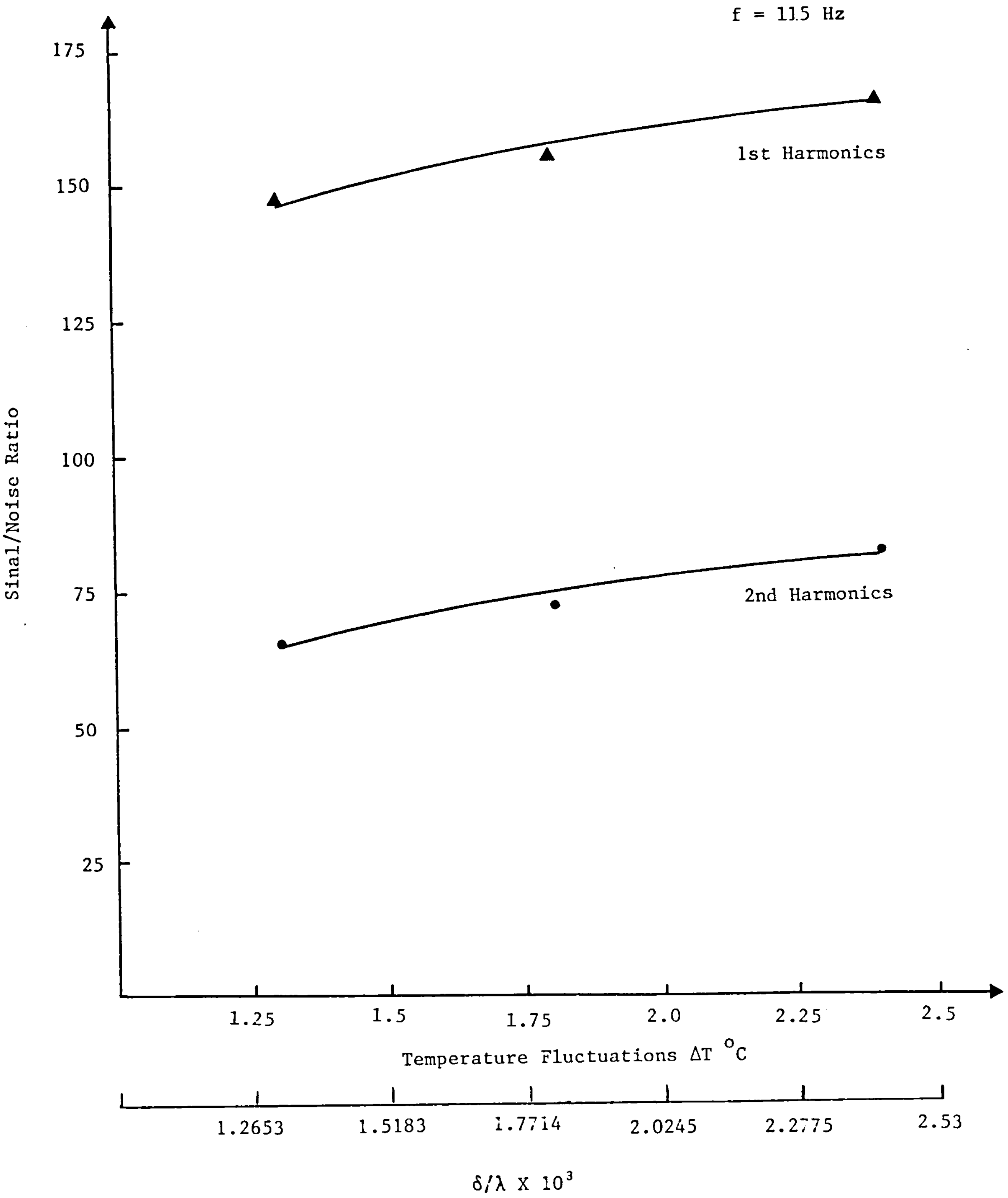

Figure (36) Signal/Noise Ratio of Both the First and Second Harmonics Using Retroreflecting Material on the Surface.

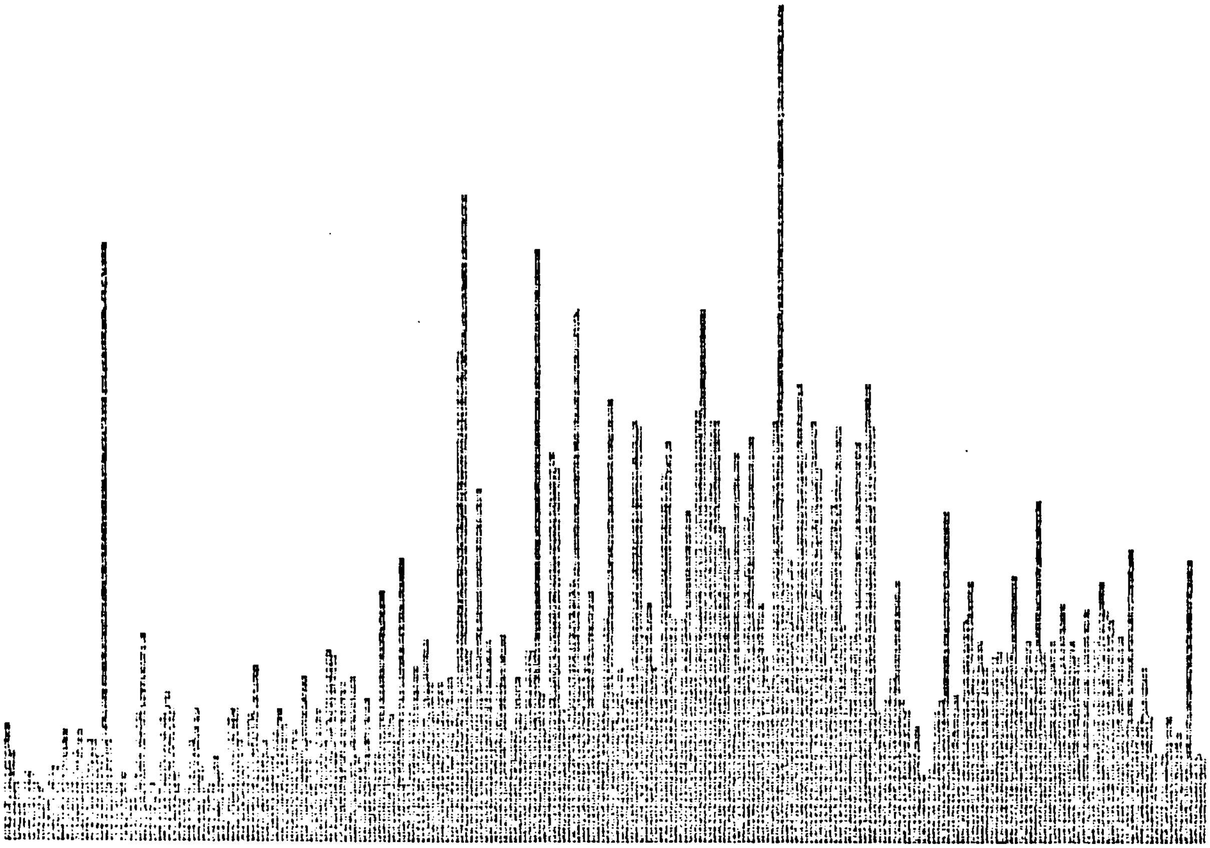

Figure (37a) The Digitized Frequency Spectrum of the Interferometer Signal Under Window Boundary Layer Disturbance.

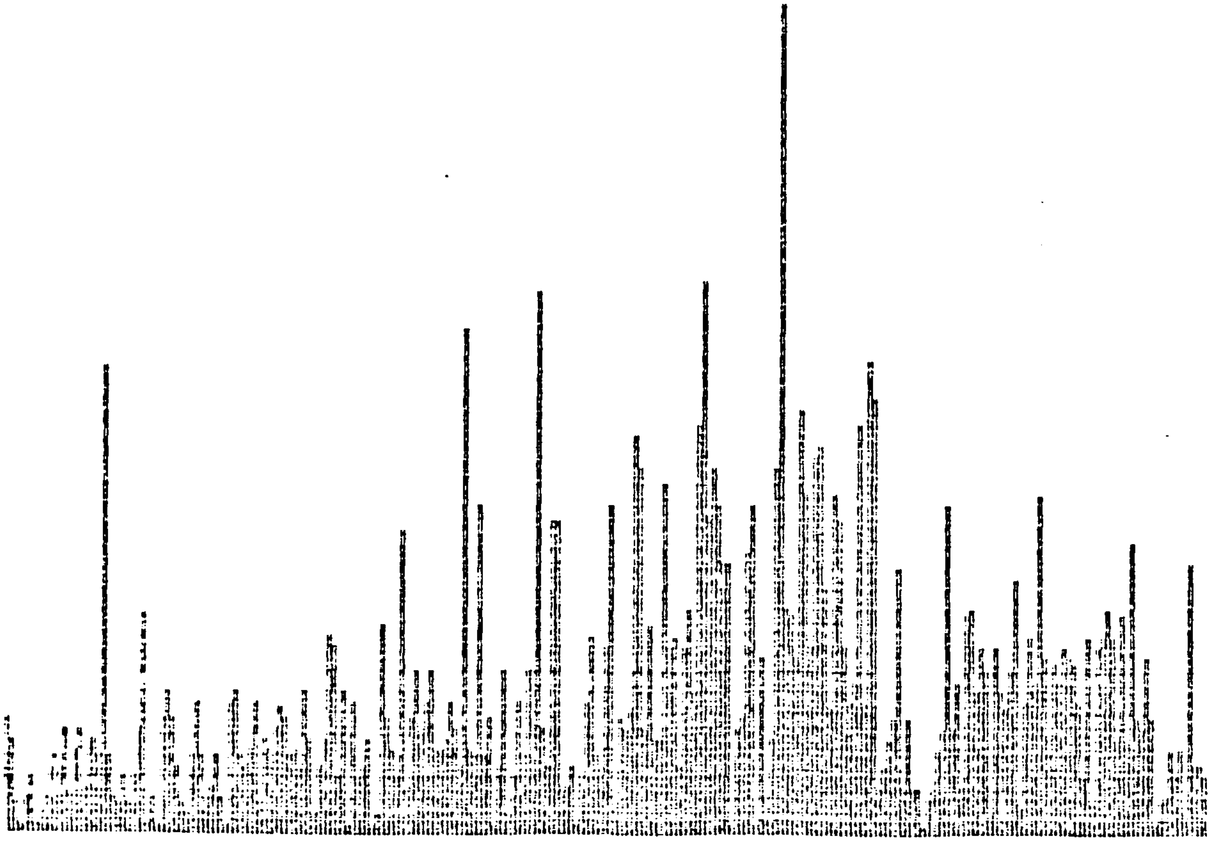

Figure (37b) The Digitized Frequency Spectrum of the Interferometer Signal After Filtering Out the Effect of Window Boundary Layer.

disturbance, and Figure 37b shows the signal after the effects of the window disturbances have been numerically filtered out. The rod heating condition corresponds to a phase difference of 0.01 λ, while the detected signal has a phase difference of 0.001 λ. The thermal boundary layer thickness for both the heating rod and the flat plate were 23 mm and 4 mm, respectively. The figure shows that when the ratio of the window disturbance to the disturbance in the transition region is on the order of 60:1, the noise becomes dominant and simple mathematical filters fail to recover the signal.

6.3 Supersonic Wind Tunnel Results

The dominant frequency of disturbances of transition was calculated based on the assumptions that the flow disturbance is as large as the boundary layer thickness, and travels with the freestream velocity. Therefore, for 1 mm boundary layer thickness and $U_\infty = 600$ m/sec, the dominant frequency was 600 kHz. Figures 38 are the time averaged signals obtained in the course of the natural transition experiment as they appeared on the oscilloscope. The frequency band of the instrument was 300 kHz, beyond which the amplification gain of the electronics drops drastically. No transition signals were observed in the time domain as evident in Figures 37. No distinct peaks were observed in the frequency spectrum obtain by a spectrum analyser. Lack of clear signals due to transition is an artifact of the low signal-to-noise ratio as calculated in Table 5. Figure 39 shows the areas of applicability of the differential interferometer.

The second possibility that led to the low signal to noise ratio is the beams coincidence as they travel through the window boundary layer. Beam coincidence is defined as the ratio of the area where the beams coincide to the beam area. The fully turbulent boundary layer at the optical access window can cause disturbance of the two beams leading to a high level of noise. Azzazy, et al, showed that large disturbances in the window boundary layer can annihilate the interferometer signals. It was established that a cut-off threshold of 60:1 unwanted disturbance to signal ratio, totally destroy the signal. However, O'Hare agreed that the dominant frequency of the fully developed window boundary layer is substantially different than the dominant frequency at transition. The full details of the window boundary layer effects still need more attention. The supersonic wind tunnel data were digitized using the Lecroy fast digitizer system which was set at 2 MHz sample rate. The data was then recorded on 266 kbytes of memory. Numerical Fourier transform techniques were used to obtain the power spectrum of the data. Figure 40, shows a sample power spectrum during the natural transition experiment at 8" from the leading edge at $Re = 2 \times 10^6$. The abscissa is the power spectrum and the ordinate is the frequency scale 0-400kHz.

A numerical filter is used to reduce the effects of background noise and window boundary layer. The filter is taken to be the spectrum at 2" from the leading edge for the natural transition experiment. Figure 41 shows the power spectrum at x = 8" using the filter. A complete set of the power spectrum before and after the filter for both the natural transition and the turbulent wedge experiments are presented in

Appendix A. The ordinate in all the figures represents the frequency with a scale 0-400 kHz and the abcissa is the power spectrum in arbitrary units. More research work will be carried out to assess the capability of the technique to measure pathlength differences on the order of $\lambda/2500$.

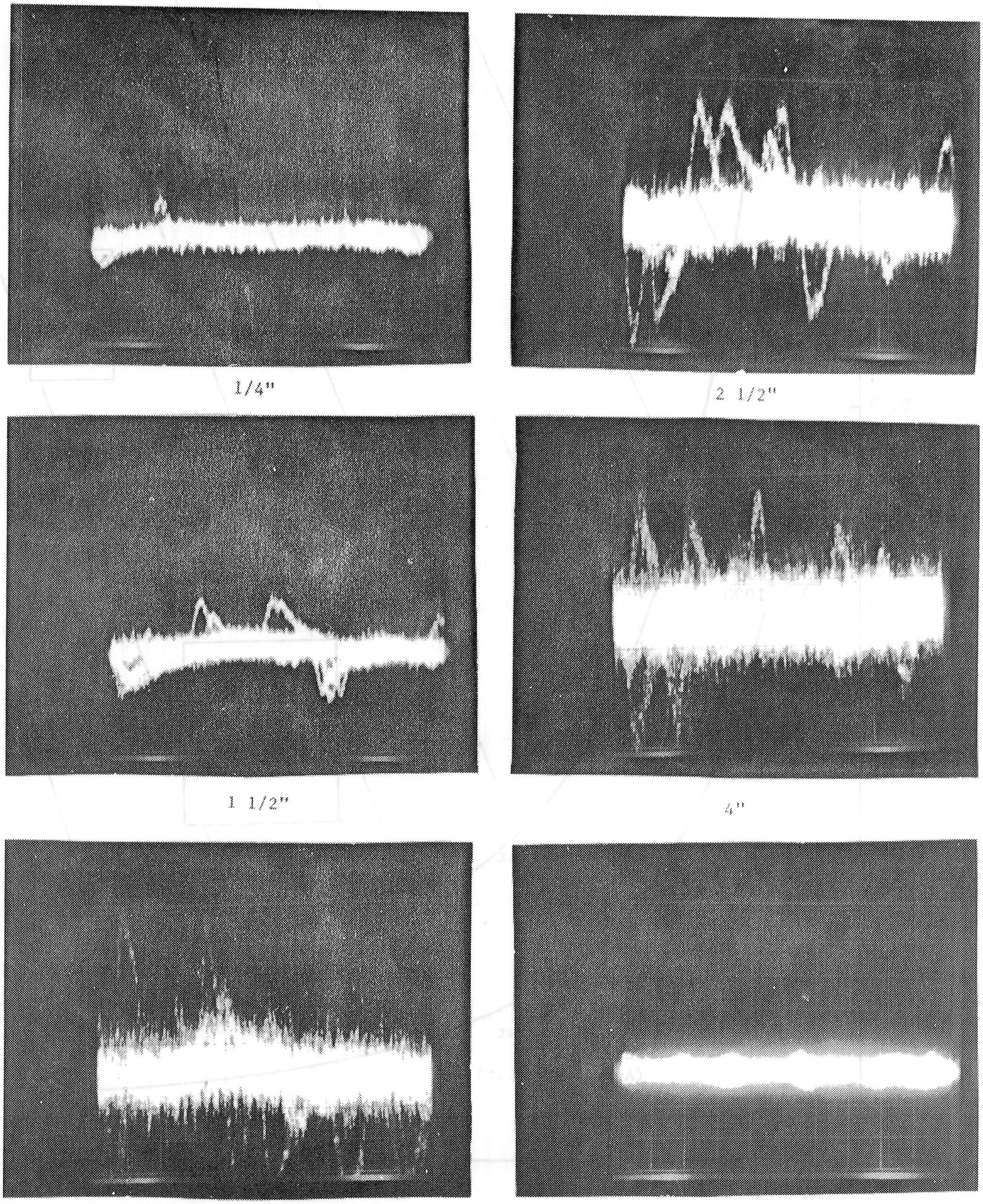

1/4"

2 1/2"

1 1/2"

4"

2"

12"

Figure (38) Time Averaged Signals of Natural Transition

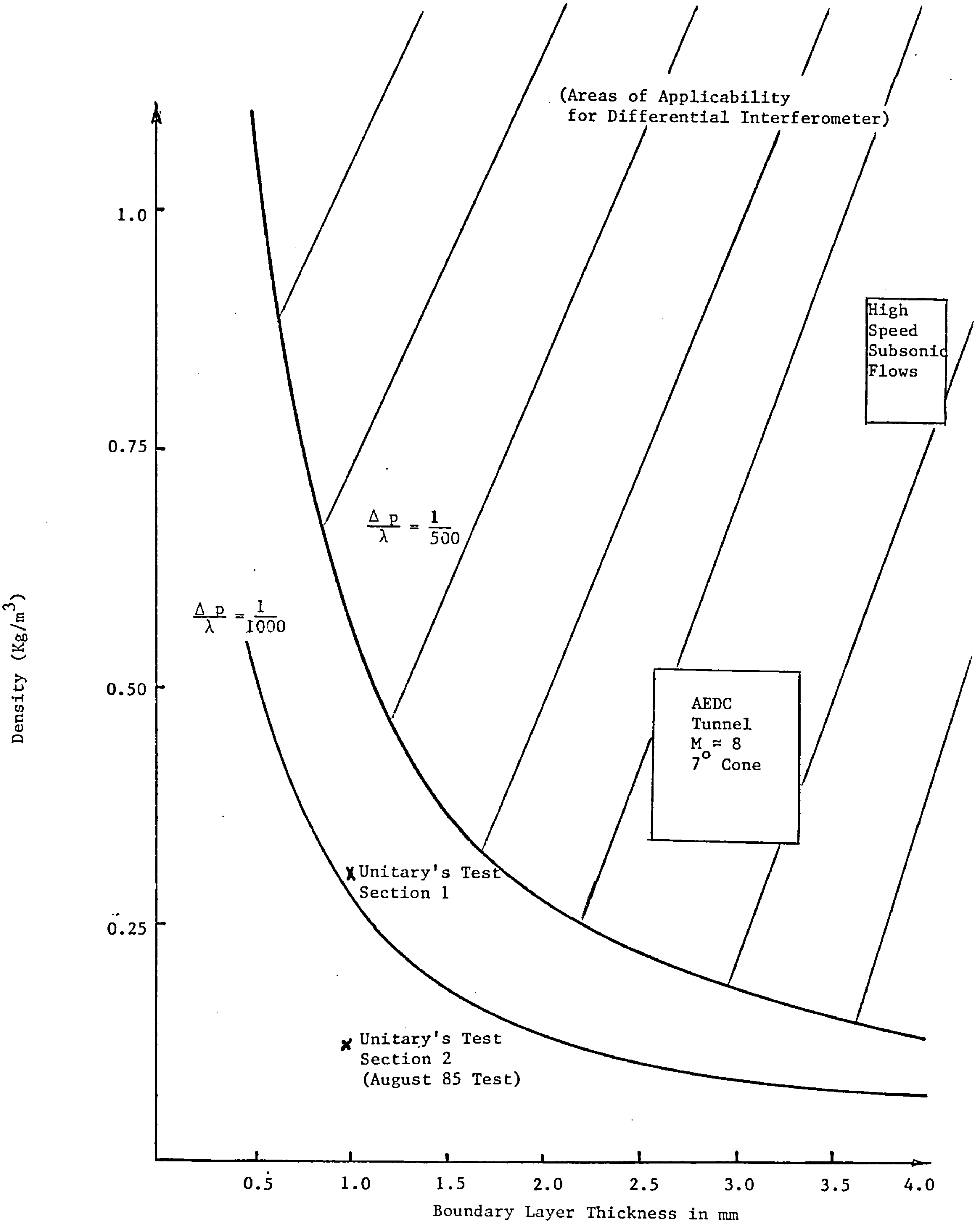

Figure(39) Areas of Applicability for Differential Interferometer.

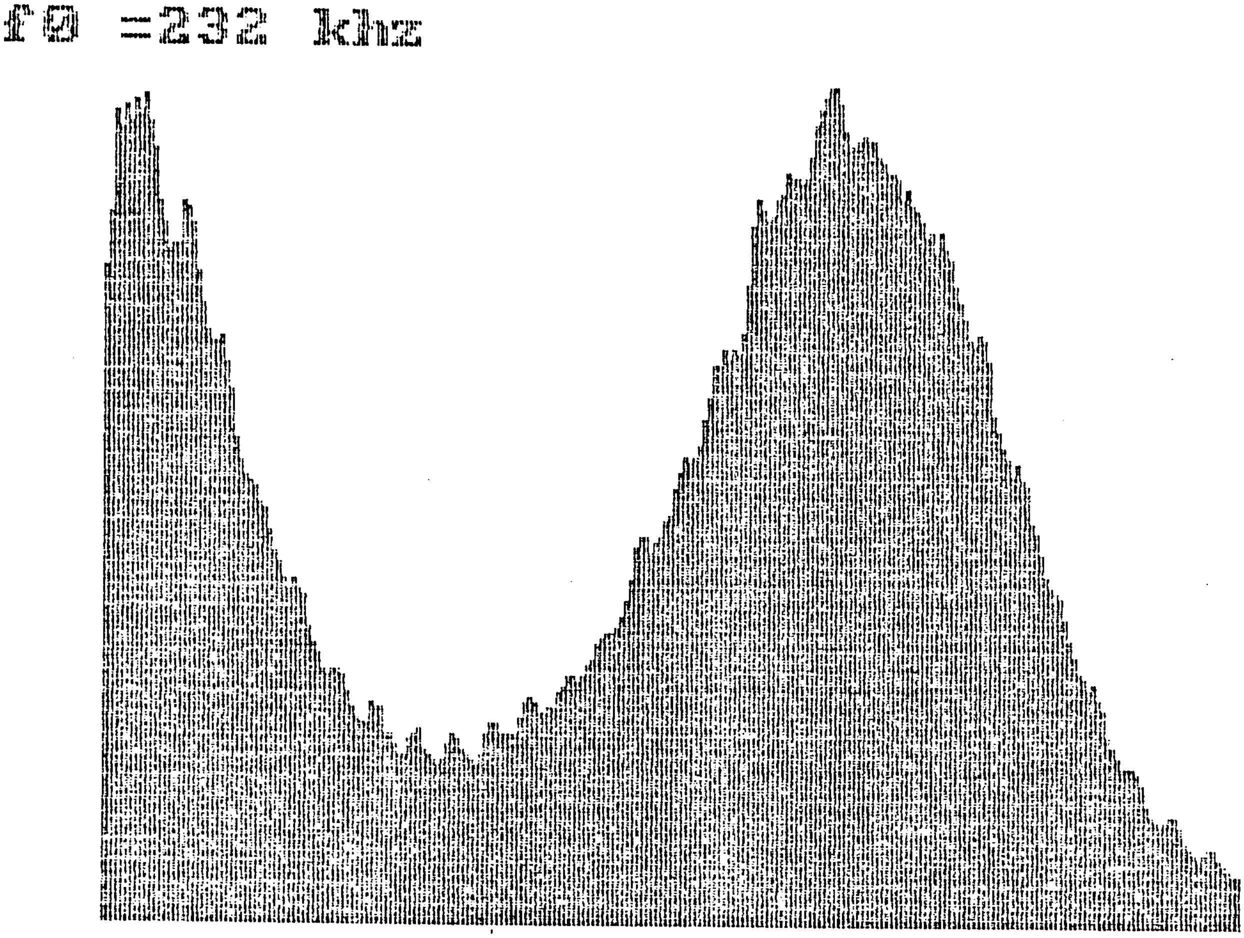

Figure (40) Digital Signal Spectrum at x = 8", and Re = 2×10^6.

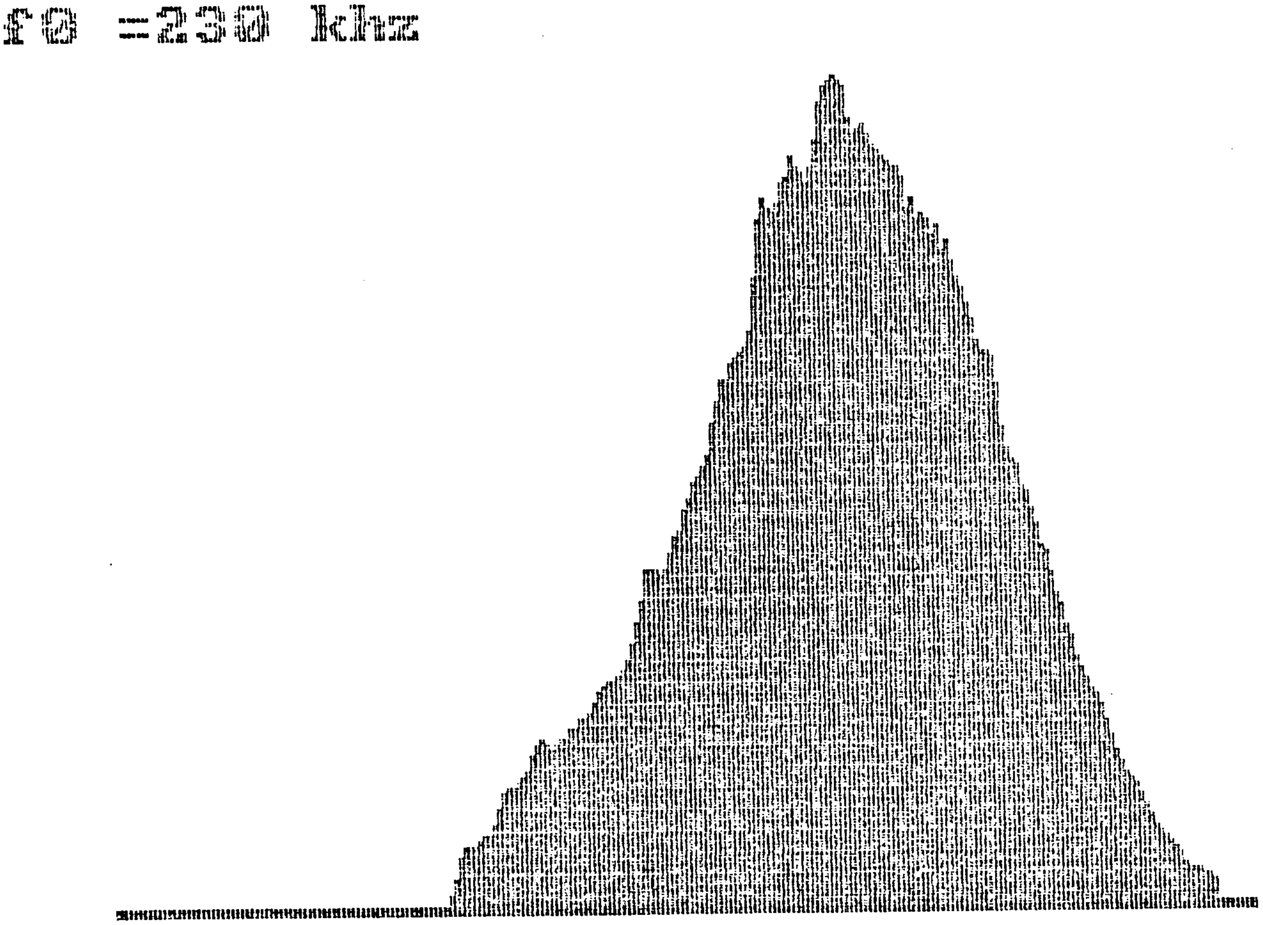

Figure (41) Signal Spectrum at x = 8", and Re = 2 x 10^6, After Using the Filter.

7.0 RECOMMENDATIONS

The following features are recommended to achieve a successful test of the differential interferometer in supersonic wind tunnels:

1. Increase the signal-to-noise ratio by increasing either or both the freestream density and the boundary layer thickness. Using Test Section I at the Unitary Plan will result in a factor of .56 increase in freestream density. Use another wind tunnel to provide larger values for the density.
2. Increasing the boundary layer thickness has the advantage of increasing the signal-to-noise ratio as well as decreasing the dominant frequency of transition.
3. Adapt better coincidence of the beams as they propagate through the window boundary layer.
4. Polish the model to achieve better flatness and reduce the noise due to surface roughness.
5. Use flow visualization techniques to have better understanding of the flow field, prior to the interferometry measurements.

8.0 REFERENCES

Azzazy, M., Modarress, D. and Hoeft, T., "High Sensitivity Boundary Layer Transition Detector," SPIE 29th International Symposium, SPIE 569-08 (1985). Also submitted to the Journal of Physics E, Scientific Instruments (1985).

Azzazy, M., "Suface Topography Using Diffuse Point Differential Interferometry", to be submitted to Applied Optics (1986), also Azzazy, M., "Diffuse Point Differential Interferometry for Contouring the Surface Profile of Camshafts", Final Report SDL No. 85-2431-02F (1985), Submitted to Cummins Diesel Engine, Co.

Batill, S. M. and Mueller, T. J., "Visualization of Transition in the Flow Over an Airfoil Using the Smoke-Wire Technique," AIAA Journal, Vol. 19, No. 3, pp. 340-345, March 1981.

Cantwell, B., Coles, D., and Dimotakis, P., "Structure and Entrainment in the Plane of Symmetry of a Turbulent Spot," J.F.M., Vol. 87, Part 4, pp. 641 (1978).

Cassels, W. A. and Campbell, J. F., "Boundary Layer Transition Study of Several Pointed Bodies of Revolution at Supersonic Speeds," NASA TN D-6063 (1970).

Coles, D. and Barker, S. J., "Some Remarks on a Synthetic Turbulent Boundary Layer," in Turbulent Mixing in Nonreactive and Reactive Flows, ed. S. N. B. Murthy, Plenum (1975).

Fancher, M. F., "A Hot-Film System for Boundary Layer Transition Detection in Cryogenic Wind Tunnels," presented to Euromech Colloquium 132 on Hot-Wire, Hot-Film Anemometry and Conditional Measurement, Lyon, France, July 1980.

Fancher, M. F., "Aspects of Cryogenics Wind Tunnel Testing Technology at Douglas," AIAA Paper No. 82-0606, 1982.

Giallorenzi, T. G., Bucaro, J. A., Dandridge, A., Sigel, Jr., G. H., Cole, J. H., Rashleigh, S. C., and Priest, R. G., "Optical Fiber Sensor Technology", IEEE Journal of Quantum Electronics, Vol. QE-18, No. 4, pp. 626 (1982)

Goodman, J. W., "Statistical Properties of Laser Speckle Patterns," in "Laser Speckle and Related Phenomena," J. D. Dainty, ed., Springer-Verlag (1976).

Havener, A. G., "Detection of Boundary-Layer Transition Using Holography," AIAA Journal, Vol. 15, No. 4, pp. 592-293, April 1977.

Havener, A. G., "Holographic Measurement of Transition and Turbulent Bursting in Supersonic Axisymmetric Boundary Layers," AIAA Paper No. 83-1724, 1983.

Hefner, J. N. and Bushnell, D. M., "An Overview of Concepts for Aircraft Drag Reduction," Von Karman Institute, AGARD-R-654 (1977).

Hough, G., ed., "Viscous Flow Drag Reduction," AIAA progress in Astronautics and Aeronautics, Vol. 72 (1980).

Laderman, A. J. and Demetriades, A., "Detection of Boundary-Layer Transition with a Laser Beam," AIAA Journal, Vol. 14, No. 1, pp. 102-104, January 1976.

Modarress, D., Doty, J. L., Trolinger, J. D., and Hoeft, T., "High Sensitivity Laser Interferometry for Detection of Boundary Layer Transition," AIAA 17th Fluid Dynamics and Laser Conference, AIAA-84-1640 (1984).

O'Hare, J., "A Nonperturbing Boundary Layer Transition Detector," SPIE 29th International Symposium, SPIE 569-07 (1985).

Perry, A. E., Lim, T. T., and Teh, E. W., "A Visual Study of Turbulent Spots," J. Fluid Mech., Vol. 104, pp. 387-405, 1981.

Saric, W. C. and Reed, H. L., "Effect of Suction and Blowing on Boundary-Layer Transition," AIAA Paper No. 83-0043, 1983.

Schubauer, G. B., and Klebanoff, P. S., "Contributions on the Mechanics of Boundary Layer Transition", NACA TN3489 (1955).

Smeets, G., "A High Sensitivity Laser Interferometer for Transient Phase Objects," Proceedings of the 8th International Shock Tube Symposium, London 1977.

Smeets, G. and George, A., "Investigation of Shock Boundary Layers with a Laser Interferometer," Proceedings of the 9th International Shock Tube Symposium, Stanford, July 1983.

Stallings, Jr., R. L., and Lamb, M., "Effects of Roughness Size on the Position of Boundary Layer Transition and on the Aerodynamic Characteristics of a 55° Swept Delta Wing at Supersonic Speeds," NASA Technical Paper 1027 (1977).

Swindel, W., Polarized Light, Benchmark Papers in Optics, Vol. 1, Dowden Huchinsen and Ross (1978).

Wygnanski, I., Sokolov, M., and Friedman, D., "On a Turbulent Spot in a Laminar Boundary Layer," J.F.M., Vol. 78, Part 4, pp. 785 (1976).

APPENDIX A

I. NATURAL TRANSITION DATA

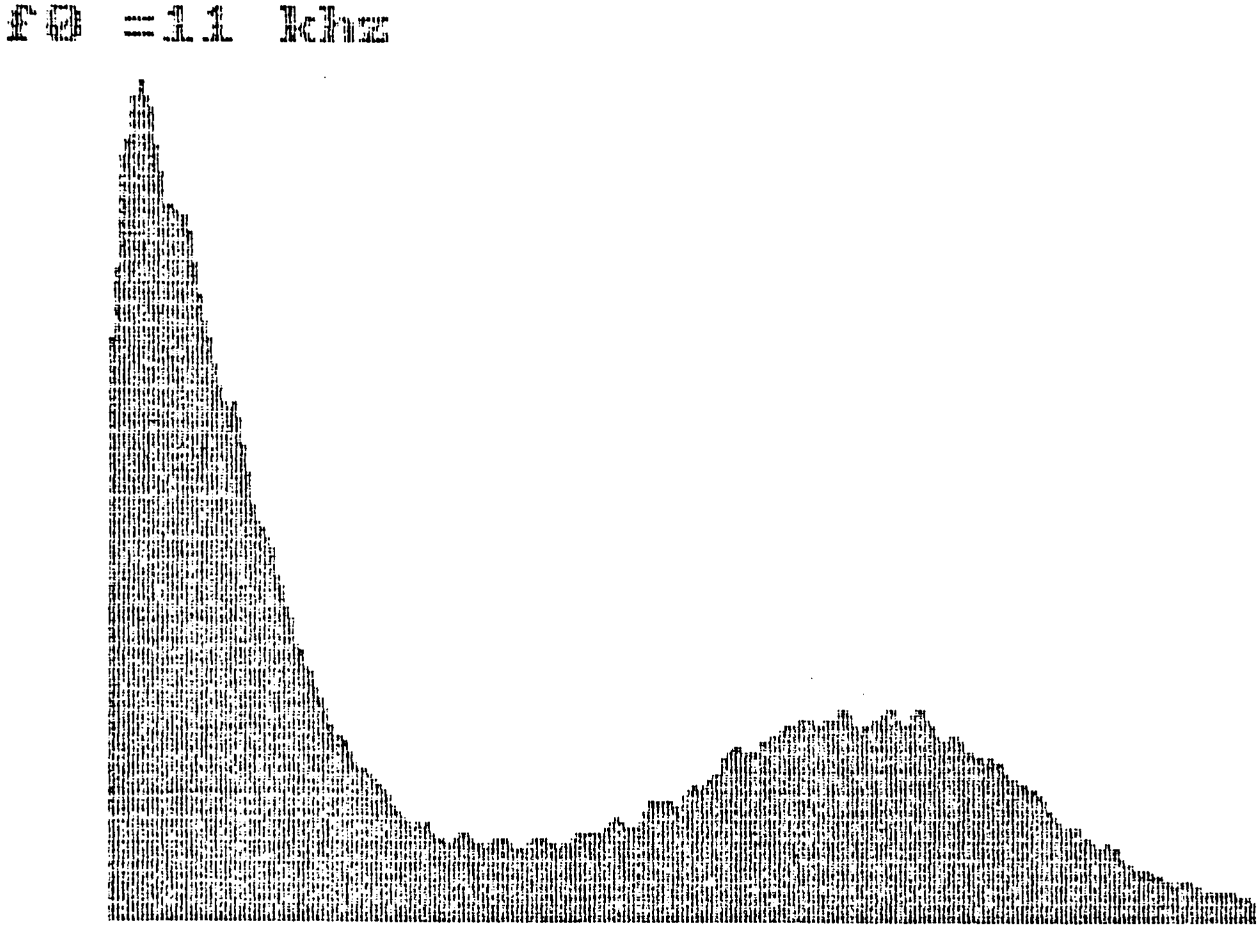

Figure A(1) x = 2" Re = 2×10^6 Filter

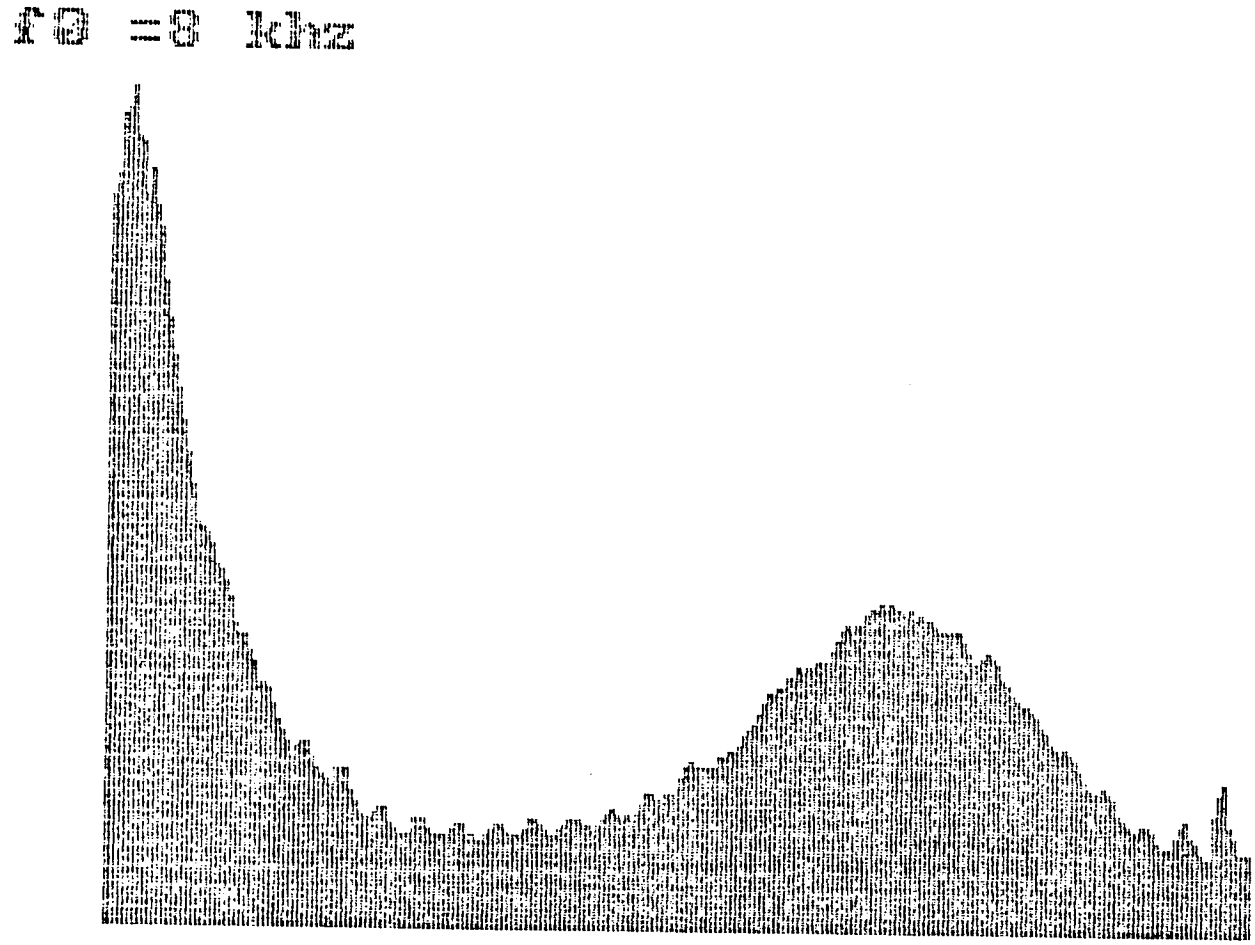

Figure A(2) x = 4" Re = 2×10^6 Before Filter

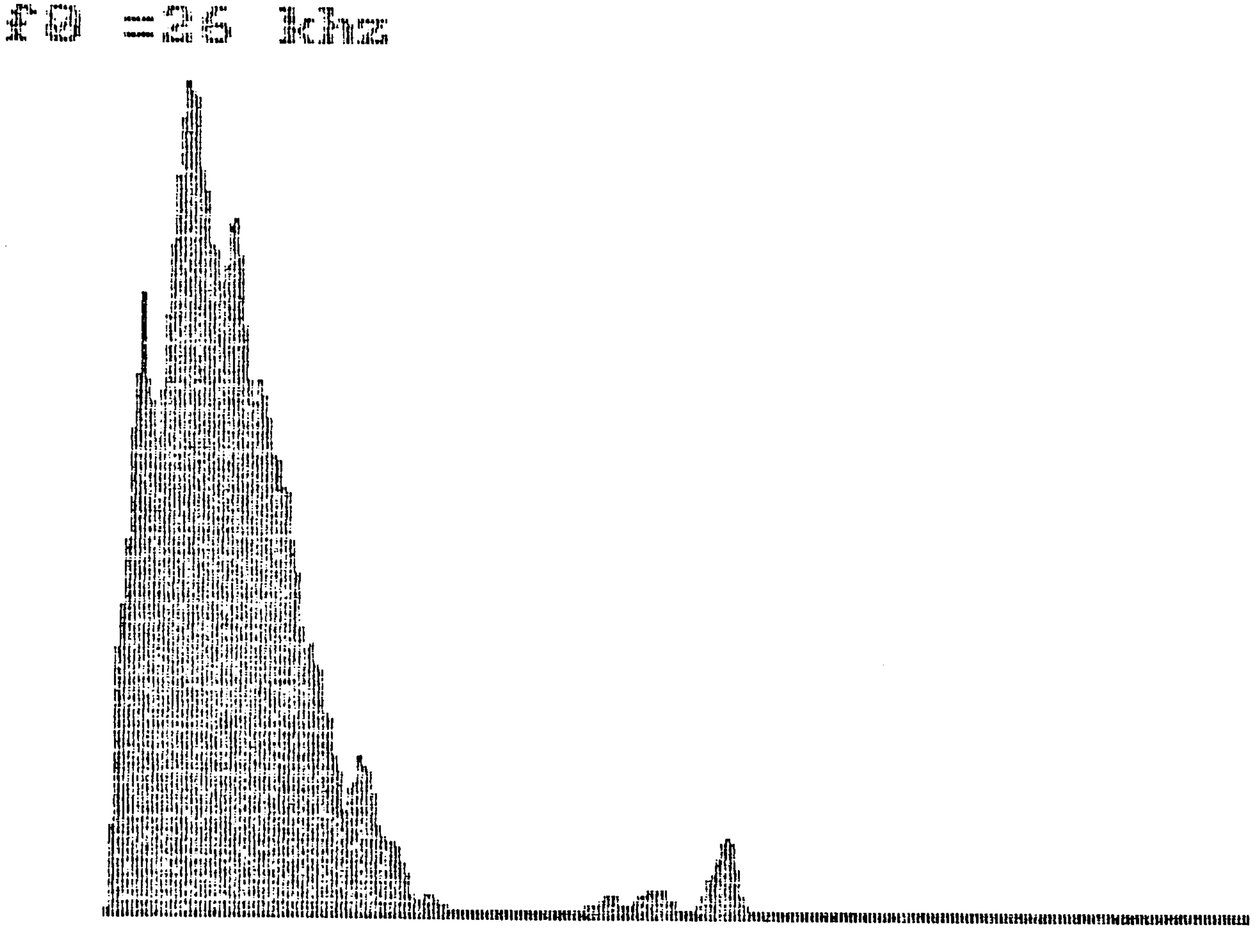

Figure A(3) x = 4" Re = 2×10^6 After Filter

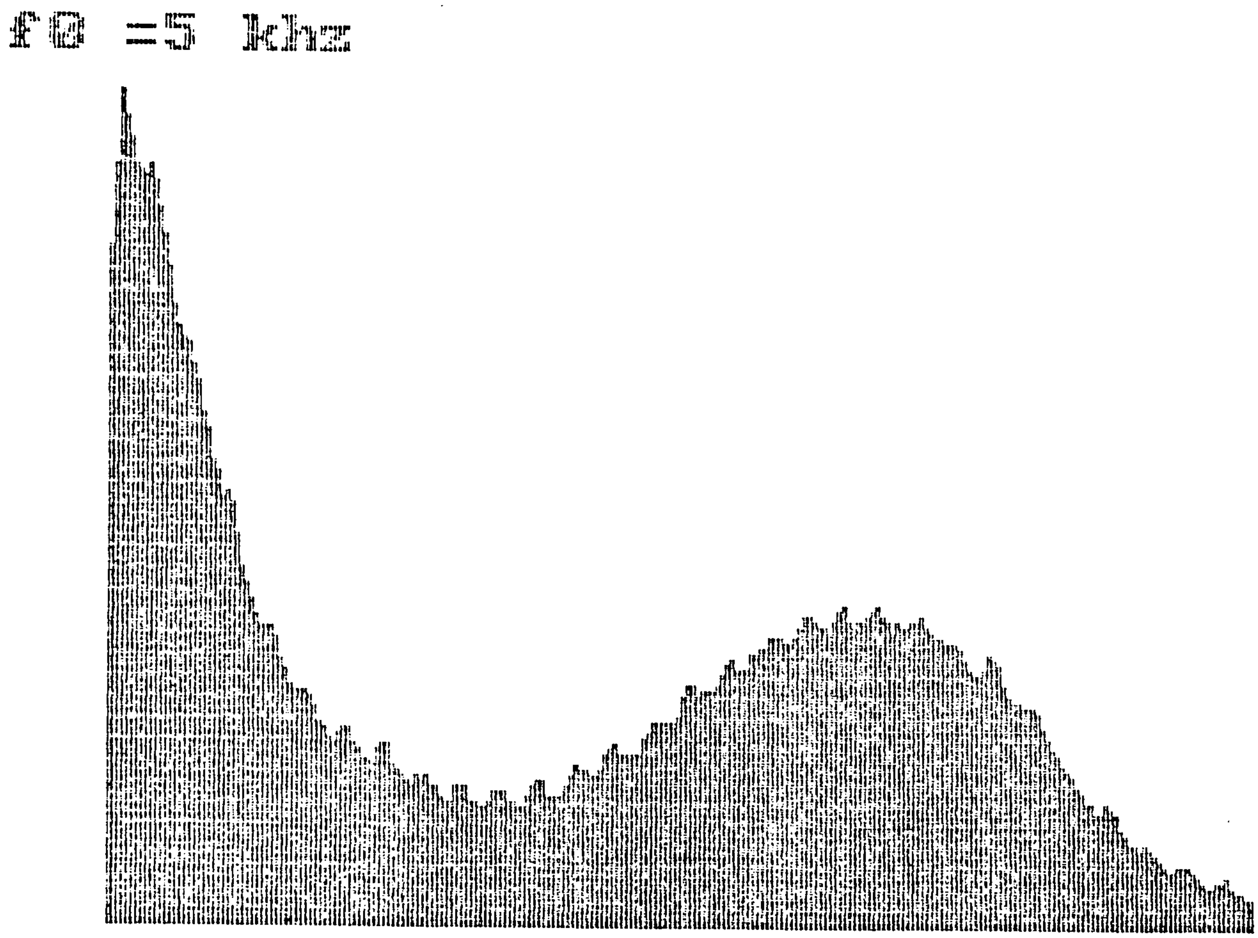

Figure A(4) x = 5" Re = 2×10^6 Before Filter

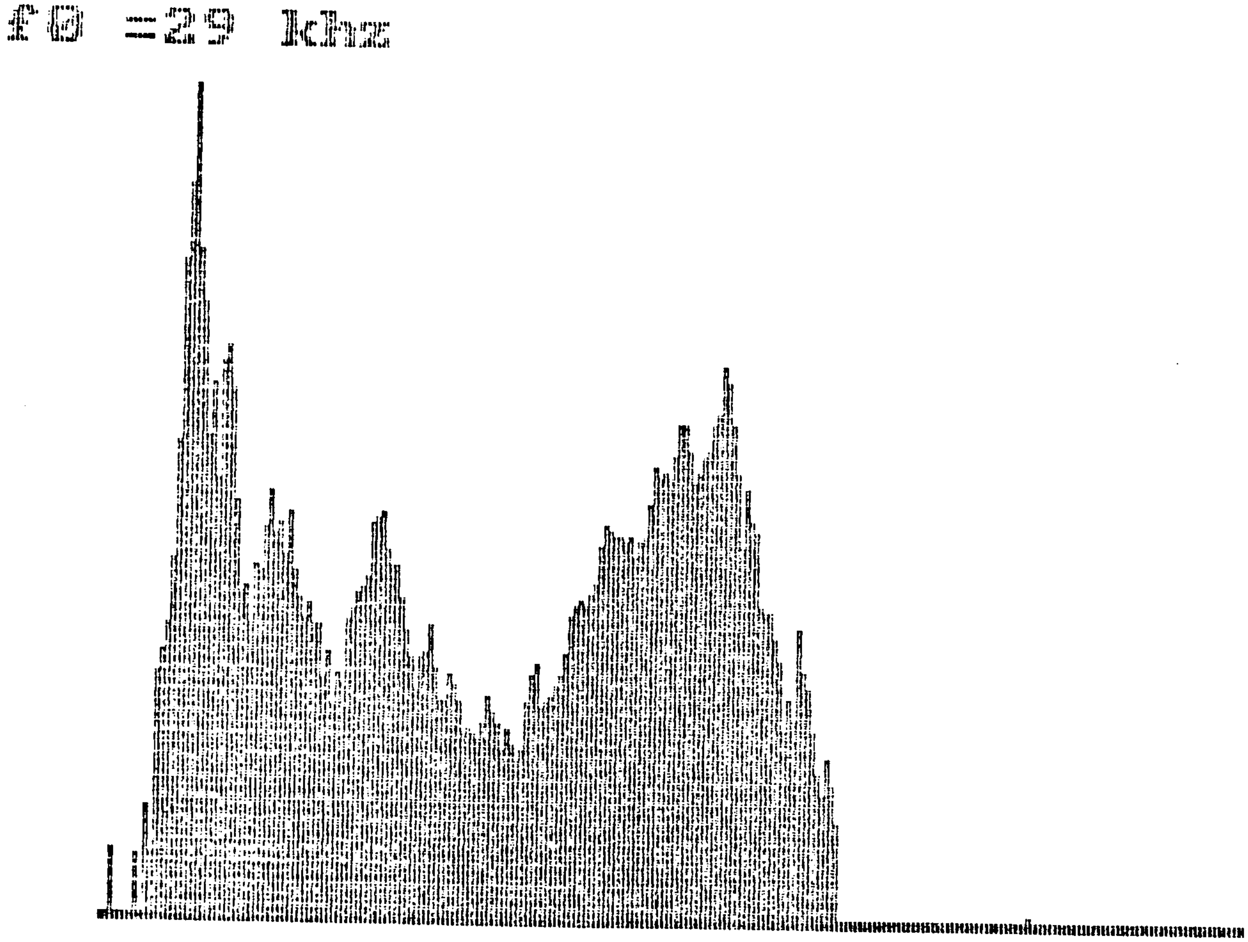

Figure A(5) x = 5" Re = 2 x 10^6 After Filter

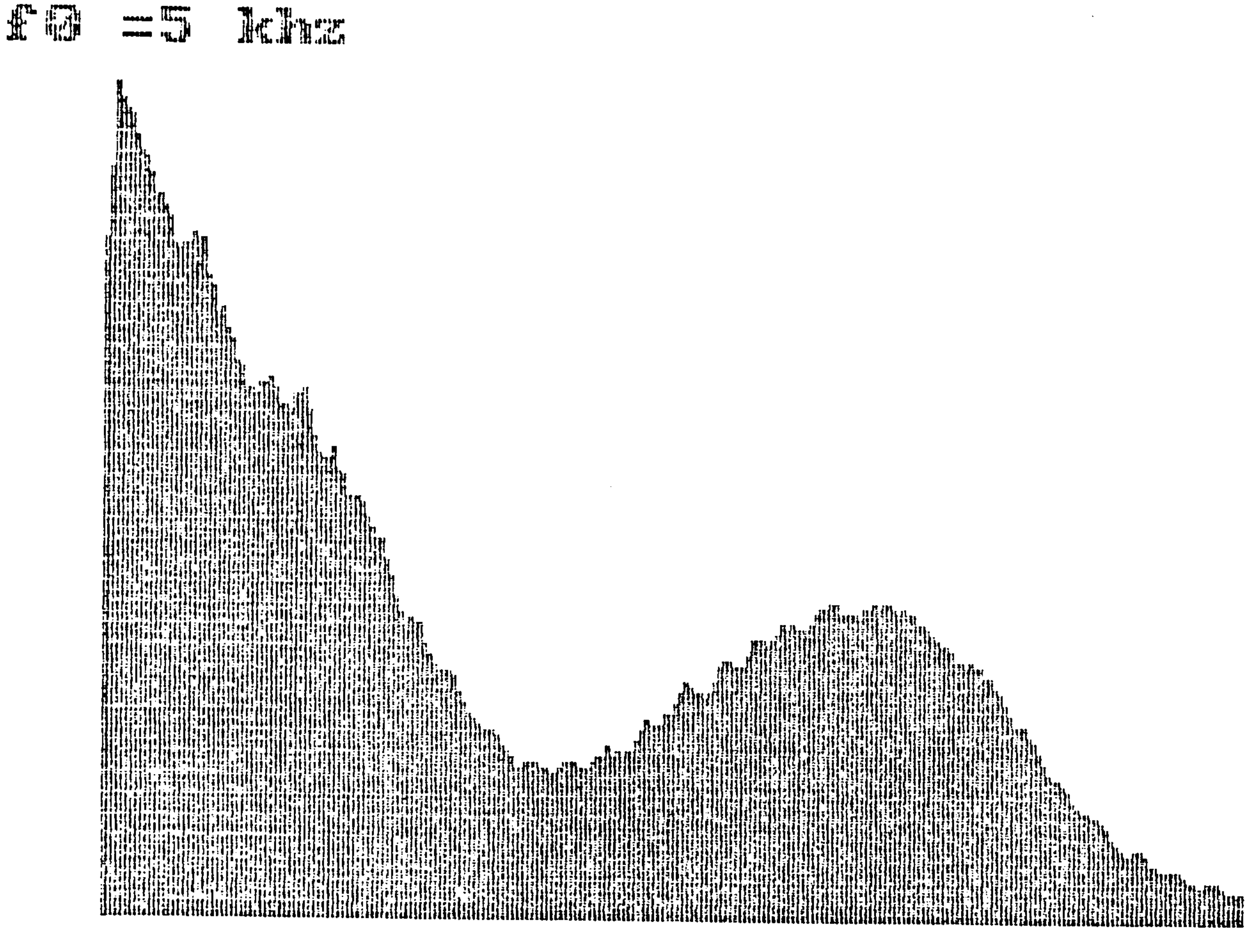

Figure A(6) x = 6" Re = 2×10^6 Before Filter

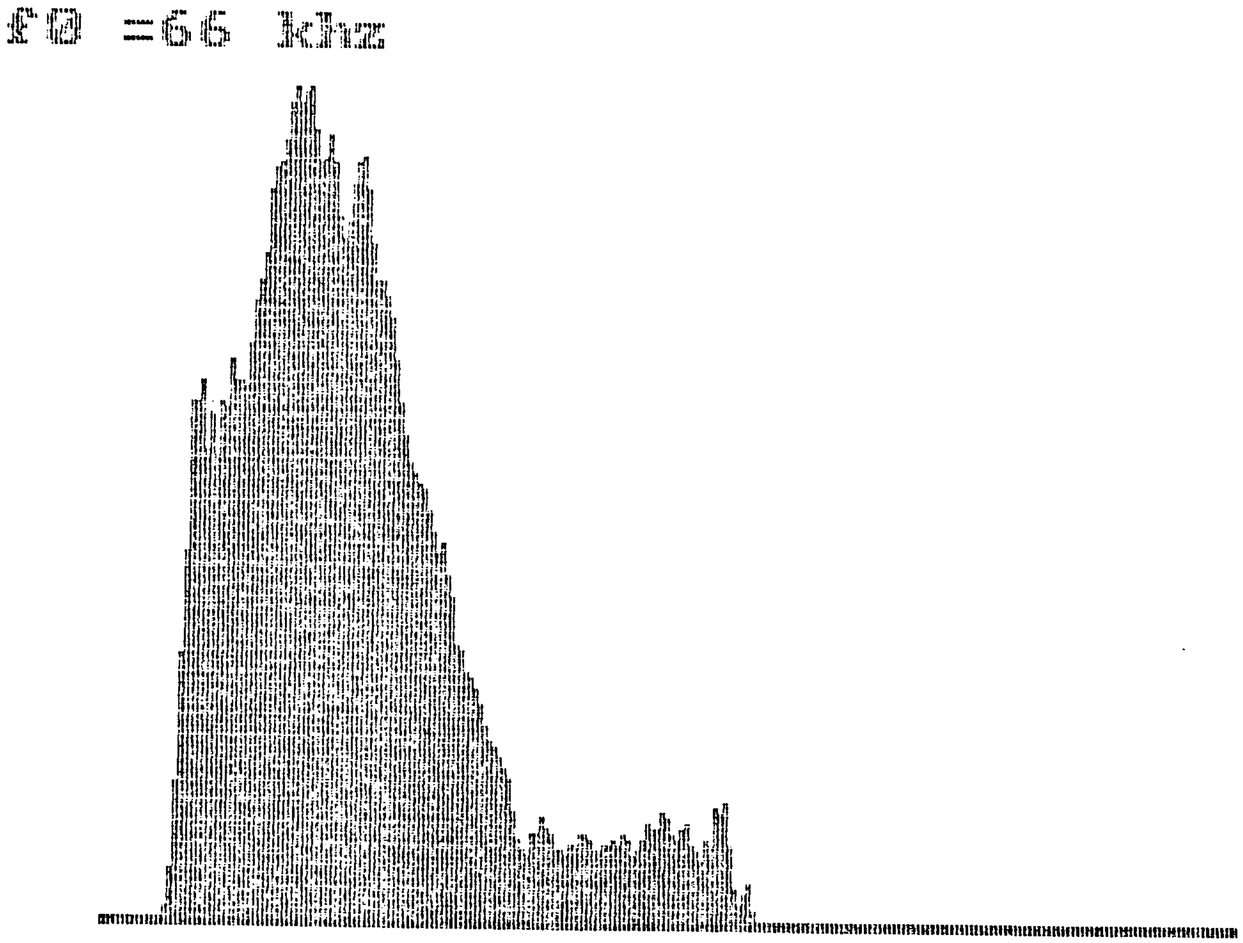

Figure A(7) x = 6" Re = 2×10^6 After Filter

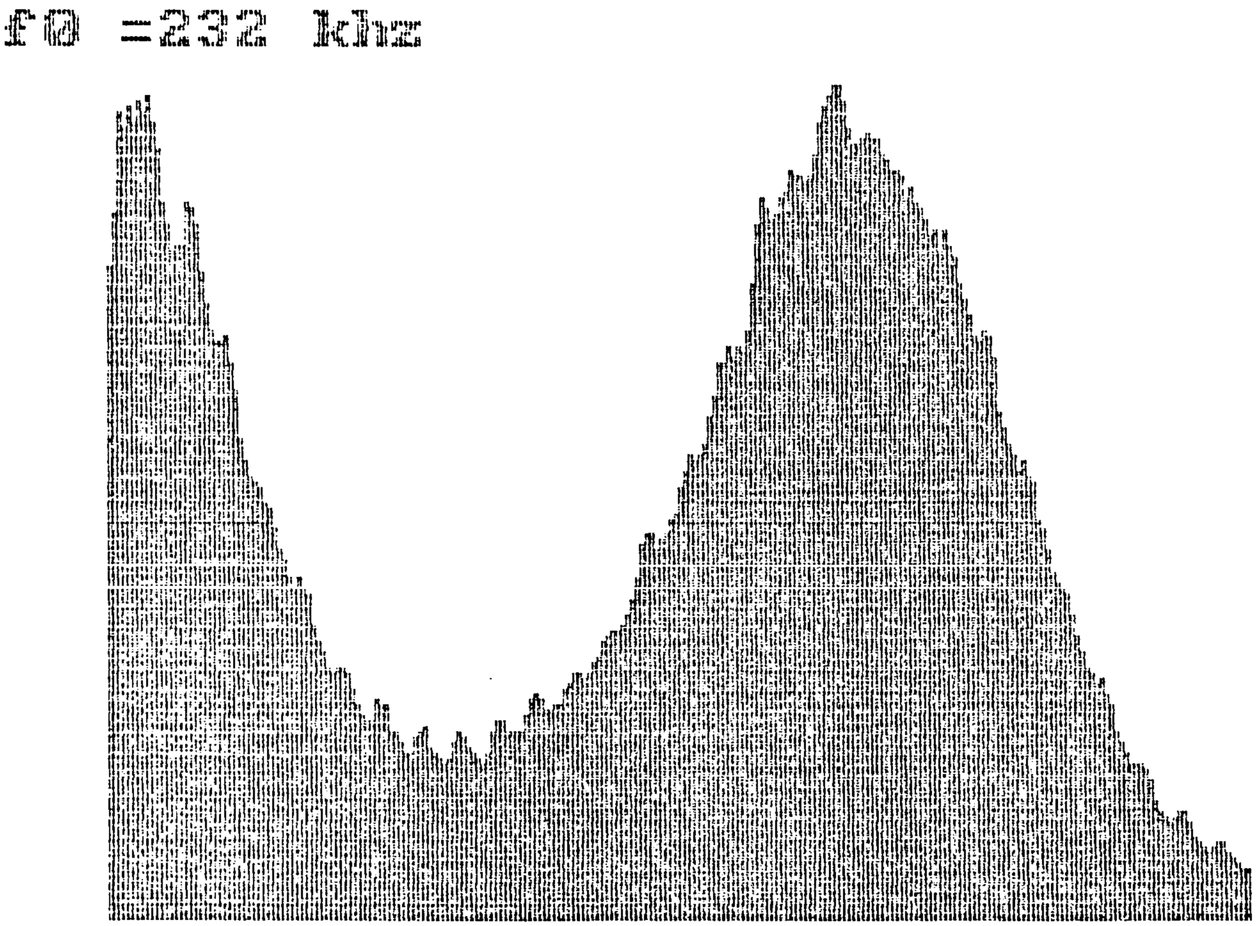

Figure A(8) x = 8" Re = 2×10^6 Before Filter

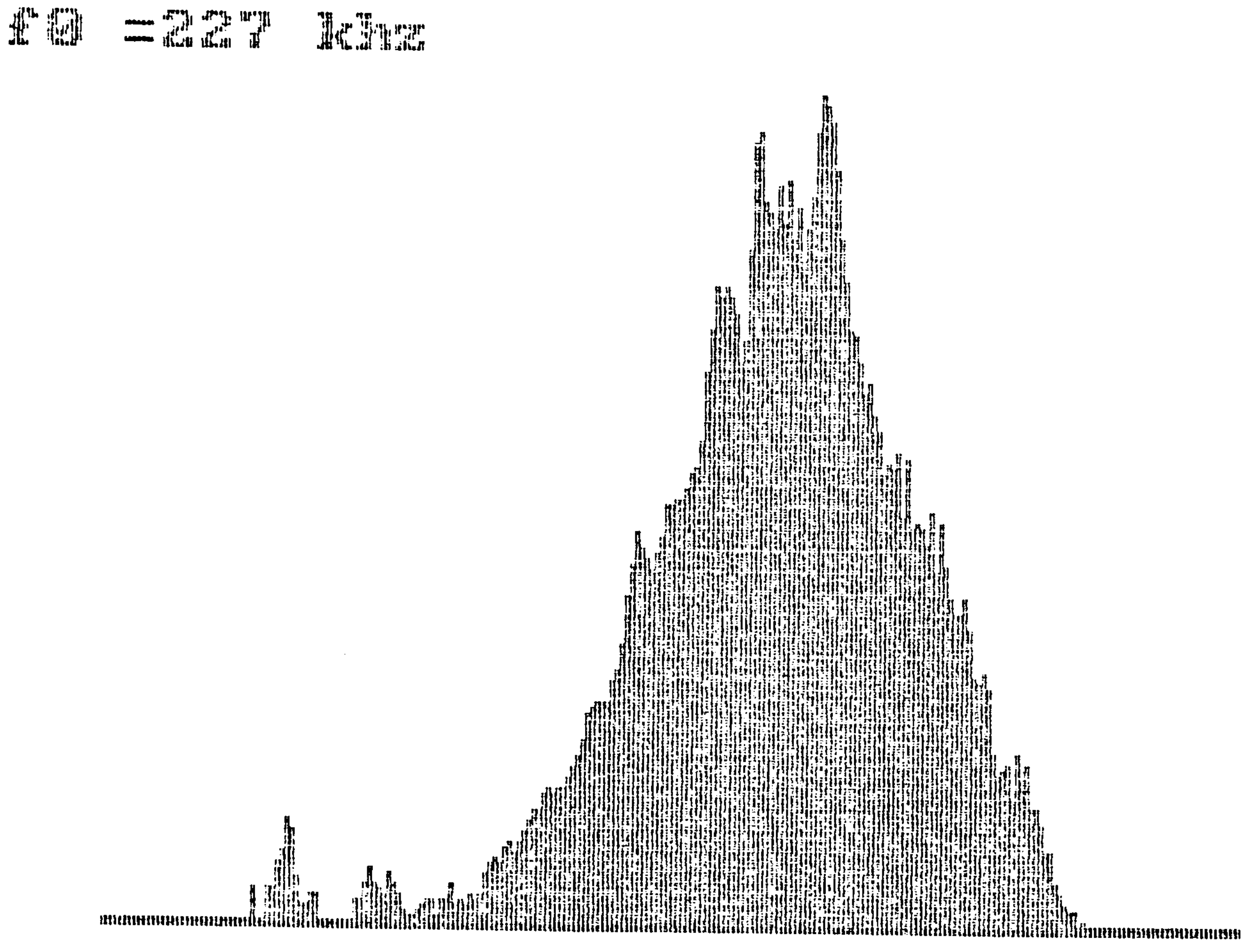

Figure A(9) x = 8" Re = 2 x 10^6 After Filter

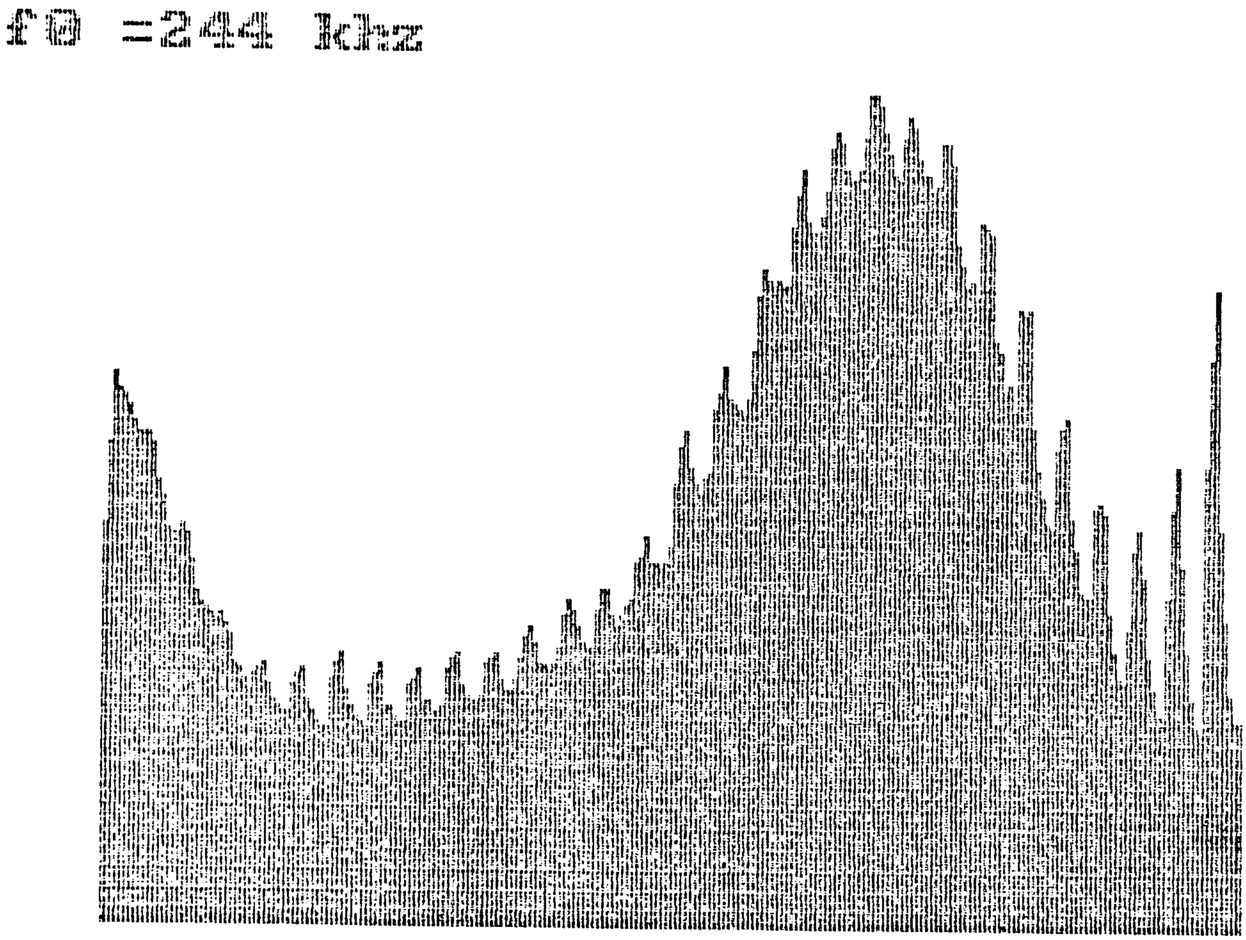

Figure A(10) x = 9" Re = 2×10^6 Before Filter

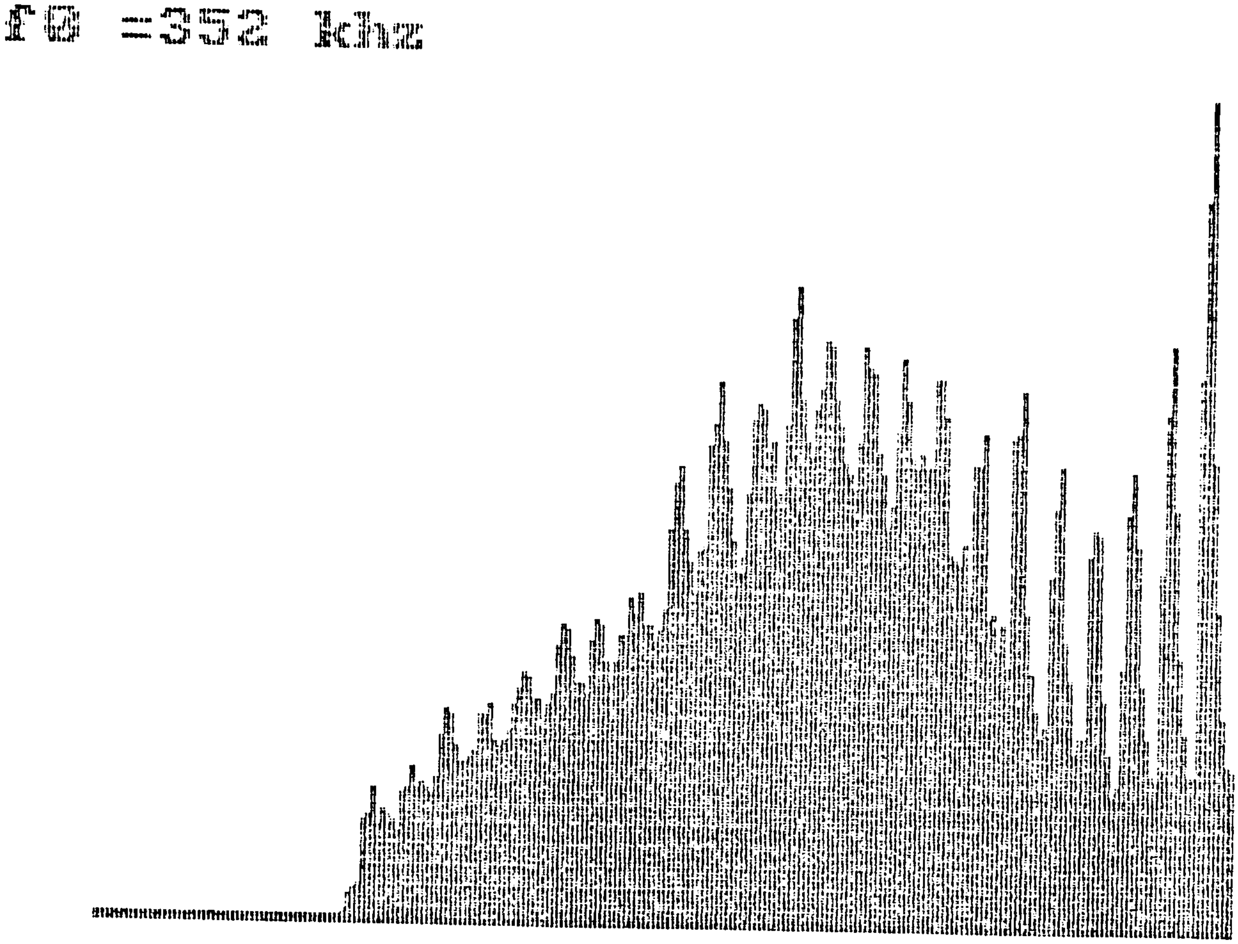

Figure A(11) x = 9" Re = 2×10^6 After Filter

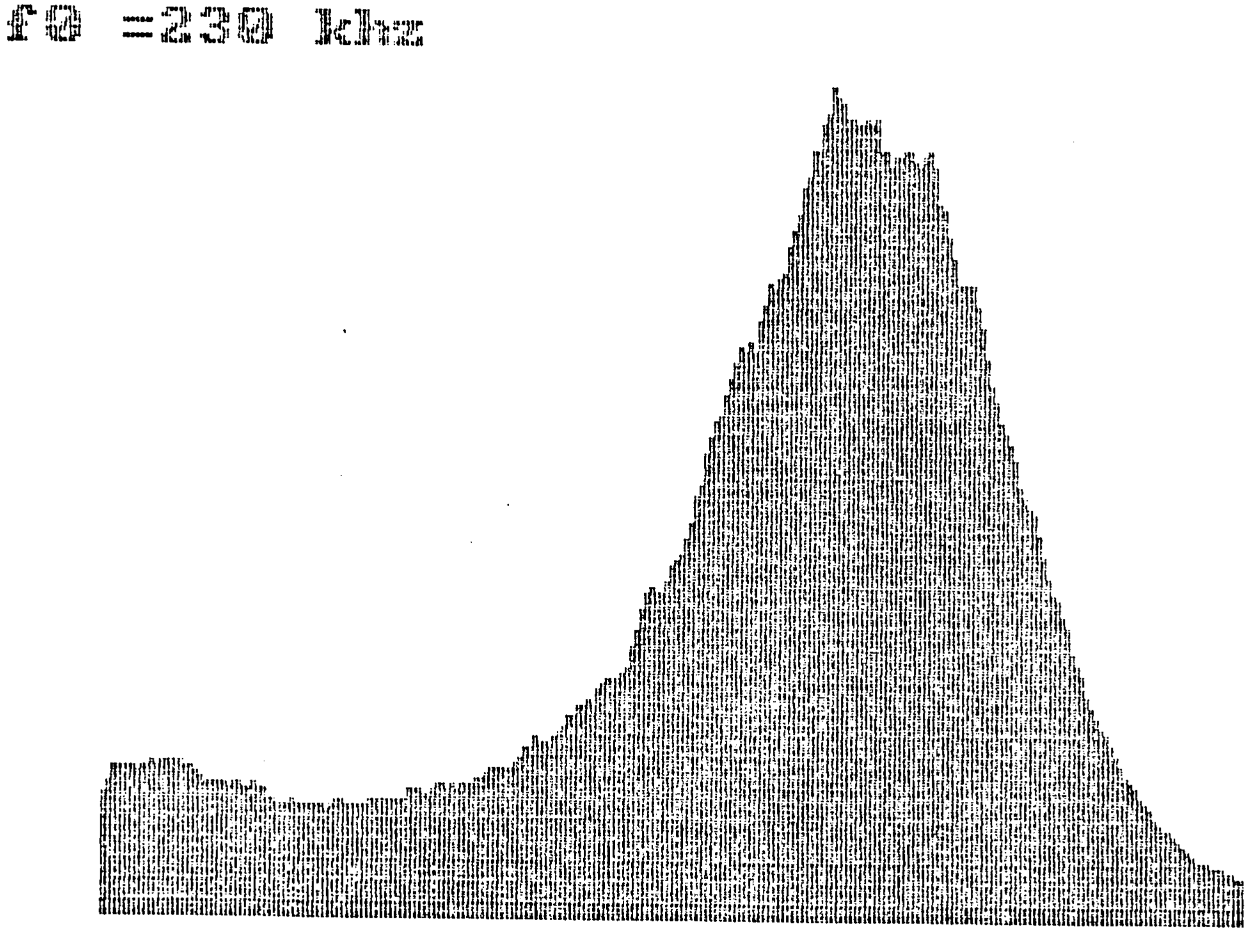

Figure A(12) x = 12" Re = 2 x 10^6 Before Filter

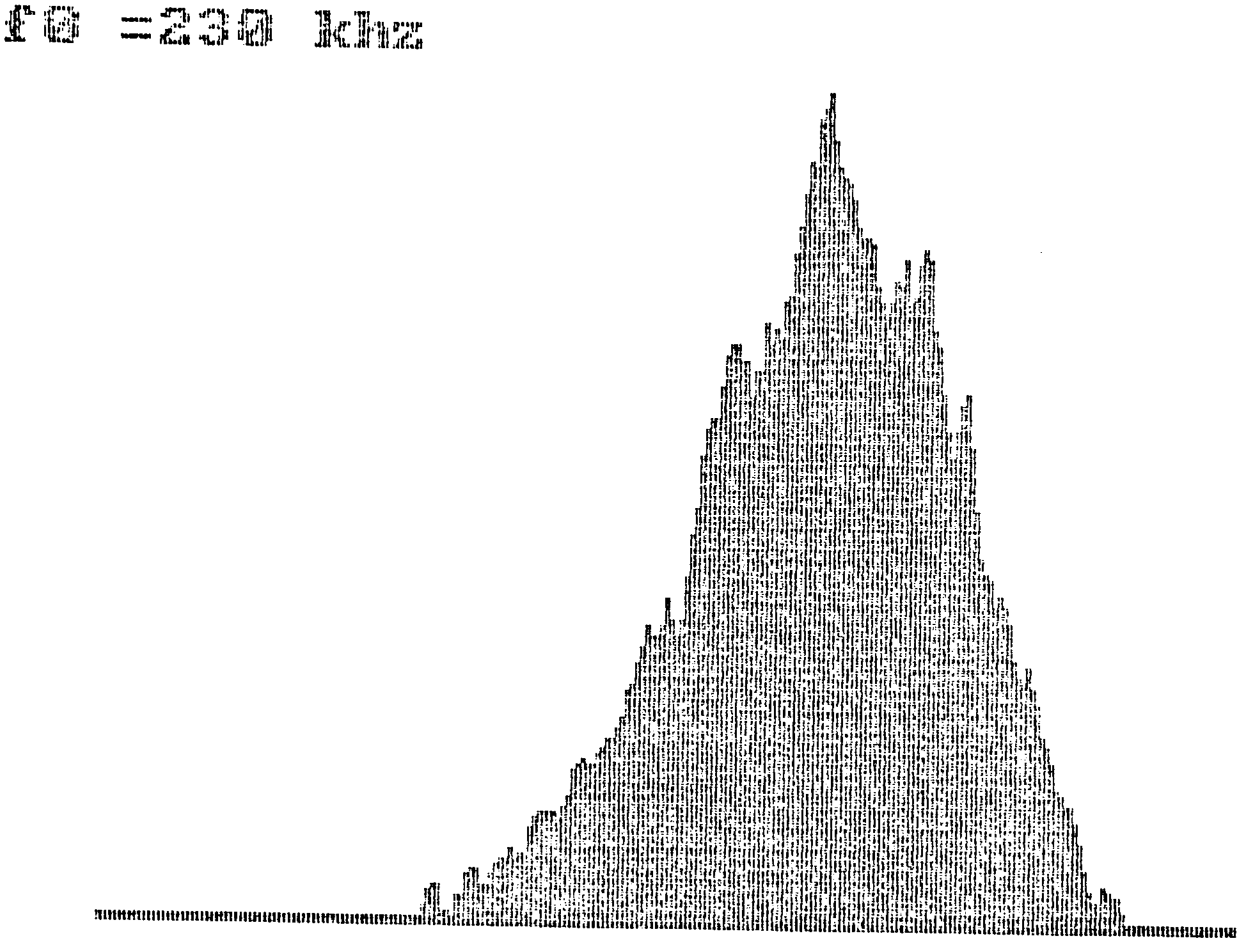

Figure A(13) x = 12" Re = 2 x 10^6 After Filter

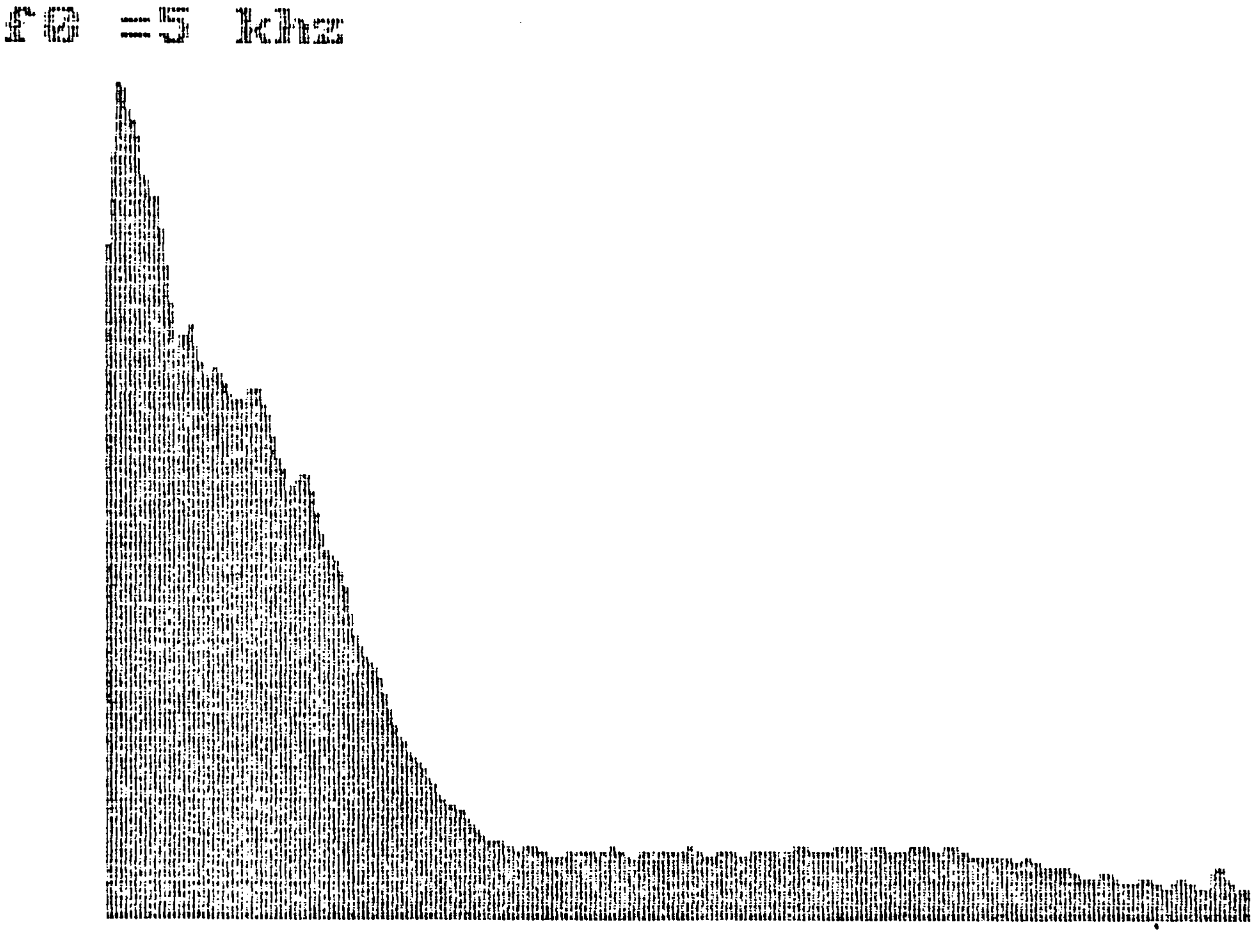

Figure A(14) x = 2" Re = 3 x 10^6 Filter

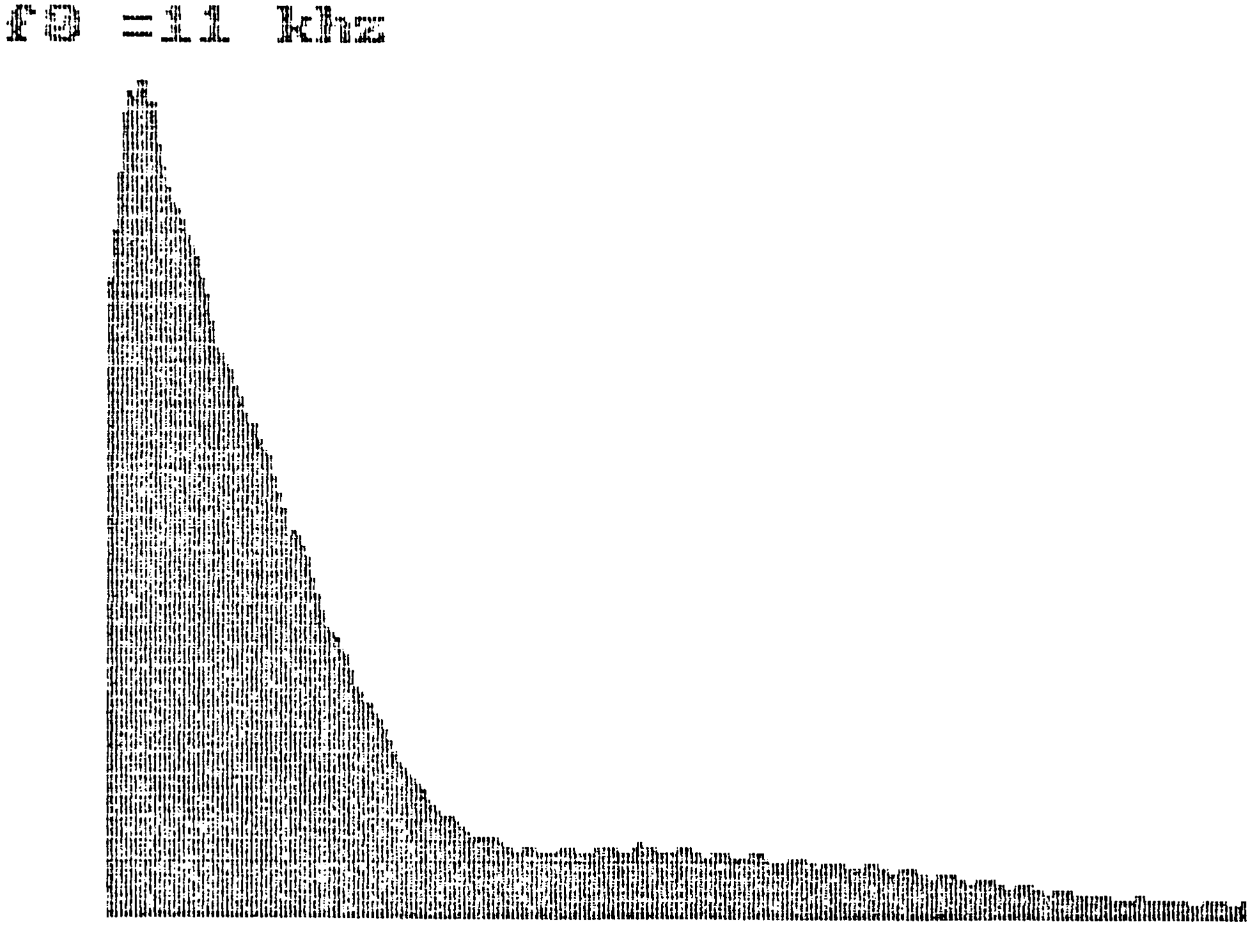

Figure A(15) x = 4" Re = 3×10^6 Before Filter

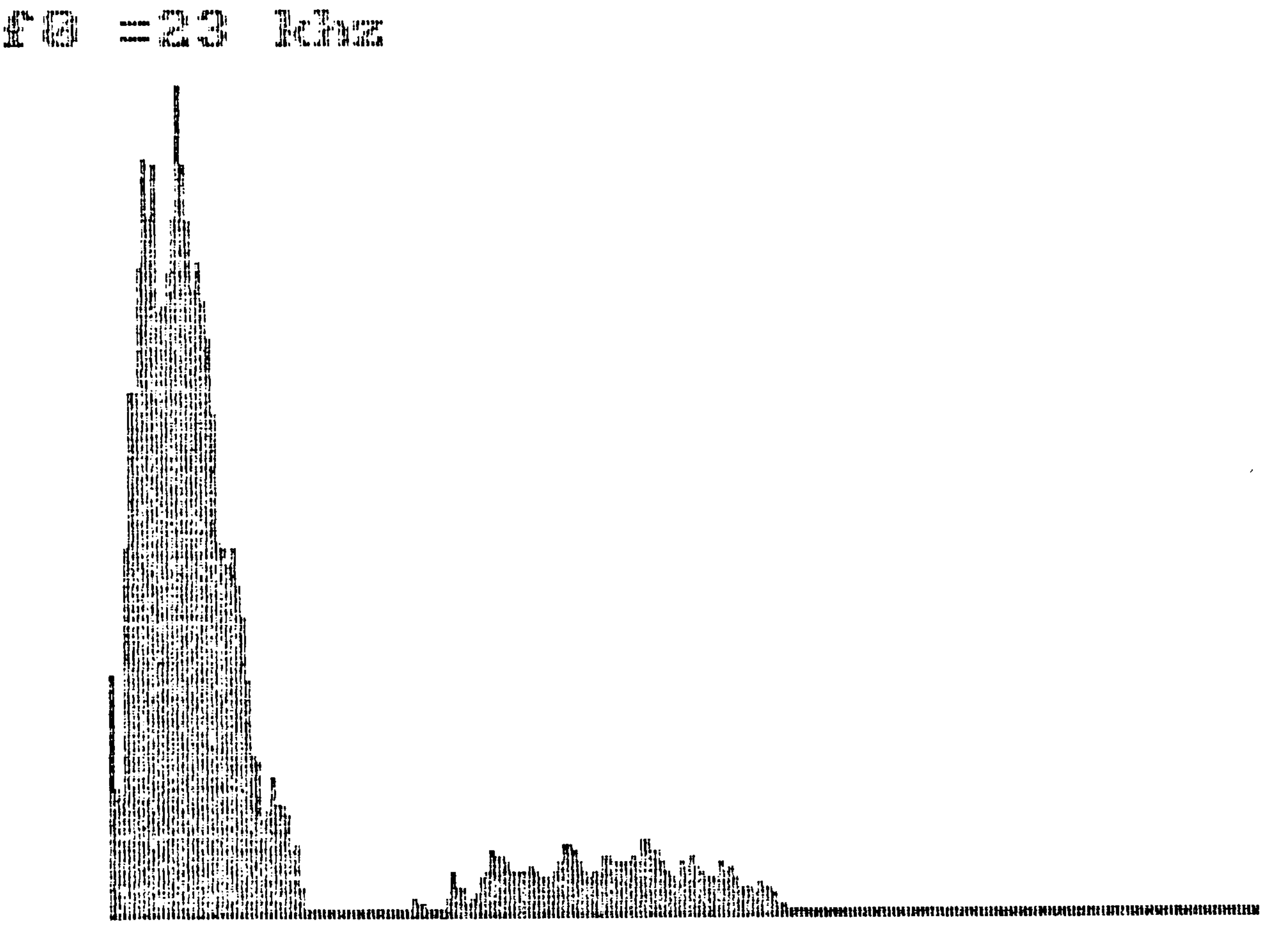

Figure A(16) x = 4" Re = 3×10^6 After Filter

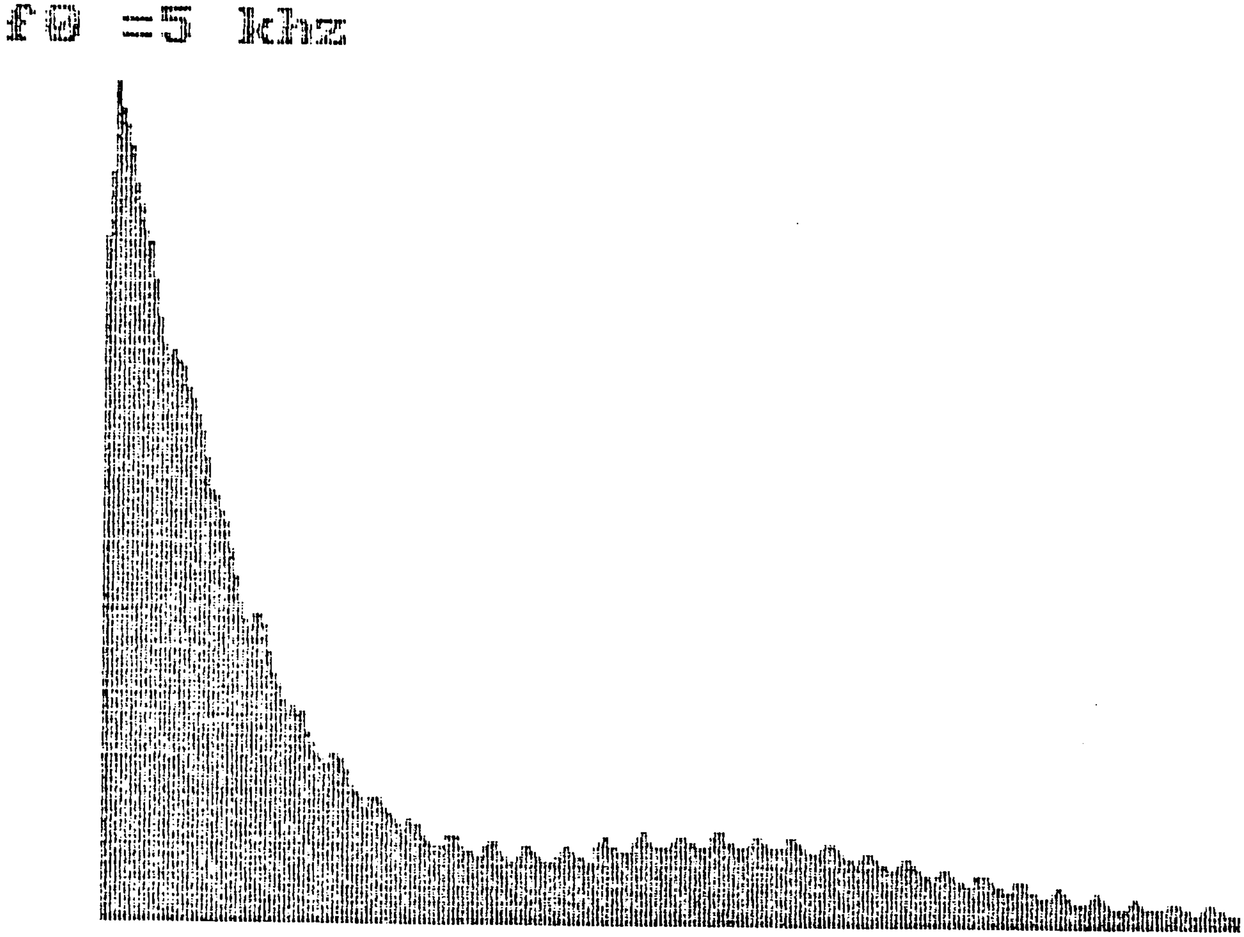

Figure A(17) x = 5" Re = 3 x 10^6 Before Filter

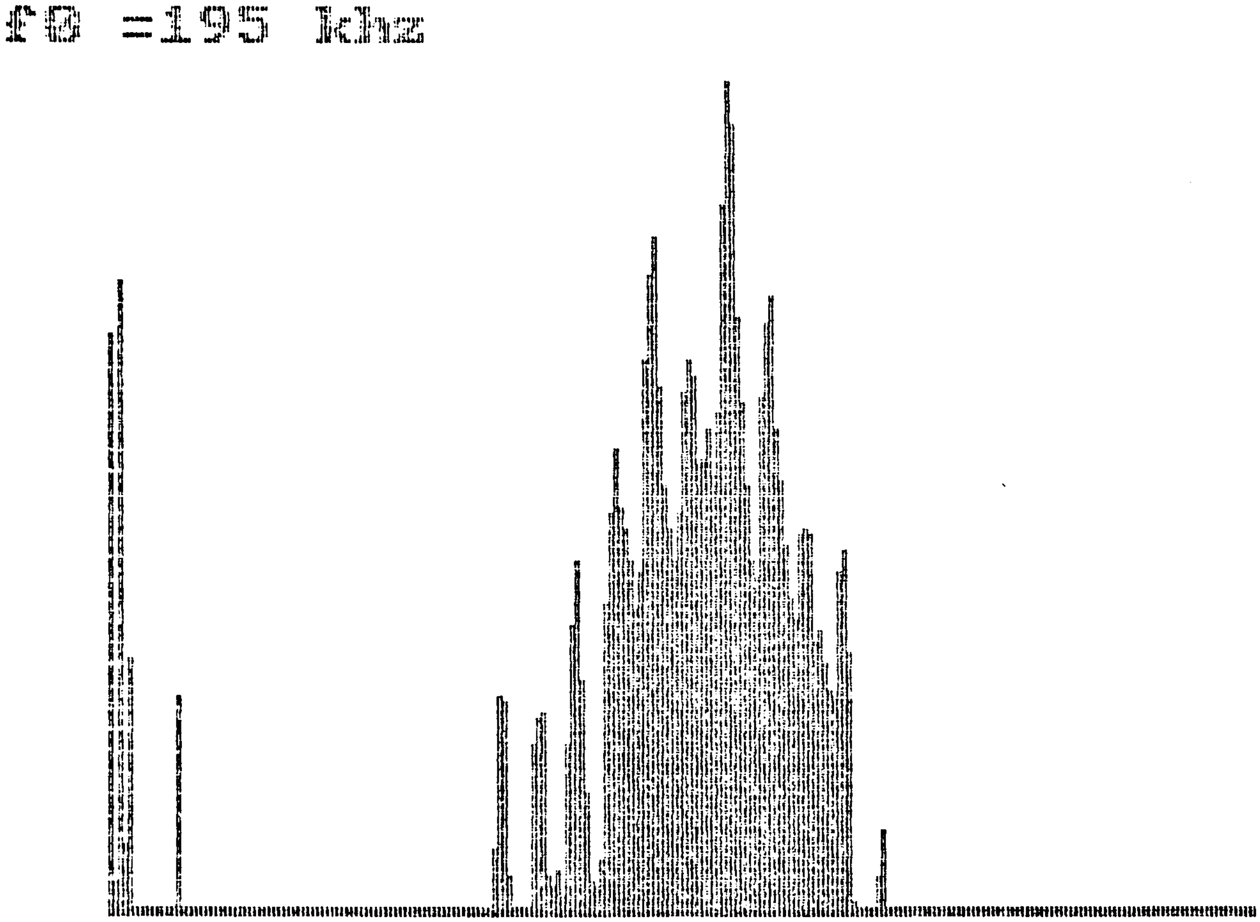

Figure A(18) x = 5" Re = 3 x 10^6 After Filter

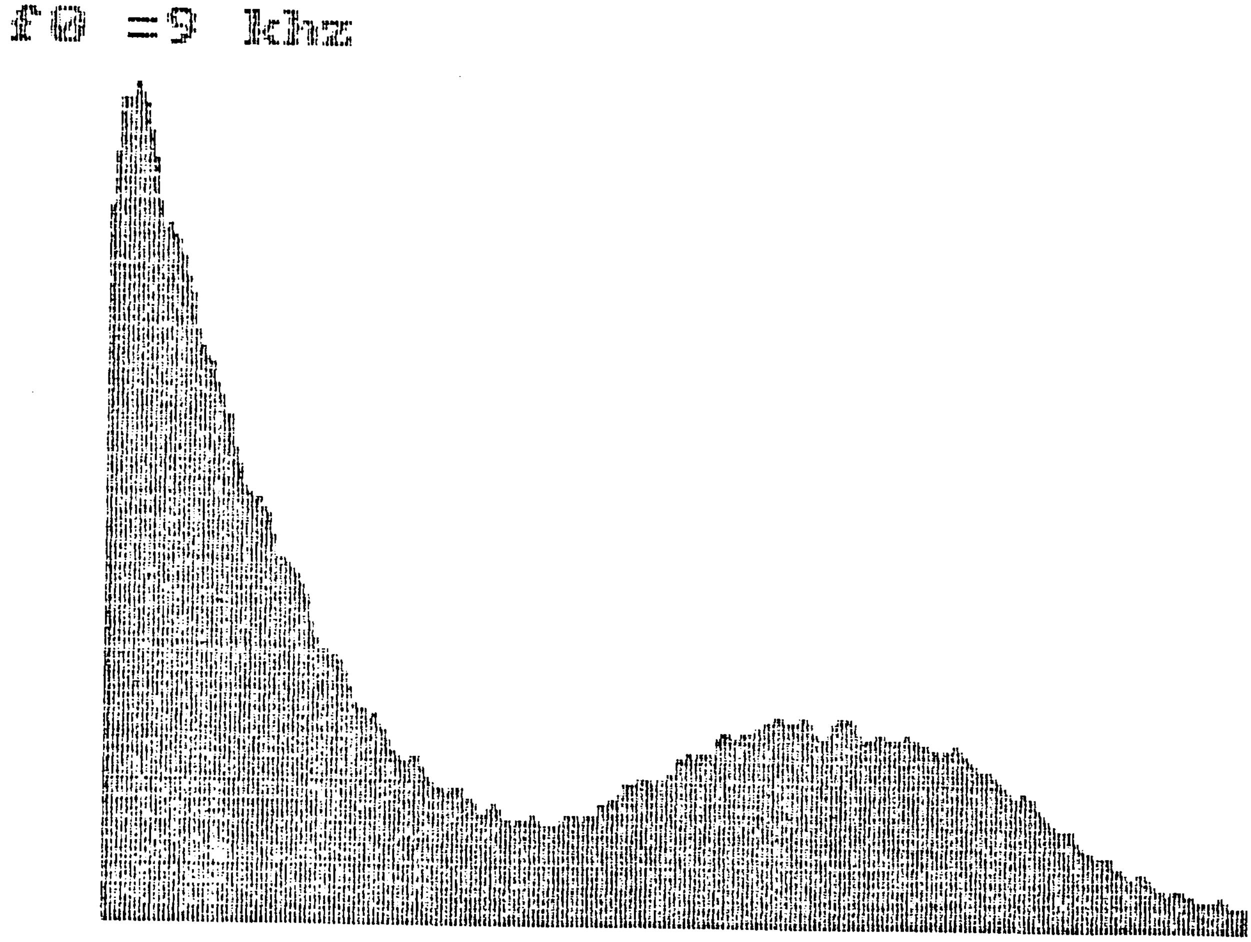

Figure A(19) x = 6" Re = 3 x 10^6 Before Filter

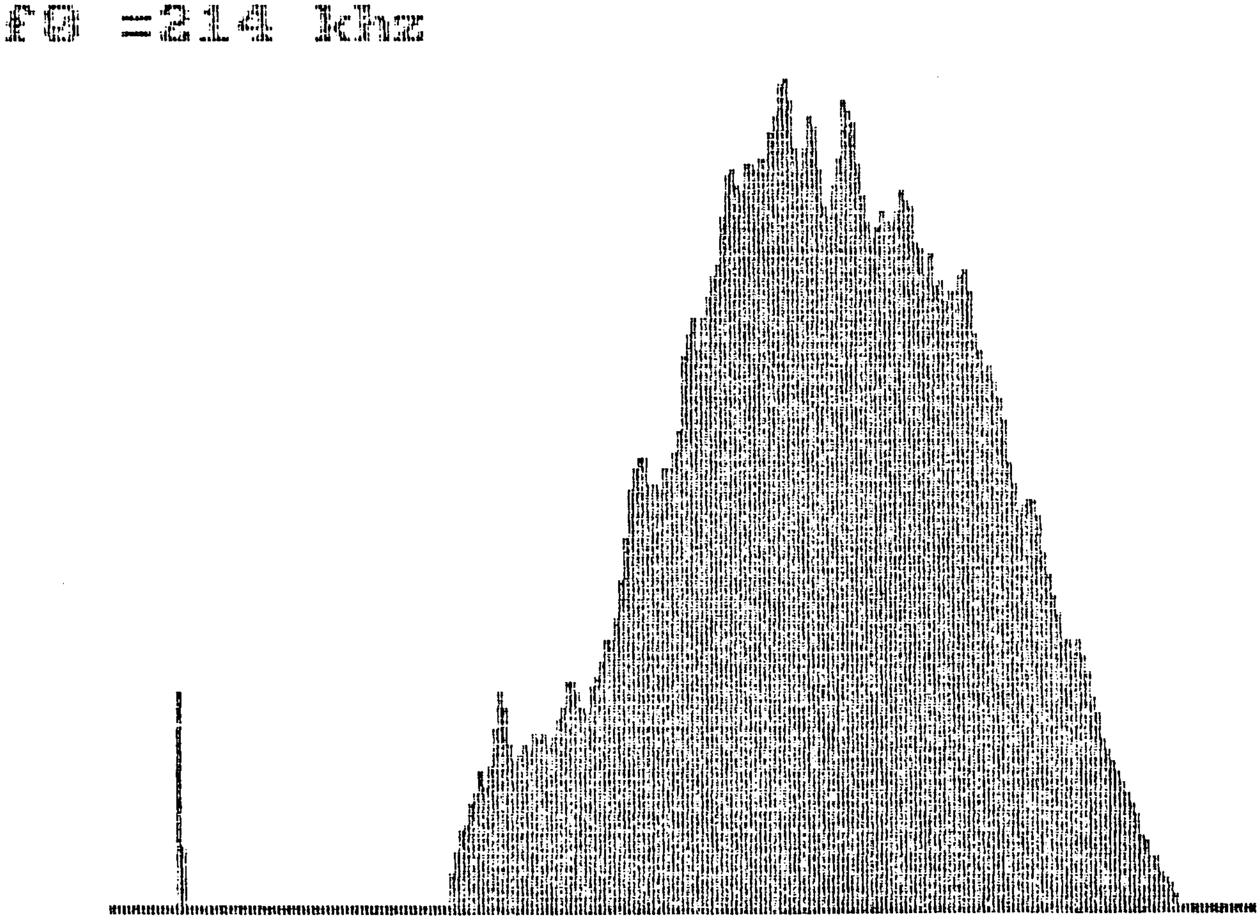

Figure A(20) x = 6" Re = 3×10^6 After Filter

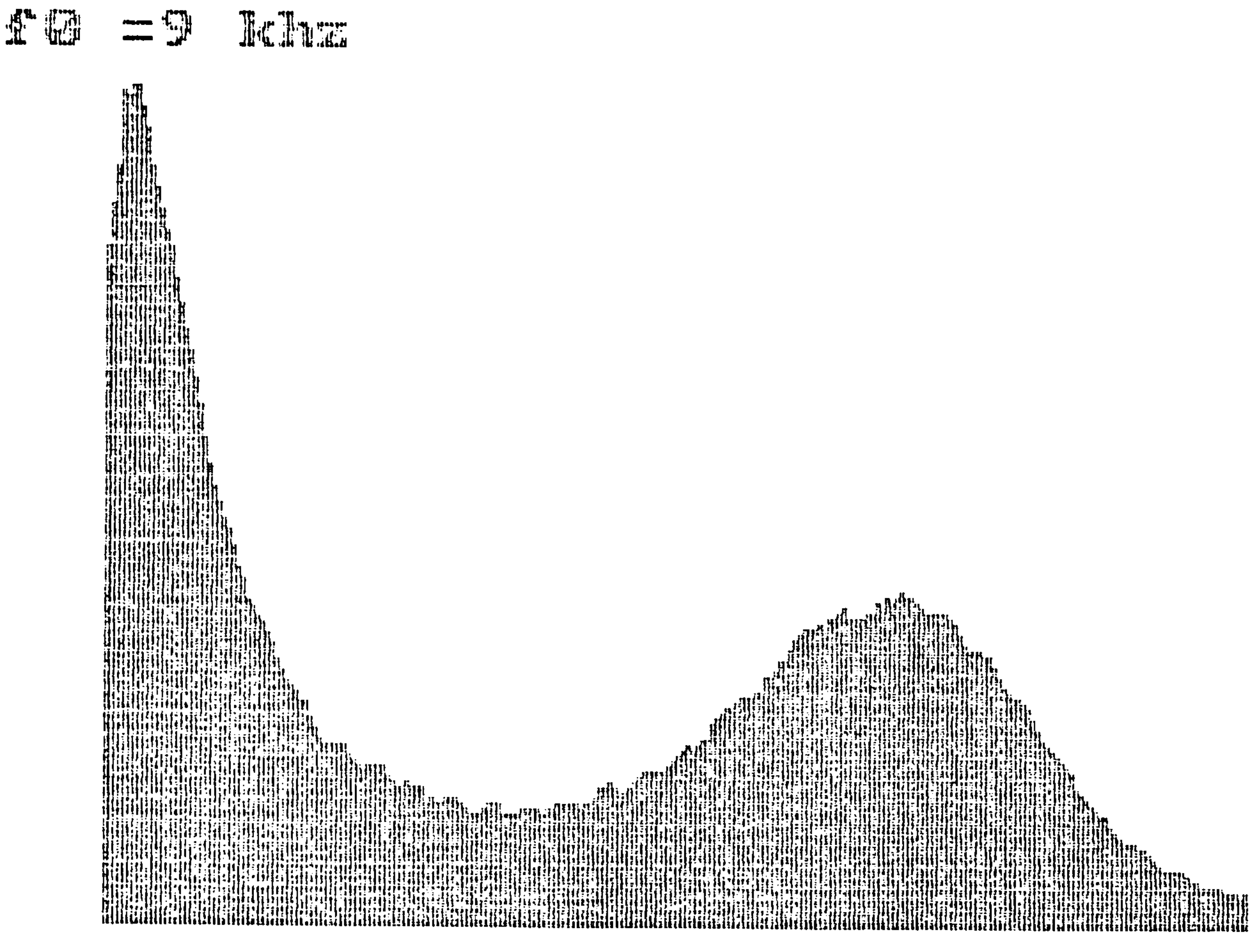

Figure A(21) x = 8" Re = 3×10^6 Before Filter

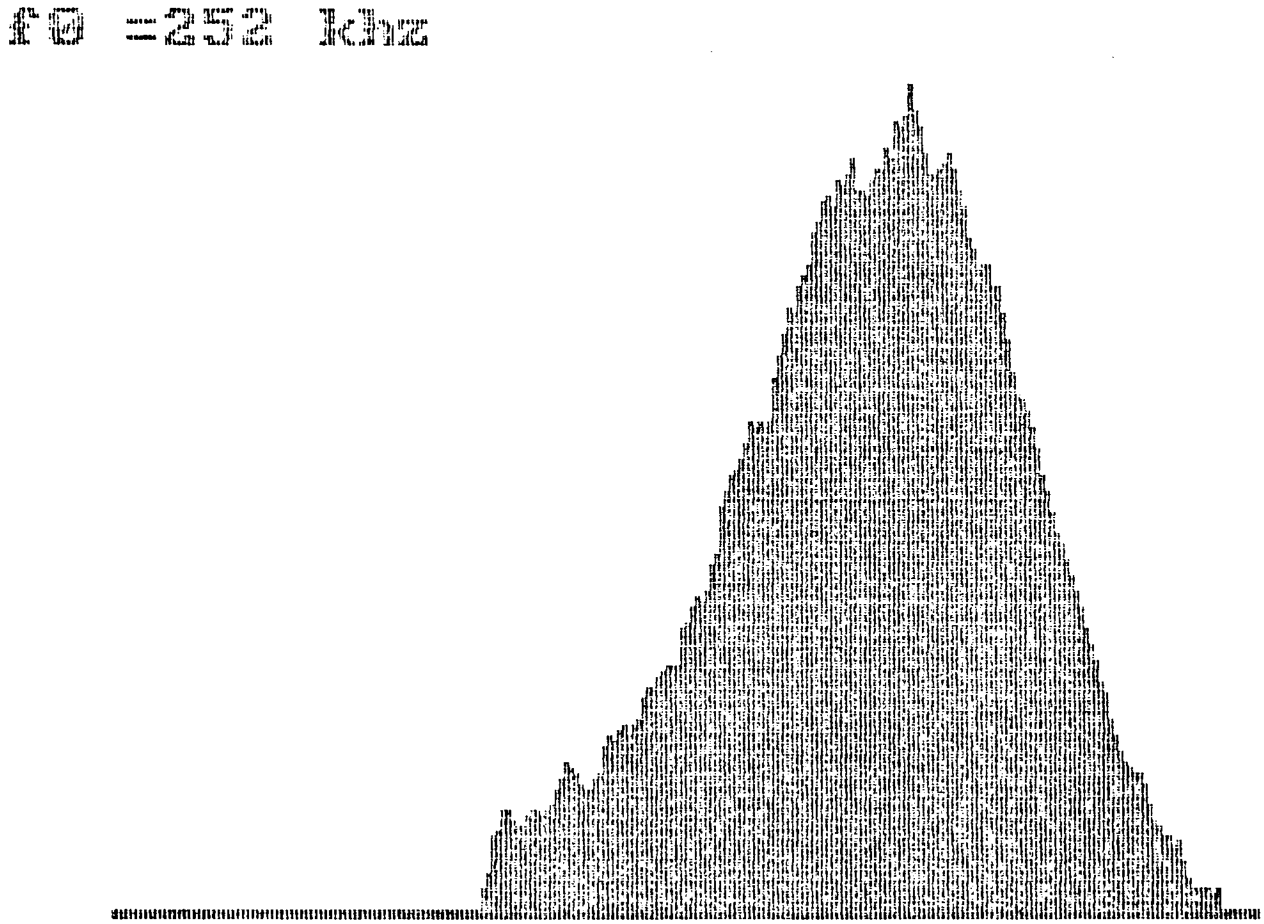

Figure A(22) x = 8" Re = 3 x 10^6 After Filter

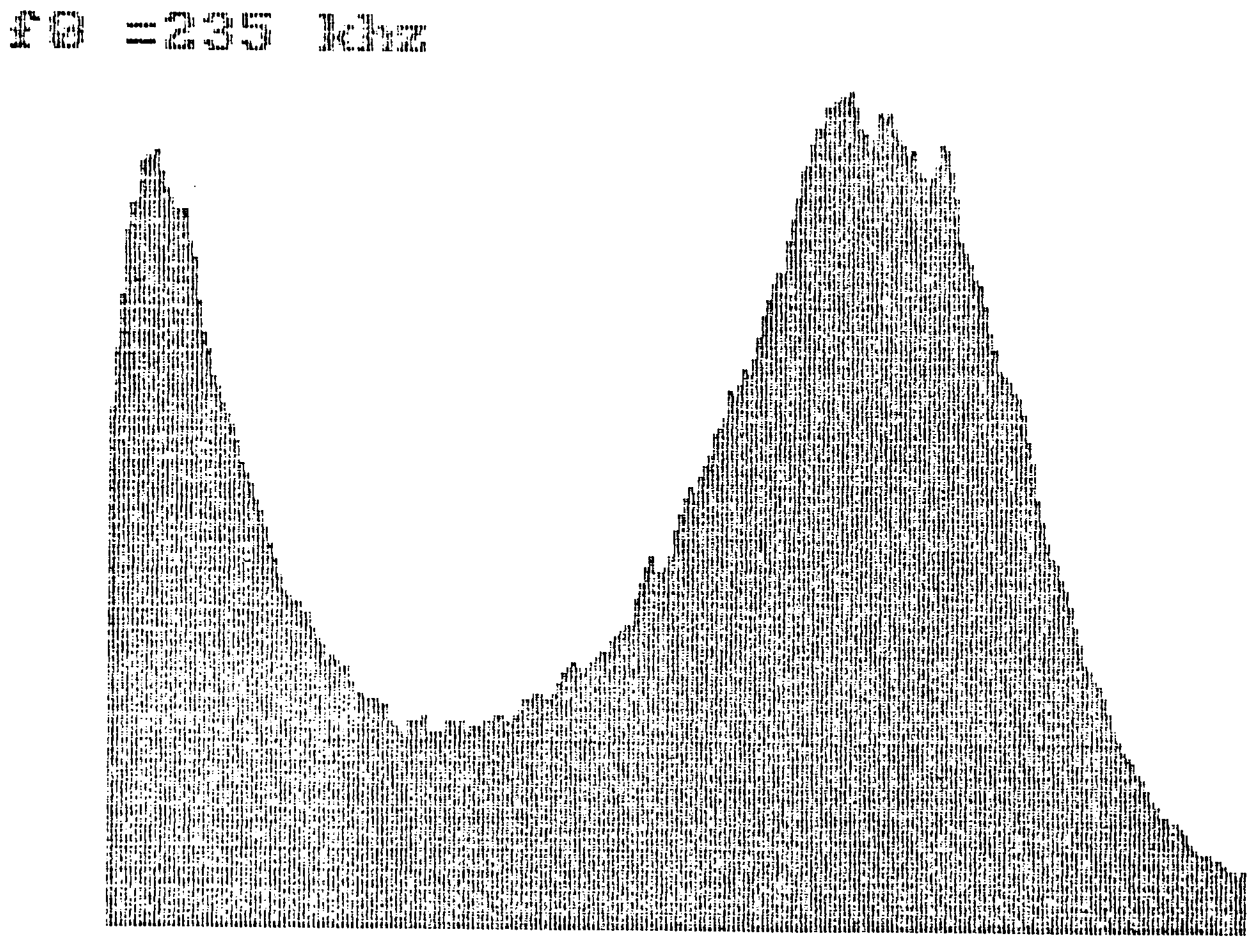

Figure A(23) x = 9" Re = 3 x 10^6 Before Filter

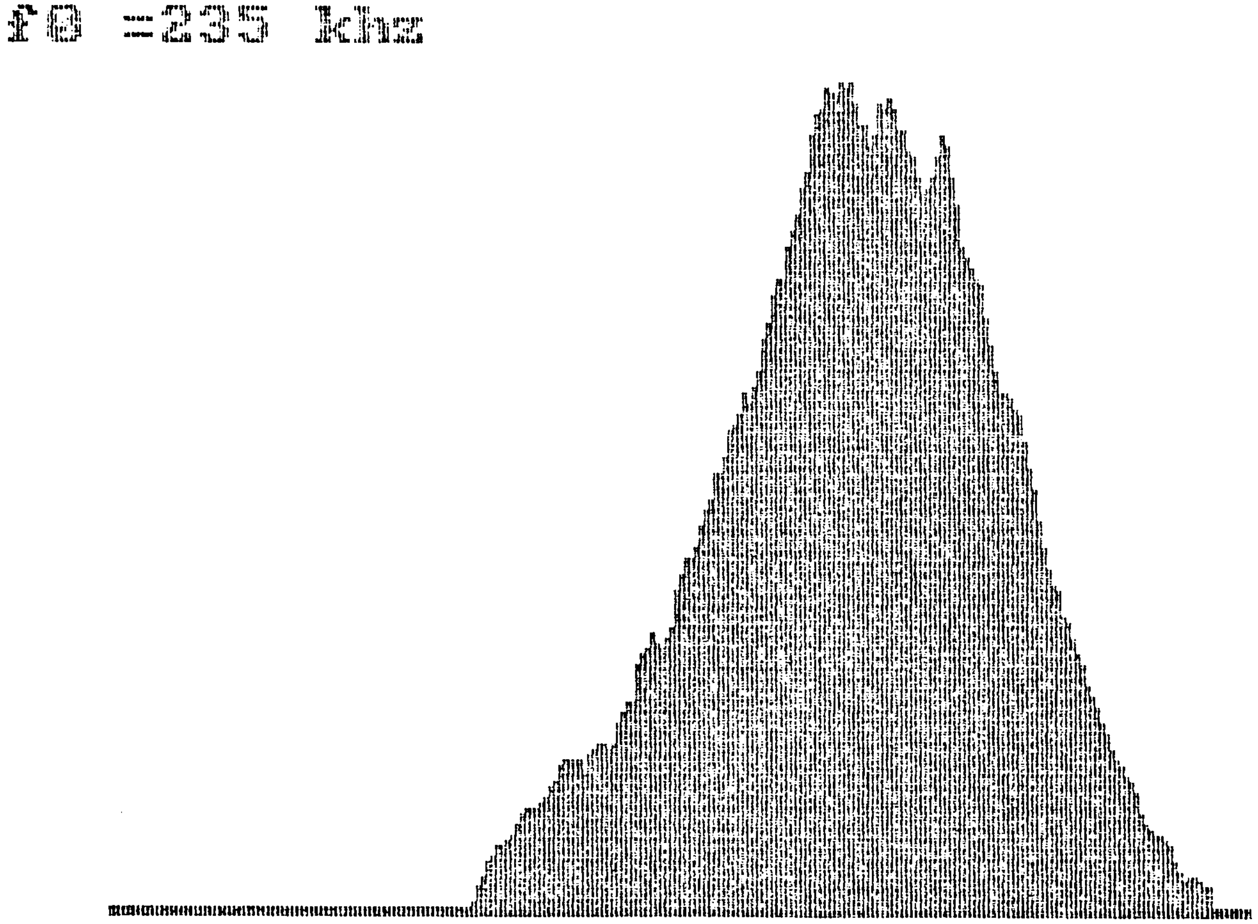

Figure A(24) x = 9" Re = 3 x 10^6 After Filter

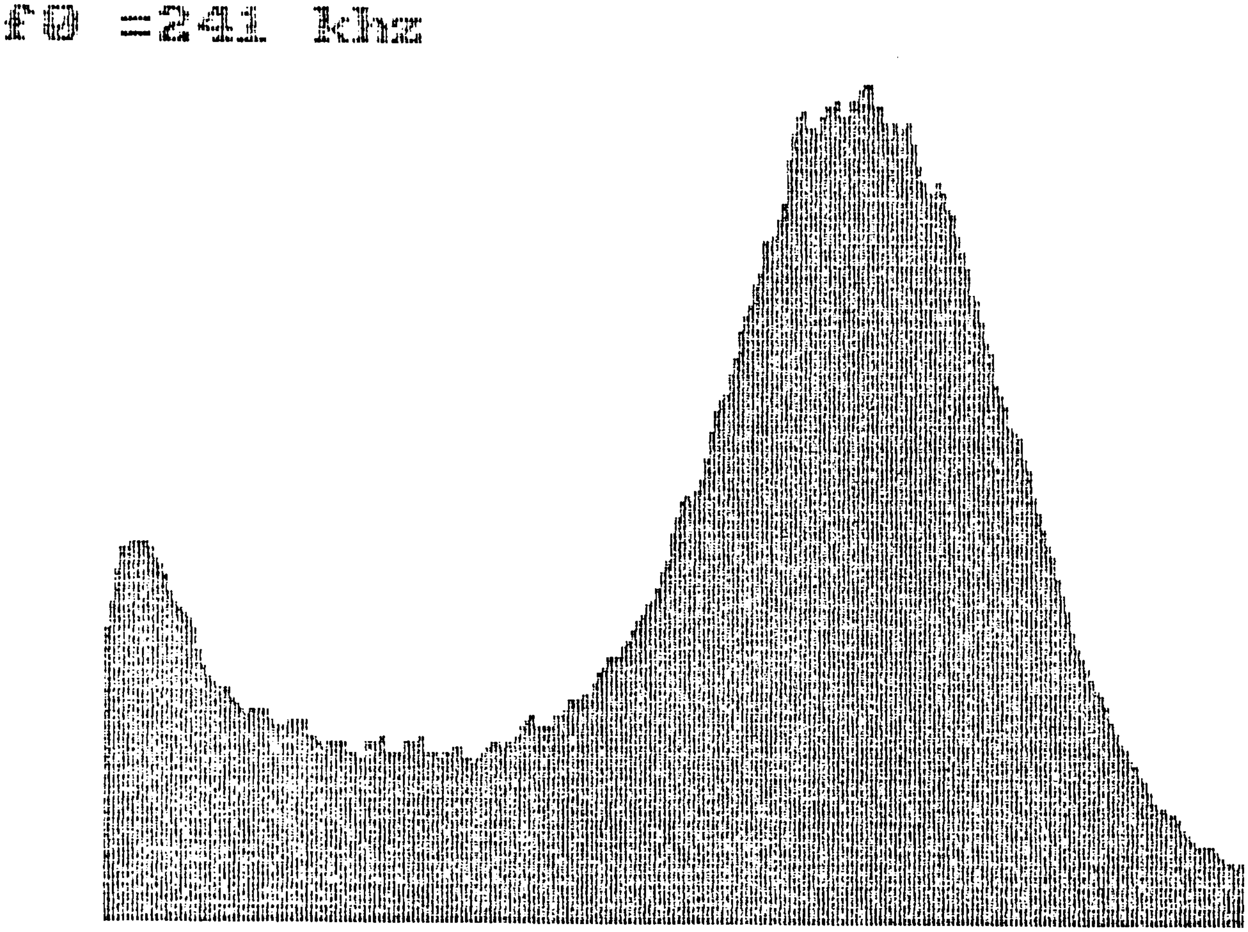

Figure A(25) x = 12" Re = 3×10^6 Before Filter

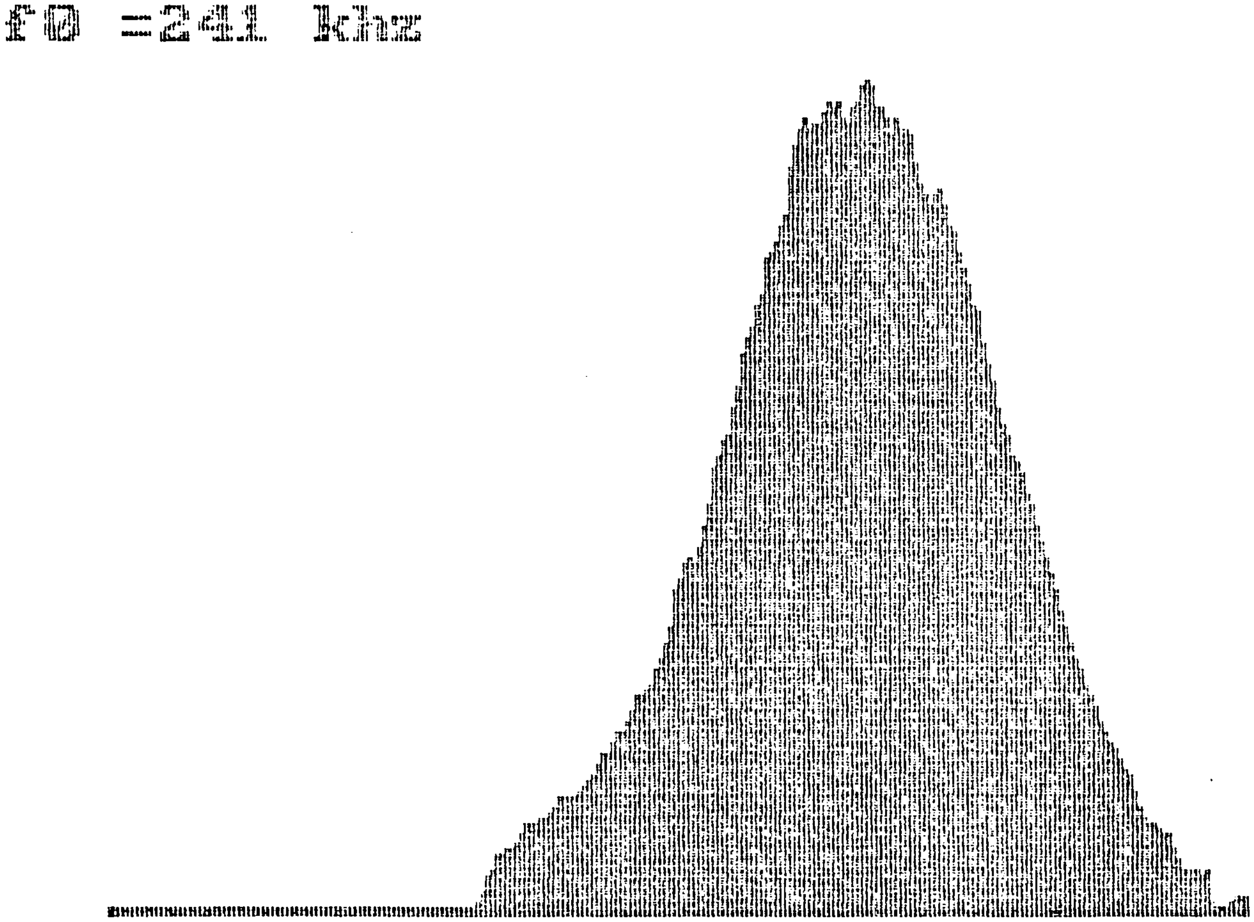

Figure A(26) x = 12" Re = 3 x 10^6 After Filter

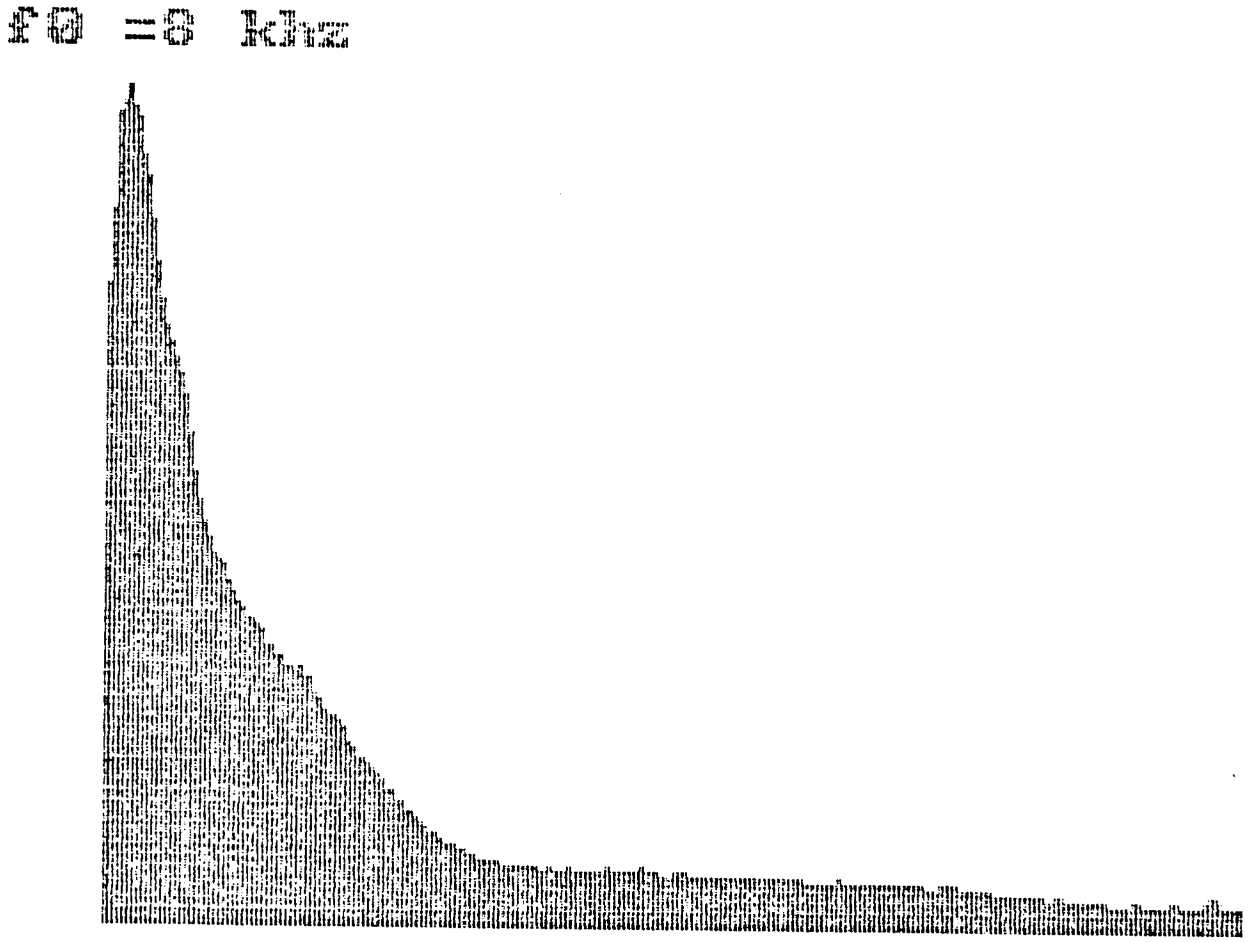

Figure A(27) x = 2" Re 4 x 10^6 Filter

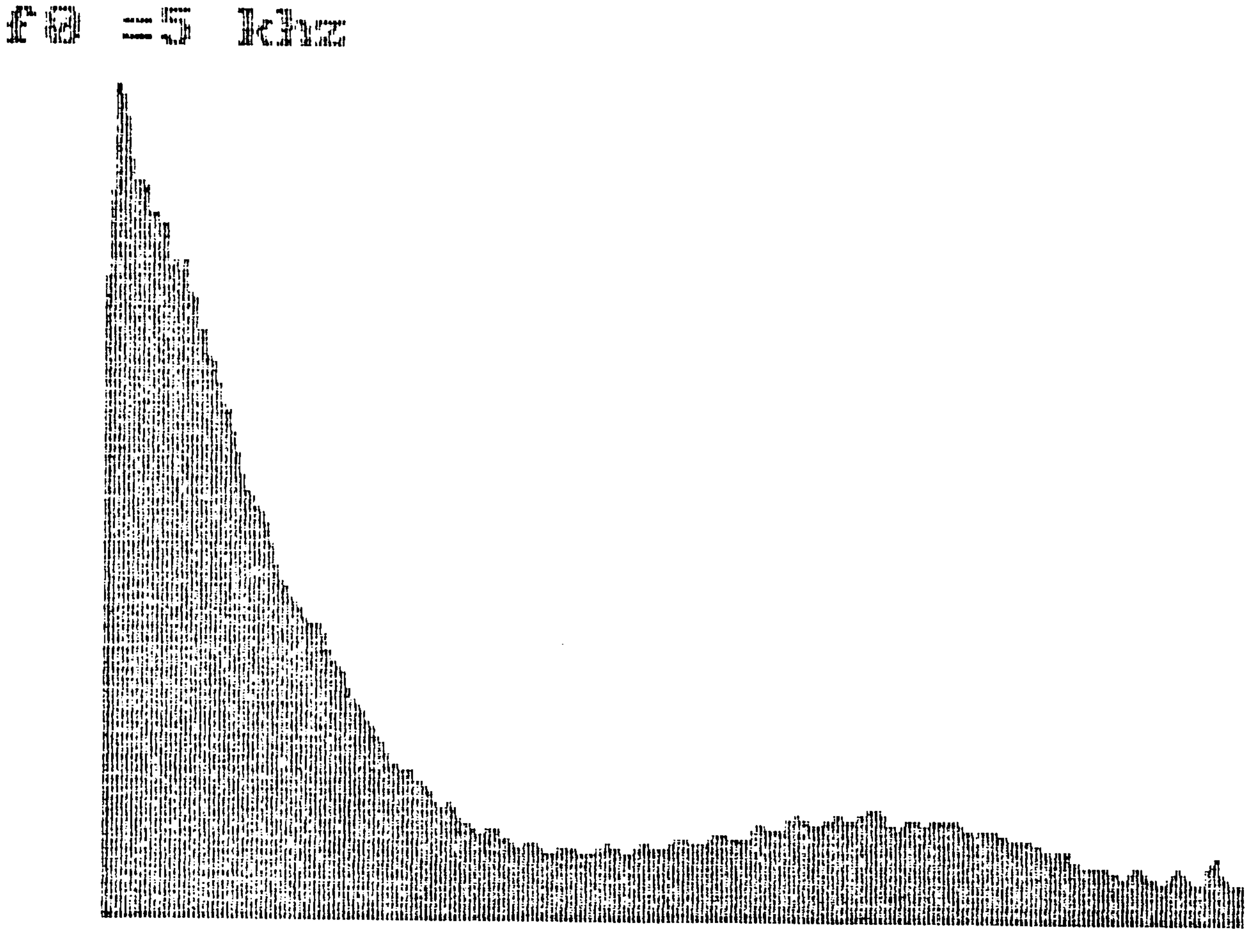

Figure A(28) x = 3" Re = 4 x 10^6 Before Filter

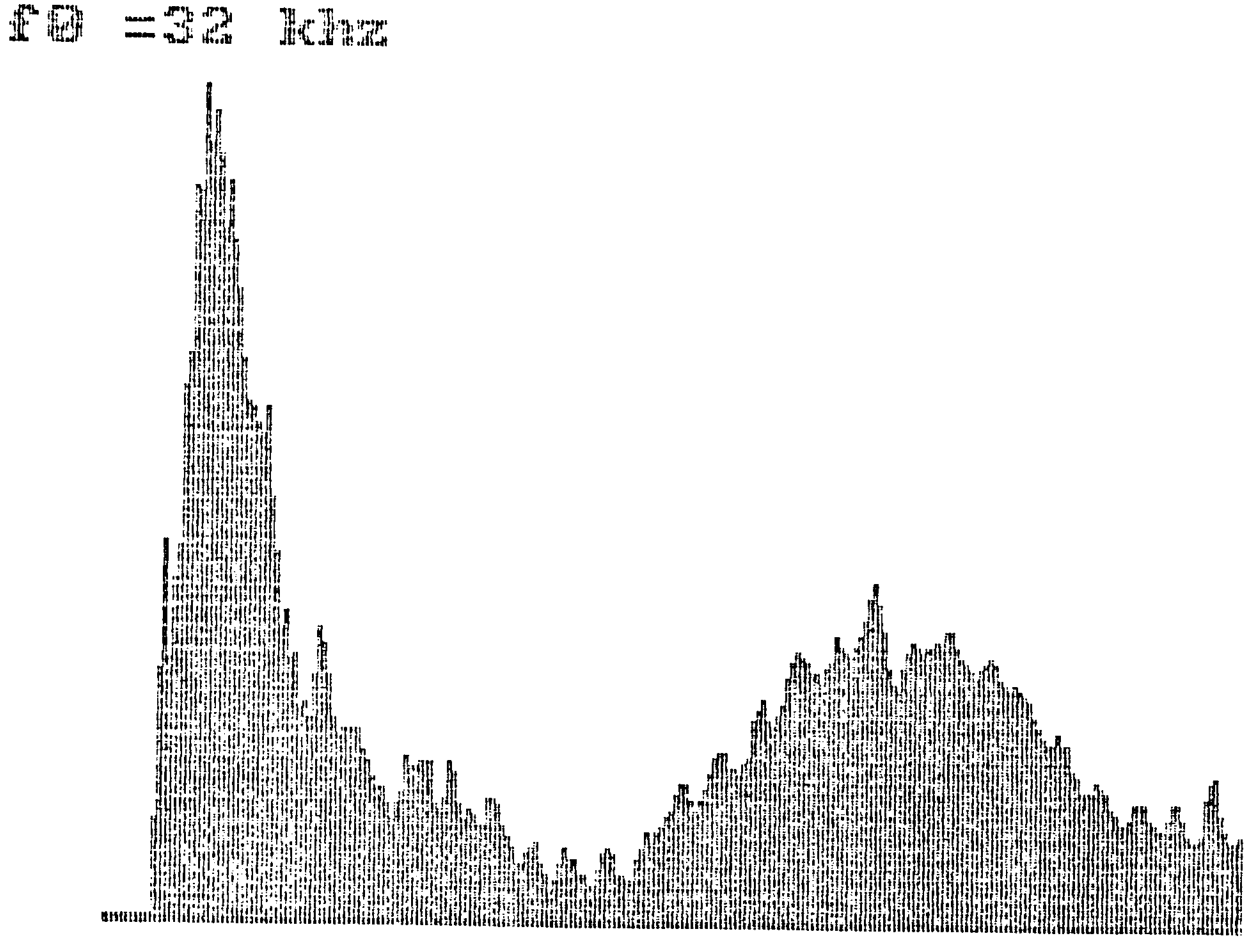

Figure A(29) x = 3" Re = 4×10^6 After Filter

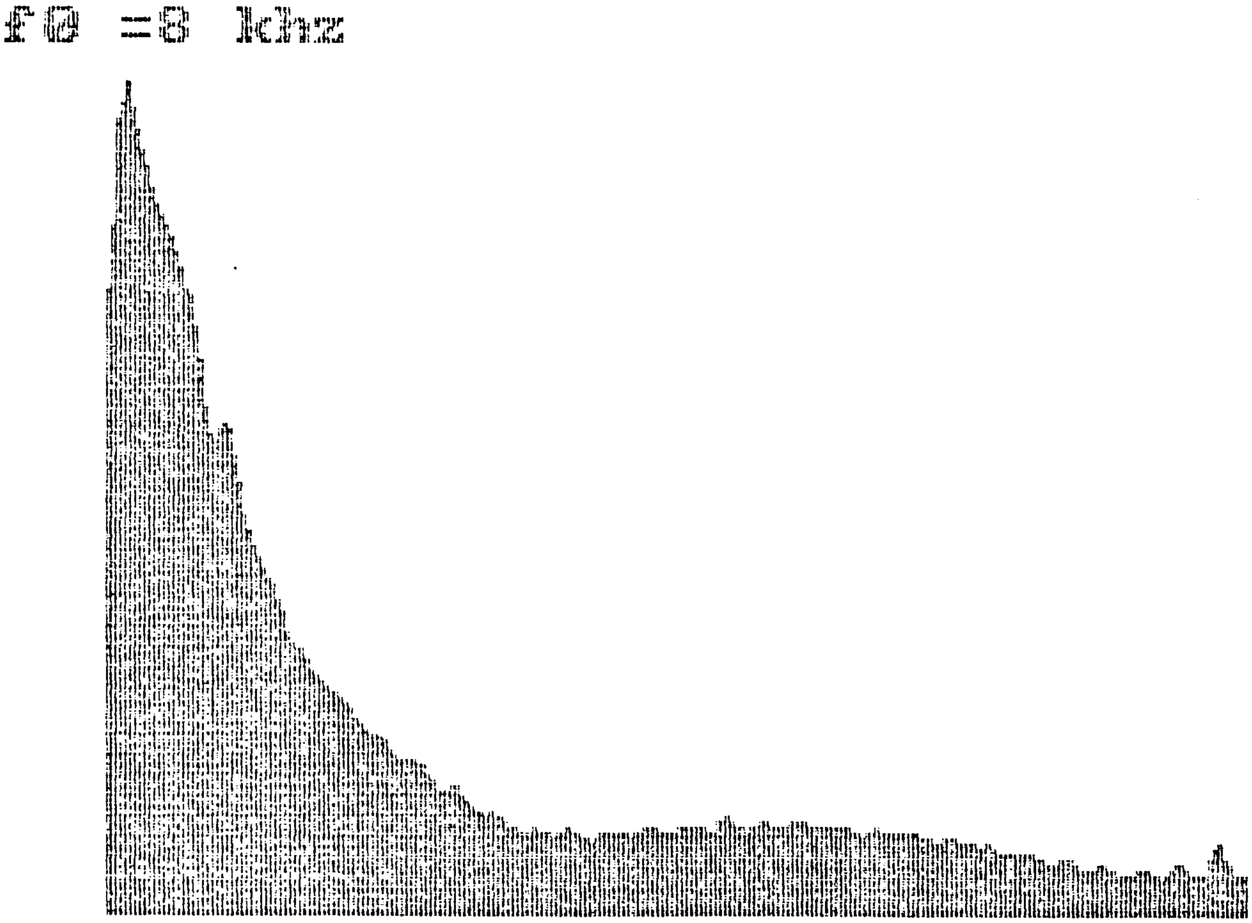

Figure A(30) x = 4" Re = 4 x 10^6 Before Filter

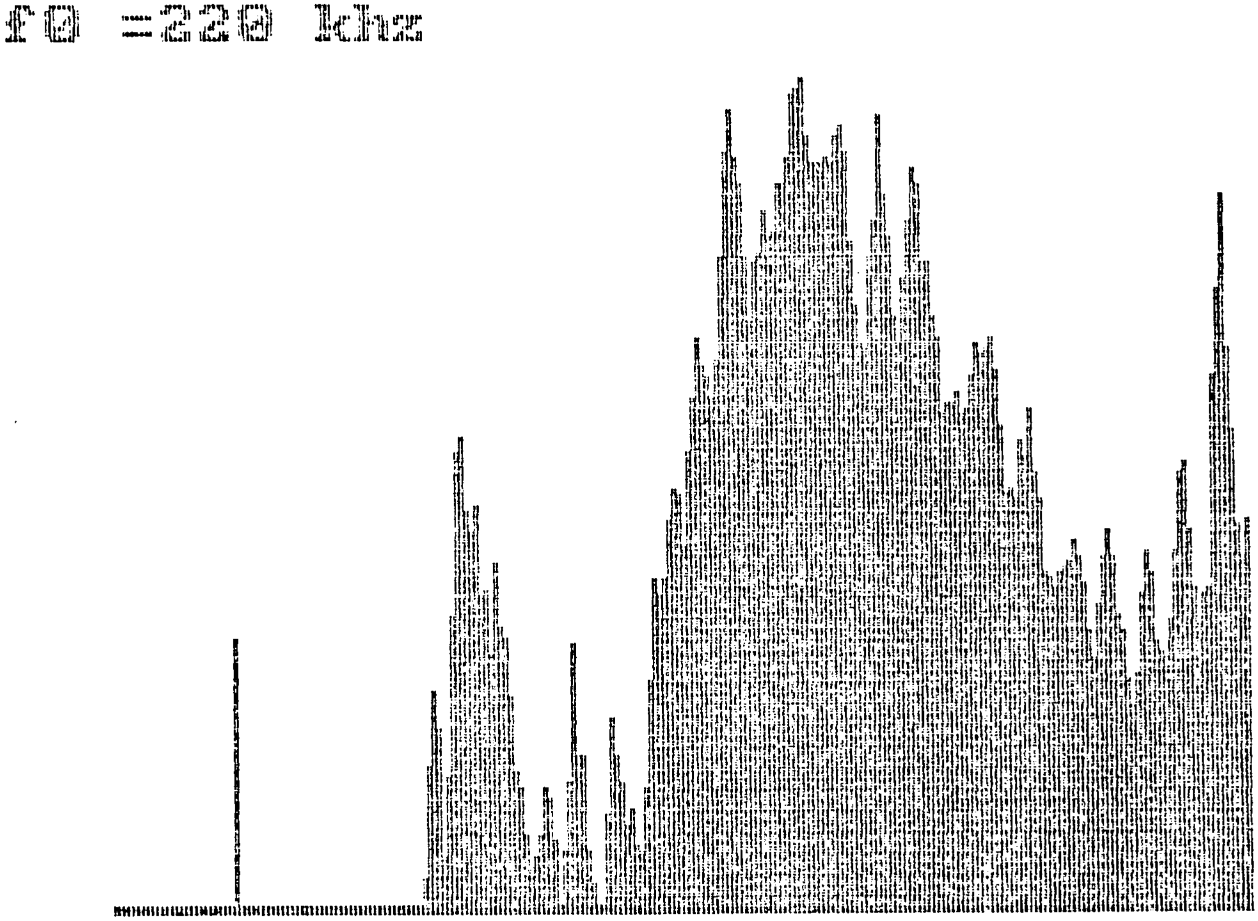

Figure A(31) x = 4" Re = 4×10^6 After Filter

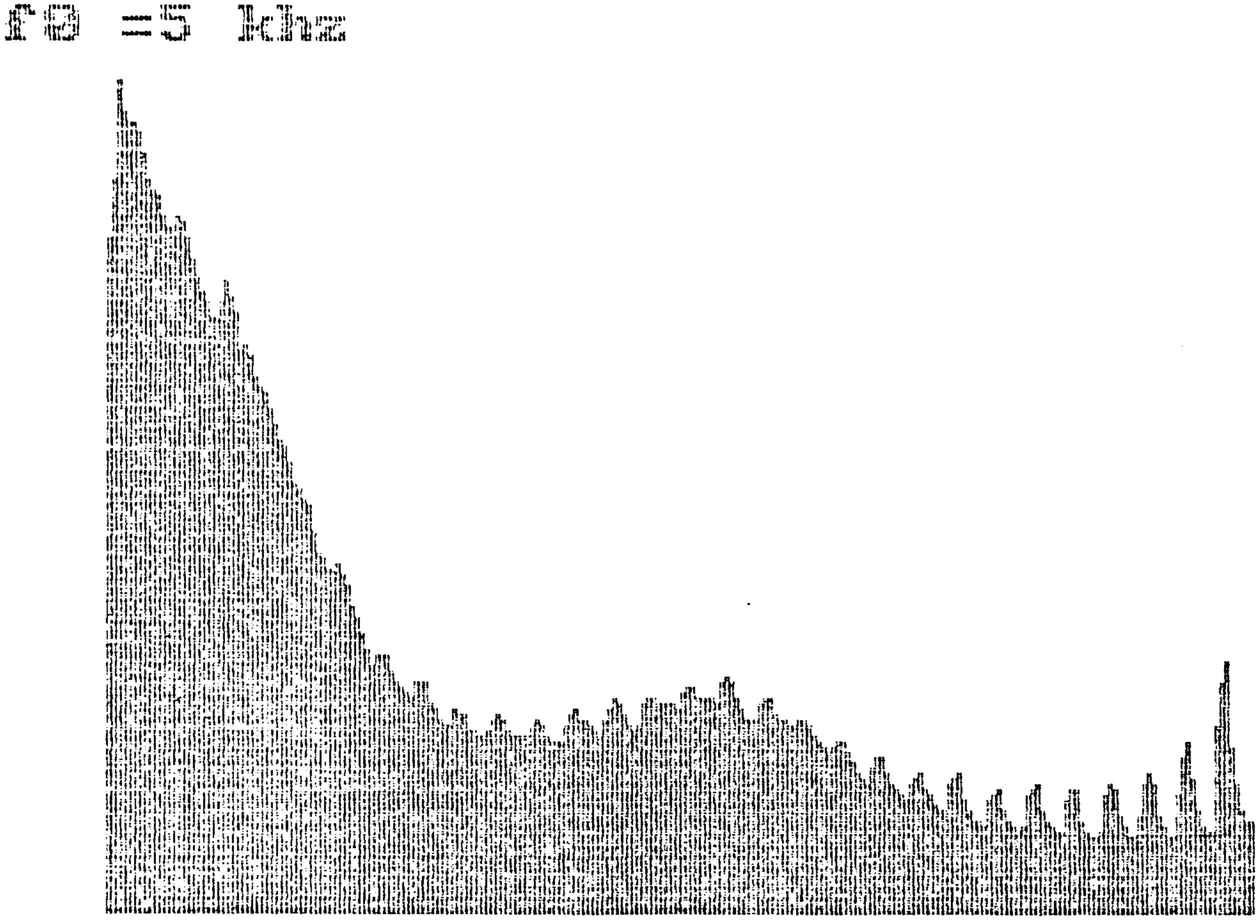

Figure A(32) x = 5" Re = 4×10^6 Before Filter

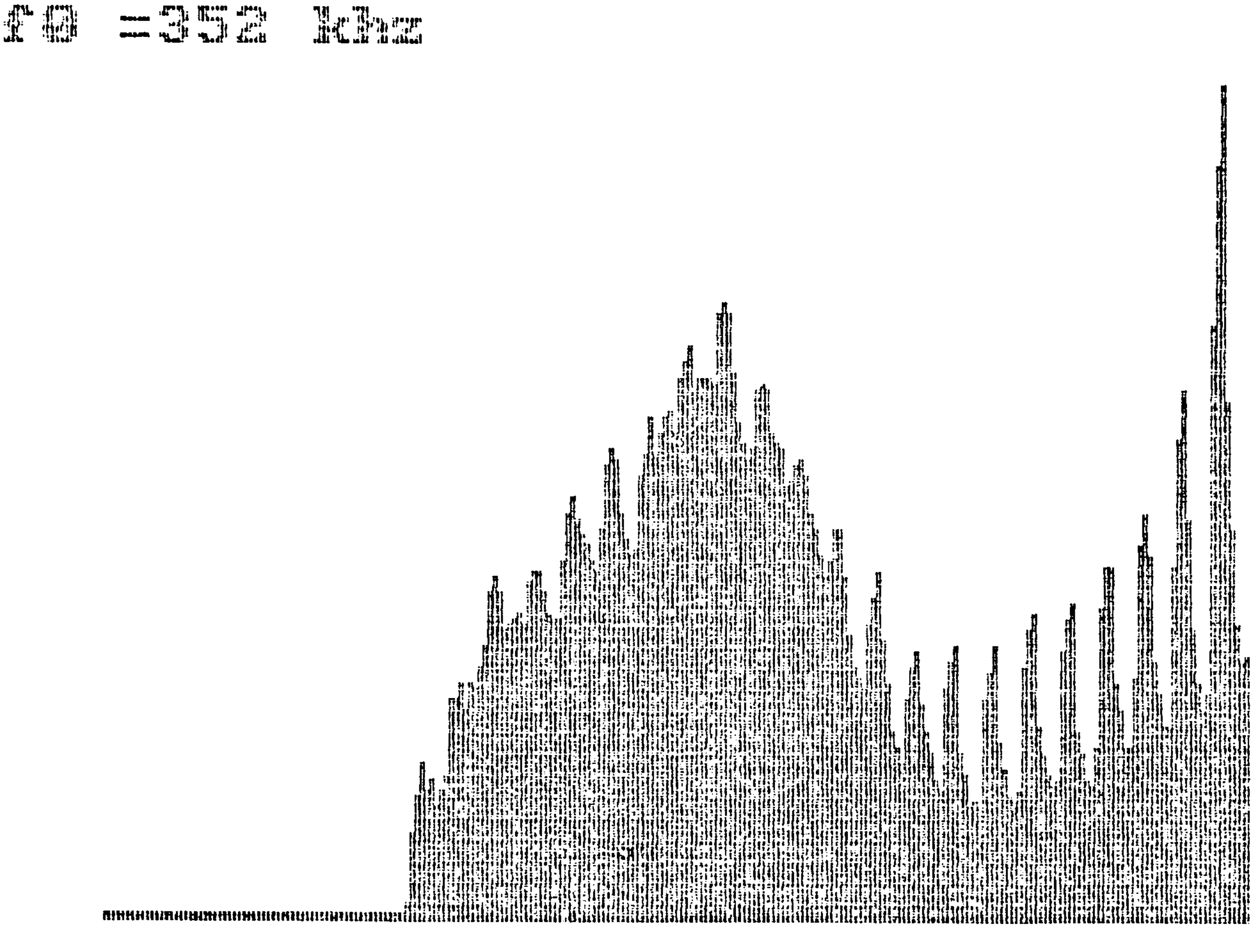

Figure A(33) x = 5" Re = 4×10^6 After Filter

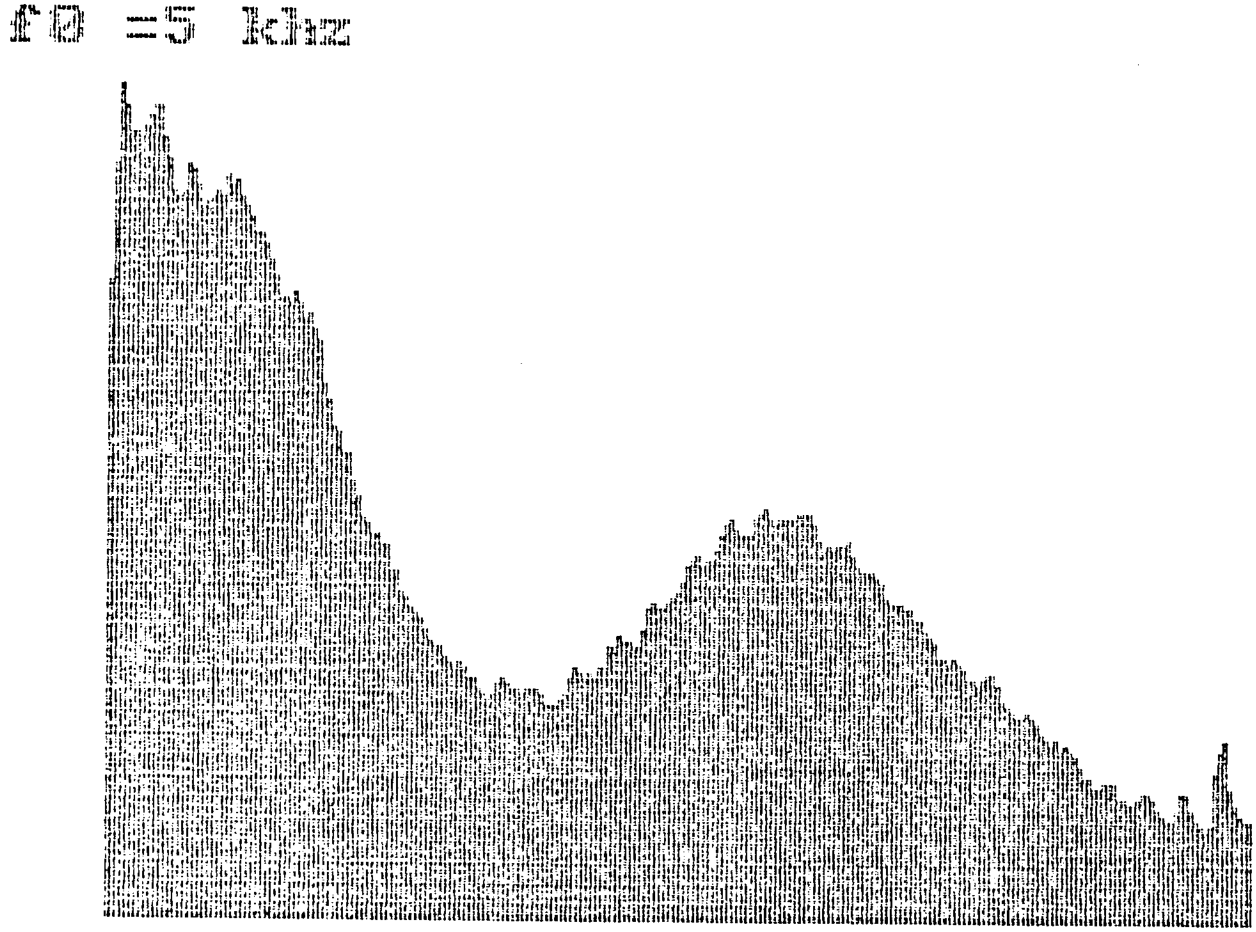

Figure A(34) x = 6" Re = 4 x 10^6 Before Filter

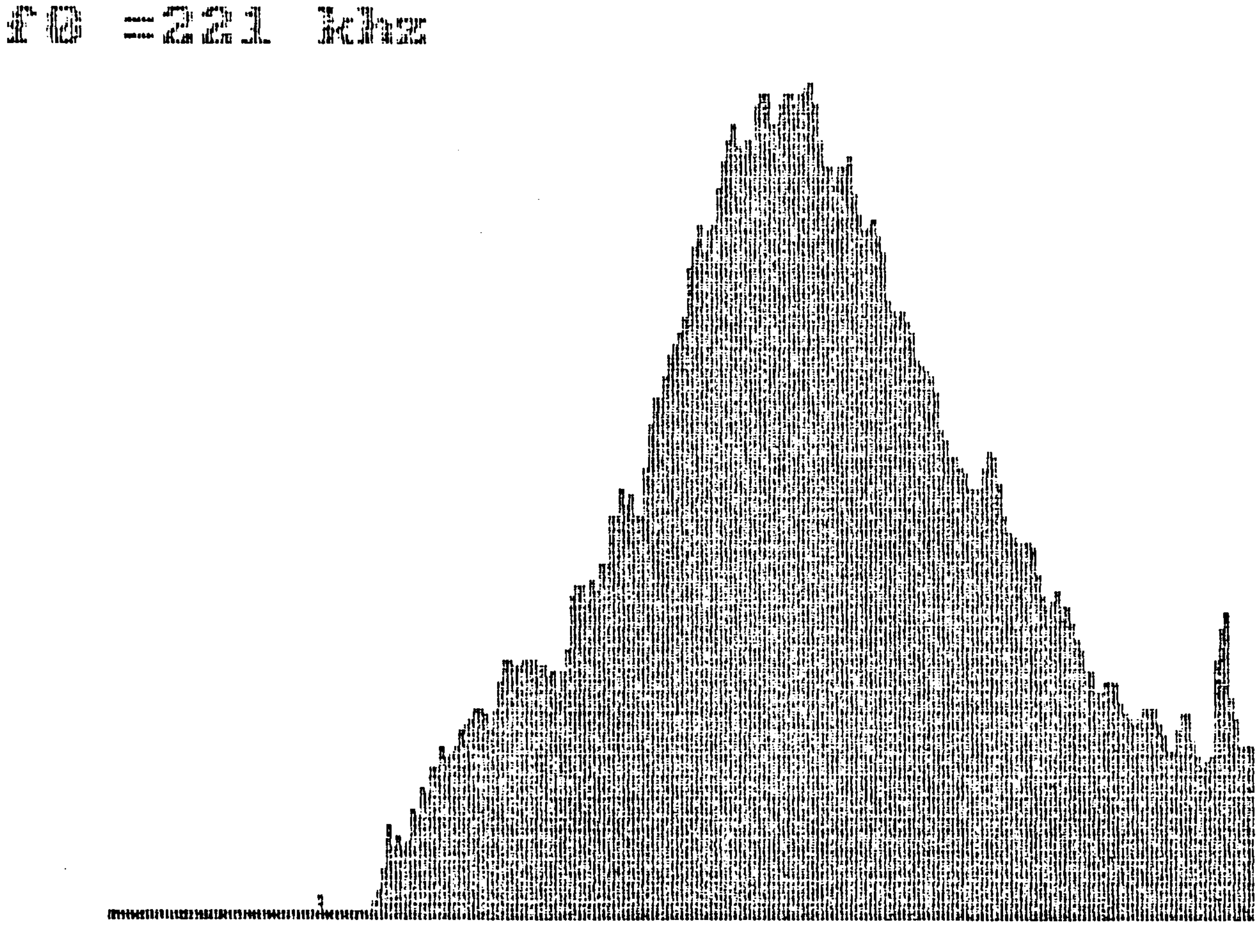

Figure A(35) x = 6" Re = 4 x 10^6 After Filter

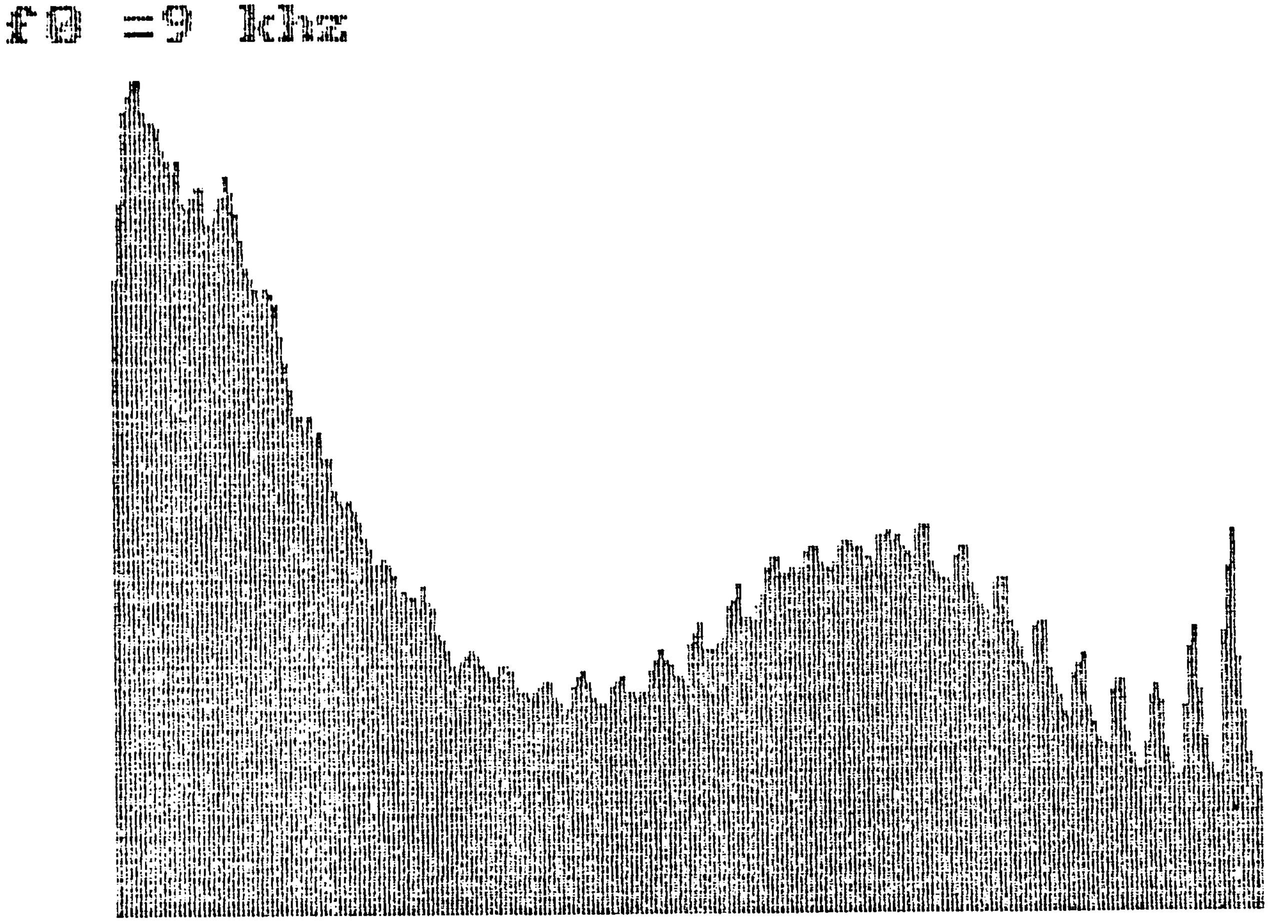

Figure A(36) x = 8" Re = 4 x 10^6 Before Filter

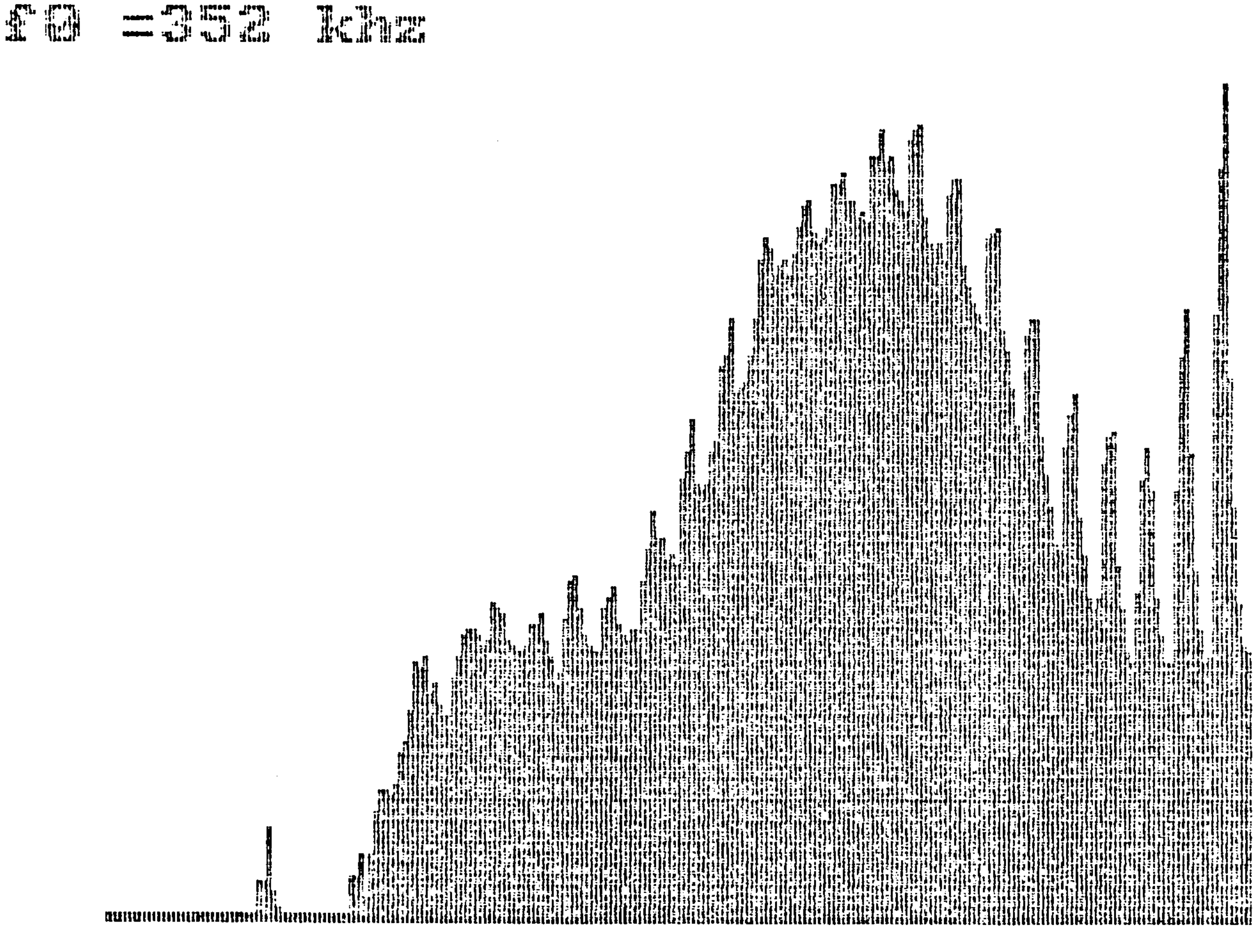

Figure A(37) x = 8" Re = 4×10^6 After Filter

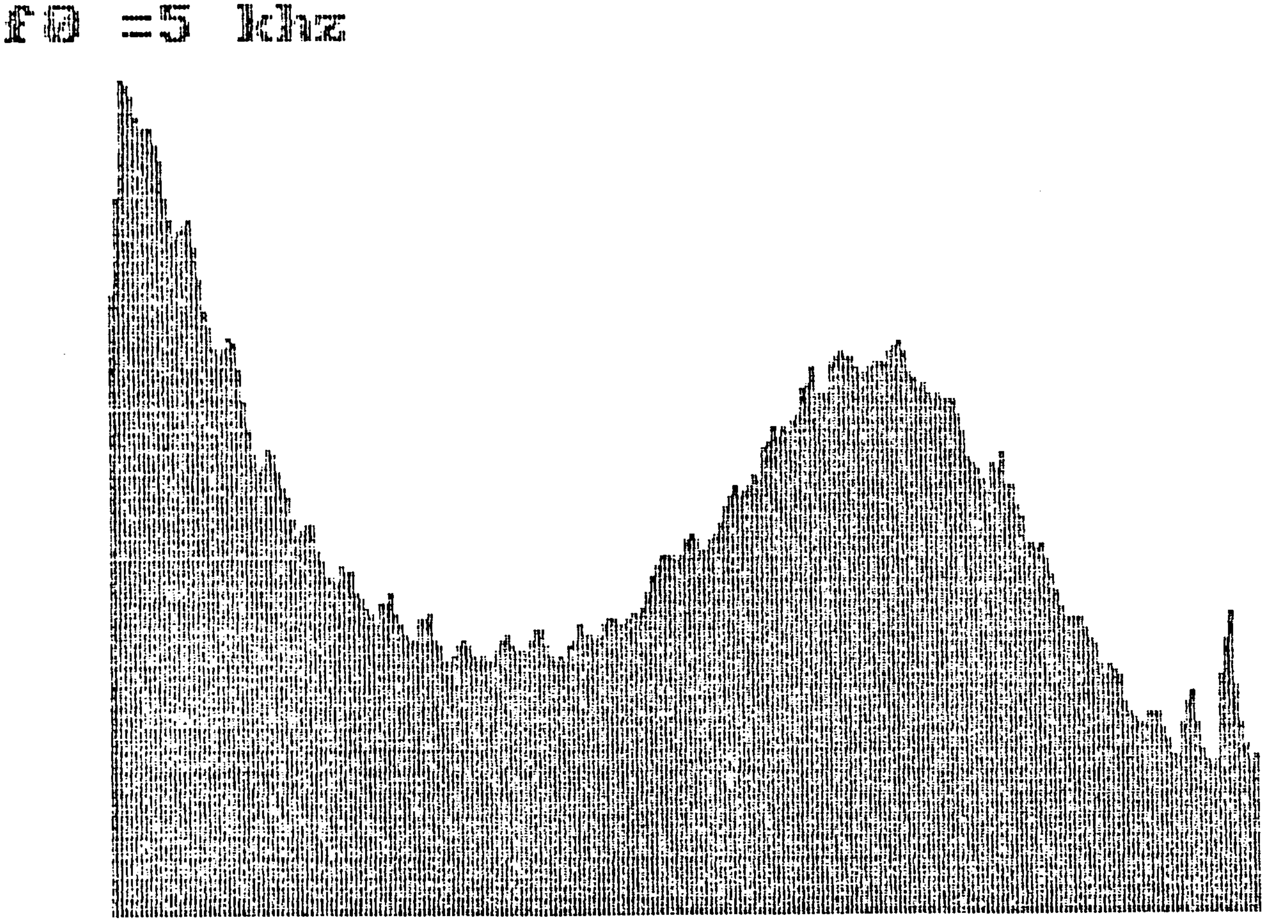

Figure A(38) x = 9" Re = 4 x 10^6 Before Filter

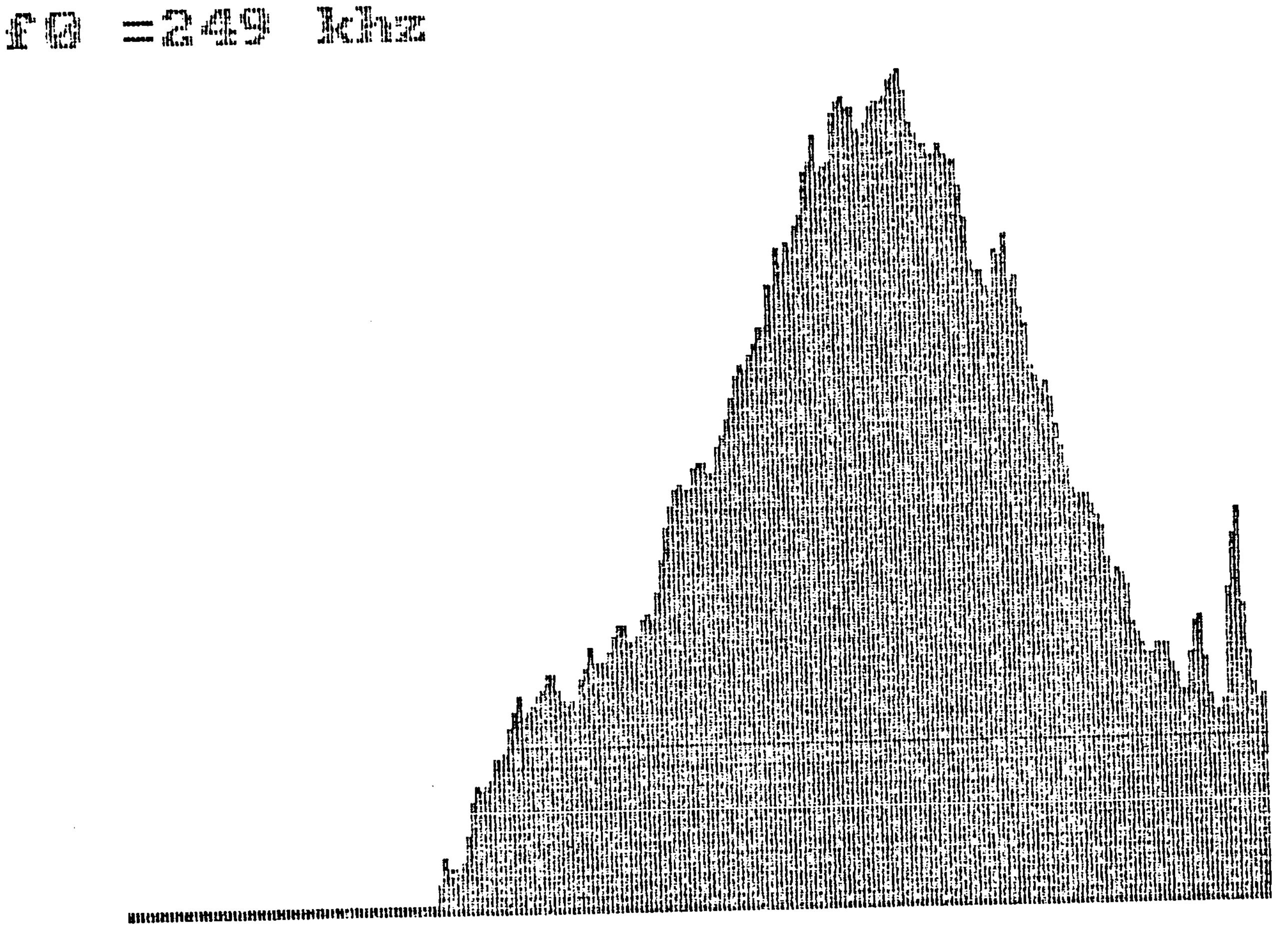

Figure A(39) x = 9" Re = 4 x 10^6 After Filter

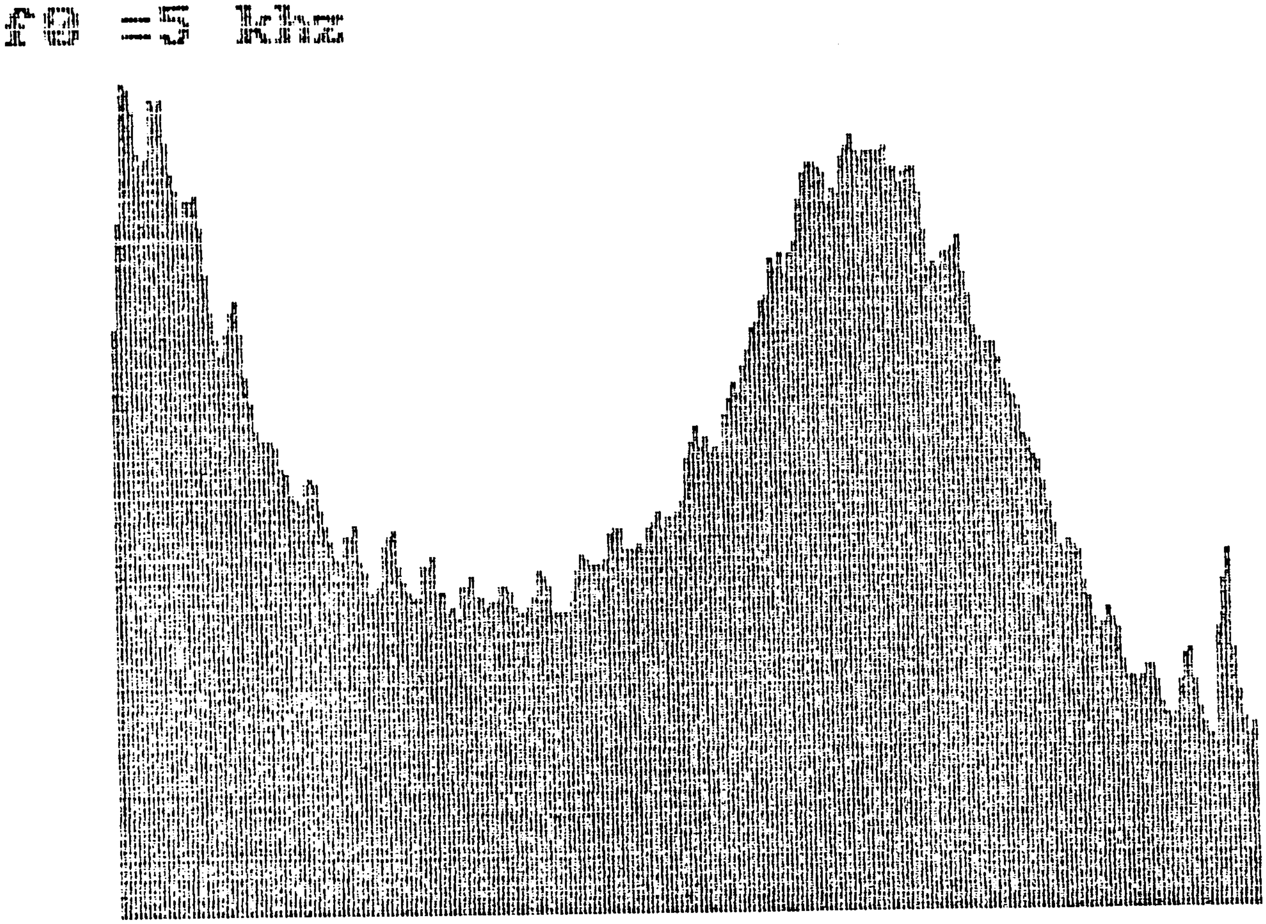

Figure A(40) x = 12" Re = 4 x 10^6 Before Filter

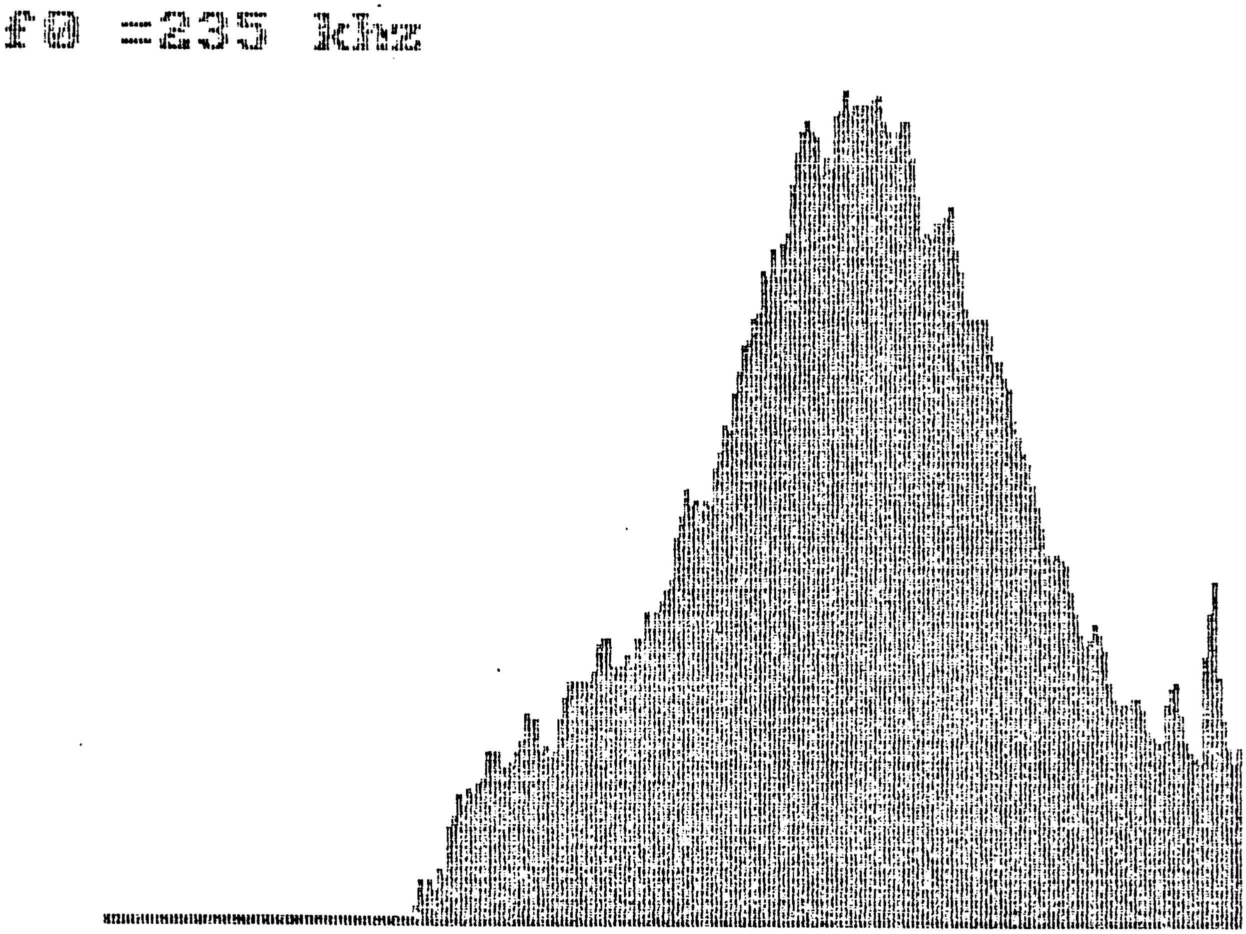

Figure A(41) x = 12" Re = 4×10^6 After Filter

II. TURBULENT WEDGE DATA

Wedge at x = 2.75" from L. E.

$Re = 2 \times 10^6$

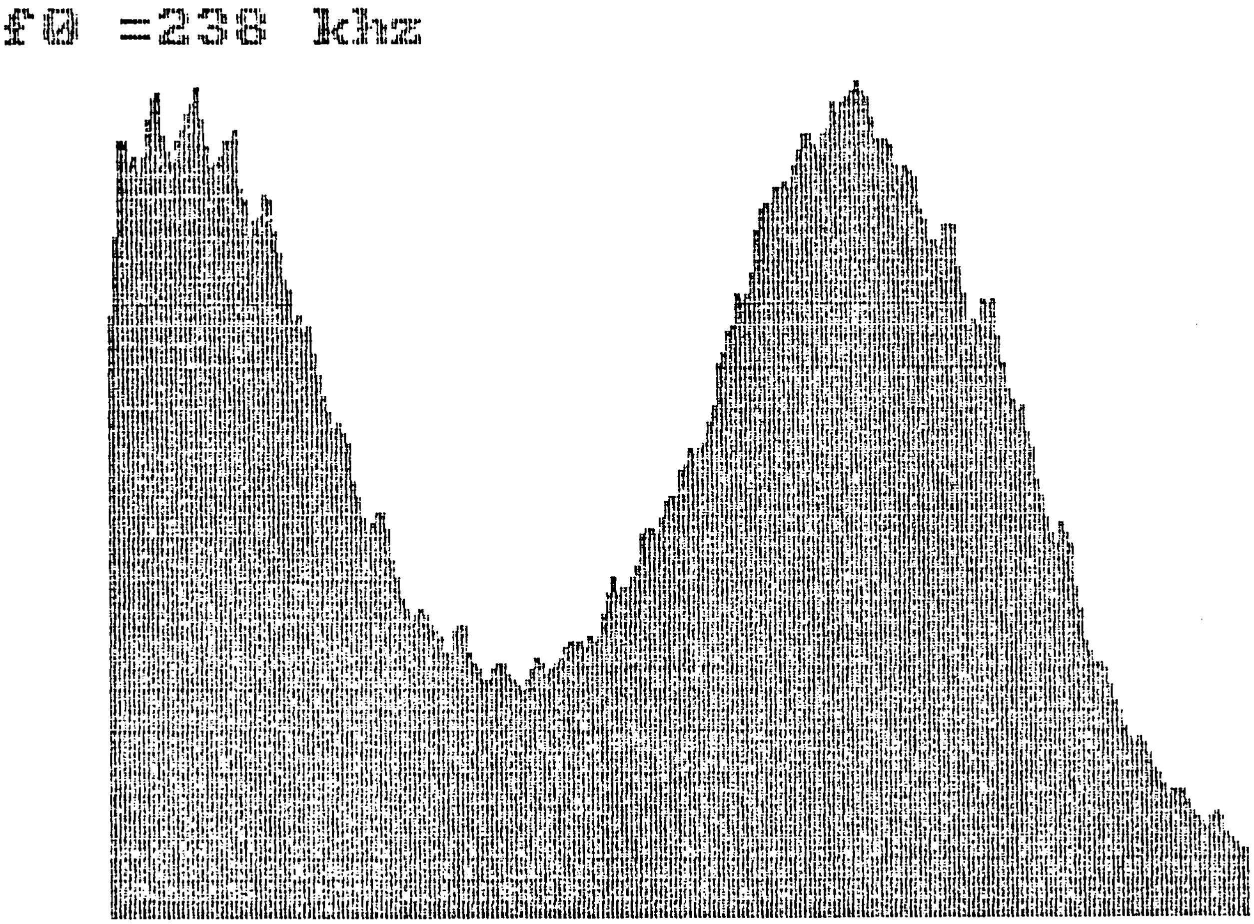

Figure A(42) x = 5" y = 1.0" Filter

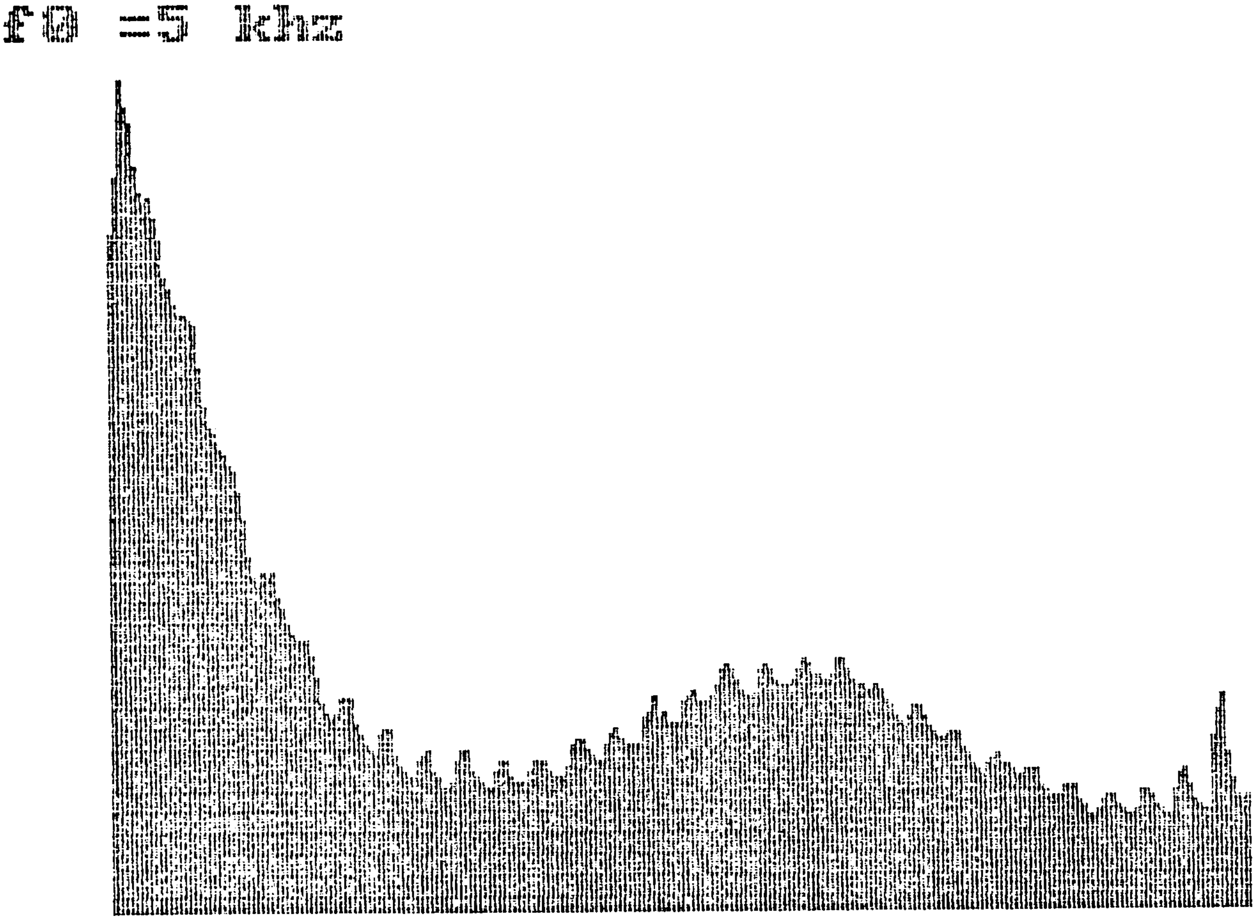

Figure A(43) x = 5" y = 0.875" Before Filter

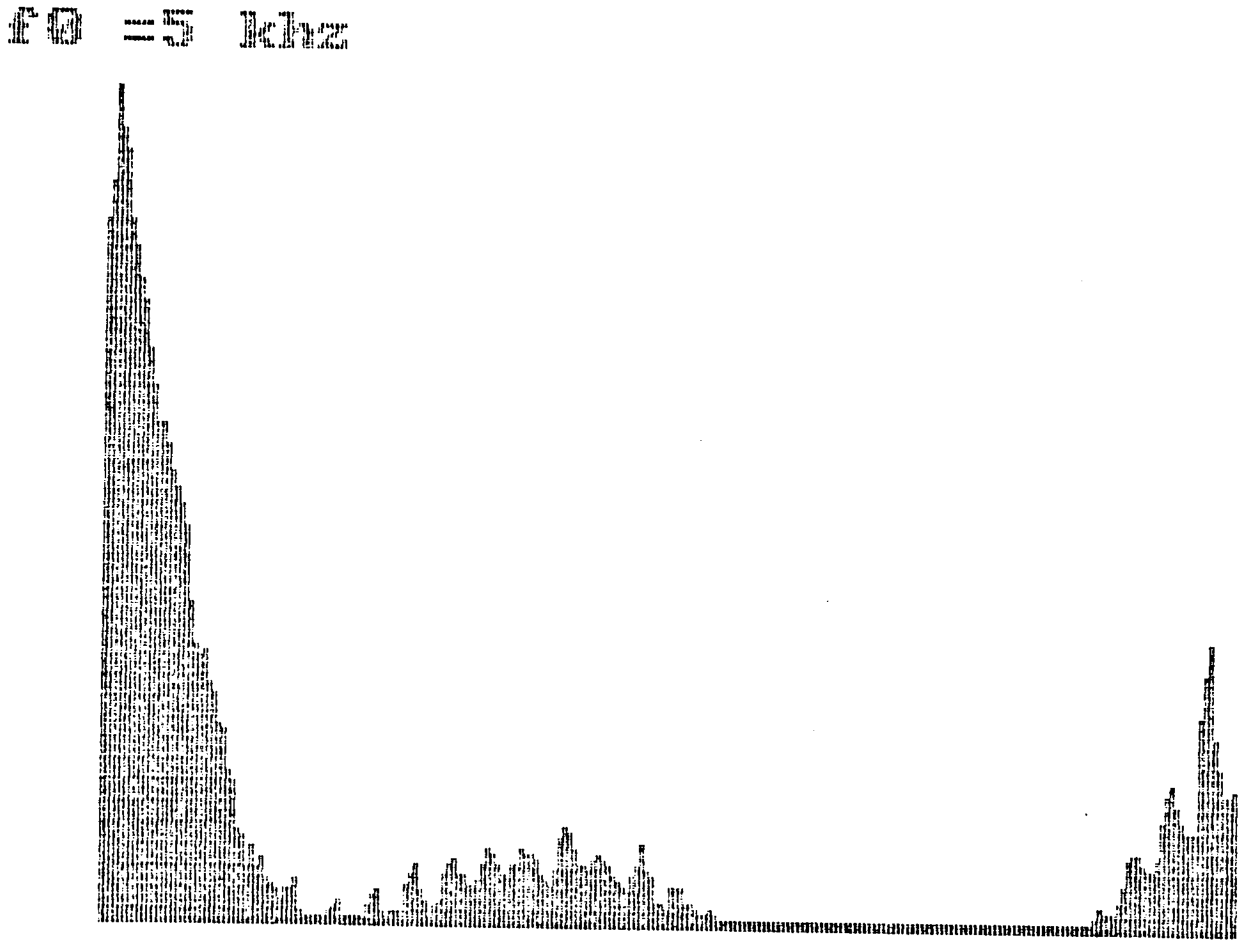

Figure A(44) x = 5" y = 0.875" After Filter

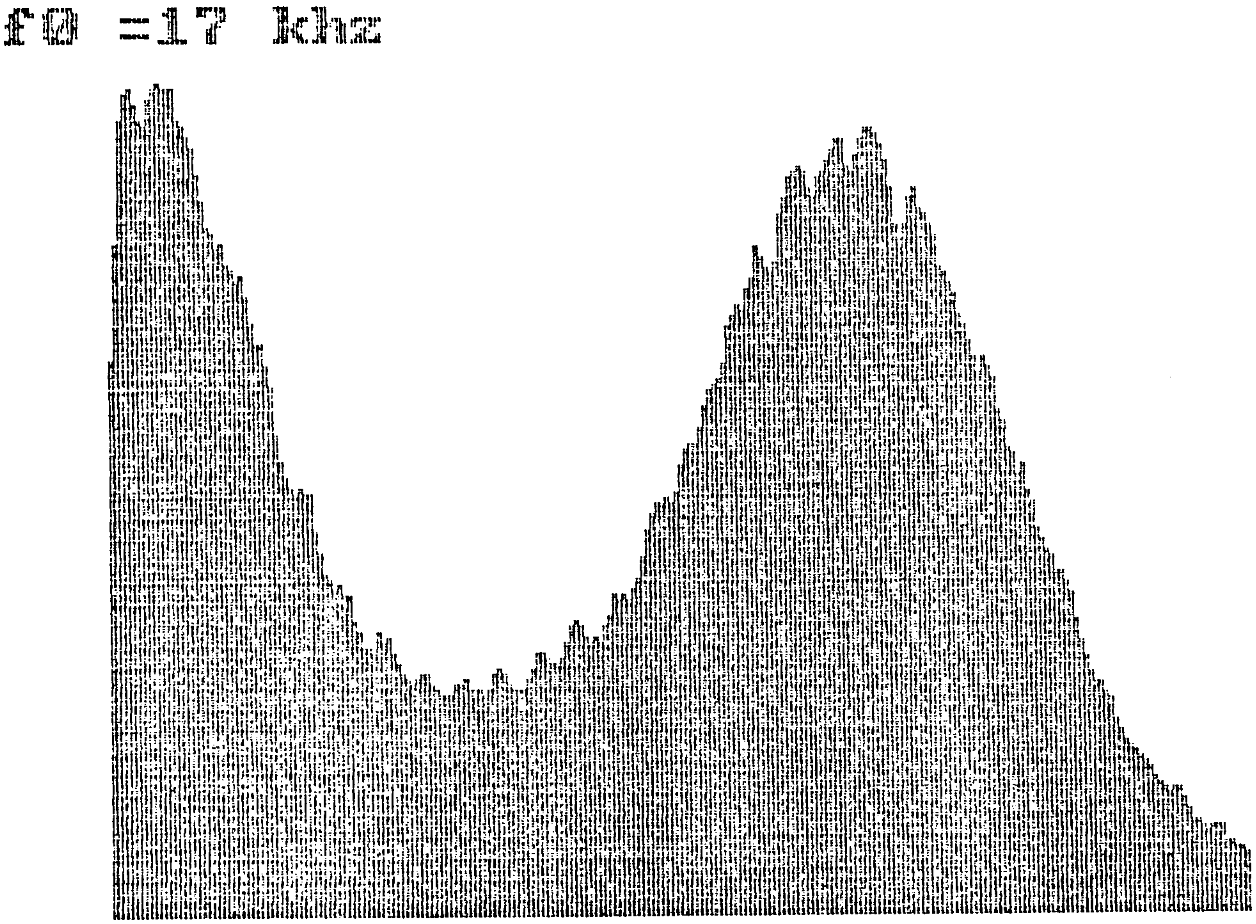

Figure A(45) x = 5" y = 0.75" Before Filter

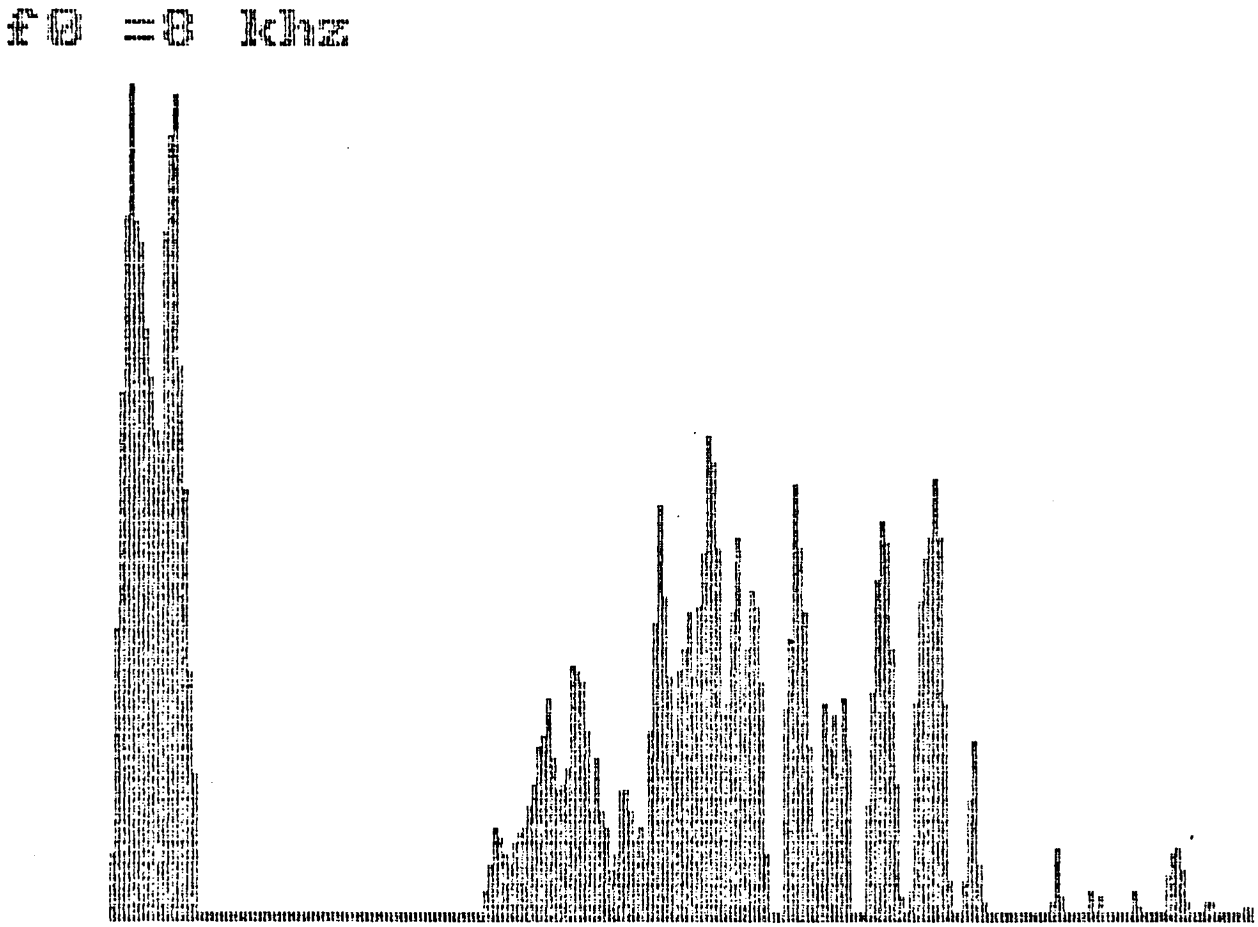

Figure A(46) x = 5" y = 0.75" After Filter

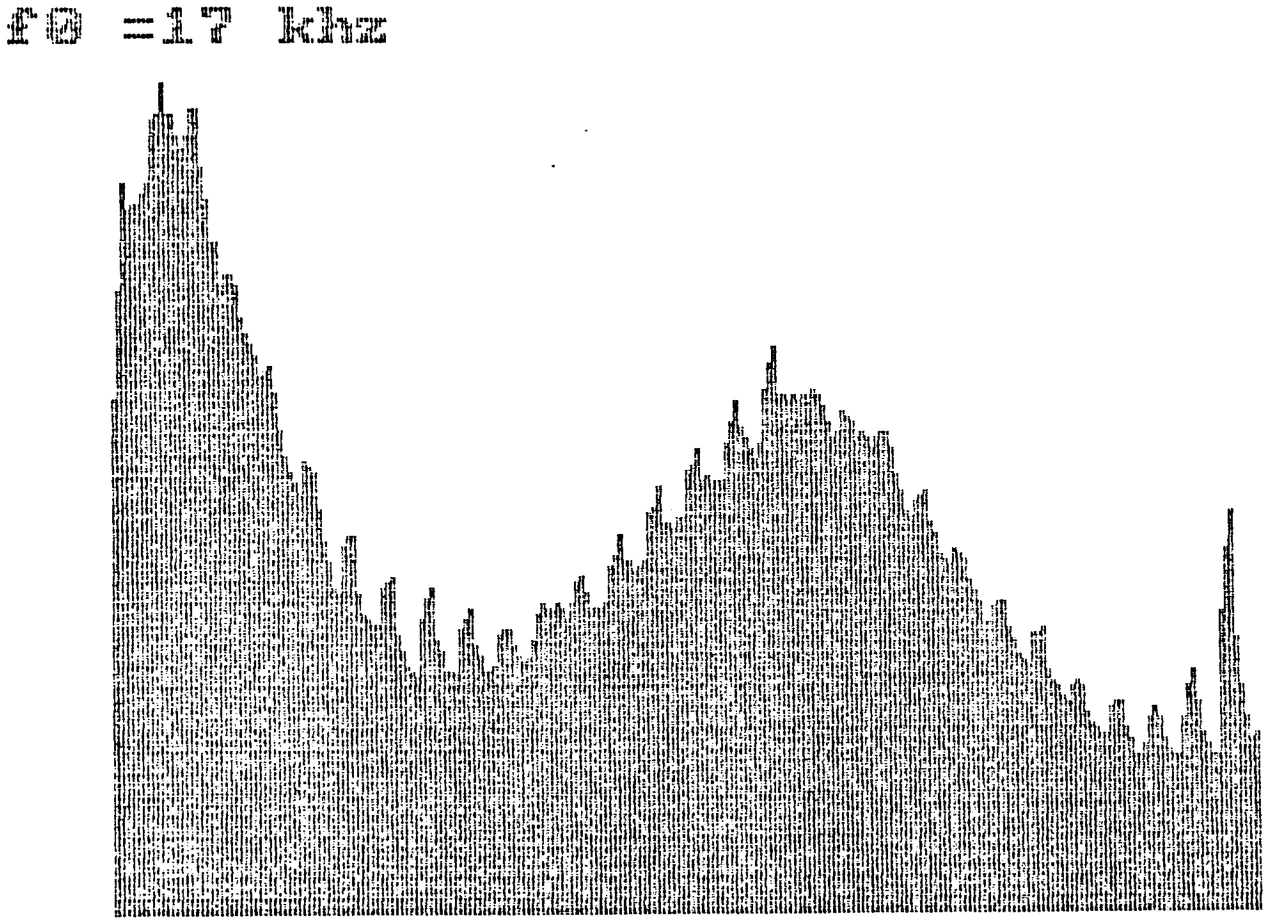

Figure A(47) x = 5" y = 0.675" Before Filter

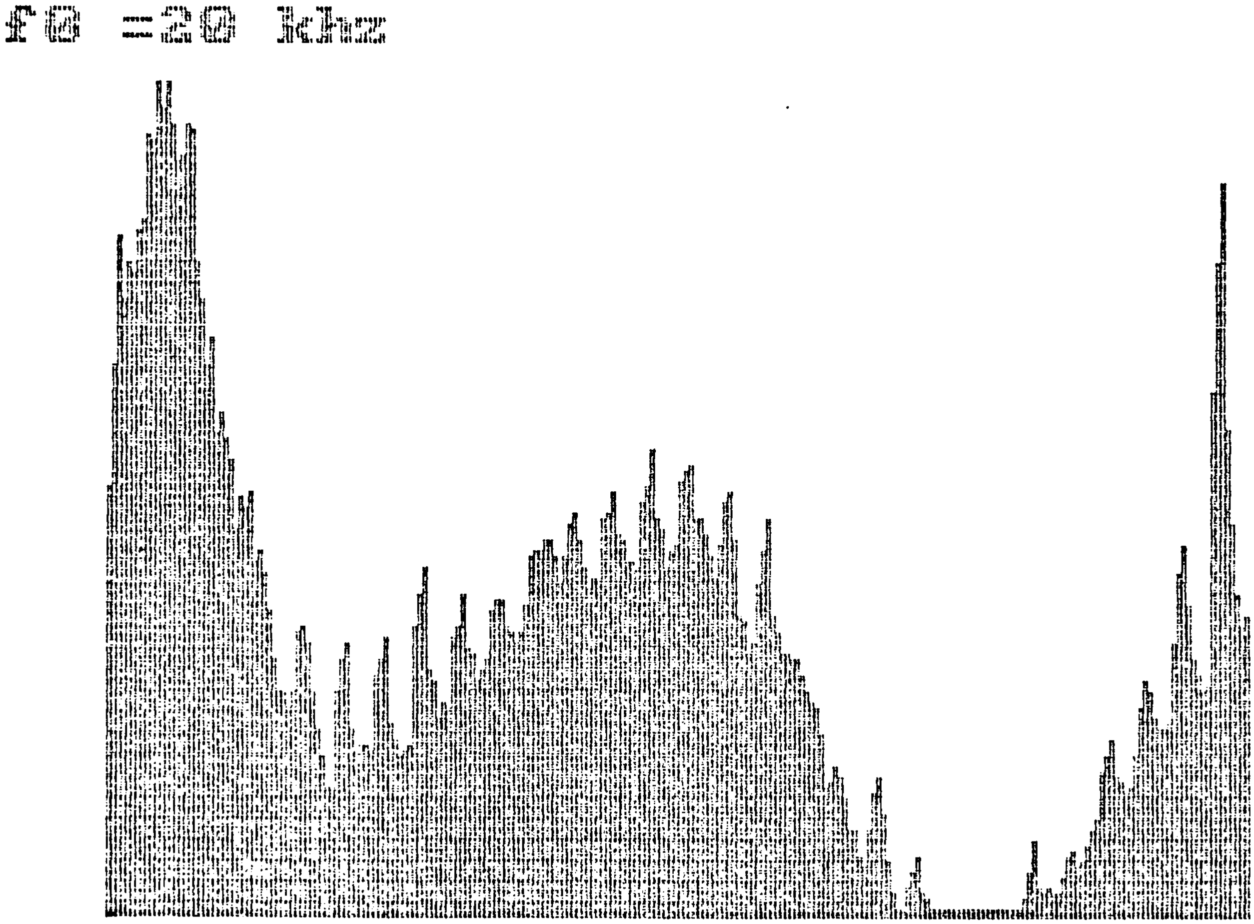

Figure A(48) x = 5" y = 0.675" After Filter

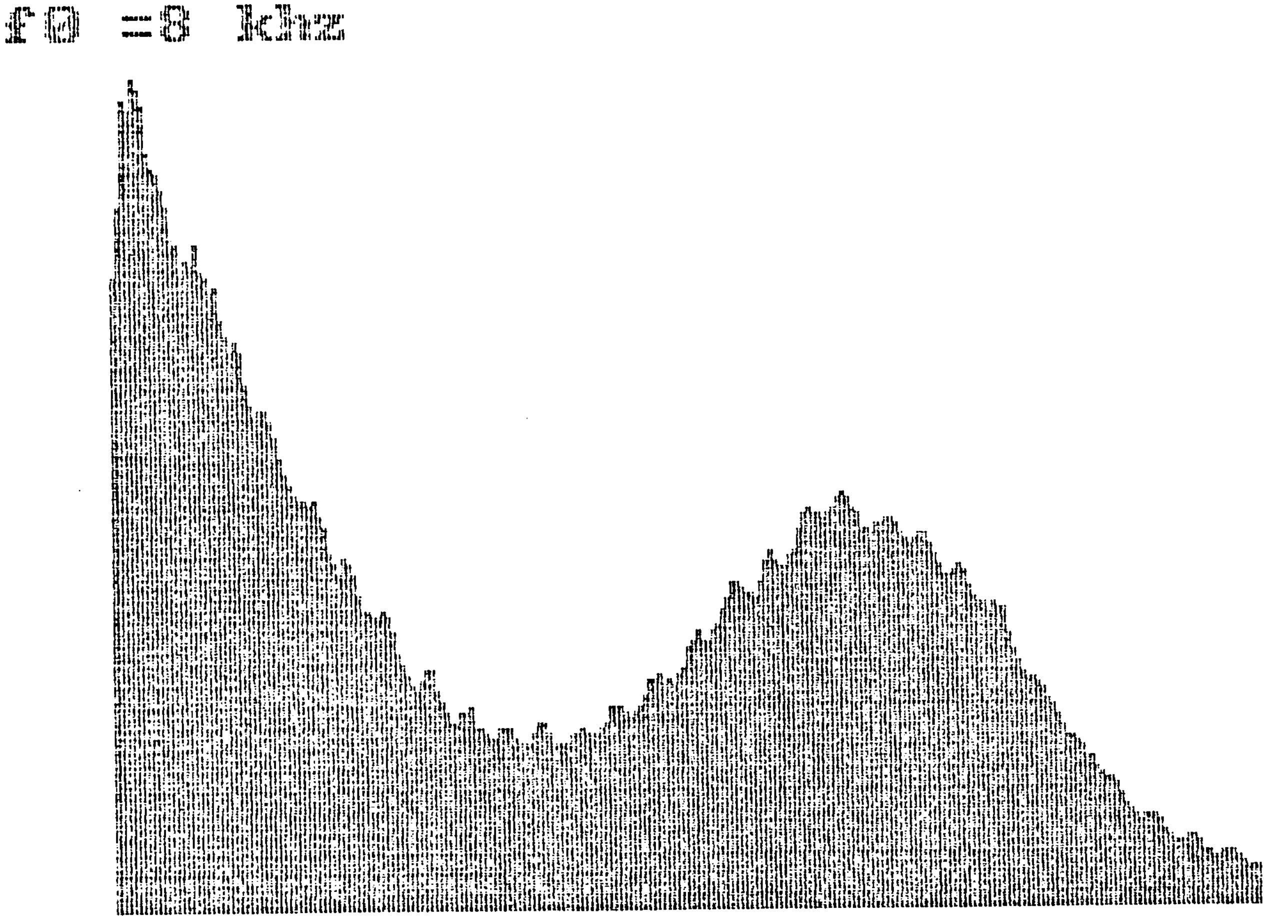

Figure A(49) x = 5" y = 0.5" Before Filter

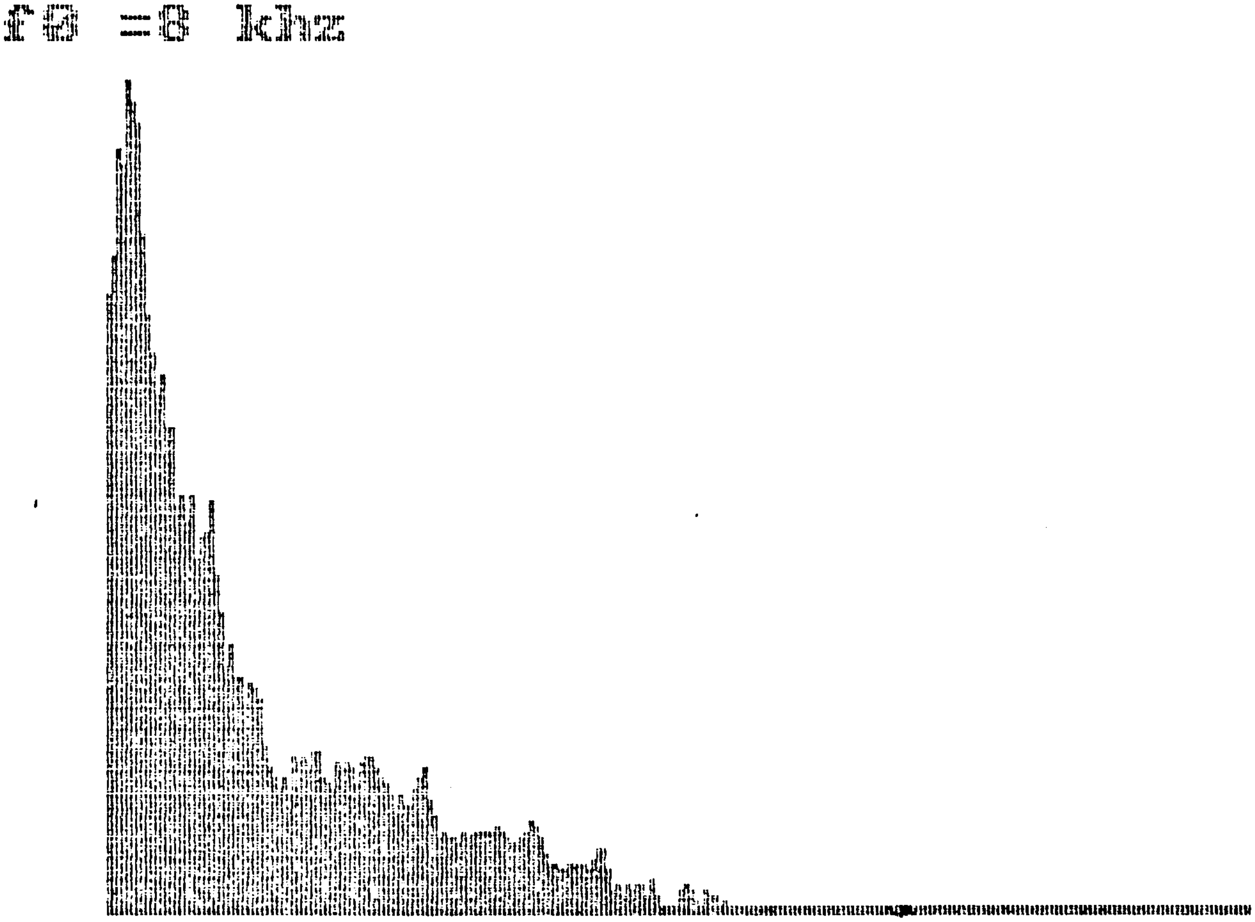

Figure A(50) x = 5" y = 0.5" After Filter

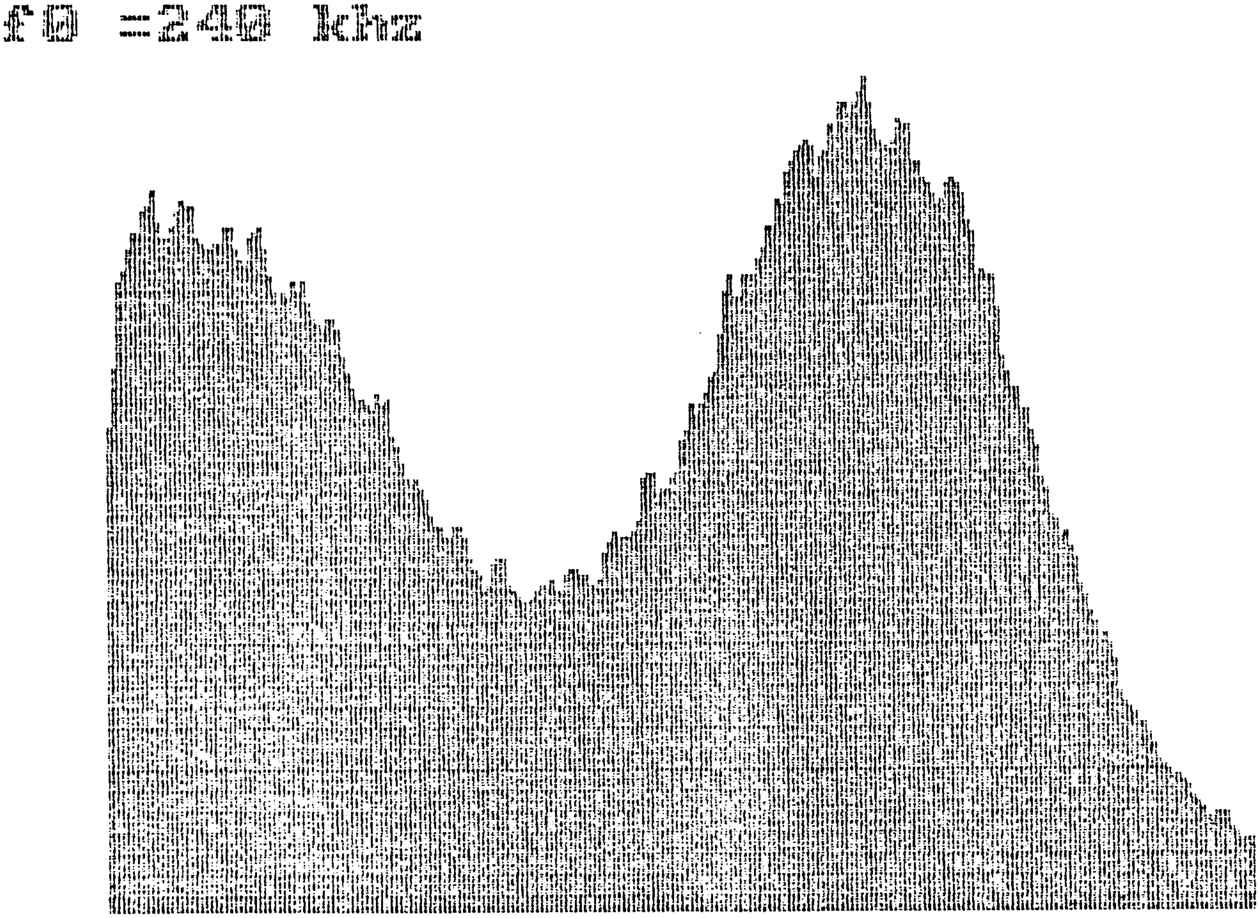

Figure A(51) x = 5" y = 0.375" Before Filter

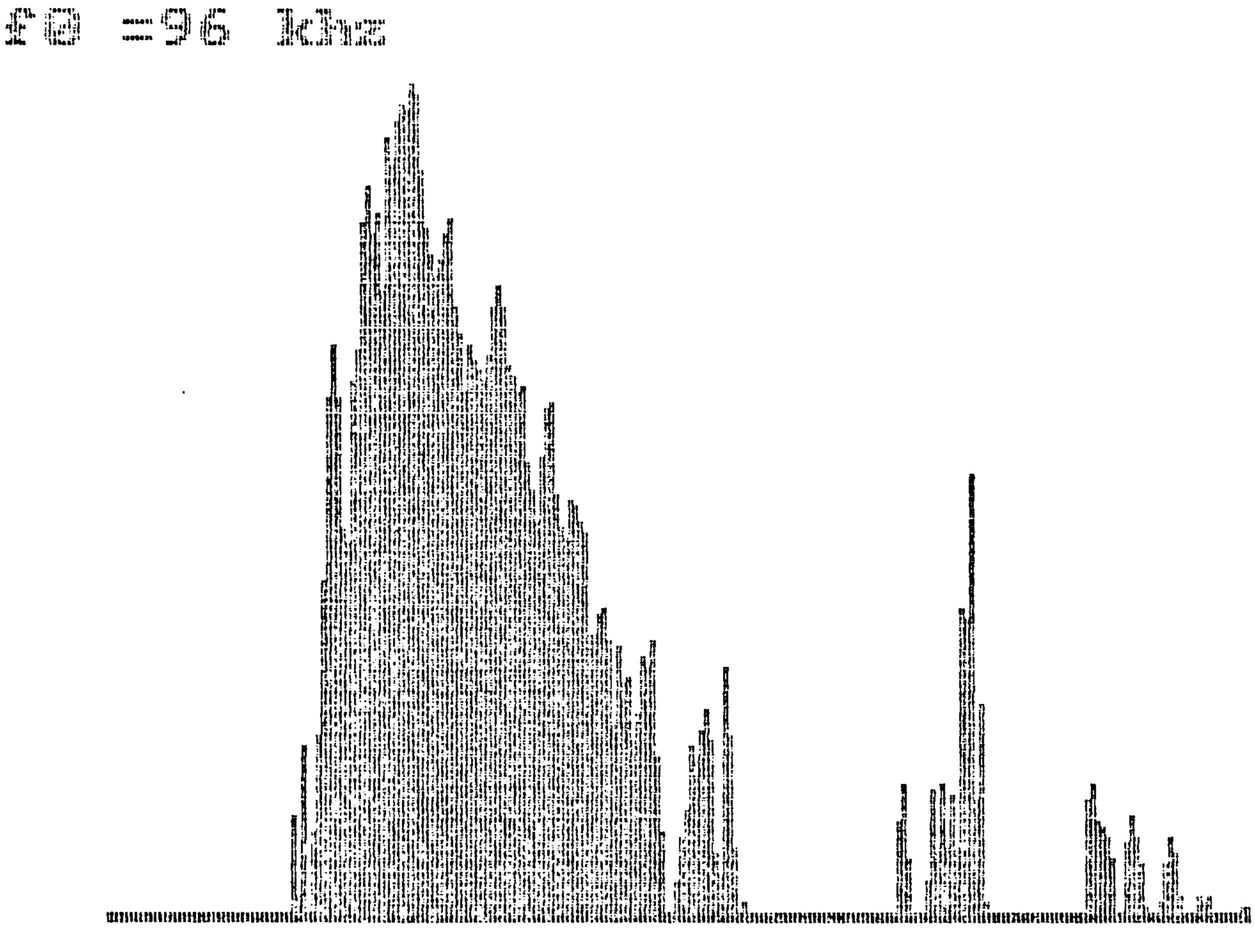

Figure A(52) x = 5" y = 0.375" After Filter

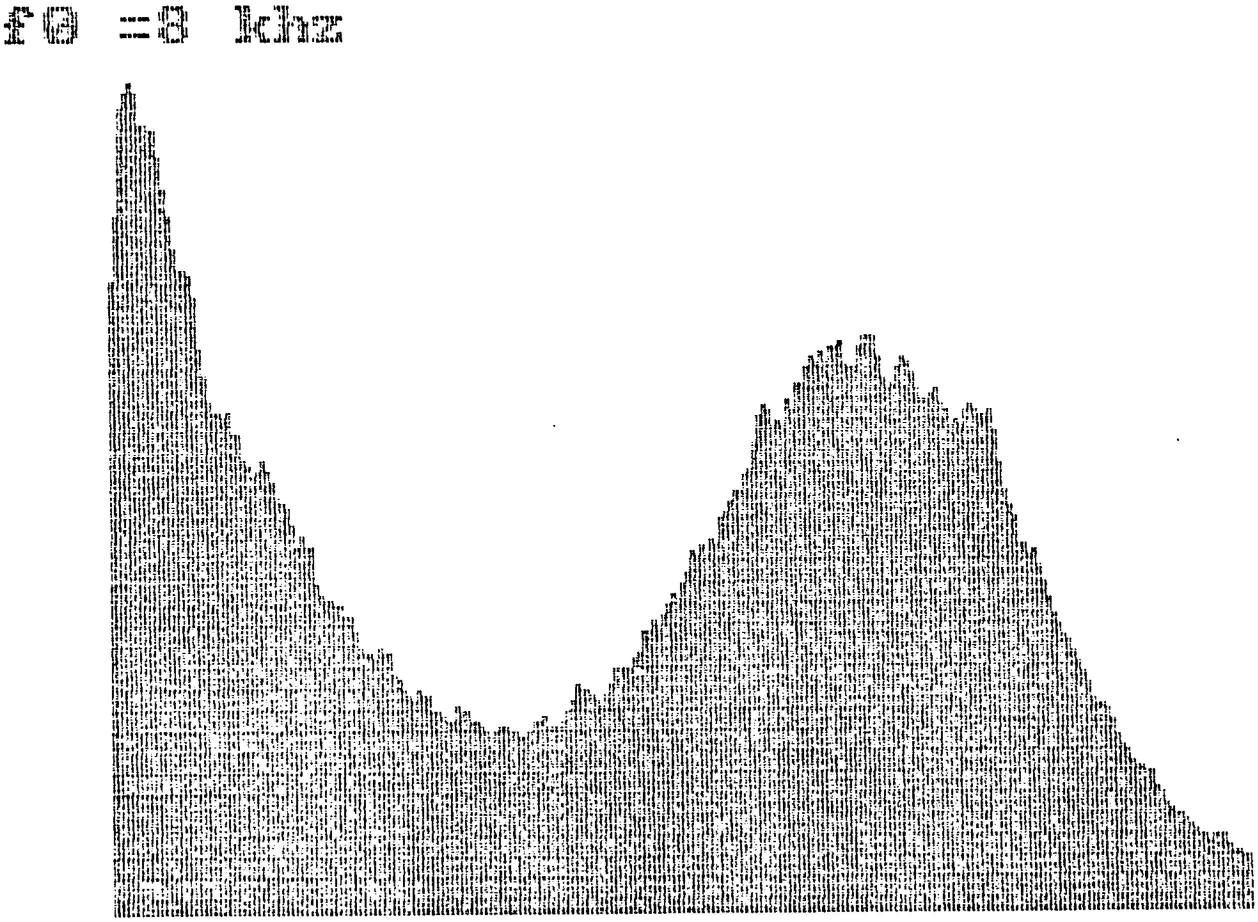

Figure A(53) x = 5" y = 0.25" Before Filter

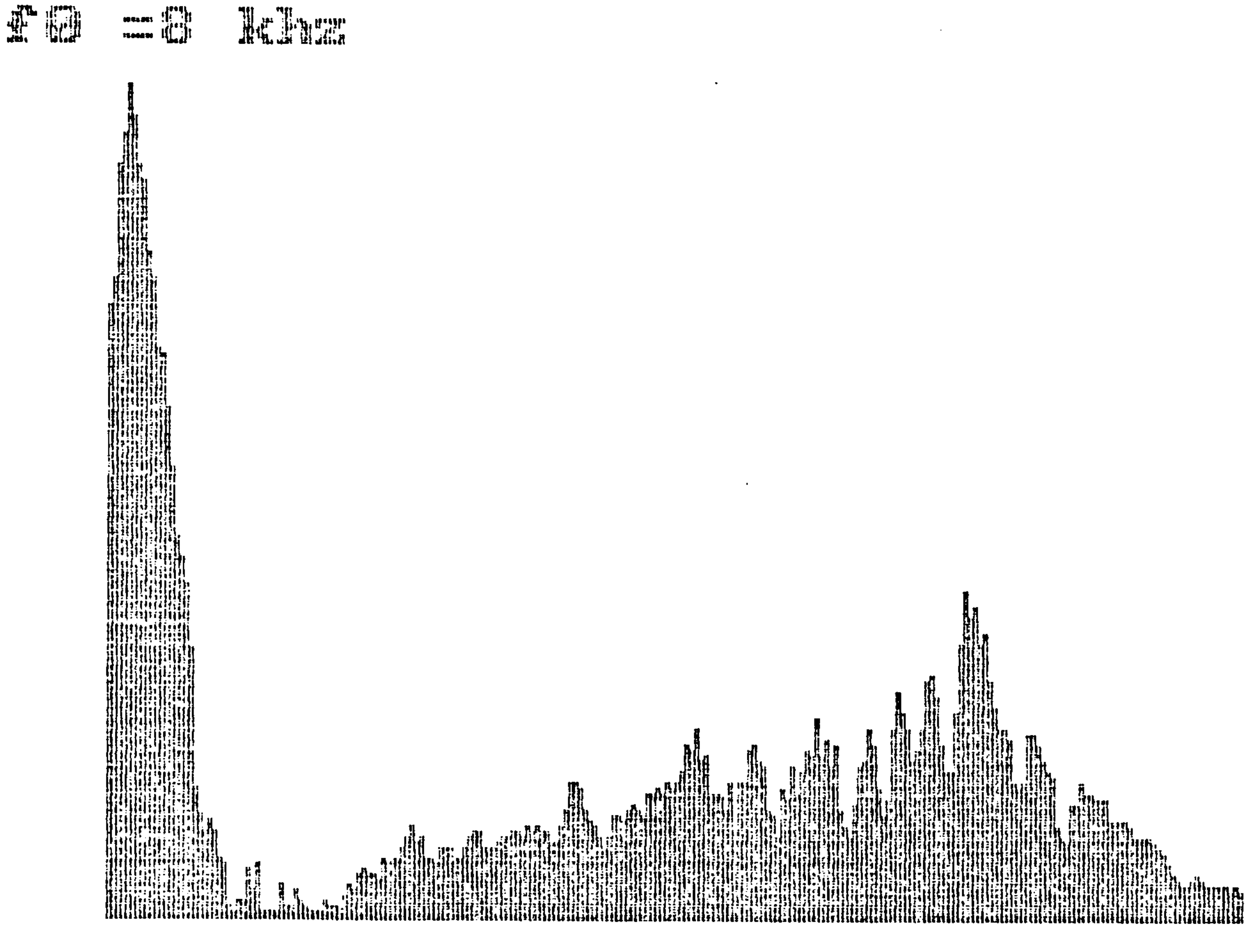

Figure A(54) x = 5" y = 0.25" After Filter

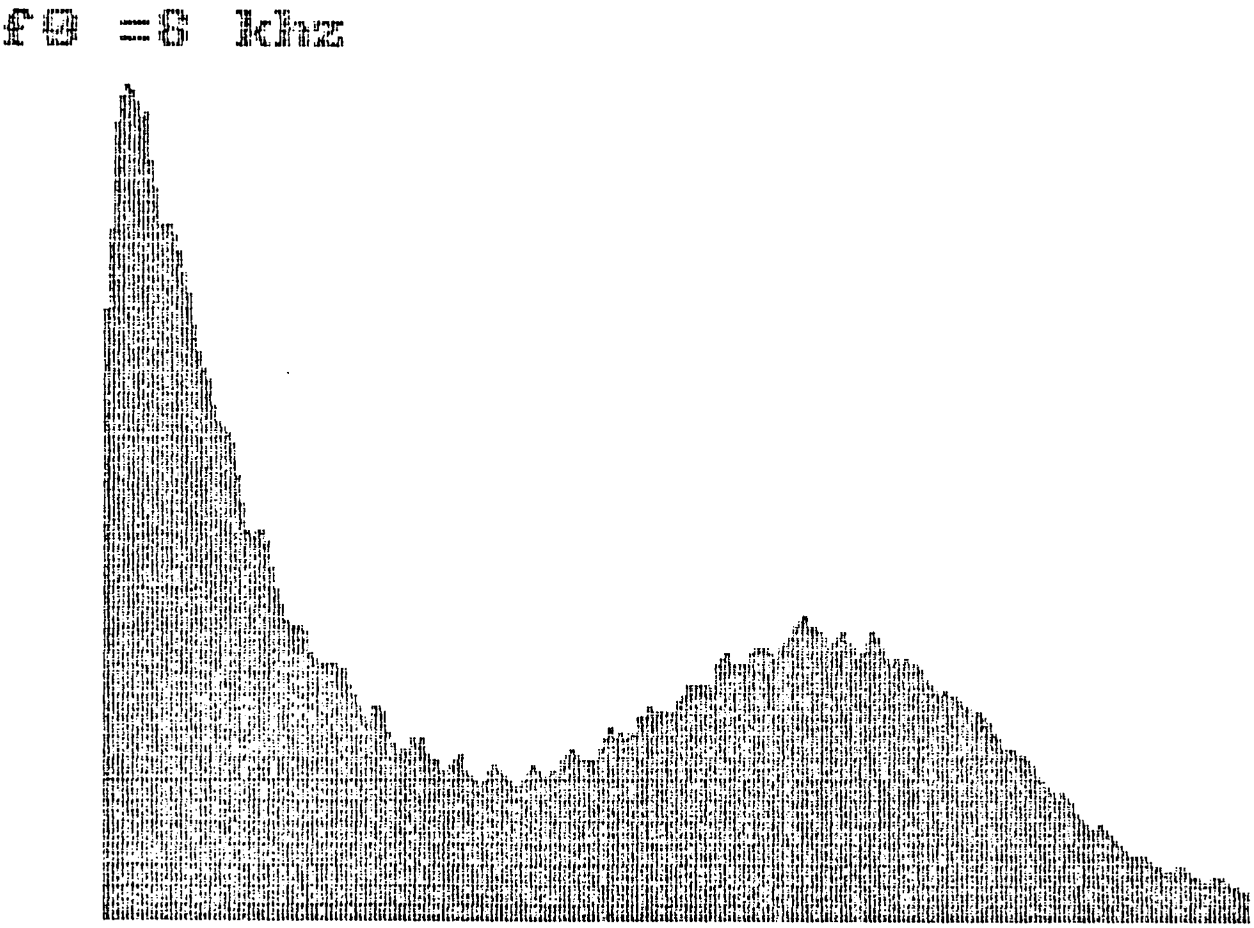

Figure A(55) x = 5" y = 0.125"Before Filter

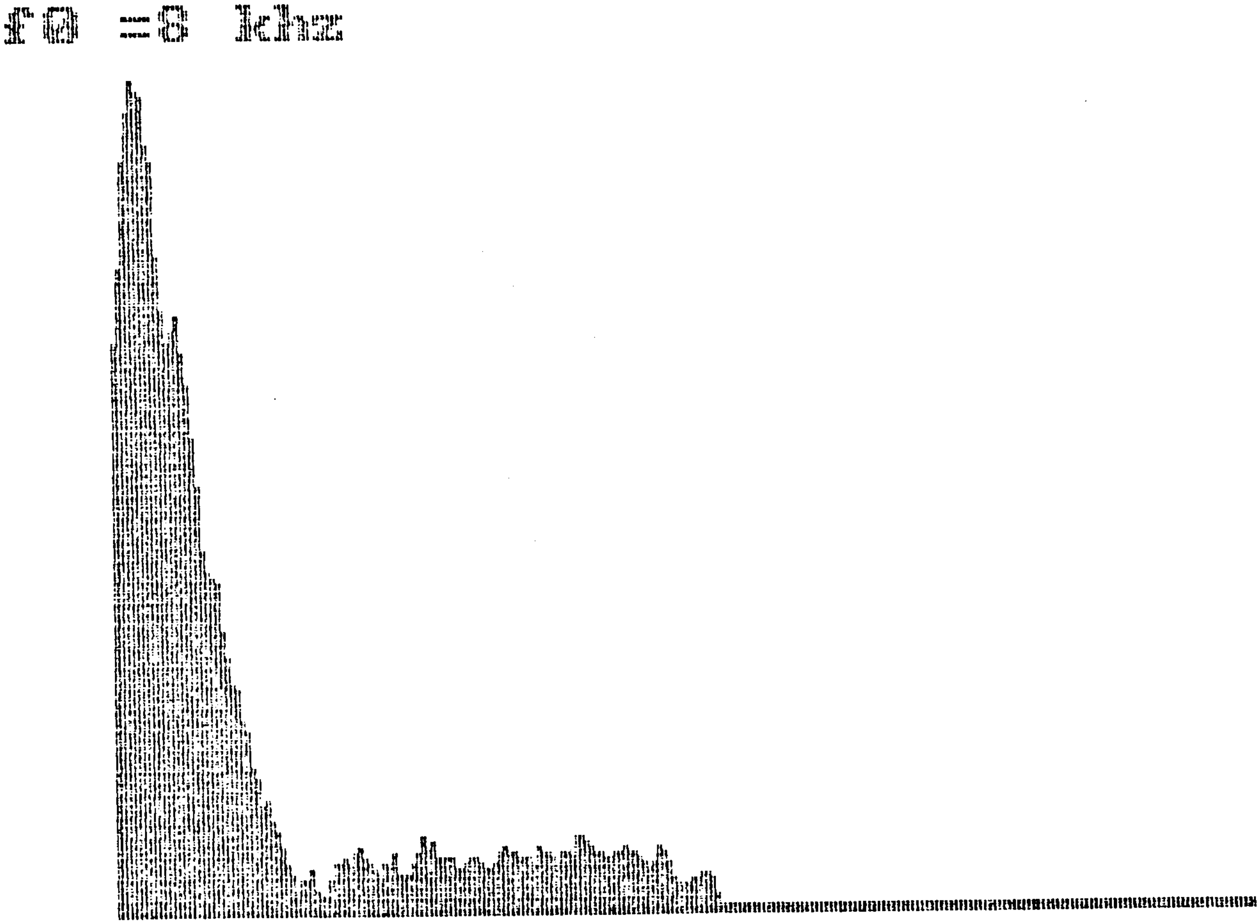

Figure A(56) x = 5" y = 0.125" After Filter

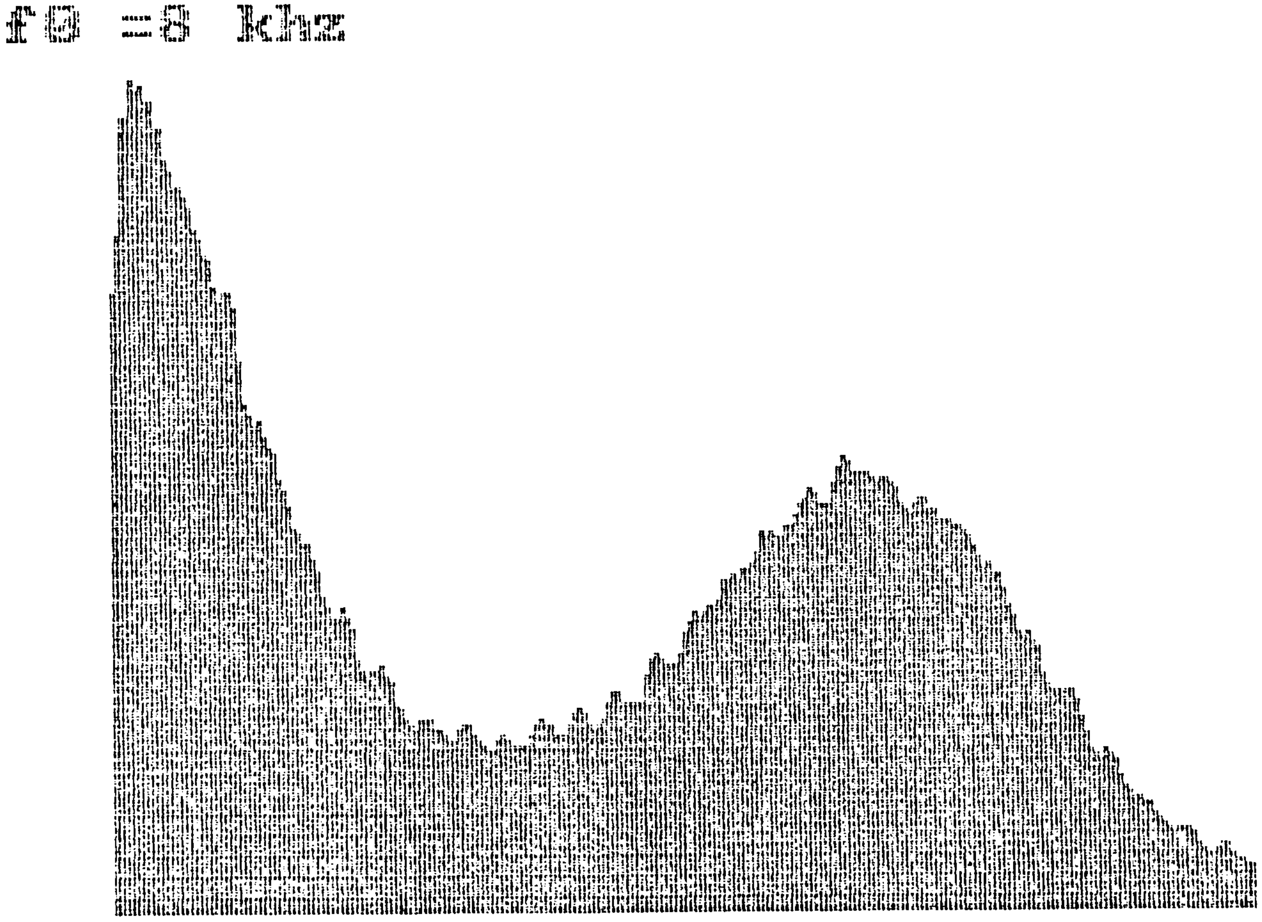

Figure A(57) x = 5" y = 0.0" Before Filter

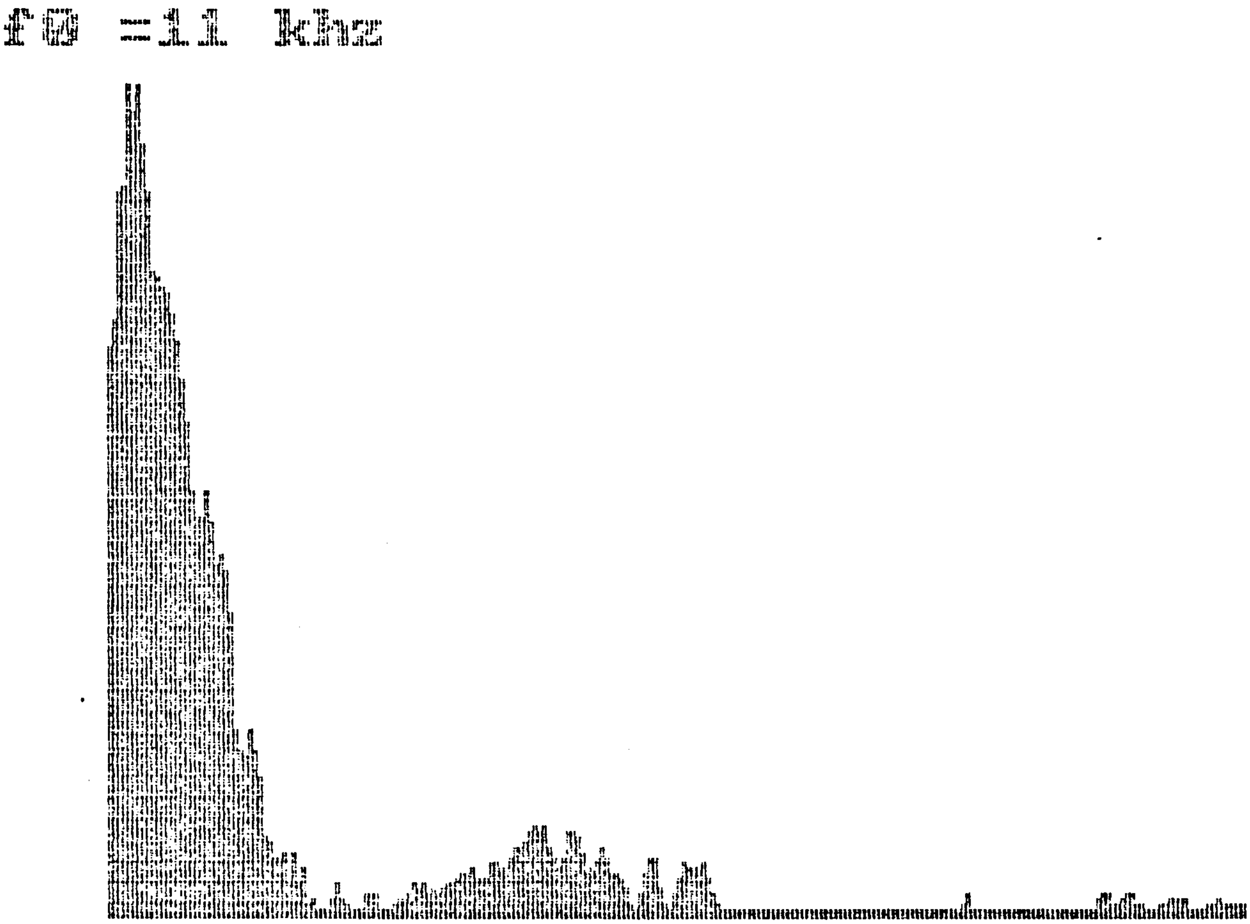

Figure A(58) x = 5" y = 0.0" After Filter

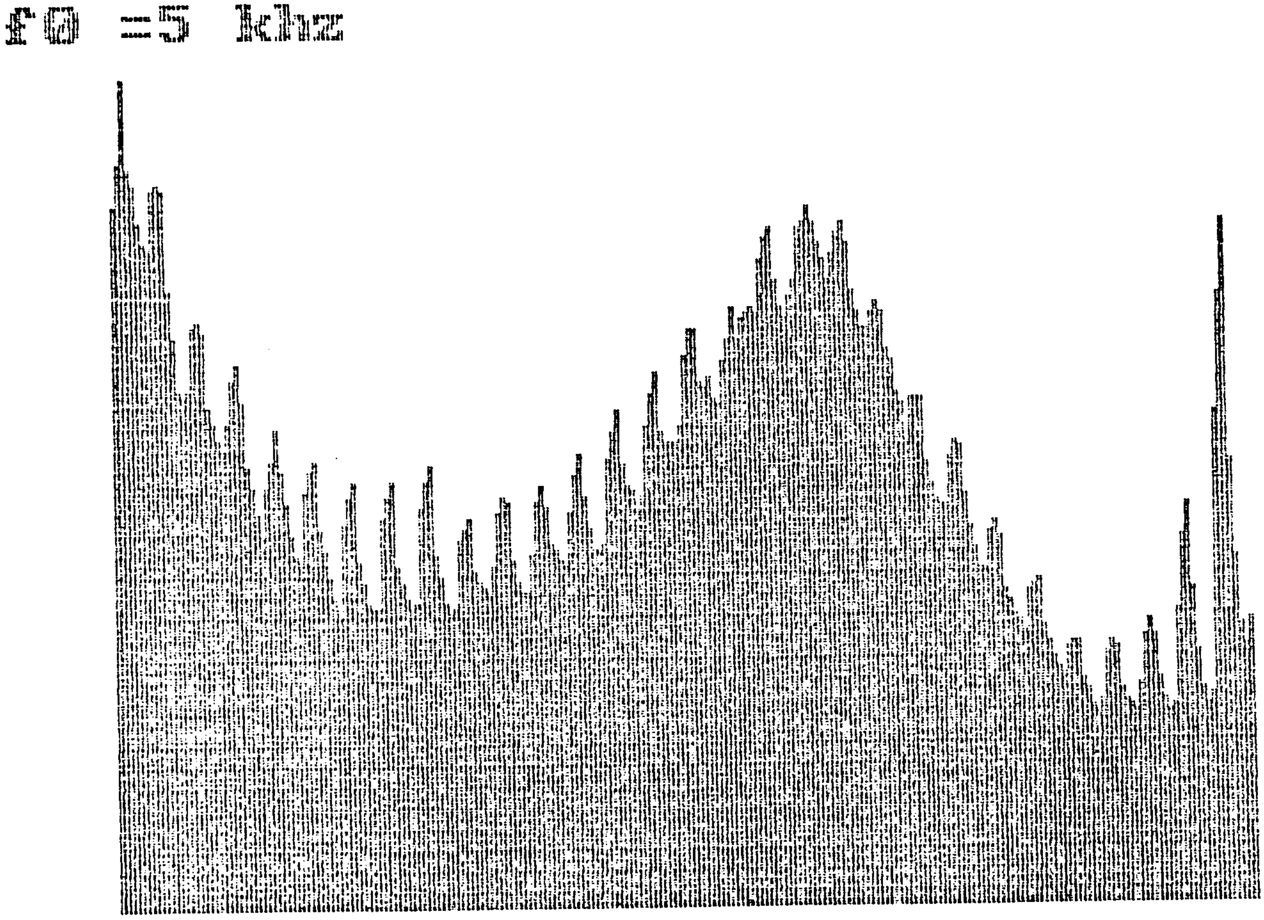

Figure A(59) x = 4" y = 1.0" Filter

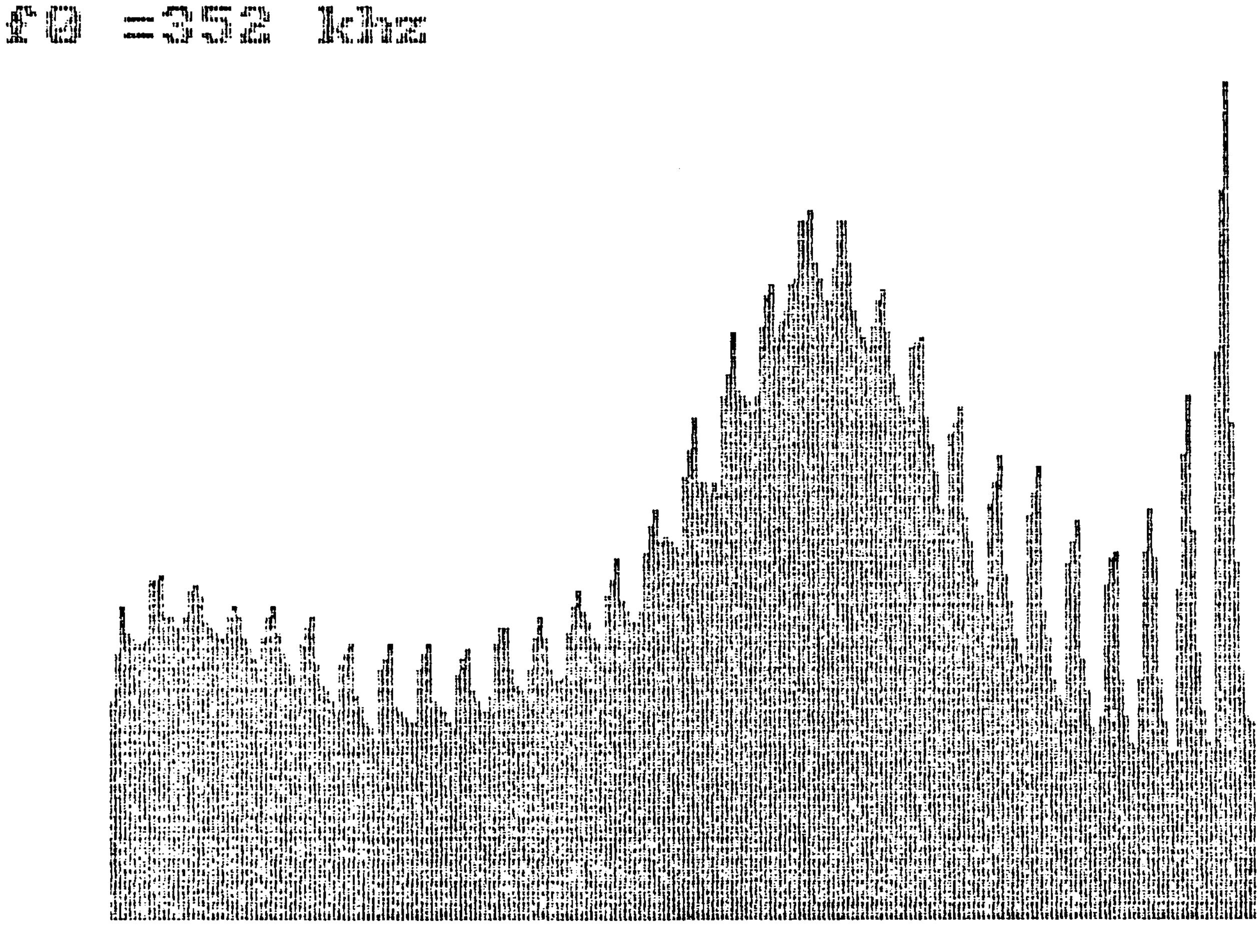

Figure A(60) x = 4" y = 0.875" Before Filter

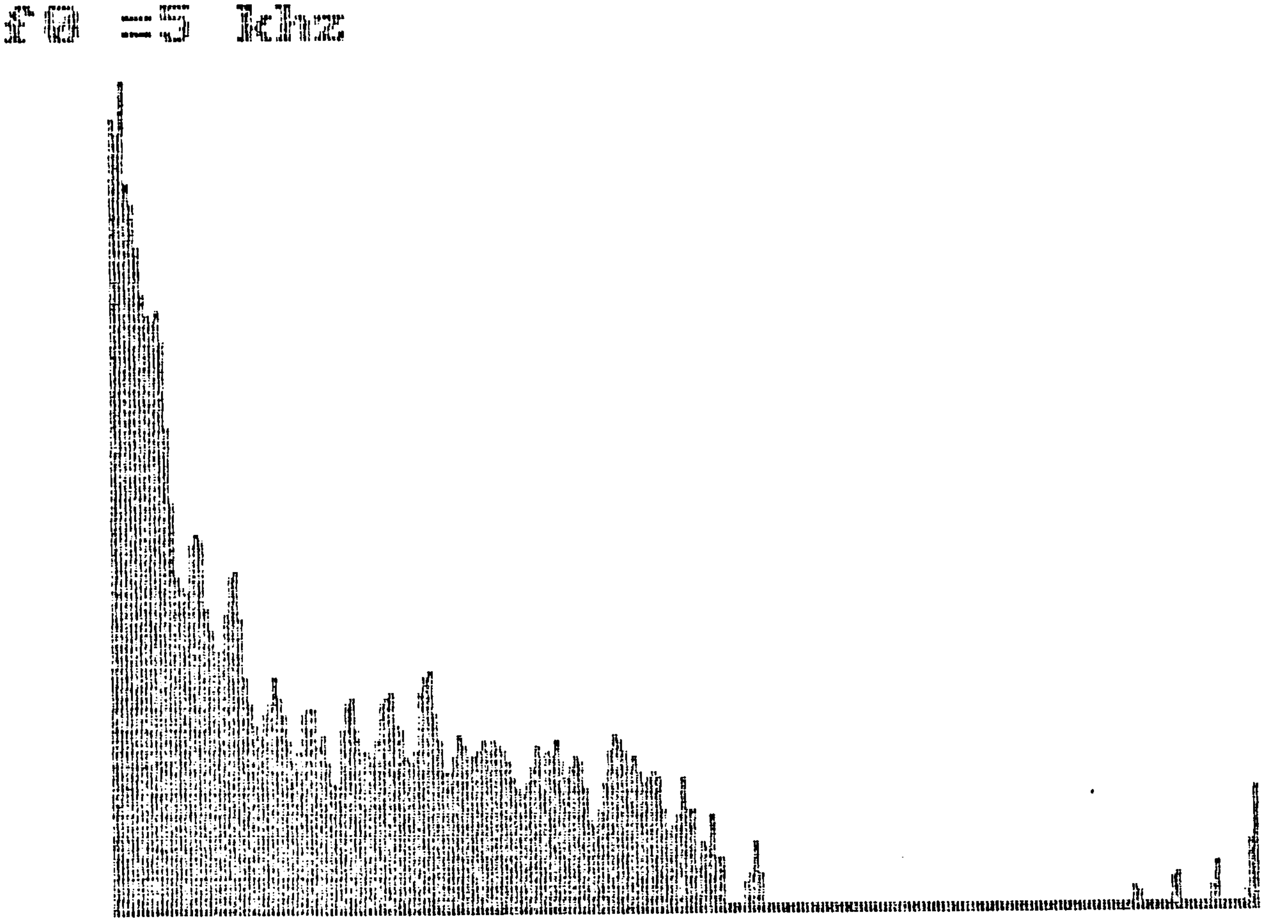

Figure A(61) x = 4" y = 0.875" After Filter

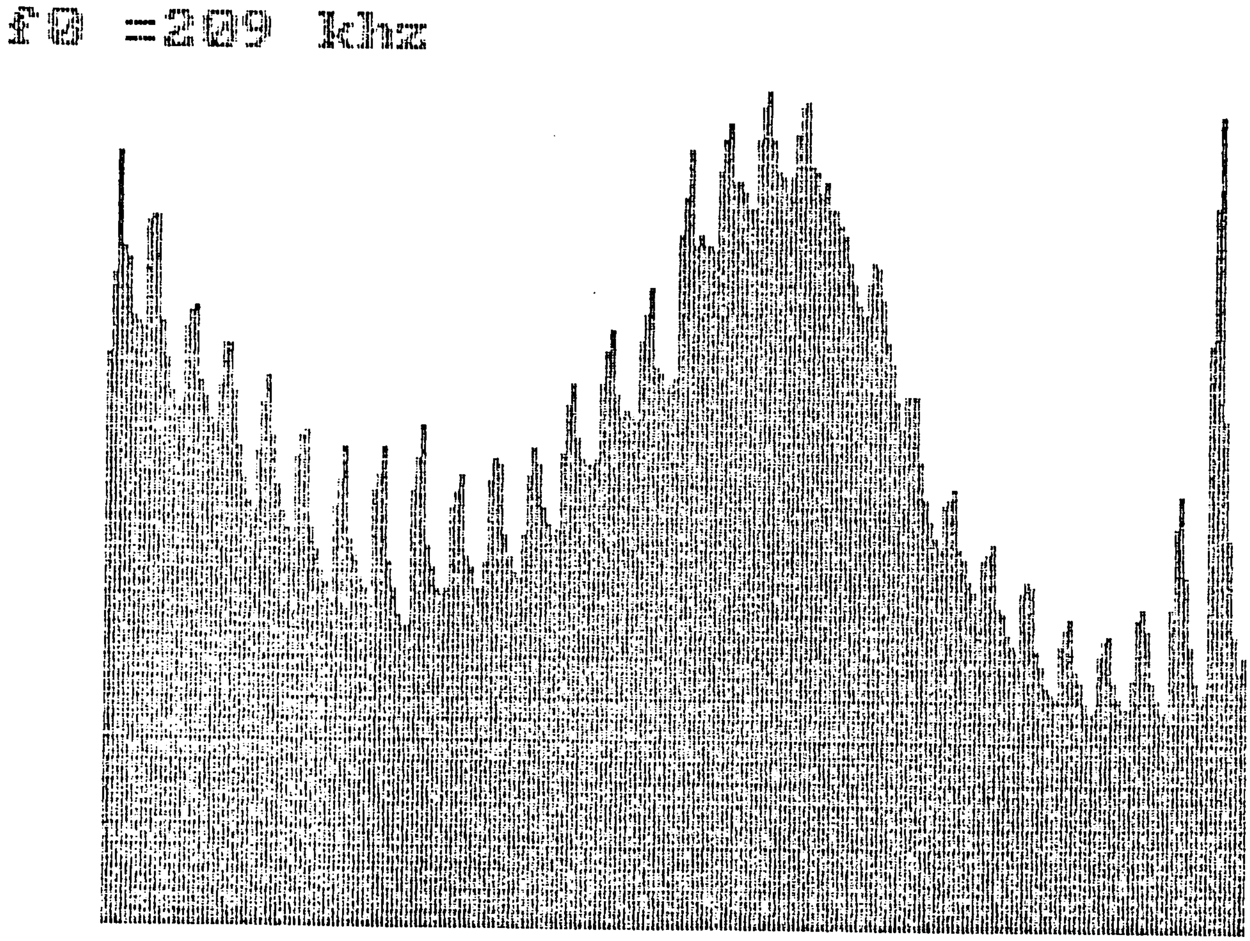

Figure A(62) x = 4" y = 0.75" Before Filter

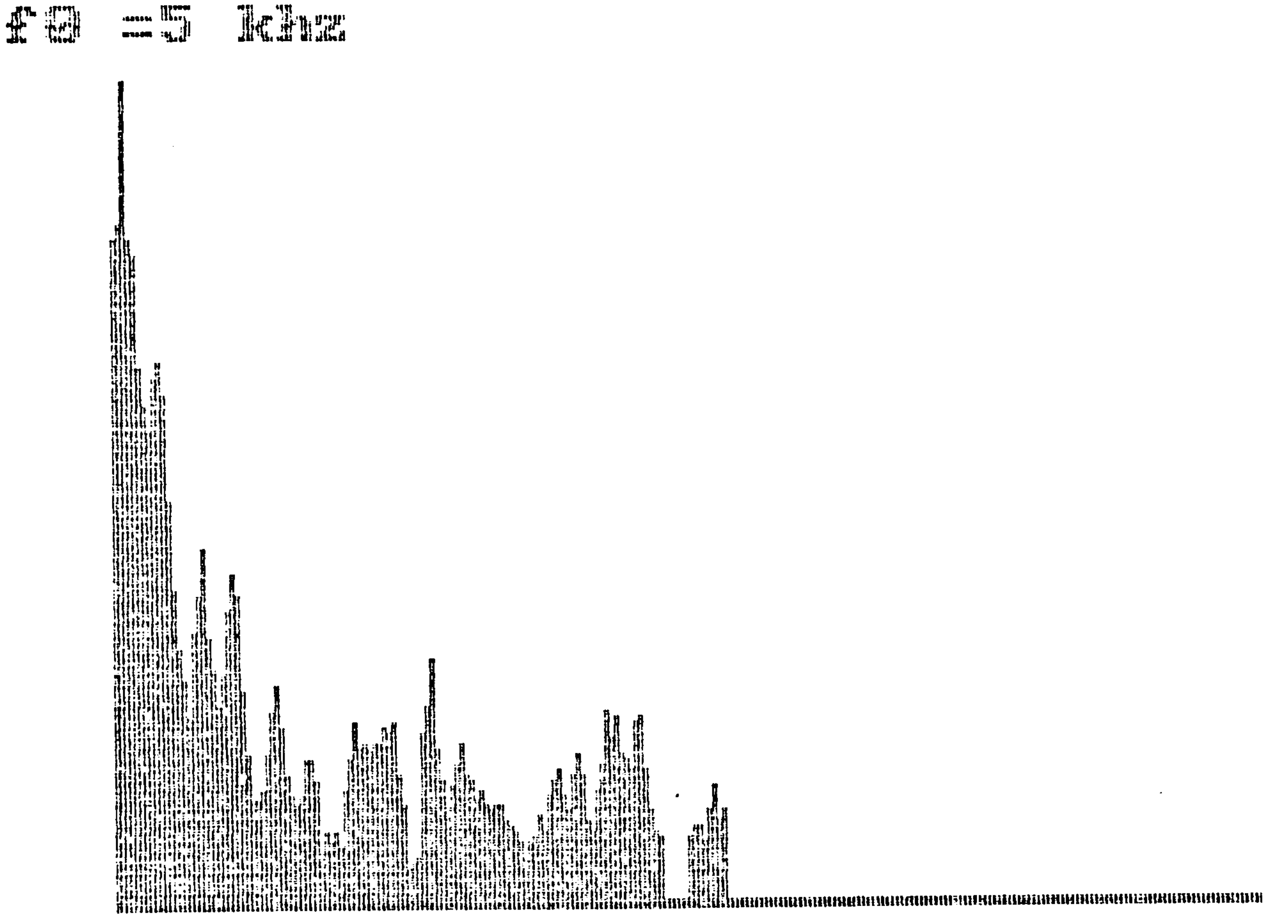

Figure A(63) x = 4" y = 0.75" After Filter

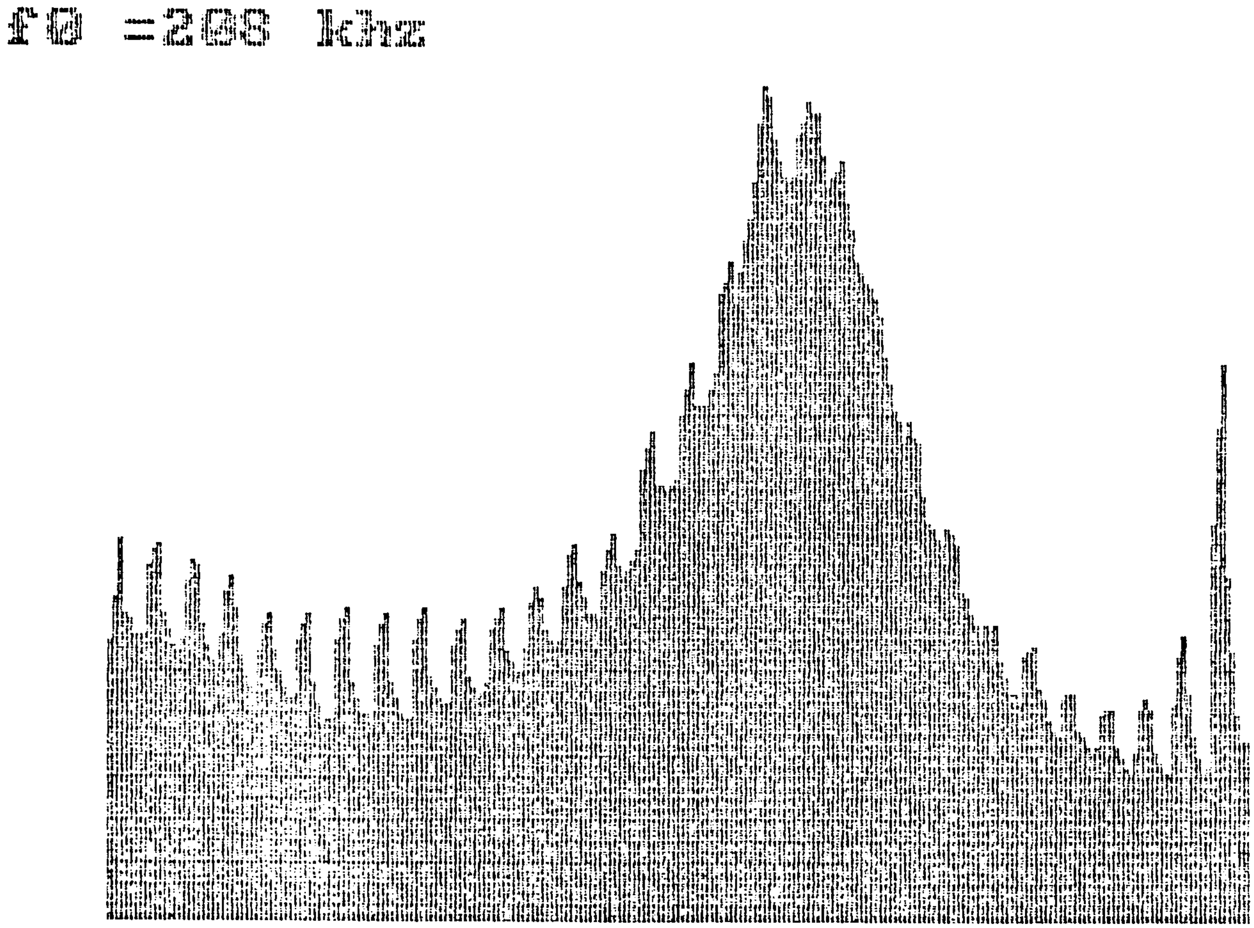

Figure A(64) x = 4" y = 0.625" Before Filter

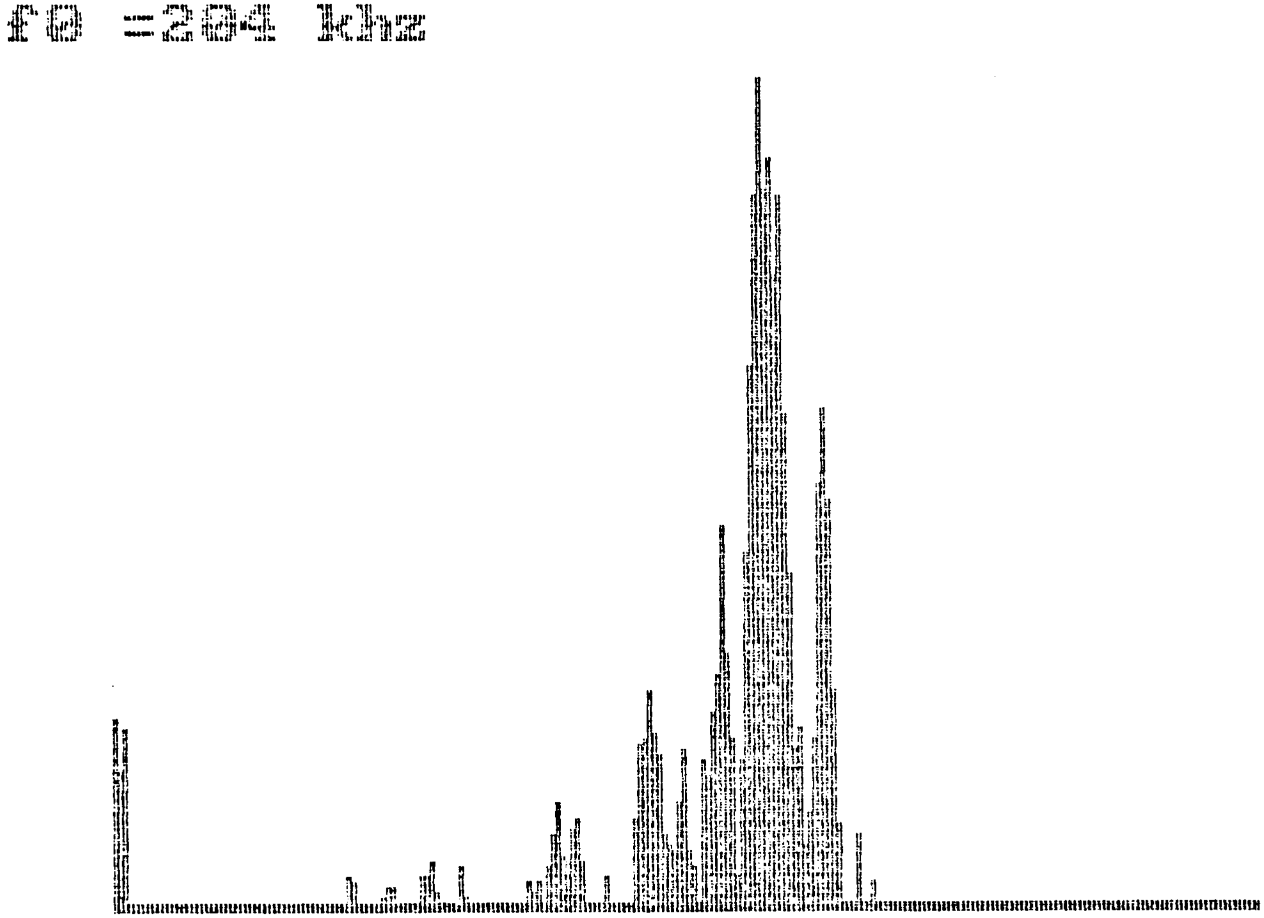

Figure A(65) x = 4" y = 0.625" After Filter

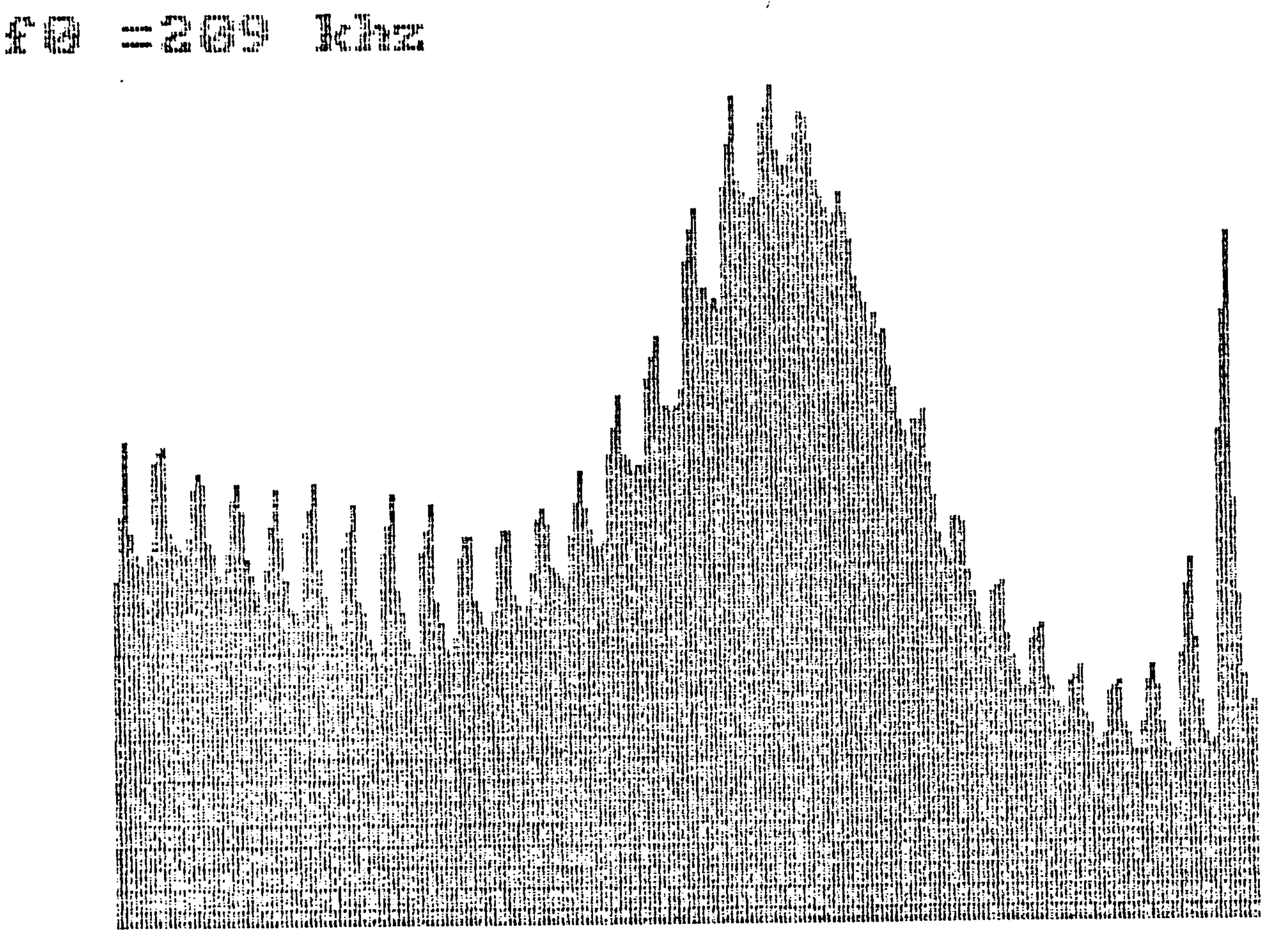

Figure A(66) x = 4" y = 0.5" Before Filter

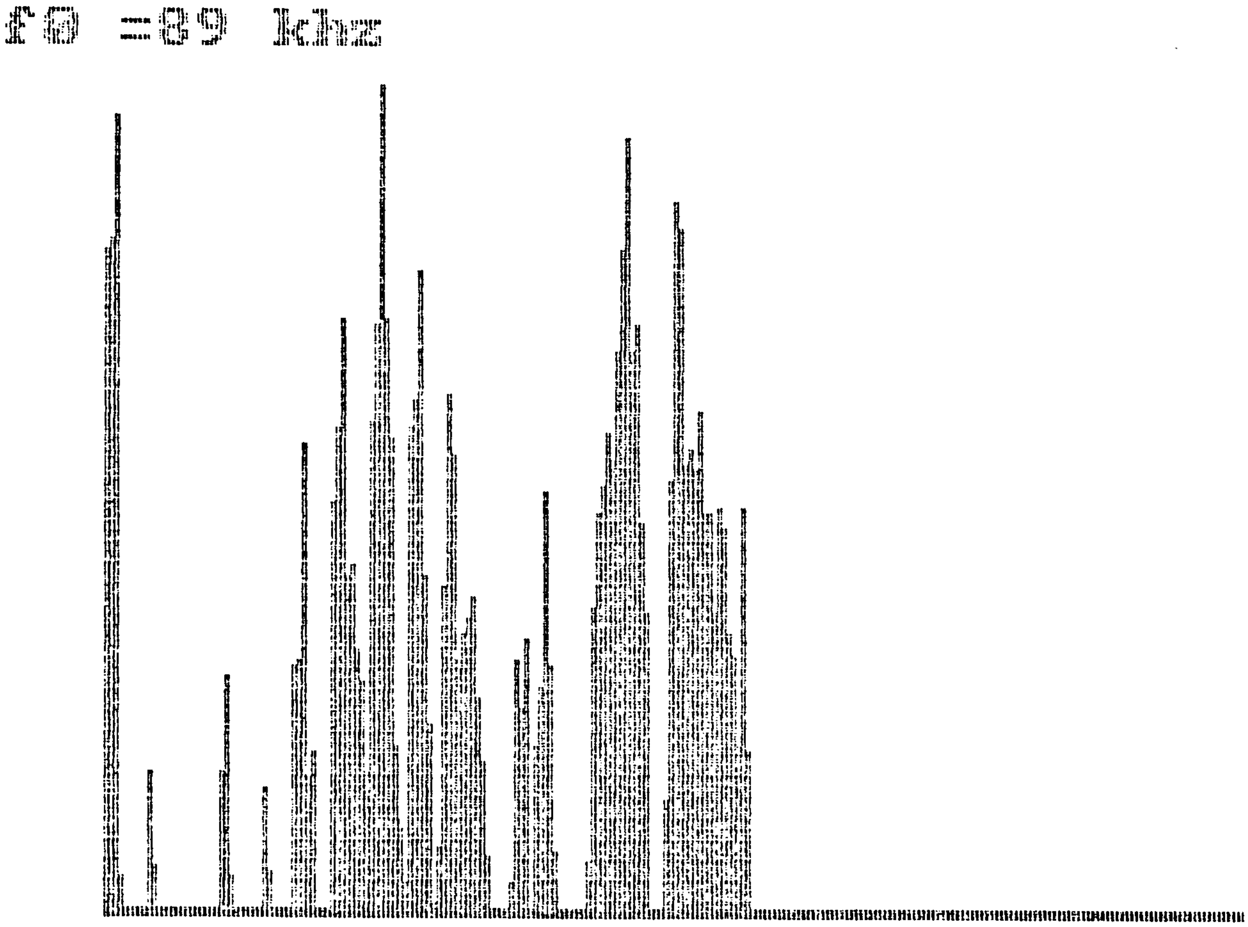

Figure A(67) x = 4" y = 0.5" After Filter

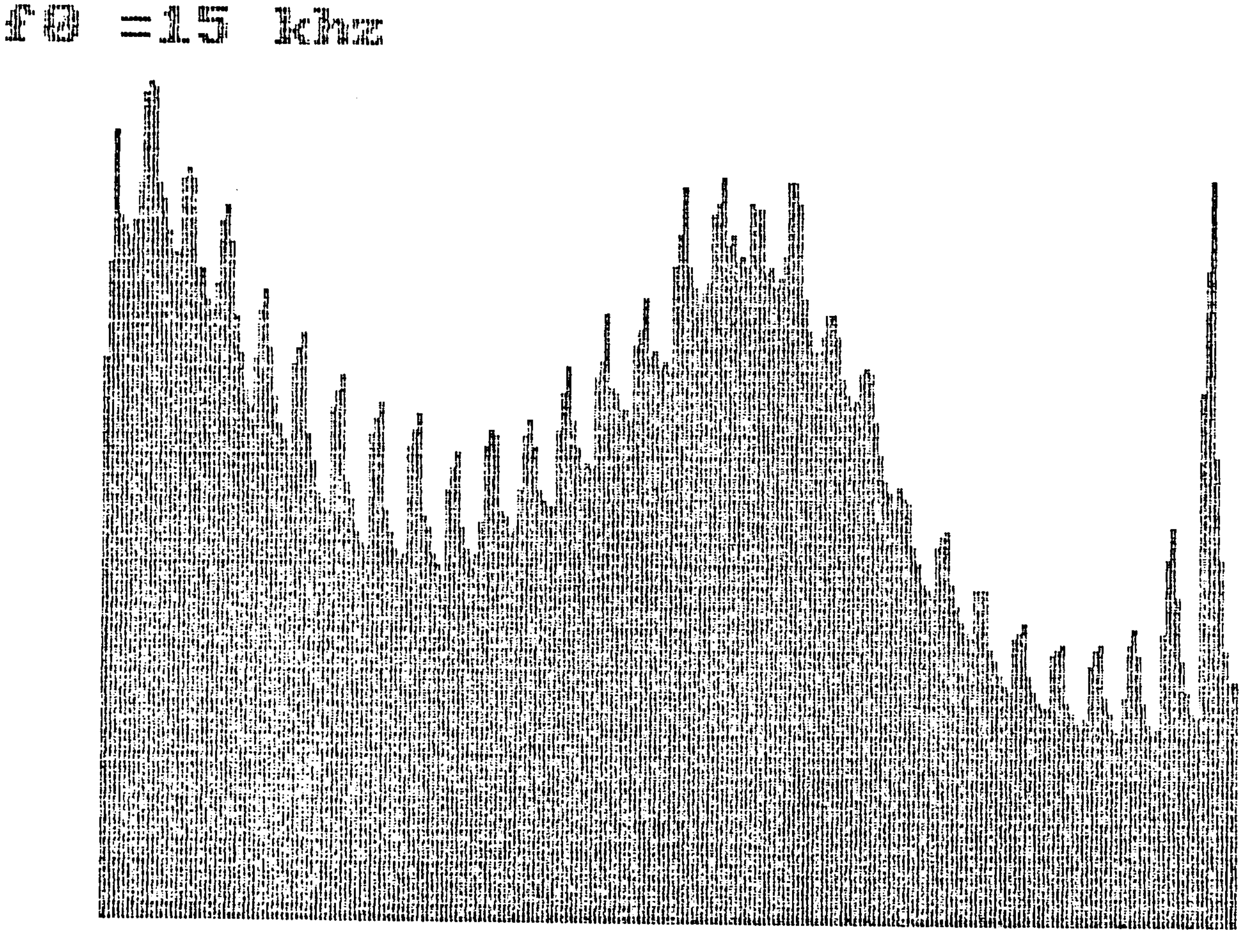

Figure A(68) x = 4" y = 0.375" Before Filter

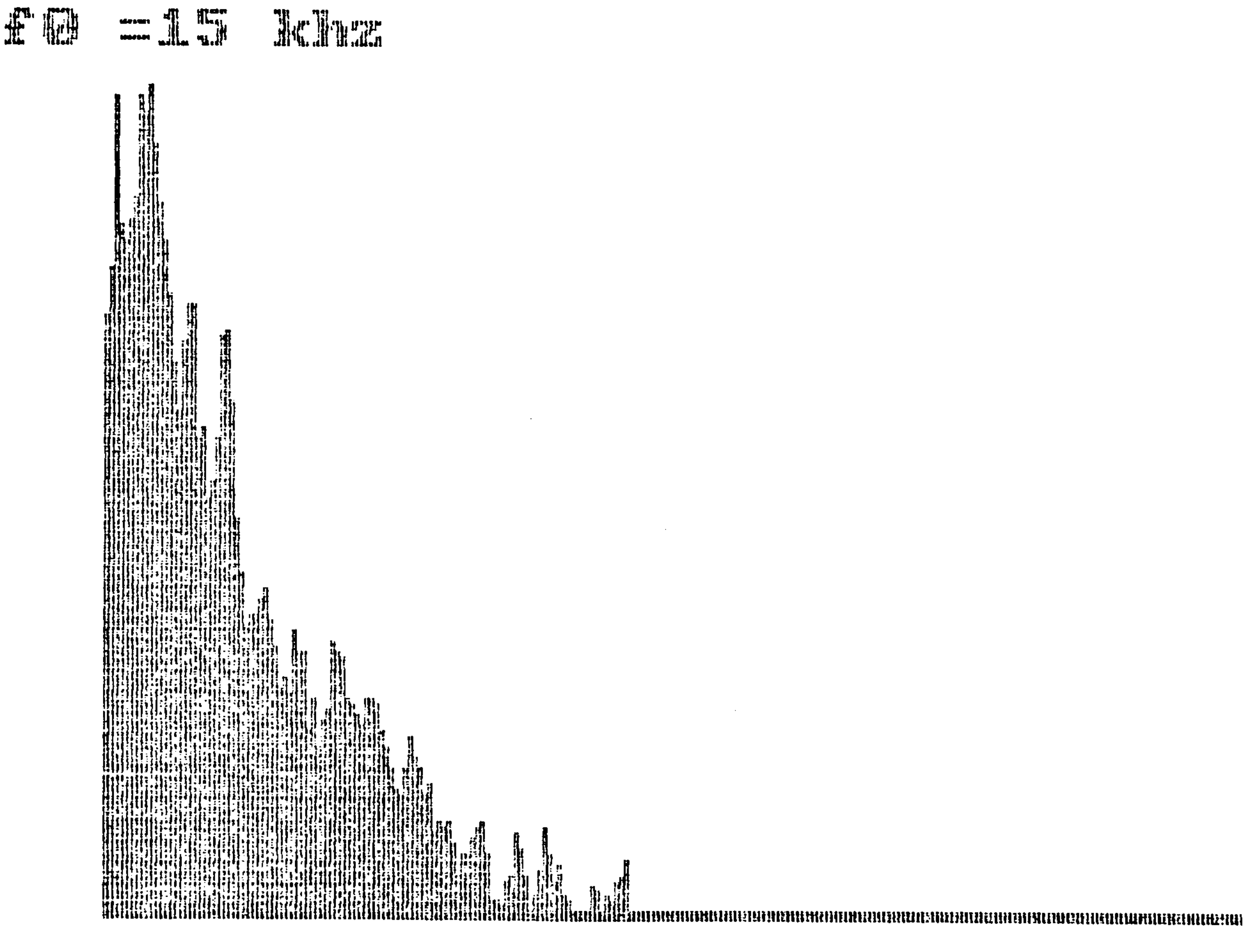

Figure A(69) x = 4" y = 0.375" After Filter

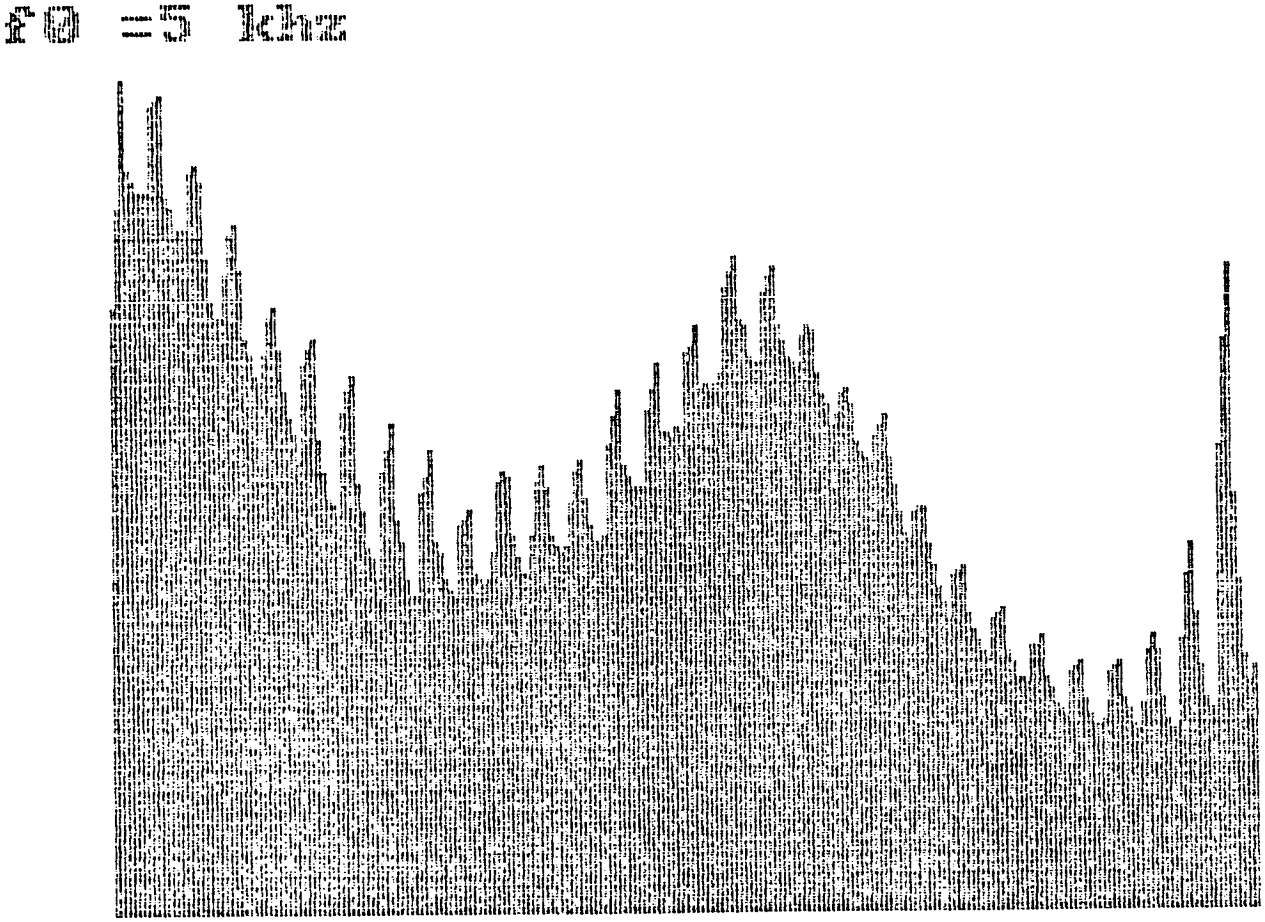

Figure A(70) x = 4" y = 0.25" Before Filter

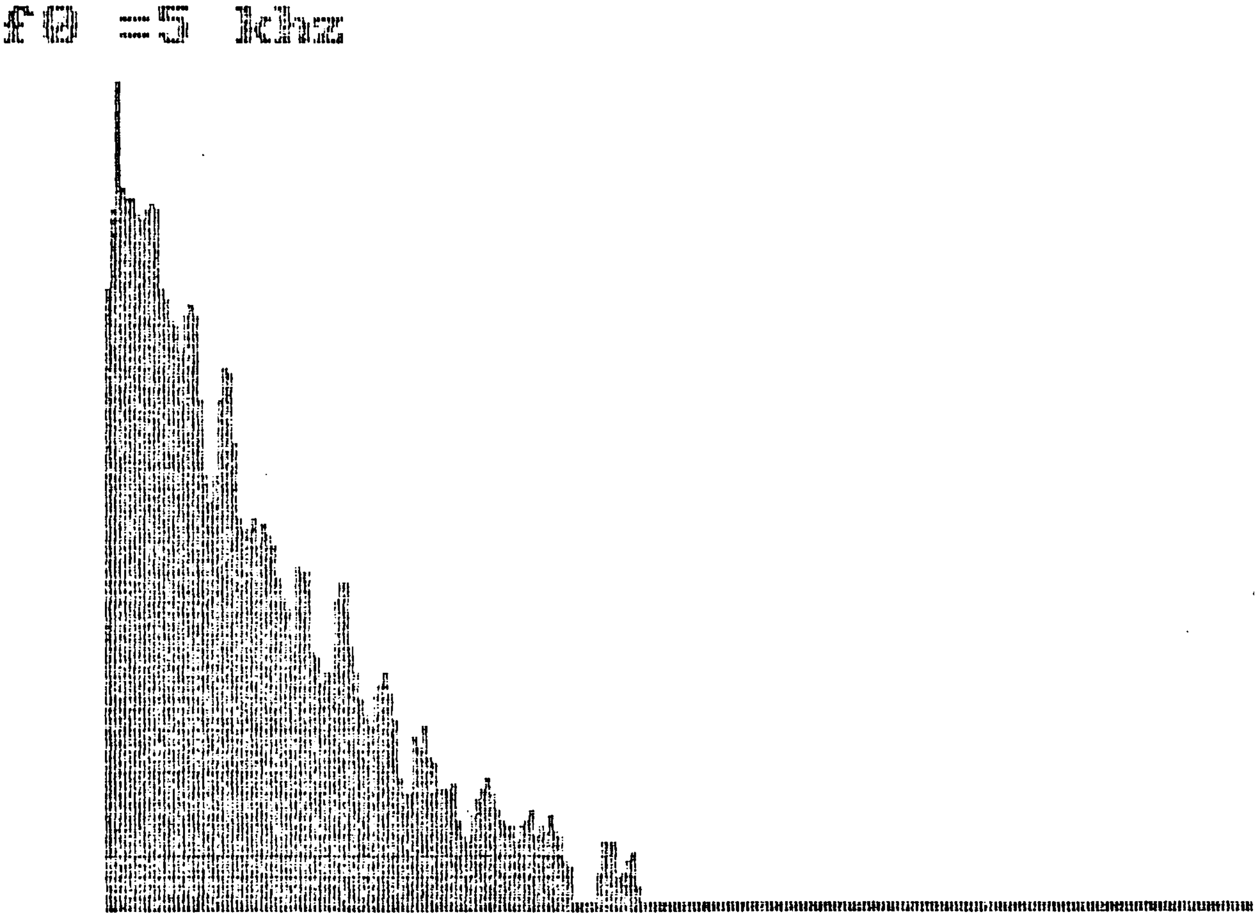

Figure A(71) x = 4" y = 0.25" After Filter

f0 =352 khz

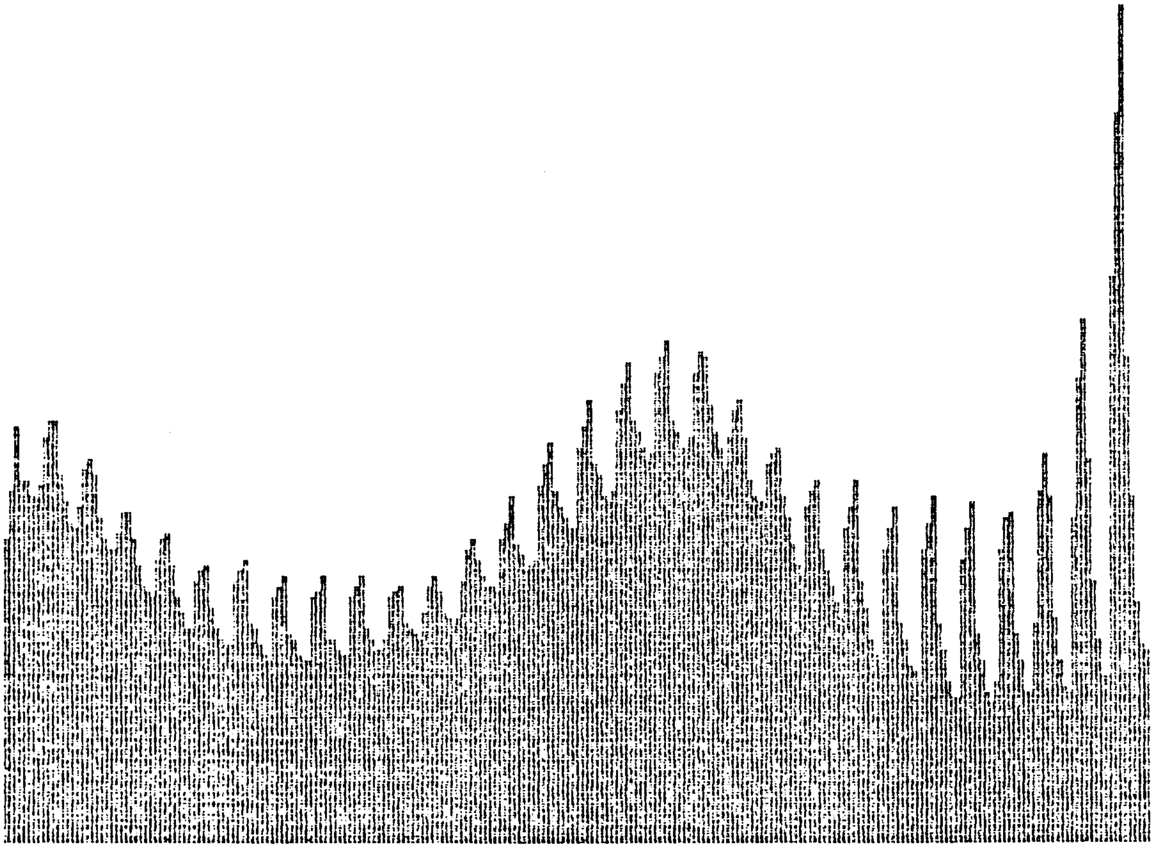

Figure A(72) x = 4" y = 0.125" Before Filter

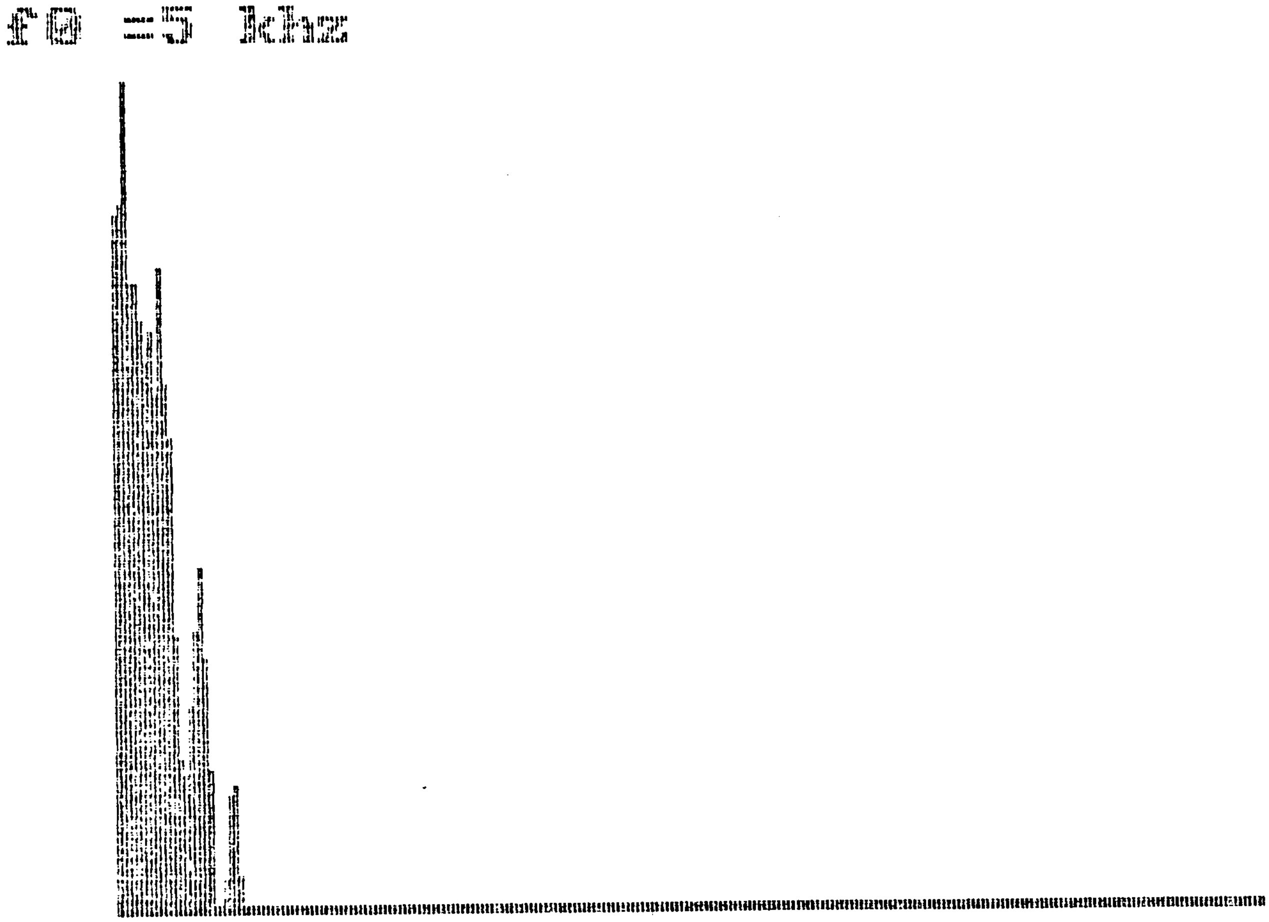

Figure A(73) x = 4" y = 0.125" After Filter

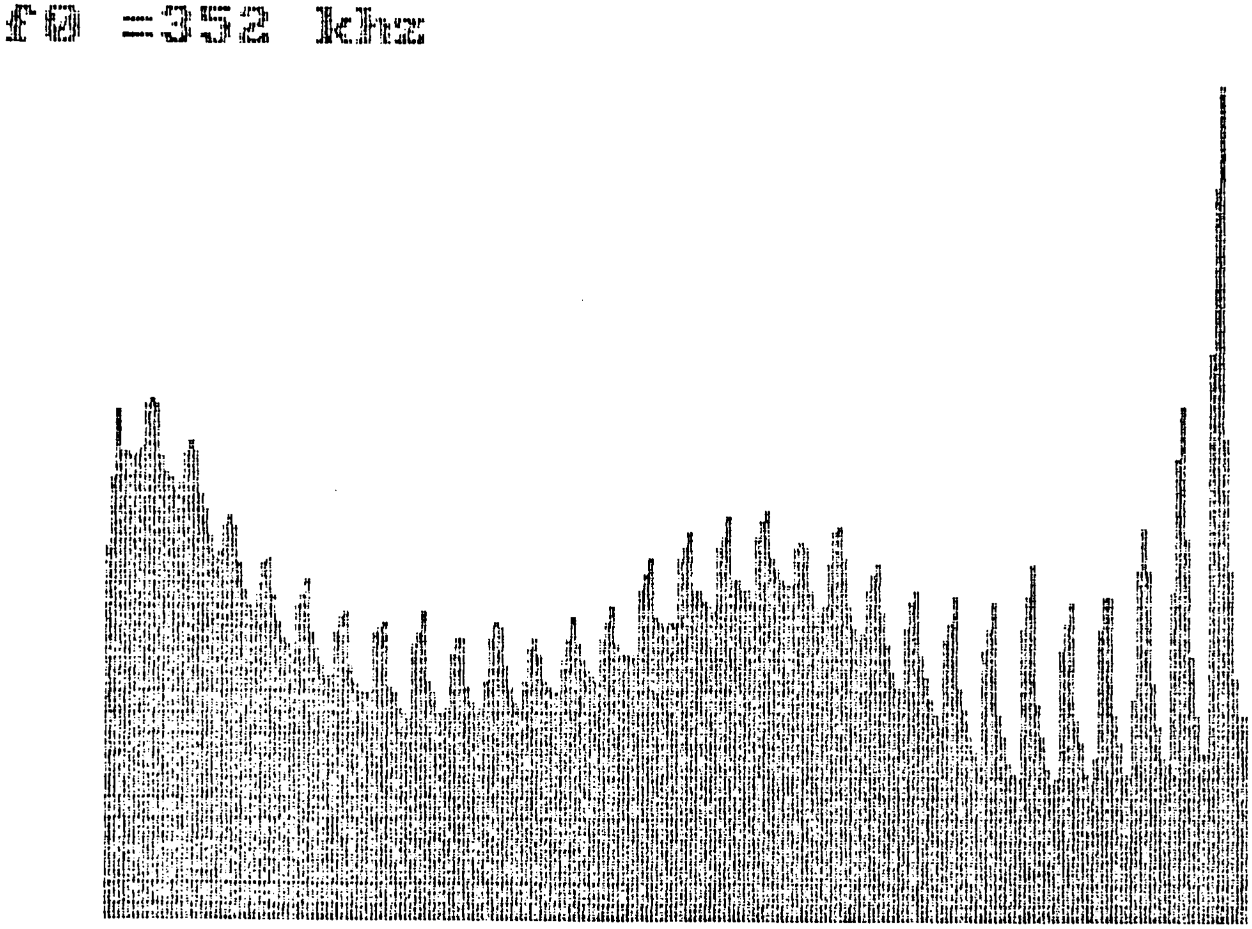

Figure A(74) x = 4" y = 0.0" Before Filter

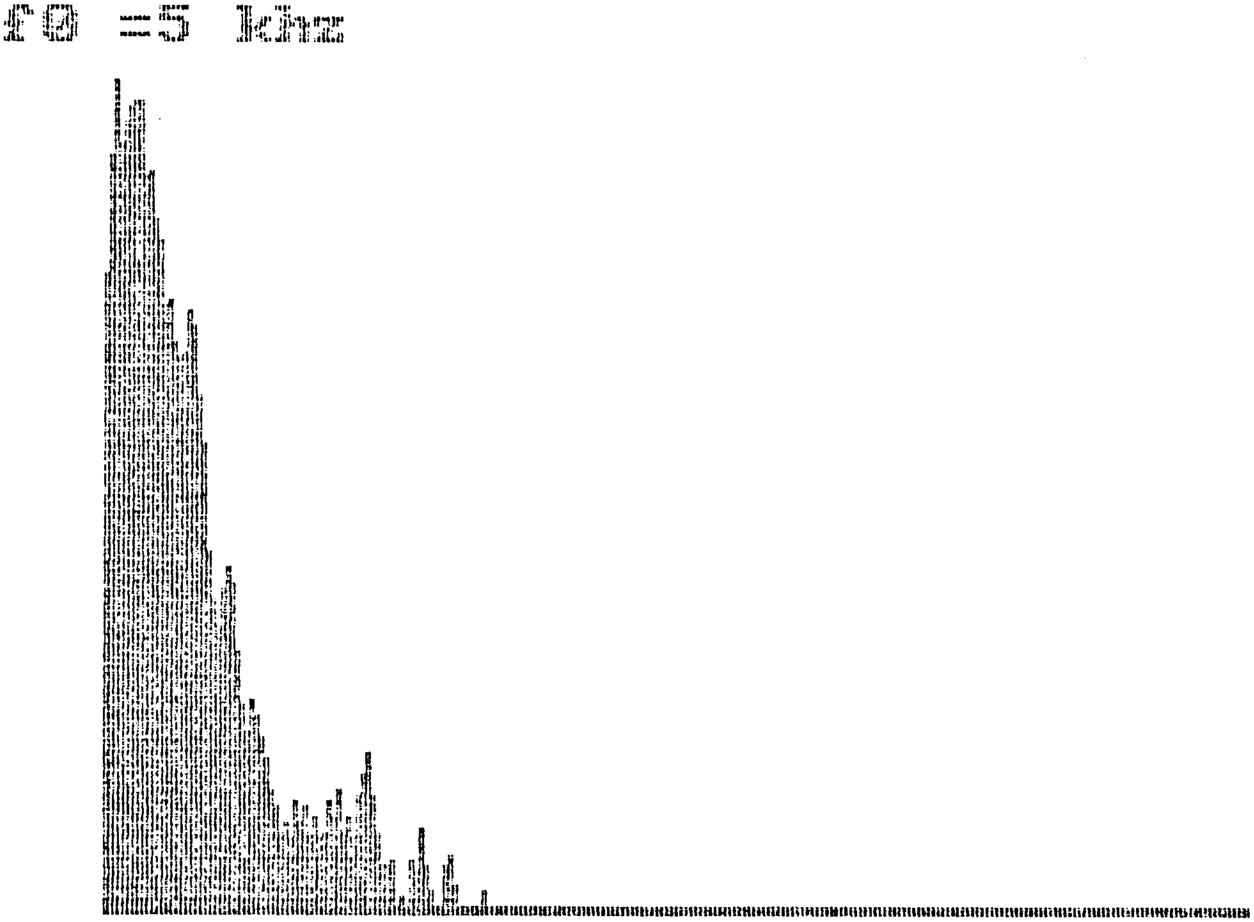

Figure A(75) x = 4" y = 0.0" After Filter

Standard Bibliographic Page

1. Report No.
NASA CR-178109

2. Government Accession No.

3. Recipient's Catalog No.

4. Title and Subtitle
"Feasibility Study of Optical Boundary Layer Transition
Detection Method"

5. Report Date
June 1986

6. Performing Organization Code

7. Author(s)
M. Azzazy, D. Modarress, and J. D. Trolinger

8. Performing Organization Report No.
SDL No. 85-2285-47F

9. Performing Organization Name and Address
Spectron Development Laboratories, Inc.
3303 Harbor Blvd., Ste. G-3
Costa Mesa, CA 92626

10. Work Unit No.

11. Contract or Grant No.
NAS1-17293

12. Sponsoring Agency Name and Address
National Aeronautics and Space Administration
Washington, DC 20546

13. Type of Report and Period Covered
Contractor Report

14. Sponsoring Agency Code
505-60-21-02

15. Supplementary Notes
Langley Technical Monitor: Robert M. Hall
Final Report for the period 22 February 1983 - 15 November 1985

16. Abstract

A high sensitivity differential interferometer was developed to locate the region where the boundary layer flow undergoes transition from laminar to turbulent. Two laboratory experimental configurations were used to evaluate the performance of the interferometer: open shear layer, and low speed wind tunnel turbulent spot configuration. In each experiment, small temperature fluctuations were introduced as the signal source. Simultaneous cold wire measurements were compared with the interferometer data. The comparison shows that the interferometer is sensitive to very weak phase variations in the order of 0.001 the laser wavelength.

An attempt to detect boundary layer transition over a flat plate at NASA-Langley Unitary supersonic wind tunnel using the interferometer system was performed. The phase variations during boundary layer transition in the supersonic wind tunnel were beyond the minimum signal-to-noise level of the instrument.

17. Key Words (Suggested by Authors(s))
Boundary Layer - Transition

Interferometry

18. Distribution Statement
Unclassified - Unlimited

Subject Category 34

19. Security Classif.(of this report)
Unclassified

20. Security Classif.(of this page)
Unclassified

21. No. of Pages
180

22. Price
A09

For sale by the National Technical Information Service, Springfield, Virginia 22161

NASA Langley Form 63 (June 1985)